

MORTEN DAM JØRGENSEN

EXOTIC
LONG-LIVED
PARTICLES

THIS THESIS HAS BEEN SUBMITTED TO THE PHD SCHOOL
OF THE FACULTY OF SCIENCE, UNIVERSITY OF COPENHAGEN

Morten Dam Jørgensen

The Niels Bohr Institute

University of Copenhagen

2100 Copenhagen Ø

Denmark

E-mail: mdj@mdj.dk

Copyright © 2014 Morten Dam Jørgensen

WWW.MORTENDAM.COM

First printing, April 2014

K^+ Ξ^0 Λ Ξ^- Σ^- K_S Ω Σ^+ Ξ^0 Λ $D^+ D_s$ B B_s B_c^+ D^0 τ Λ_c Ξ_c^0 Ξ_c^+ Ξ_{cc}

Abstract

A search for hadronising long-lived massive particles at the Large Hadron Collider is conducted with the ATLAS detector. No excess events are found. Based on statistical analysis, upper limits on the production cross section are observed to be between 0.01 pb and 0.006 pb for colour octet particles (gluinos) with masses ranging from $300 \text{ GeV}/c^2$ to $1400 \text{ GeV}/c^2$, and 0.01 pb to 0.004 pb for colour triplet particles (stops and sbottoms) with masses ranging from $200 \text{ GeV}/c^2$ to $900 \text{ GeV}/c^2$. In the context of Supersymmetry with decoupled sfermion and sboson sectors (Split-SUSY), this gives a lower limit on the gluino mass of $989 \text{ GeV}/c^2$, and $683 \text{ GeV}/c^2$ for the stop mass and $618 \text{ GeV}/c^2$ for the sbottom mass.

In addition, a new method is presented that improves the speed (β) estimation for long-lived particles in the ATLAS tile calorimeter with a factor of 7 improvement in resolution at low- β and a factor of 2 at high- β . An additional advantage of the new method is that the β -response is flat within the range of acceptance ($0.2 < \beta \leq 0.9$) with an average β -resolution of 2.2%. The resolution of the speed estimate using the ATLAS pixel tracker has been improved by a factor of 3 at low β to a factor of 2 at higher β . The new method also introduces a flat response compared with previous methods.

Furthermore, a simulation of magnetically charged monopoles is conducted. Based on simulation, magnetic monopoles with Dirac charges $g_D > 10$ will predominantly be trapped in the LHC beam-pipe if produced within ATLAS. Two regions are identified as optimal for the extraction of the beam-pipe in a magnetometer-based search.

Finally, a contribution has been made to the proposed IceCube low-energy extension called PINGU which will improve the neutrino sensitivity to $E_\nu \sim 1 \text{ GeV}$. Motivated by indirect searches for Dark Matter annihilation in the sun, a likelihood based reconstruction method is developed that allows neutrino interaction vertex, energy, and direction estimation at this energy. The method provides a fast estimate based on a newly developed parametric model and multi-dimensional nested sampling. In addition, two neutrino flavour detection algorithms are developed which allow separation of charge-current muon events from other neutrino events.

Resumé

Eksistensen af massive partikler med lang levetid og farveladning er blevet afsøgt ved hjælp af the Large Hadron Collider og ATLAS detektoren ved CERN. Der er ikke fundet evidens for sådanne partikler. En statistisk analyse af resultatet har ledt til en øvre grænse for produktionstværsnittet af farve-oktet partikler (gluinoer) på mellem 0.01 pb og 0.006 pb for partikel masser i intervallet $300 \text{ GeV}/c^2 - 1400 \text{ GeV}/c^2$. For farve-triplet partikler (stop og sbottom) med masser i intervallet $200 - 900 \text{ GeV}/c^2$ er produktionstværsnittet mindre end 0.01 – 0.004 pb, disse grænser antager et konfidensinterval på 95%. Under hypotesen, at der er tale om Supersymmetriske partikler, hvor sfermion og sboson sektorerne er uforbundede (Split-SUSY), kan disse produktionsgrænser tolkes som grænser for minimum massen for hhv. gluinoer, stops og sbottoms. Gluinoer med masse mindre end $989 \text{ GeV}/c^2$, stops med masse mindre end $683 \text{ GeV}/c^2$ og sbottoms med masse mindre end $618 \text{ GeV}/c^2$ er udelukkede.

Hertil er en ny metode udviklet, der forbedrer hastighedsestimeringen (β) i forbindelse med partikler med lang levetid. Metoden forbedrer hastighedsopløsningen i Tile-kalorimeteret i ATLAS med en faktor 7 for lave β værdier og en faktor 2 for høje β -værdier. Den nye metode giver et fladt response med konsistente β -estimer i intervallet ($0.2 < \beta \leq 0.9$) med en middel β -opløsning på 2.2%. β -opløsningen i forbindelse med ATLAS' Pixel Tracker er også forbedret med en faktor 2 – 3 i forhold til tidligere metoder. Her er β -response også fladt i samme interval som for Tile-kalorimeteret.

Derudover er en simulation foretaget af magnetisk ladede monopoler. Simulationen viser at monopoler med en Dirac-ladning $g_D > 10$ typisk vil stoppe i LHCs vakuum rør før de når instrumenteringen i ATLAS. To regioner er blevet identificeret som optimale for en magnetometerbaseret analyse.

Bidrag til den nyeligt foreslåede IceCube opgradering kaldet PINGU er præsenteret. Vha. PINGU kan man undersøge eksistensen af Mørkt stof ved indirekte at observere neutrino fluks fra solen. Bidragene er i form af en ny teknik til rekonstruktion af neutrino energi, retning og interaktionspunkt i PINGU detektoren. Teknikken bygger på en parametrisering af signalpropagationen i IceCube. To teknikker udviklet til genkendelse af neutrino typer er også præsenteret.

Preface

Everything we see around us is made of particles. As we don't see many things popping in and out of existence it may sound unintuitive that most particles studied by physicists today, are so fleetingly short-lived that they barely exist, before fragmenting into less-massive particles. The particles that remain, for at least awhile once produced, we call *long-lived*. Before we get to such specifics, an explanation may be in order, for what are particles, and how do we relate a solid object such as a tree or a rock to them?

At its surface a rock is cold or warm, rough or shiny, most are heavy compared to other things but the weight varies as well. The physics of stones, plants and people are basically the same, but to understand that we must make a series of jumps in scales. Take your hand for example. It is made of cells, which again contains many things needed to sustain and replicate them. These things such as DNA, are again made of molecules, which are more or less complex arrangements of atoms. Molecules can exist because it is possible for atoms to share one or more *electrons*, the first fundamental particle we'll meet on our journey. Electrons have certain properties such as electric charge a specific mass and other properties discovered during the twentieth century such as *particle spin*.

Electrons are also long-lived (or more likely completely stable). Electrons while not entirely massless, are but tumbleweed compared to the atomic nucleus. The nucleus of atoms contains densely packed protons and neutrons each nearly 2000 times heavier than an electron. Like the Sun fixating our planetary system so does the nucleus create a point around which we are likely to find electrons. The exact location of the electrons are not well-defined, contrary to the precise astronomical predictions we have on the planetary bodies in our solar system. A special kind of behaviour described by *Quantum Mechanics* governs the movement and properties of electrons and also nuclei. Here at the scales 10^{10} times smaller than what we usually think of, the laws of nature are not deterministic. At the atomic scales, physics is probabilistic in nature; if there is a chance that an electron can be somewhere, however improbable, it still can happen. Modern technology such as computers and light emitting diodes are based on this quantum mechanical principle. The reason electrons keep within the vicinity of the nucleus, is that they all have electric charge. The electrons are negatively charged while the protons in the nucleus are positively charged. The mutual attraction of these particles binds the atom together. "Squishy splashy matter" (at room temperature) such as water are bound together not by explicitly sharing electrons¹ but rather by some of the charge in one atom to be attracted to some of the charge in another forming a loose bond² (Figure 1).

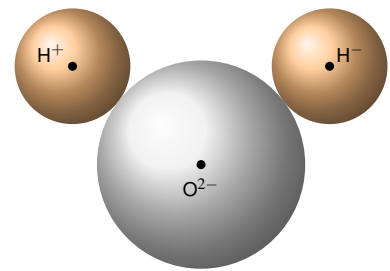


Figure 1: A water molecule consisting of two hydrogen atoms and a oxygen atom is bound by the Van der Waals force or 'residual electric force'. The reason why the atoms stick together is that their geometry produces a dipole (like a magnet) even if the individual atoms are neutral. A similar residual force binds protons and neutrons in the nucleus of atoms.

¹ Called covalent bonds

² Ionic bonds is another type of charge-sharing where ions (atoms missing or having additional electrons making them non-neutral) are electrically attracted to each other.

Why this is relevant to particle physics and not just biochemists, is because of its resemblance to what happens inside the nucleus. Having a bunch of protons packed together is like trying to stick the positive poles of two magnets together, they don't really want to do it a whole lot. As opposite attract, identical repulse. Something much stronger than the electric force must keep the protons bound together. What keeps the nucleus bound is called the *Nuclear Force*, which is a residual force from something called the *Strong Force* that binds the constituents of the protons together. Neutrons are made of the same constituents as protons but in a mixture that cancels its electric charge, it therefore helps containing the positive protons by "adding" more of the nuclear force relative to the electric force. The constituents of the nuclei are called *quarks*. Like electrons quarks are also believed to be fundamental particles without further structure inside. Quarks have both electric charge which comes in fractions of the electron's charge and also another type of charge called *colour*. Like the pixels on your phone screen the name colour is inspired by the fact that not one type of charge but three, are needed to explain the behaviour of quarks. Quarks have never been seen to roam around alone, they are always bound together to form colour neutral objects such as protons and neutrons, we call this sad lack of independence on their behalf for *confinement* which is a defining feature of the physics of quarks called *Quantum Chromodynamics*. While quarks don't get out much, they have excellent recreative opportunities within their confines. Unlike gravity and the electric forces that becomes stronger at short ranges, the strong force in some sense becomes weaker at short distances. This behaviour called *asymptotic freedom*, effectively means that quarks are freely interacting particles when observed at short ranges. Short ranges translates into high energies in particle physics, and that let's us jump to the experimental side of this story.

When tying a bolt or sewing with a needle, the tool and the material must match in scale. When looking at bacteria in a microscope the light reflecting of the organism must also have a shorter wavelength than the details we want to observe. Visible light such as red light is 0.7 micrometers in wavelength allows us to discern feature about half that length. A virus is only around 0.1 micrometer in diameter and visible light is no longer sufficient if we want to study its details. One of the neat things about quantum mechanics is that particles was found to have *wave-like* properties and waves (light is electromagnetic waves) particle properties. So if the wavelength of the visible light is too long for viruses what is then the wavelength of an electron? It depends on the speed of the particle, but *electron microscopes* typically have a hundred thousand times more resolving power than optical telescopes. To study the constituents of atoms, nuclei and perhaps quarks the wavelength of the incoming particle must be shorter than the scale of the object we wish to study. We "tune" this wavelength by accelerating particles to very high speeds increasing their momentum enough to penetrate and resolve details smaller than the size of protons. The length scales of modern collider 'microscopes' are around 10^{-18} m which is why we haven't seen any details of the particle world with earlier methods. It is also the reason why we continue to build new larger accelerator facilities around the world, there is no knowing what lies further within, it is a quest for the deepest knowledge, we know how to collect from nature.

At the very other end of the distance scale is the universe we inhabit. Strange as it may sound, the smallest and the largest is intimately linked. That the universe at some point in history was much denser energy wise is by now common knowledge. The ‘Big Bang’ is a likely conclusion when we extrapolate all observations of the cosmos back in time. The extremely high energy densities that must have been our universe at its birth resembles the collision energies studied with particle colliders. Our colliders are hence not just microscopes but also telescopes and time machines, for they tell us the story of the birth and early development of our universe. Cosmos also holds mysteries that astrophysicists hope can be solved by particle physics. A force feeble next to the nuclear and electromagnetic force is *gravity*. Astrophysicists have known and studied the motion of celestial objects long before the birth of any other science, and gravity was the earliest modelled force of nature. Nevertheless there is something amiss in our universe if we are to believe *General Relativity*, the current theory of gravity. It seems that gravity is overrepresented compared to the visible mass out there, the missing mass is simply called *dark matter*. Among other things dark matter must be long-lived, moderately massive but also invisible to light sensitive detectors. If dark matter *is* matter it may be something particle physicists can find, at least indirectly, at collider experiments.

At the Large Hadron Collider (LHC) at CERN in Geneva we are collecting data from billions of proton collisions. The collision energies are the highest humanity has ever achieved, and it opens up for the discovery of new particles such as dark matter and other particles. One class of such new particles, are the ones that are long-lived. They, like protons and electrons, have “reasons” not to decay into simpler particles. These reasons are normally ascribed to a conserved quantity such as electric charge mentioned earlier. Conserved quantities are the product of a deeper idea called *symmetry*. All actions in nature that returns the object under manipulation to its original state is called symmetry transformations. As we will see in later chapters, this by definition implies that some conserved quantity must exist. As conservation means that it is hard if not impossible to get rid of a specific quantity, some stable particle must carry the quantity for no other reason than that the quantity is “more stable” than the particle. In this thesis it is assumed that some currently undiscovered particles for various reasons are long-lived. It is not of much concern exactly why this is, before a potential discovery. That said, mankind has always wondered about what *could be* out there, and plenty of such suggestions have been produced. These would-be theories such as *Supersymmetry* and *Extra Dimensions* help serve as guiding predictions for experimental searches.

My work the last three years have taken me through the search for long-lived particles in various forms. What these forms have in common is that technical imagination have lead to better ways of looking for such particles. *The thesis* is, that by imagining what such particles would do to matter it moved through, it is possible to devise methods of observing them. Based on these methods we search and either discover or exclude (under specific circumstances) the existence to new particles.

Outline

The attempt of this thesis is to connect a series of studies I took part in during my time as a PhD student at the Niels Bohr Institute in Copenhagen, Denmark. Some parts are omitted for instance a short study on the *Angular distributions of $H \rightarrow ZZ \rightarrow 4\mu$* [70] and are very educational study on how to *reconstruct charged particles with high-resolution CMOS pixel sensors*. The remaining three subjects I have worked on are: charged long-lived particles, trapped magnetic monopoles and neutrino event reconstruction and identification. These remaining subjects are covered in this thesis in more-or-less the time proportion I have been working with them.

Five parts constitutes this thesis. The first part *Searches for long-lived massive particles and theoretical motivations* in an introduction to the theoretical and phenomenological nature of long-lived particles in the context of the Standard Model and new theories, in particular Supersymmetry. The part closes with a listing of previous searches for long-lived particles.

The second part *Principles of particle detection* provides a review of common ways particles can interact with matter, and how these interactions are measured with detectors in ATLAS (and IceCube). The production of colliding particles is discussed in a chapter dedicated to the Large Hadron Collider.

In the third part *Searches for long-lived particles with ATLAS at the LHC*, my work on long-lived particle searches with ATLAS is presented. The initial chapters in this part of the thesis involves the development and improvement of two types of particle speed estimators that are crucial in searches for long-lived particles in ATLAS. The last chapter is a review of a search we conducted for coloured and charged long-lived particles (R-Hadrons) with LHC data recorded in 2011 [111]. The search evolved from a similar search done in 2010 [105] with my participation.

The next part, *Prospects for future searches with ATLAS at the LHC* studies how far the continued search for long-lived particles in ATLAS can be expected to be sensitive given a specific model assumption. A simulation study of the acceptance of magnetic monopoles trapped in the LHC beam-pipe after being produced within ATLAS [83] closes the part.

A very different avenue of research is pursued in *Low mass dark matter detection with IceCube*. The IceCube neutrino detector at the South Pole is already actively searching for Dark Matter with high masses. An upgrade called PINGU [122] will enhance the sensitivity to low-mass Dark Matter, a region of contested interest due to intriguing results from other experiments. My work in this part is very practical and focused on how to detect and reconstruct neutrinos that indirectly can point to dark matter annihilation within the Sun.

The author's contributions and acknowledgements

The work described in this thesis is done by me with the exception of the estimation of systematic uncertainties in Section 9.6. That being said none of the work I have done could be possible without considerable collaboration and contributions from many sources. It will not do my collaborators enough justice to simply claim some area as specifically mine alone, fruit-

ful scientific ventures are collaborations where ideas are formed with equal inspiration and perspiration from others. Nevertheless I hope to claim responsibility over the following areas without overstepping my bounds too much:

- Long-lived particles in ATLAS
 - Introduction of a common data-format for long-lived particles searches in ATLAS (now called LLP-D3PD and maintained by Sascha Mehlhase).
 - Design and implementation of Calorimeter dE/dx estimators [63].
 - Improvements to Pixel detector dE/dx speed estimation (Chap. 7).
 - Improvements to Tile Calorimeter Time-of-Flight estimation (Chap. 8).
 - Initial input to monte carlo signal definitions, trigger selection and pre-selection (Sec. 9.3).
 - Design and implementation of Event selection (Sec. 9.4).
 - Implementation of a Data-driven background estimation based on earlier works by others, (in particular Troels Petersen) (Sec. 9.5).
 - Computation of theoretical cross sections and integrated luminosity (Sec. 9.2.2).
 - Statistical hypothesis testing, computation of upper limits (Sec. 9.7).
 - Production of fancy limit plots (Sec. 9.8).

This leaves out important work in the calibration of estimators, production of data files, estimating systematic uncertainties and not least handling the editorial work of our publication. For these tasks I have been happy to work with Troels Petersen, Sascha Mehlhase, Simon Heisterkamp, Martin Spangenberg and our colleagues at Technion in Israel and Genova in Italy.

- Trapped Magnetic Monopoles
 - My contributions to this work was mostly in thoughts and ideas during the practical tests done at ETH In Zurich.
 - Some initial data analysis was done by me
 - The study in Section 10.3 is entirely new and only inspired by our publication.

This study was to me an excursion into alternative experimentation and taught me a great deal about how smaller studies are conducted. I am deeply grateful to David Milstead and Philippe Mermod for letting me ‘tag along’ on their venture. During the work for this thesis, Terry Sloan helped with insights into the dynamics of monopole energy loss and I thank him for his very helpful and prompt guidance.

- IceCube-PINGU Reconstruction
 - All methods described in this thesis (Chap. 11) are designed, developed and implemented by me, the Event Shape method was proposed by Troels Petersen.

My PINGU work was done in the last year of my study. The backstory is that I wanted to try something else than ATLAS physics after having contributed to two analyses. The seemingly infinite patience of my supervisor Troels Petersen allowed me this opportunity, when he suggested that I could join PINGU which Denmark at that time way hoping to join. As the new ‘Dane’ in IceCube, D. Jason Koskinen became my *de facto* co-supervisor who helped me with access and explanations of the workings of IceCube before he arrived for his position at the Institute in august of 2013. None of the projects I have undertaken in PINGU have seen fruition yet (neither has the experiment) but hopefully the work I have initiated will be continued by others. Joakim Sandroos, a current research assistant at our group has taken over on one of the particle identification methods (Event Shapes Sec. 13.2) and I hope it will show its usefulness in time.

- MIMOSA CMOS Pixel detector reconstruction

In the interim period between ATLAS and IceCube I found work in studying track reconstruction in beam telescopes. As a research project it proved ultimately unsuccessful, but the lessons learned, inspired the work on simulation and reconstruction at PINGU. The study was based on detectors purchased by our group here at the Niels Bohr Institute from the University of Strasbourg. The sensors were given to Ulrik Uggerhøj’s group at the University of Aarhus, where they constructed a beam telescope, a custom magnet and performed tests with the setup at SPS CERN. Ulrik and his PhD students Tobias Nyholm Wistisen, Kristoffer Andersen and Rune Mikkelsen all helped by providing insight into the setup and workings of their telescope and not least access to their raw data.

My first and foremost acknowledgement is to Troels Petersen who as my supervisor have given me opportunity to develop my own research interests and provided valuable feedback, inspiration and no small amount of patience.

Work in high-energy physics is done in collaborations based on the infrastructure designed by collaborations, supported by nations of nations – in short, a full acknowledgement is beyond the scope of this small section. Nevertheless I will like to thank my collaborators in ATLAS, IceCube and the LHC accelerator team for their structural support and for providing an exciting possibility for studying phenomena scarcely imaginable by people living just a generation or two back. I would also like to thank the Lundbeck foundation for supporting my study through their Fellowship grant, awarded to my supervisor Troels Petersen.

For editing and proofreading this thesis I would like to thank Almut Pingel, Jørn Dines Hansen and Troels.

Having been part of the local ATLAS (and recently IceCube) group at the Niels Bohr Institute for nearly seven years has meant a lot to me. It is hard to understate the formative experience of being in such an environment for that long, I cannot mention all the present and recent members of the group during my time here, but aside from the ones already mentioned; Jørgen Beck Hansen, Mogens Dam, Stefania Xella and Peter Hansen have all been great mentors and colleagues for an aspiring physicist.

This thesis as a PDF file, illustrations, source code and personal
datasets are available at:

<http://llp.gluino.com>

Contents

Abstract 5

Resumé 7

I Searches for long-lived massive particles and theoretical motivations

- 1 On the longevity of particles 23
- 2 The Standard Model 27
 - The particle content of the Standard Model 27
 - Electroweak theory 27
 - Quantum Chromodynamics 29
 - Long-lived particles in the Standard Model 30
 - Neutrinos 32
- 3 Proposed models with massive long-lived particles 39
 - A need for a new theory 39
 - Supersymmetry 40
 - Split-Supersymmetry 46
 - Other models with LLPs 46
 - Dark matter 48
 - Previous searches 50
 - Conclusion 51

II Principles of particle detection

- 4 Particle detection and identification 55
 - Electromagnetic interactions 55
 - Hadronic interactions 62
 - Particle identification 63
 - Summary 67

5	The Large Hadron Collider	69
	Hadron Colliders	69
	The CERN Accelerator Complex	70
	Luminosity	72
6	The ATLAS detector	75
	The Magnet system	77
	Tracking system	78
	Calorimeters	81
	Muon system	83
	Speed estimation in ATLAS	86

III Searches for long-lived particles with ATLAS at the LHC

7	Pixel based mass estimator	89
	dE/dx from the pixel detector	89
	Pseudorapidity correction	95
	Mass estimation	97
	Results	100
	Conclusion	104
8	Calorimeter β estimation with ATLAS	105
	The Tile calorimeter	105
	Simulation of signal samples	107
	Characteristic features of LLPs	108
	Calorimeter based time measurements for SMP detection	108
	Correction to CaloCell time	111
	Projective correction for cubic calo cells	114
	Combined result	116
	Summary	117
9	Search for long-lived coloured particles in ATLAS with 2011 LHC data	121
	Introduction	122
	Data and Simulated samples	124
	Trigger Selection	134
	Event Selection	137

Background Estimation	145
Treatment of Systematic Uncertainties	148
Statistical interpretation	150
Results	152
Conclusion	153

IV Prospects for future searches with ATLAS at the LHC

10 Future searches for Long-lived particles at the Large Hadron Collider	159
The LHC in 2015	159
Future sensitivity to Split-Supersymmetry with ATLAS	161
Trapped monopoles	166
Conclusion	170

V Low mass dark matter detection with IceCube

11 IceCube and PINGU	175
Detectors	177
PINGU	177
12 Fast neutrino reconstruction with PINGU	179
Modelling light propagation in ice	179
Preliminary results	184
Outlook and conclusion	185
13 Particle identification of low energy neutrinos with PINGU	187
Superluminal hits	187
Global Event Shapes	188
Conclusion	190
14 Thesis conclusion	191

VI Appendices

A Schematics	195
References	206



*Searches for long-lived
massive particles and
theoretical motivations*

The theme of this thesis is Long-Lived massive Particles (LLPs). Commonly, they are also termed ‘metastable’, ‘detector-stable’ or simply ‘stable’ particles. The confusion is remedied by a common definition, they are particles that are *stable at the scale of observation*, i.e. they decay outside the particle detector instrumentation. This criteria means that we can measure their properties directly instead of studying effects of secondary particles from their decay, as is normally the case in collider experiments.

Whether or not a particle decays within a certain length, is determined by a combination of the particle’s lifetime at rest and the speed with which it travels relative to the detector. The lifetime of a particle at rest is $\tau = \hbar/\Gamma$, where Γ is the total width of the particle (see sec 2.4.1). For a particle in motion this translates into a traversed distance¹

$$c\tau \sim \frac{c\beta\gamma\hbar}{\Gamma}. \quad (1.1)$$

The general purpose detectors at the LHC are $\mathcal{O}(10 \text{ m})$ in radii, which corresponds to a total width $\Gamma_{stable} \sim 10^{-17} \text{ GeV}$ for non-relativistic particles.

General purpose particle detectors such as ATLAS and CMS are designed to measure and identify SM long-lived particles. These are the indirect signatures recorded to reconstruct properties of rapidly decaying massive particles such as Higgs bosons or top quarks. To clearly distinguish the long-lived particles in the SM from the ones presented in this thesis, we note that no SM particles with a rest mass larger than $2 \text{ GeV}/c^2$ is considered long-lived at the LHC, whereas the particles we are hunting weigh in excess of $200 \text{ GeV}/c^2$, and we could call them ‘long-lived massive particles’. Because accelerator technology has advanced from low to higher energies, new kinds of long-lived particles are typically *massive* in the sense that their masses are larger than any particle type previously observed directly. The last constraint on ‘long-lived particles’ is that they must be electrically observable, carrying either electric or magnetic charge at least at some point in their lifetime traversing the detector. Neutral long-lived particles such as neutrinos can be inferred indirectly from recoil and are naturally just as long-lived but the experimental signature requires an entirely different analysis.

¹ Here c is the speed of light, \hbar is the reduced planck constant, β the particle speed in fractions of c and $\gamma = 1/\sqrt{1-\beta^2}$ the Lorentz boost factor.

Definition: long-lived massive particles are in this context:

- Stable throughout the detector.
- Massive compared to known long-lived particles.
- Electrically or magnetically charged.

Searches for LLPs are motivated by both theories and prior empirical evidence. All matter around us is made of long-lived particles, and when humanity began a deeper search we found new types of long-lived particles such as muons, pions and positrons. From a theoretical point of view long-lived particles are often introduced by necessity into theories through conserved quantities, that are otherwise required to make the theory resilient against obvious faux pas, such as letting protons decay instantly (as in Supersymmetry's R-parity conservation). Even if the theory has an elaborate structure of decays and interactions, the conserved quantity must be either annihilated by its anti-quantity or carried by a long-lived particle.

Chapter 3 will motivate the theoretical reasons for this kind of search and list some of the experimental searches for long-lived particles. The relevance of LLPs in nature as well as in unverified theory makes this type of search an unending endeavour. While relic abundances in the universe, previous searches and excluded models all point towards exclusion of additional LLPs in nature, they are impossible to rule out, due to the extreme nature of these particles.

This work is limited in scope to strongly interacting, electrically charged, detector-stable massive particles while the methodology is kept general enough to cover any search for electrically (multi-)charged particles produced by some mechanism and decaying beyond the calorimeter in most general purpose experiments. This dual scope is sometimes reflected in ambivalent constraints, that is displayed in the analytical workflow (Sec. 9) where a more model specific assumption might have improved a limit but was kept loose to allow wider interpretation of the result.

This leads to the last premise for this kind of experimental work, quantification of the overall sensitivity to a new class of unobserved particles. From the point of view of the experimentalist (me) a search for any new phenomena is a balance between the direct falsification of a specific hypothesis posed by a theory and the minimisation of theoretical bias tainting the possibility of detecting the unexpected. Searches for long-lived particles are entirely detector driven, no model of associated production is really needed as long as we can guarantee the purity of the objects we want to observe. As massive LLPs have no natural background a null experiment can be set up without knowing anything more about the object, than the detection efficiency and mis-identification probability, both numbers that can be estimated from simple studies of already known objects.

Even with the possibility of a 'zero-signal-model' search for anything beyond the Standard Model, we tend to rest our searches on some basic phenomenological model. This lets us guide the search in regions where nothing similar to the signal hypothesis exists. The signal studied in this thesis exhibit the same signatures as low-mass protons or kaons but at much higher mass. This reoccurrence allows for the signal optimisation without a signal model. In practice some estimators such as Time-of-Flight (ToF) are impossible to use with less massive particles as the detector systems involved are destructive to the very same particles we want a time measurement from.

The theoretical model applied to the LLPs in this work, is based on the hypothetical framework called Supersymmetry – lending particle names such as 'gluinos', 'stops' and 'sbottoms' to what is simply colour octets and

triplets. The actual simulation of what these objects will do in our detector, is only considering the colour charges and not the underlying hypothesis. This is an important point to remember as the generality of this work is easily lost in supersymmetry definitions. A further point is that searches such as this are inclusive when it comes to mass, charge, spin and so on. Our search is ‘colour-blind’ and only cares for the particles electrical properties. That means that even though hadrons are not charge-stable in the same sense as electrons or other elementary charged particles, they still represent a conservative estimate for these objects, the only difference is a lower detection efficiency. As for multi-charged particles (MCPs), some of the estimators saturates at high levels of ionisation easily induced by MCPs which limits the sensitivity somewhat (in practice to $|q| \sim 3$ in ATLAS) but otherwise the only difference is the linear underestimation of momentum due to² $p \sim 0.3BqR$. If the momentum is measured to be more than 100 GeV we still observe the new particle but at a systematically reduced mass estimate, a discovery nevertheless.

In summary, this work can be considered a ‘worst case’ scenario on the search for long-lived charged particles, it can be reinterpreted as colour-neutral and/or multi-charged particles as well as coloured particles. At the LHC sufficient resources are available for specific searches but this work and similar ones can serve as unfolding manuals to the willing.

² See Section 4.3.1

p: momentum

B: magnetic field strength

q: particle charge

R: bending radius of the particle track in the magnetic field.

2

The Standard Model

The subject of this thesis is *physics beyond the Standard Model*. Some of it is not even motivated by theoretical predictions, it nevertheless requires knowledge of the current theory to exceed it. That is why this short review of the Standard Model (SM) of particle physics will precede the actual subject matter. I will start by introducing the theory, its constituent particles and some of the interesting complexities. That is followed by a quick listing of shortcomings presented by our ever ambitious, promethean field of physics.

2.1 The particle content of the Standard Model

In the Standard Model both forces and matter are represented as particles. The forces are mediated between matter particles by integer spin bosons. The matter particles themselves are fermions (all spin-1/2) and are either *quarks* or *leptons*. Each of these classes comes in three *generations* with a particle-doublet in each. The generations are progressively more massive (Table 2.1). The leptons are the electron (e^-), the muon (μ^-), the tau (τ^-) as well as three corresponding neutral neutrinos (ν_e, ν_μ, ν_τ). The quarks also form three generations with electric charges ($2/3e, -1/3e$) for each generation. Quarks are confined in hadronic bound states forming either baryons (qqq) or mesons ($q\bar{q}$), fermions and bosons respectively. All particles in the Standard Model have distinct anti-particle counter-parts with opposite electric charge. The neutrinos could be either Dirac or Majorana nature. If they are found to be Majorana particles, they are their own anti-particles. For the electromagnetic force, that couples to charged particles, the photon (γ) is the force mediator. For the weak force three force mediators exist, the neutral Z^0 , the charged W^+ and W^- , all particles in the Standard Model couples to the weak force. The strong force is mediated by eight gluons (g) that couple to quarks (and themselves). The charge they couple to is called colour and comes in three compared to the single charge type of electromagnetism (Table 2.2). Only quarks carry colour charge. The last fundamental particle in the Standard Model is the Higgs boson. It is not a force-carrier per se, but a consequence of the Higgs-mechanism that gives mass to the W and Z bosons.

2.2 Electroweak theory

The Electroweak Theory (EWT) forms the unification of two theories. Quantum electrodynamics (QED) describes the interactions of electrically charged particles and photons, while the Weak force theory describes the flavour

Table 2.1: Fermions in the Standard Model. Grey lines represent generations. All charged particles have opposite sign anti-particles, Ref. [125].

Name	Flavour	Mass [MeV/c ²]	Charge [e]	Colour	Spin [\hbar]
Quarks					
Up	u	2	+2/3	<i>R, G, B</i>	1/2
Down	d	5	-1/3	<i>R, G, B</i>	1/2
Charm	c	1275	+2/3	<i>R, G, B</i>	1/2
Strange	s	95	-1/3	<i>R, G, B</i>	1/2
Top	t	173070	+2/3	<i>R, G, B</i>	1/2
Bottom	b	4180	-1/3	<i>R, G, B</i>	1/2
Leptons					
Electron	e	0.511	-1	0	1/2
Electron-neutrino	ν_e	< 2 eV/c ²	0	0	1/2
Muon	μ	105.66	-1	0	1/2
Muon-neutrino	ν_μ	< 0.19 MeV/c ²	0	0	1/2
Tauon	τ	1776.82	-1	0	1/2
Tau-neutrino	ν_τ	< 18.2 MeV/c ²	0	0	1/2

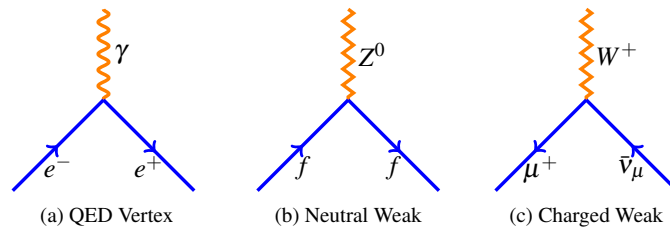
changing nature of weak interactions. The two theories unify at energies $\mathcal{O}(100 \text{ GeV})$ into the electroweak theory. The theory is defined by a $SU(2) \times U(1)$ gauge symmetry.

All interactions between electrically charged particles in QED can be represented in terms of photon exchange (Figure 2.1a). Contrary to QED, EWT allow both neutral particle and charged particle interaction. This is allowed by the neutral Z^0 and the charge carrying W^\pm mediators. In Neutral Current (NC) interactions (Figure 2.1b) a quark or lepton of any type emits a Z^0 that can decay into a charged particle pair or neutrals¹. Charge Current (CC) interactions (Fig 2.1c) are mediated by the charged W^\pm , which allow the W to decay to a single charged particle and a neutral particle², conserving remaining quantum numbers such as Lepton numbers in the classic β -decay: $d \rightarrow u + W^- \rightarrow u + \bar{\nu}_e + e^-$.

¹ The large mass of the Z^0 allow the particle to decay to a variety of particle states (70% hadrons, 20% neutrinos and 10% charged leptons) [125].

² The W^\pm decay into hadrons 70% of the time and $l^\pm \nu$ 30% of the times [125].

Figure 2.1: Fundamental vertices in Quantum Electrodynamics and Electroweak theory.



The lepton sector allows for weak interactions within each generation (allowing $\mu^- \rightarrow \nu_\mu + e^- \bar{\nu}_e$ but not $\mu^- \rightarrow e^-$). In the quark sector, only colour (and the electric charge carried by the W^\pm) is conserved and *flavour* can change, meaning the type of quark. The flavour change is modelled by assuming that the weak force couples to pairs,

$$\begin{bmatrix} u \\ d' \end{bmatrix}, \begin{bmatrix} c \\ s' \end{bmatrix}, \begin{bmatrix} t \\ b' \end{bmatrix} \quad (2.1)$$

where d' , s' and b' are linear combinations of d , s and b quarks, where their

Name	Label	Force	Mass [GeV]	Relative strength	Range ^b [m]	Spin
Gluon	g (x8)	Strong	0	10^{38}	10^{-15}	1
Photon	γ	Electromagnetic	0	10^{36}	∞	1
W	W^\pm	Weak	80.385	10^{25}	10^{-18}	1
Z	Z^0	Weak	91.188	10^{25}	10^{-18}	1
Graviton*	G	Gravitational	0	1	∞	2
Higgs	H^0	— ^a	125.9	—	—	0

mixing coefficients are captured by the CKM matrix:

$$\begin{bmatrix} d' \\ s' \\ b' \end{bmatrix} = \begin{bmatrix} V_{ud} & V_{us} & V_{ub} \\ V_{cd} & V_{cs} & V_{cb} \\ V_{td} & V_{ts} & V_{tb} \end{bmatrix} \begin{bmatrix} d \\ s \\ b \end{bmatrix}. \quad (2.2)$$

2.2.1 Electroweak unification

In the electroweak theory, electromagnetism and the weak interactions are symmetrical at a unification scale around 246 GeV. When at lower energies the symmetry is (spontaneously) broken, we see the ‘difference’ between the two theories expressed by the force-mediating ‘gauge’ bosons in the weak sector gaining mass. The spontaneous symmetry breaking is introduced by the Higgs-mechanism that causes the W^\pm and Z^0 to gain 80 and 91 GeV of mass relative to their massless electromagnetic sibling, the γ . Why does this describe the differences in range and rate of weak decays relative to electromagnetic interactions? A way the fundamental forces are expressed by particles is through the uncertainty principle. By reversing Heisenberg’s equation [132], it allows us to ‘borrow’ an amount of energy ΔE as long as its energy is returned in time Δt , satisfying

$$\Delta E \Delta t \approx mc^2 \Delta t > \frac{\hbar}{2}. \quad (2.3)$$

This particle borrowed from the vacuum is called ‘virtual’ and can be ‘off-shell’, violating energy conservation for a brief time. Rewriting (2.3) we can express the maximum range a massive particle can possibly travel,

$$R \approx \frac{\hbar}{2mc} \quad (2.4)$$

From this we see that a massless particle such as the photon has infinite range³ while the massive W^\pm and Z^0 bosons have a maximum range of $R \sim 10^{-18}$ m. Which relative to the electromagnetic force make it look weak as it suppresses the reaction probability (see the relative ranges in Table 2.2).

2.3 Quantum Chromodynamics

Quantum Chromodynamics (QCD) is manifested as the strong force. It binds quarks together into hadrons, that based on the spin content can be either baryons or mesons. Like the residual electromagnetic force (the Van der Waals force) binds molecules together at atomic scales, so does the *residual strong force* bind protons and neutron together into nuclei. In QCD the conserved charge is colour. While only one type of charge is present in QED three such charges exists in QCD. This gives us an SU(3) symmetry. Photons

Table 2.2: Gauge bosons in the Standard Model.

^a The Higgs boson is not a force exchanging particle.

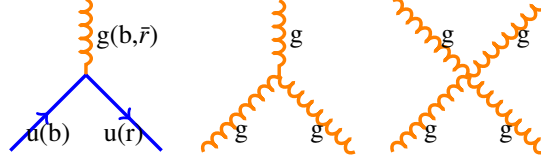
^b The range of the force is calculated as in Sec. 2.2.1.

* The graviton is a hypothetical particle, not a part of the Standard Model (or classic General Relativity) but represents gravity in comparison with the other forces.

Source: Particle Data Group 2013 [125], Griffiths 2008 [55].

³ The story breaks with QCD and the massless gluon. Here asymptotic freedom is enacted to account for the range. Before QCD, H. Yukawa proposed a hypothetical ‘pion’ with a mass around 100 MeV to mediate the force that would leave the strong force range around the observed $R \sim 10^{-15}$ m.

can not carry electric charge itself, that is not the case for the force mediator in QCD; the *gluon* can itself carry colour (and anti-colour). To account for the trinity of charge 8 gluons exists. Because gluons can carry colour, they themselves can form bound states, the *glueballs*. The possible vertices are also a bit more complicated:



Not only does the gluon carry colour pairs, the gluons can bind to themselves, creating a rich combinatorial phenomenology.

Another difference from QED is the way the strong force acts over distance. While the electromagnetic force gets weaker over distance, the strong force just gets stronger. This leads to the concepts of confinement and asymptotic freedom. Quarks are considered free particles at small distance scales, which is called asymptotic freedom. But when quarks are separated from each other, their interaction force is not decreased like in electromagnetism. A new quark pair is created from vacuum to balance the colour field creating new bound states. This leads to confinement as quarks are always found ‘hadronised’ into colour neutral bound states. We will see how this concept is central to the search for long-lived coloured particles in the later chapters.

2.4 Long-lived particles in the Standard Model

Before searching for new kinds of massive long-lived particles, it is instructive to realise that the Standard Model already supplies us with plenty of light long-lived particles. At collider timescales any particle that does not decay before leaving the detector volume⁴, is considered ‘stable’. That means protons, neutrons, deuterons, electrons, muons and neutrinos. Aside from these particles, many baryon and meson states are relatively long-lived.

⁴ If we assume zero stopping power in the calorimeters.

Type	Lifetime τ_0 [s]	Mass [MeV/c ²]
γ^0	∞	0
ν_i^0	$\infty?$	~ 0
e^\pm	∞	0.511
p^\pm	∞	938.3
n^0	881.5*	939.6
μ^\pm	2.2×10^{-6}	105.7
K_L^0	5.1×10^{-8}	497.7
π^\pm	2.6×10^{-8}	139.6
K^\pm	1.2×10^{-8}	493.7
Ξ^0	2.9×10^{-10}	1314.8
Λ^0	2.6×10^{-10}	1115.7
Ξ^\pm	1.6×10^{-10}	1321.3
Σ^\pm	1.5×10^{-10}	1197.5
K_S^0	9.0×10^{-11}	497.7
τ^\pm	2.9×10^{-13}	1776.9

Table 2.3: Selected long-lived particles from the Standard Model

* When the neutron is free of a nucleus.

2.4.1 Particle decay

A substantial part of particle physics-terminology is inherited from atomic and nuclear physics, for instance the decay rate or ‘width’ Γ of a particle is the probability per unit time of a particle to decay. As in nuclear physics, the decay rate is statistical in nature and only valid for an ensemble of particles. In a population of N particles, the decrease in the population due to decay is

$$dN = -\Gamma N dt. \tag{2.5}$$

For a population the size at a time t is

$$N(t) = N(0)e^{-\Gamma t}. \tag{2.6}$$

The mean lifetime is the reciprocal decay-rate:

$$\tau_0 = \frac{\hbar}{\Gamma} \tag{2.7}$$

In the study of long-lived particles this is naturally a critical value (Table 2.3).

Some particles have multiple ways to decay. The τ -lepton can decay in many ways: 17% of the times into a muon $\tau \rightarrow \mu \bar{\nu}_\mu \nu_\tau$ and just as often into an electron, and the rest of the times into various ‘modes’ containing quarks. The total decay rate of tau particles is then

$$\Gamma_{\text{tot}} = \sum_{i=1}^n \Gamma_i. \quad (2.8)$$

And the mean lifetime is

$$\tau_{0_{\text{tot}}} = \frac{\hbar}{\Gamma_{\text{tot}}}, \quad (2.9)$$

which in case of taus is $\tau_{0_{\text{tot}}} \approx 2.9 \times 10^{-13}$ s [125], when summing roughly 215 different decay modes. The fraction of a specific decay Γ_i of the total is called the branching ratio:

$$\text{BR}_i = \frac{\Gamma_i}{\Gamma_{\text{tot}}}. \quad (2.10)$$

When all possible decay modes have been calculated the mean lifetime is then easily determined from (2.9).

Due to relativistic effects, even a tau particle with its 0.3 ps lifetime can be observed to travel some distance at sufficiently high momenta:

$$\tau = \tau_0 \gamma = \frac{\tau_0}{\sqrt{1 - \frac{v^2}{c^2}}} = \frac{\tau_0}{\sqrt{1 - (p / \sqrt{p^2 + m^2})^2}} \quad (2.11)$$

$$\bar{d}_{p=100 \text{ TeV}} = c\beta \tau_0 = 8.69 \times 10^{-7} \text{ m} \quad (2.12)$$

$$\bar{d}_{p=100 \text{ TeV}} = c\beta \tau = 4.89 \text{ m} \quad (2.13)$$

At sufficiently high momenta even taus can be considered long-lived, in fact a 2 PeV τ -particle has a mean travel distance of roughly, a hundred meters in IceCube.

In both ATLAS and IceCube the relativistic lifetime is an important parameter in particle reconstruction and identification. With a wide range of long-lived Standard Model particles available and good momentum reconstruction we are able to emulate the detection signatures of new types of particles as well as develop calibration techniques based on these SM particles.

In Figure 2.2, some of the common long-lived particles in the Standard Model (ignoring the stable ones) are shown. What is not visible on the plot are the particle masses but all of them weigh less than 10 GeV, only the π , K and μ s are sufficiently long-lived at low momentum to achieve sufficient range to be directly detectable in ATLAS. A further glance at the figure reveals ‘families’ of lifetimes. Ignoring the leptons, we see four groupings of hadrons. These arise from conservation rules preferring certain decay-modes, while increased mass of the hadrons opens the decay phase-space to new heavier secondary particles.

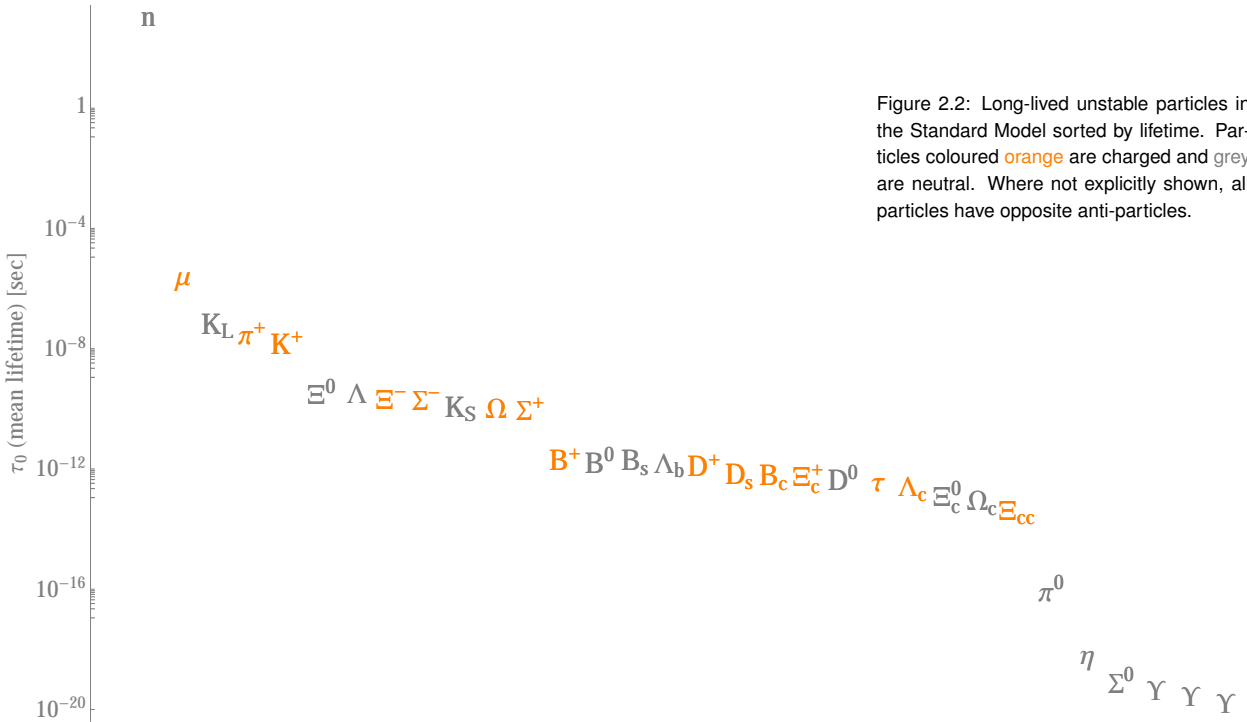


Figure 2.2: Long-lived unstable particles in the Standard Model sorted by lifetime. Particles coloured orange are charged and grey are neutral. Where not explicitly shown, all particles have opposite anti-particles.

⁵ 'neutral small ones'

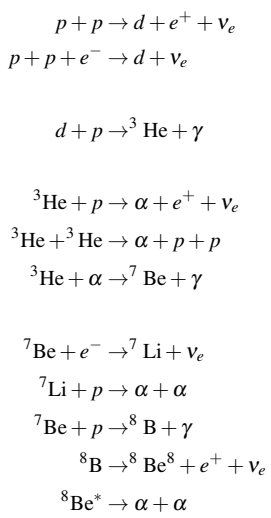


Figure 2.3: The stellar pp-reaction chain. The neutrino fluxes from the pp-chain can be seen in Figure 2.4 for the Sun.

2.5 Neutrinos

Neutrinos were postulated by W. Pauli in 1930 [78] in order to explain the continuous energy spectrum of electrons observed in β -decays ($n \rightarrow p + \beta^- + \bar{\nu}_e$). The interaction cross section of these neutrinos⁵ seemed too small for practical observation. Nevertheless in 1956 Cowan et al. succeed in detecting the elusive particle [34]. Neutrinos only interact through the weak force by either CC or NC exchange. The cross section for neutrino interactions is indeed quite small $\sim 10^{-38} \text{ cm}^2 \sim 10 \text{ fb}$ for nucleon interactions [125].

2.5.1 Neutrino Oscillations

By the mid twenties the Sun's energy was proposed to be produced in nuclear fusion [40]. The actual process was not easily explained, H. Bethe proposed [20] in 1939 that stars with solar masses or smaller could drive a proton-proton fusion chain (Figure 2.3). The pp-chain essentially fuses protons into helium-4 nuclei (α particles) and releases photons and neutrinos in the process. The energy released in photons and kinetic energy of α particles would keep the Sun's hydrostatic equilibrium counter-balancing the gravitational collapse by heating. Proving stellar nuclear synthesis was attempted by measuring the neutrino flux, the only part of the pp-chain that left the centre of the sun unscathed. As can be seen from the processes in Figure 2.3, five reactions lead to neutrino emission. The energy spectrum (Figure 2.4) and the relative flux from each of these reactions are quite characteristic. While the primary pp reaction has the highest neutrino flux, the Boron-8 reaction contributes the highest energy to the neutrino and was selected as the target

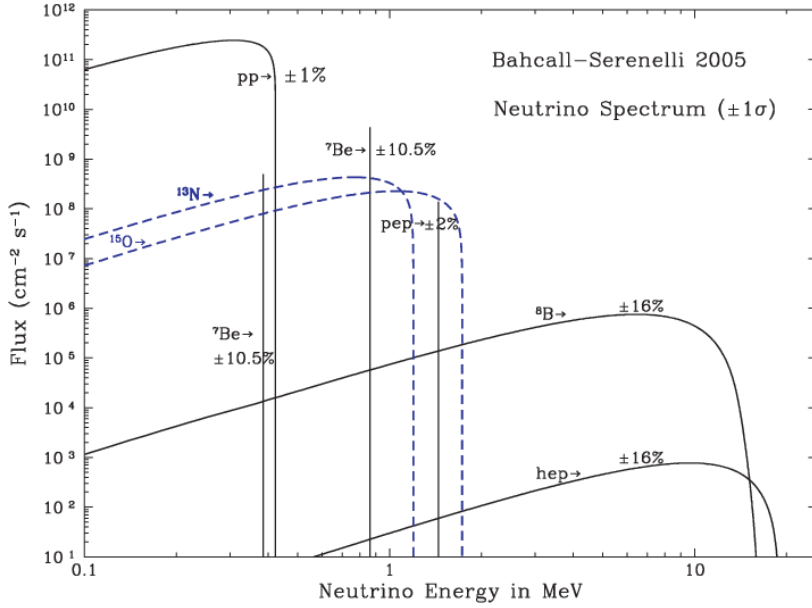


Figure 2.4: Solar neutrino flux from the various reactions listed in Figure 2.3, Ref. [14].

for experimental verification by the Davis experiment in 1968 [36].

The result from the Davis experiment was an observation of only $\sim 1/3$ of the predicted neutrino flux. The deficit did not raise much alarm in the beginning as both the experiment and the prediction were wildly ambitious. The deficit assumed a complete extraction of 33 argon atoms out of a tank filled with 615 tons of tetrachloroethylene. On the theory side the solar Standard Model was a complex model relying on nuclear, statistical and gravimetric physics. Later experiments confirmed the deficit, and the deficit became known as *solar neutrino problem*. In 1968, B. Pontecorvo suggested [80] a strikingly simple explanation: *electron neutrinos would transform into muon or tau neutrinos in-flight*, which would then go unnoticed in the ν_e -sensitive experiments. In 2001 the Sudbury Neutrino Observatory (SNO) conclusively showed [127, 128] that the missing solar neutrinos are in fact oscillating into muon neutrinos. The mathematical introduction of oscillations into the Standard Model resembles the mixing of quark states due to the CKM matrix introduced in Electroweak theory. The formalism described here is in principle valid for an arbitrary number of neutrino flavours, but the LEP experiments [6] showed that only three light neutrinos are allowed in the Standard Model. Neutrino mixing can be modelled by introducing a unitary mixing matrix named the Pontecorvo–Maki–Nakagawa–Sakata (PMNS) matrix:

$$\begin{bmatrix} \nu_e \\ \nu_\mu \\ \nu_\tau \end{bmatrix} = U \begin{bmatrix} \nu_1 \\ \nu_2 \\ \nu_3 \end{bmatrix} = \begin{bmatrix} U_{e1} & U_{e2} & U_{e3} \\ U_{\mu 1} & U_{\mu 2} & U_{\mu 3} \\ U_{\tau 1} & U_{\tau 2} & U_{\tau 3} \end{bmatrix} \begin{bmatrix} \nu_1 \\ \nu_2 \\ \nu_3 \end{bmatrix}. \quad (2.14)$$

It is the left-handed *flavour eigenstates* that interacts with other particles, while it is the right-handed mass-eigenstates that *propagates* as free particles. The flavour eigenstates then evolve in a complicated manner due to the mixing of the mass eigenstates.

The actual PMNS matrix can be parameterised by 6 parameters [65]⁶

⁶ Like the CKM matrix.

where three are mixing angles and three are complex phases:

$$U = \begin{bmatrix} 1 & 0 & 0 \\ 0 & c_{23} & s_{23} \\ 0 & -s_{23} & c_{23} \end{bmatrix} \begin{bmatrix} c_{13} & 0 & s_{13}e^{-i\delta_{CP}} \\ 0 & 1 & 0 \\ -s_{13}e^{i\delta_{CP}} & 0 & c_{13} \end{bmatrix} \begin{bmatrix} c_{12} & s_{12} & 0 \\ -s_{12} & c_{12} & 0 \\ 0 & 0 & 1 \end{bmatrix} \times \text{diag}(e^{i\alpha_1/2}, e^{i\alpha_2/2}, 0) \quad (2.15)$$

$$= \begin{bmatrix} c_{12}c_{13} & s_{12}c_{13} & s_{13}e^{-i\delta_{CP}} \\ -s_{12}c_{23} - c_{12}s_{23}s_{13}e^{i\delta_{CP}} & c_{12}c_{23} - s_{12}s_{23}s_{13}e^{i\delta_{CP}} & s_{23}c_{13} \\ s_{12}s_{23} - c_{12}c_{23}s_{13}e^{i\delta_{CP}} & -c_{12}s_{23} - s_{12}c_{23}s_{13}e^{i\delta_{CP}} & c_{23}c_{13} \end{bmatrix} \times \text{diag}(e^{i\alpha_1/2}, e^{i\alpha_2/2}, 0) \quad (2.16)$$

The notation is shorthand for $c_{ij} \equiv \cos \theta_{ij}$, $s_{ij} \equiv \sin \theta_{ij}$, where θ_{12} , θ_{13} and θ_{23} are the mixing angles. It has not been confirmed whether neutrinos are in fact their own anti-particles or not, that is whether they are Majorana or Dirac particles. This is captured by the two phases α_1 and α_2 in the fourth matrix. Additionally, δ_{CP} is a possible CP-violating phase called the Dirac phase.

With (2.16) each flavour eigenstate can be written as a superposition of the mass eigenstates,

$$\langle \nu_\alpha | = \sum_i U_{\alpha i} | \nu_i \rangle. \quad (2.17)$$

The oscillation effect is observed for propagating neutrinos, where we can describe the actual propagation as a time-dependent solution of Schrödinger's equation, for each of the mass eigenstates $|\nu_j\rangle$:

$$i \frac{d}{dt} |\nu_j(t, \vec{x})\rangle = H |\nu_j\rangle = -\frac{1}{2m_j} \Delta |\nu_j\rangle. \quad (2.18)$$

The solution is a plane wave equation, that in the relativistic limit ($E \gg m$) reads

$$|\nu_j(L)\rangle = e^{-im_j^2 \frac{L}{2E_j}} |\nu_j(0)\rangle. \quad (2.19)$$

The solution is given as a function of travel distance L . Substituting the plane wave solution (2.19) into (2.17), we find the flavour eigenstate after the particle has traveled a distance L

$$|\nu_\alpha(L)\rangle = \sum_j U_{\alpha j} e^{-im_j^2 \frac{L}{2E}} |\nu_j\rangle. \quad (2.20)$$

The transition probability $T_{\alpha \rightarrow \beta}$ is then [65]:

$$P(\nu_\alpha \rightarrow \nu_\beta) = |\langle \nu_\beta | \nu_\alpha(L) \rangle|^2 \quad (2.21)$$

$$= \left| \sum_i U_{\alpha i}^* e^{-im_i^2 \frac{L}{2E}} U_{\beta i} \right|^2 \quad (2.22)$$

$$= \delta_{\alpha\beta} - 4 \sum_{i>j} \text{Re}(U_{\alpha i}^* U_{\beta i} U_{\alpha j} U_{\beta j}^*) \sin^2 \left[\frac{(m_i^2 - m_j^2) L c^3}{4E\hbar} \right] + 2 \sum_{i>j} \text{Im}(U_{\alpha i}^* U_{\beta i} U_{\alpha j} U_{\beta j}^*) \sin \left[\frac{(m_i^2 - m_j^2) L c^3}{2E\hbar} \right] \quad (2.23)$$

In (2.21), E is the neutrino energy and as before L is the oscillation distance. The mass splittings $\Delta m_{ij}^2 \equiv m_i^2 - m_j^2$ between two mass eigenstates i and j , together with the three mixing angles θ_{12} , θ_{13} and θ_{23} , are the fundamental observables in neutrino oscillations. (2.21) holds for an arbitrary number of neutrino flavours and whether $\alpha \neq \beta$ or not. If Δm_{ij}^2 is zero that is if the neutrinos are massless or have identical mass, the oscillations disappears – oscillations imply masses.

2.5.2 Matter effects

Neutrinos that traverse matter can interact with the surrounding particles by the neutral current (NC) exchange of a Z^0 boson. This effect occur for all neutrino flavours, and does not change the mass eigenstates nor the phases. Electron neutrinos do however have an additional possibility of charge current (CC) interactions with the surrounding electrons that gives raise to changes in the mass eigenstates, and through (2.21) affects the flavour eigenstates and the parameters in (2.16). The effect is in some ways similar to optical refraction of light in matter and is called the *MSW effect* after L. Wolfenstein, S. Mikheyev and A. Smirnov [133]. In short, the effect on electron neutrinos can be modelled as an additional potential,

$$V_{CC} = \pm\sqrt{2}G_F N_e, \quad (2.24)$$

where G_F is Fermi's constant and N_e is the electron number density in the medium. The sign in (2.24) implies that the effect acts oppositely for anti-electron-neutrinos. The potential is added to the model by extending the hamiltonian in (2.18) with an additional factor,

$$A = \pm \frac{2\sqrt{2}G_F N_e E_\nu}{\Delta m^2}. \quad (2.25)$$

A consequence of the MSW effect is the possibility of an oscillation resonance if $A = \cos 2\theta$. The effect occurs only for either neutrinos or antineutrinos depending on the sign of Δm^2 . The density profile of the Earth together with the MSW resonance effect creates a rich survival probability profile for atmospheric neutrinos as we will see in later chapters.

2.5.3 Current status on neutrino parameter measurements

The neutrino sector is described by the absolute masses of the three neutrinos together with their mixing angles and a possible CP violating phases. Describing neutrino oscillations requires less information as the relative mass differences are sufficient to fully determine the transition probabilities. At the time of writing, the absolute mass values are still unknown, but all the oscillation parameters have been measured to some extent. We know the values of all oscillation parameters except the sign of Δm_{32}^2 and the octant of the θ_{23} angle. Both of these indeterminacies are due to the measurement of squared values instead of the bare parameters. The sign of Δm_{32}^2 is required to determine how the mass hierarchy is defined (Sec. 2.5.4).

θ_{12} and Δm_{21}^2 The mixing angle θ_{12} is known as the solar mixing angle (θ_{sol}) as it is determined by measuring the ν_e flux from the sun (Figure 2.3).

The oscillations of ν_e from the Sun are enhanced as they traverse the sun, due to the MSW effect. Another way to measure θ_{12} and Δm_{21}^2 is by $\bar{\nu}_e$ radiation from nuclear reactors. Here KamLAND [123] has measured neutrino fluxes with a 180 km baseline. A combination of results from both reactor and solar neutrino experiments estimates [129]:

$$\tan^2 \theta_{12} = 0.443_{-0.025}^{+0.030} \quad (2.26)$$

$$\Delta m_{21}^2 = 7.46_{-0.19}^{+0.20} \times 10^{-5} \text{ eV}^2 \quad (2.27)$$

$$\text{sgn}(m_2 - m_1) = 1. \quad (2.28)$$

θ_{23} and Δm_{32}^2 The θ_{23} angle is sometimes referred to as θ_{atm} as it was first measured with atmospheric neutrinos by Super-Kamiokande in 1998 [100]. Atmospheric neutrinos are produced when cosmic rays (primarily protons) interact with nuclei in the atmosphere and cause showers of secondary particles. The hadronic collision generates a large number of charged pions that dominantly decays to muons and muon-neutrinos. Atmospheric neutrinos are produced everywhere in the Earth's atmosphere, with energies in the GeV-range compared to the solar and reactor neutrinos in the MeV range.

Today θ_{23} and Δm_{32}^2 are also measured by so-called long-baseline experiments where muon-neutrinos are produced at particle accelerators and intercepted by dense detectors at the first oscillation minima. One such experiment is MINOS. For MINOS a ν_μ beam is prepared at Fermilab with a peak energy around 7 GeV. Two detectors one near to the production point (~ 100 m away) and one far, around 735 km away in the Soudan mine measure the disappearance of the ν_μ neutrinos. The latest result from MINOS is [124],

$$\sin^2(2\theta_{23}) = 0.950_{-0.036}^{+0.035} \quad (2.29)$$

$$\Delta m_{32}^2 = 2.41_{-0.10}^{+0.09} \times 10^{-3} \text{ eV}^2. \quad (2.30)$$

θ_{13} The last mixing angle θ_{13} has only recently been measured and found to be > 0 which opens up for possible CP-violating mixing [125, Chap. 13]. The first significant measurement of θ_{13} was reported by the Daya Bay collaboration [116] in 2012. The latest result is

$$\sin^2(2\theta_{13}) = 0.092 \pm 0.016(\text{stat.}) \pm 0.005(\text{syst.}). \quad (2.31)$$

Table 2.4 summaries the currently known and unknown neutrino mixing parameters from the Particle Data Group [125].

2.5.4 Neutrino mass hierarchy

The two mass splittings Δm_{21}^2 and Δm_{32}^2 are fairly well determined, and also the sign of Δm_{21} has been found to be positive, determining the mass ordering between two of the three mass eigenstates. That leaves one last degeneracy in the mass hierarchy, namely the sign of Δm_{32} (Figure 2.5). Two possibilities exists:

$$\text{Normal: } m_1 < m_2 \ll m_3 \quad (2.32)$$

$$\text{Inverted: } m_3 \ll m_1 < m_2$$

Table 2.4: Neutrino mixing parameters

Parameter	Value
$\sin^2(2\theta_{12})$	0.857 ± 0.024
Δm_{21}^2	$(7.50 \pm 0.20) \times 10^{-5} \text{ eV}^2$
$\sin^2(2\theta_{23})$	> 0.95
Δm_{32}^2	$(2.32 \pm 0.1) \times 10^{-3} \text{ eV}^2$
$\sin^2(2\theta_{13})$	0.095 ± 0.010
$\tilde{\delta}_{CP}$? $[0 - 2\pi]$
α_1	?
α_2	?

^a: The mass difference between Δm_{31}^2 and Δm_{32}^2 is small enough to assume they are the same, relative to Δm_{13}^2 .

?: Unknown values as of 2013. Ref. [125].

The colourings in Figure 2.5 represents the flavour content in each mass eigenstate.

With the discovery of a relatively large mixing angle for θ_{13} it is possible to determine the mass hierarchy in multiple ways. One of these is with a low energy upgrade of the IceCube detector (Chapter 11). This upgrade called PINGU (Chapter 11.2) would make it possible to determine the hierarchy at a low cost compare to alternative collider and reactor based efforts.

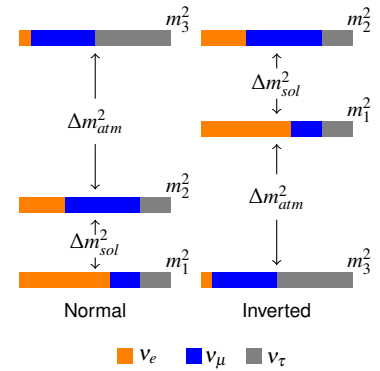


Figure 2.5: Neutrino Mass Hierarchy. The undetermined sign of the Δm_{32} mass splitting is leaving two orderings open, either a normal hierarchy or an inverted one where the m_3 mass eigenstate is the lightest.

3 Proposed models with massive long-lived particles

3.1 A need for a new theory

The accepted description of how particles interact and decay are formulated in the Standard Model (SM) of particle physics (see Chapter 2 for an introduction). The Standard Model has so far proved extremely successful in part thanks to its underlying reliance on quantum field theory (QFT) that makes the model extensible and allows the inclusion of new phenomena as they are discovered. That said, certain limitations to the theoretical reach makes it relevant to question the completeness of the theory. The following limitations are in particular striking omissions, and so serves as motivation for new theories that goes Beyond the Standard Model (BSM):

- *Gravity*: The inclusion of gravity into a renormalisable quantum field theory a requirement to include it in the Standard Model, has faced serious problems. Alternative theories such as superstring theory and loop quantum gravity attempt to unify particle physics and gravity.
- *Dark Matter*: Astronomical and cosmological observations seem to show that the Standard Model only accounts for 4% of all matter in the universe (see Sec. 3.5). 26.8% seems to be dark matter interacting gravitationally and weakly [126].
- *Neutrino masses*: The Standard Model is constructed with massless neutrinos. We know that neutrinos oscillate between flavours, which imply that neutrinos have masses, albeit small ones (Sec. 2.5).
- *Baryon asymmetry*: The observable universe is made mostly of baryonic matter. When considering that the most dominant processes in the Standard Model conserves charge and parity (CP) it seems odd that Baryonic antimatter is not more prevalent in the universe. CP-violation do happen in the Standard Model as we saw with the CKM matrix in Section 2.2 but not the any extent that explains why antimatter is so seemingly rare.

Undiscovered predictions: The Standard Model also has a few predictions left to be discovered, in particular a type of matter known as glueballs (Sec. 2.3), but that can hardly be held against the theory.

Theoretical inadequacies: While the Standard Model works perfectly fine as it is, some find its number of free parameters (28) unsatisfactory and

want a more fundamental theory. A deeper problem lies in the large difference in scales between electroweak symmetry breaking happening around $\mathcal{O}(100 \text{ GeV})$ which defines the scale of the SM in general and the Planck scale at 10^{19} GeV where space-time is believed to be quantised. The large difference between the two scales is particularly problematic for the Higgs mass. Renormalisation of higher order loop corrections requires the definition of a cut-off scale Λ that defines an upper validity range and where the loop integration is performed to. This cut-off scale is usually taken to be $\Lambda_{GUT} = \mathcal{O}(10^{16} \text{ GeV})$. When calculating the loop contributions to the scalar Higgs mass one finds that the loop contribution from diagrams such as the one shown in Figure 3.1, where the Higgs particle radiates and reabsorbs a virtual particle pair give rise to a loop correction that scales quadratically with the cut off scale¹

¹ λ_f is the coupling strength of the fermion to the Higgs field and m_f is the mass of the fermion(s) in the loop.

$$m_H^2 = m_0^2 - \frac{|\lambda_f|^2}{8\pi^2} \Lambda^2 + \mathcal{O}\left(\ln \frac{\Lambda^2}{m_f^2}\right), \quad (3.1)$$

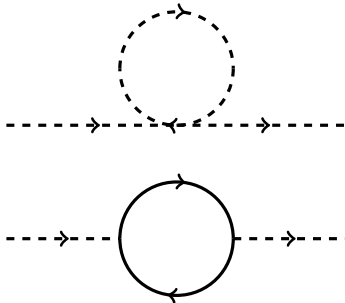


Figure 3.1: First order quantum loop corrections to the physical Higgs mass from virtual fermions (bottom) and bosons (top).

For fermions these corrections scales linearly with mass and are $\mathcal{O}(m_f)$ while the corrections needed to keep the mass of $m_H \sim 125 \text{ GeV}/c^2$ are of $\mathcal{O}(\Lambda_{GUT})$. This precarious balance between such extremely large numbers means that m_0^2 in (3.1) must be known to ~ 20 digits to give the observed value. Such precision tuning is found to be *unnatural* and the problem is called the *Hierarchy problem*.

The shortcomings of the Standard Model have motivated many attempts to extend and replace it with new particle fields, more general symmetries or even completely new paradigms of reality. One thing they all have in common, is that they must describe the observations of particle experiments no matter how the theory interprets the data points behind the scene. Most alternative models contain some freedom in their parameter space and some of that space usually allows for new types of long-lived particles.

A common denominator for these challenges is that no strict experimental evidence points to a singular solution. Due to complementarity the allowed model-space is fairly restricted if the theories are not allowed to break with QFT. Many new models are therefore described as extensions to the Standard Model and not direct replacements. One approach that has been developed over the last forty or so years is called *Supersymmetry* (SUSY). It exploits the last viable untapped symmetry allowed without violating Lorentz invariance. The resulting theory is really treated more as a framework where various mass scale breaking schemes generate new sectors of particles. To guide the search for LLPs we adopt SUSY terminology to describe the particles of interest.

3.2 Supersymmetry

Symmetry is a governing principle in the construction of the Standard Model. For every conserved quantity in the theory a symmetry exists [75]. Supersymmetry stems from the idea that all the interactions in the SM should be combined into one symmetry group. It was found by Coleman and Mendula [30] in 1967 that such a symmetry group was not feasible. Later it was discovered by Wess and Zumino [131] that a supersymmetric group was

possible, and finally in 1975, Haag, Lopuszanski and Sohnius [57] managed to construct a non-trivial extension of the Poincaré group which is what is called supersymmetry today.

The *super*-symmetry is a space-time symmetry where generators Q map fermionic states into bosonic and vice-versa:

$$Q|Fermion\rangle = |Boson\rangle, \quad Q|Boson\rangle = |Fermion\rangle. \quad (3.2)$$

To manage this transformation, the operator Q must itself be of fermionic nature carrying spin-half. Q and its hermitian conjugate Q^\dagger are called *supercharges*. This further imply that the operator must satisfy the following algebra²

$$\{Q_a^\dagger, Q_b\} = (\boldsymbol{\sigma}^\mu)_{ab} P_\mu \quad (3.3)$$

where σ^μ are Pauli matrices, P_μ is the four-momentum and $\{A, B\} = AB + BA$. The generality of this algebra means that every field (and particle) in the theory is affected by the SUSY contribution, leading to the following implications

- *Super-partners* of opposite spin statistics are manifested for all particles in the theory. These bosonic and fermionic states are ordered in supersymmetric multiplets or *supermultiplets* which are irreducible representations of the supersymmetric algebra and hence closed under transformations of Q and Q^\dagger .
- Before electroweak symmetry breaking (EWSB) (see Sec. 2.2) the supermultiplets are massless.
- After EWSB the superpartners have equal mass as Q and Q^\dagger commute with the generators of the Poincaré group.
- Quantum numbers of the superpartners must be identical as Q and Q^\dagger are neutral with respect to internal gauge symmetries.
- The square of the generator Q is equal to the four momentum which causes the concatenation of two supersymmetry transformations to form a translation in space-time.

These implications have deep consequences for the manifestation of the theory. If any superpartners with masses equal to the known Standard Model particles exists, they would have been long discovered, rendering the purest supersymmetrical theory false. For SUSY to be viable it must be a spontaneously broken symmetry where the superpartners have large enough masses for them to go undiscovered (so far).

3.2.1 A supersymmetrical Standard Model

Applying the principle of supersymmetry to the known Standard Model particles effectively multiplies the number of particles by two and in addition requires further particles in the Higgs sector to accommodate the EWSB mechanism. To navigate through this explosion of new particles, a naming scheme has been invented where symbols for superpartners have a ‘ \sim ’

² Further detail is beyond the scope of this short introduction. See [79] for a complete introduction to the subject.

added, and the names of SUSY scalars are prefixed with an ‘s’, while SUSY fermions are postfixed with ‘ino’ compared with the regular Standard Model names. With this notation the super-partner of a top quark becomes a ‘stop sparticle’ denoted \tilde{t} , and a gluon super-partner becomes a ‘gluino’ or \tilde{g} .

When the minimal required number of SUSY fields is added to the SM, it results in the fields and particles listed in Table 3.1. The new particles added to the Higgs sector are needed to accommodate EWSB in this context. The fields are listed before SUSY and EW breaking. This version of SM-SUSY is called the *Minimal Supersymmetric Standard Model* (MSSM) which is a convenient benchmark model for SUSY but by no means motivated beyond any other SUSY scenario. In fact the MSSM extension is due to the recent discovery [106, 113] of a Higgs boson at $125 \text{ GeV}/c^2$, under some tension.

Table 3.1: Particle fields in the Supersymmetry extended Standard Model.

Supermultiplet	SM field	Superfield
Q	Quarks: (u_L, d_L)	Squarks: $(\tilde{u}_L, \tilde{d}_L)$
U	\tilde{u}_R	\tilde{u}_R^*
D	\tilde{d}_R	\tilde{d}_R^*
L	Leptons: (ν_L, l_L)	Sleptons: $(\tilde{\nu}_L, \tilde{l}_L)$
E	\tilde{l}_R	\tilde{l}_R^*
G	Gauge bosons: $g^a, a = 1, \dots, 8$	Gauginos: \tilde{g}^a
W	$W^\alpha, \alpha = 1, 2, 3$	\tilde{W}^α
B	B	\tilde{B}
H ₁	Higgs bosons: (H_1^0, H_1^-)	Higgsinos: $(\tilde{H}_1^0, \tilde{H}_1^-)$
H ₂	(H_2^+, H_2^0)	$(\tilde{H}_2^+, \tilde{H}_2^0)$

Without claiming perfect agreement with nature, MSSM is still interesting from a phenomenological perspective as it represents many of the dominant effects of SUSY and is readily calculable and thus available in a variety of computer codes for quantitative predictions.

As mentioned earlier SUSY must be a broken symmetry as no degenerate mass states have been observed for any SM particles. The breaking of SUSY can be constructed in multiple ways and is one of the major variations to the model assumptions when searching for MSSM SUSY experimentally.

The breaking of the symmetry is done through what is called ‘soft SUSY breaking’ where additional terms are added to the SUSY Lagrangian. These terms are not invariant under SUSY transformations but not contributive at the high energies of the (unbroken) SUSY scale. By allowing the superpartners to couple to these terms they can gain masses, different than their SM partners.

To implement SUSY breaking it is common to define a “hidden sector” where the symmetry is spontaneously broken. To induce the soft breaking, particles in this hidden sector couples to the supermultiplets in the *visible* MSSM sector via hypothetical messenger fields to manifest the soft breaking terms in the lagrangian density. This *mediation* between the hidden and the visible sector can take place in different ways depending on model assumptions.

The most common SUSY breaking scenarios are called Gauge Mediated

Supersymmetry Breaking (GMSB), Minimal Supergravity (mSUGRA) and Anomaly Mediated Supersymmetry Breaking (AMSB).

As a broken symmetry, many of the fundamental particles in Table 3.1 share quantum numbers which allows for superpositional particle states. To accommodate these, mixing matrices and CP-violation phase parameters are introduced into the lagrangian, expanding the number of free parameters dramatically³. To retain some of the beauty of the unbroken theory, many of the scenarios attempt to relate these parameters to each other. mSUGRA for instance is a constrained scenario (CMSSM) where only five parameters actually exists at the unification scale ($m_0, m_{1/2}, A_0, \tan\beta, \text{sign } \mu$). These parameters then unfold at the electroweak scale into a specific mass and mixing spectrum during the soft breaking phase. The resulting mixing of gauginos and higgsinos leads to the formation of *neutralinos* χ_n^0 and *charginos* χ_n^\pm . Also the heavy sleptons $\tilde{\tau}_L$ and $\tilde{\tau}_R$ will mix to form mass eigenstates $\tilde{\tau}_1$ and $\tilde{\tau}_2$. Similarly, in the quark sector stops and sbottoms form mass mixing states.

³
 21 mass parameters
 36 mixing angles
 48 CP-violation phases
 =105 free parameters

3.2.2 *R-parity*

In many MSSM models, baryon and lepton-number conservation are violated. As a consequence the proton will undergo rapid decay, something clearly not in tune with observation. To avoid this theoretical disaster a conserved quantity called *R-parity* is introduced

$$R = (-1)^{3(B-L)+2S}. \quad (3.4)$$

B and L are baryon and lepton numbers respectively and S is the particle spin. This means that all SM particles have $R = +1$, while SUSY particles have $R = -1$. Besides avoiding proton decay to SUSY particles, R-parity implies that SUSY particles must be pair-produced if produced by SM interactions

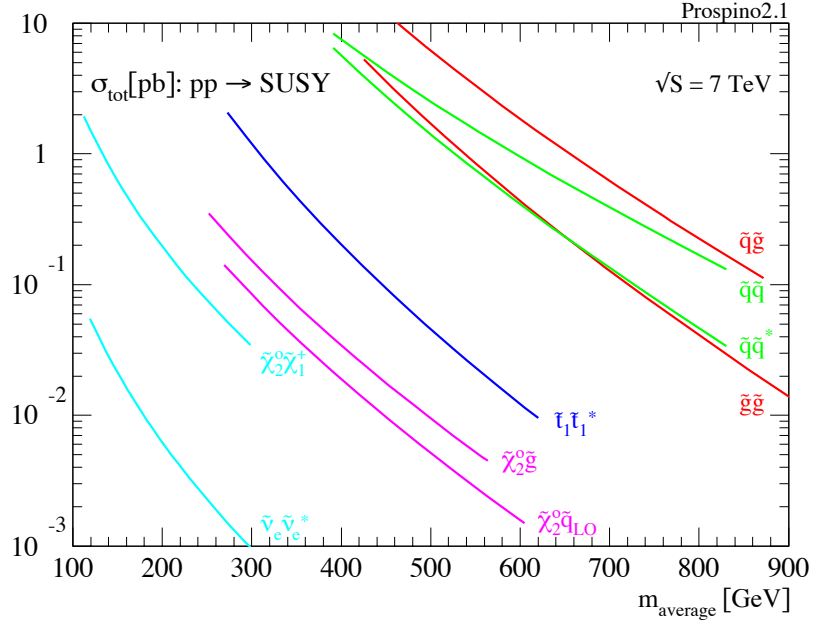
$$R_{tot} = R_1^{SM} R_2^{SM} = 1^2 = R_1^{SUSY} R_2^{SUSY} = (-1)^2 = 1. \quad (3.5)$$

It also have the important consequence that the supersymmetric particle with the lowest mass must conserve *R-parity*, and hence is stable by not being able to decay to SM particles. This *Lightest Supersymmetric Particle* (LSP) can be a dark matter candidate. Depending on the definition of ‘dark’, most ascribe only SUSY models with a Weakly Interacting Massive Particle (WIMP) as the LSP any dark matter candidacy. This is most often a neutralino χ_n^0 . The main motivation for introducing R-parity was originally to avoid proton decay. It is still possible to avoid proton decay while still leaving certain R-parity violated for some particles by tuning the ‘level’ of violation i.e. by how long-lived certain particles are. Such SUSY models are called R-parity Violating SUSY or RPV-SUSY and host a number of LLP candidates.

3.2.3 *SUSY production at the LHC*

At the Large Hadron Collider SUSY particles can only be produced in pairs if we assume the MSSM and R-parity conservation. The dominant production mechanism at the hadron collider is through strong interactions of either gluon-gluon, gluon-quark or quark-quark pairs. The most dominant of these

Figure 3.2: MSSM cross sections at the LHC at $\sqrt{s} = 7$ TeV. The cross sections are computed including first order loop corrections or Next-To-Leading Order (NLO). Ref. [17]



is gluon-gluon up to a certain energy (Sec. 9.2.1). Weak processes could also lead to production of charginos, neutralinos and sleptons but the hadronic nature of the LHC greatly favours the strong interactions, as can be seen in Figure 3.2.

3.2.4 SUSY decay processes

It is illustrative to summarise the possible decay mechanisms of the various SUSY particles even if we are studying long-lived particles where such decays are ignored. This is relevant if we would be interested in meta-stable particles that decay somewhere within the detector volume i.e. if the decay length is $0.1 \text{ m} < c\tau < 10 \text{ m}$.

Gluinos decay through $\tilde{g} \rightarrow q\bar{q}$, if it is kinematically allowed, otherwise they can decay through a virtual squark to neutralinos or charginos $\tilde{g} \rightarrow q\bar{q}^{(\prime)}\chi^{0/(\pm)}$. In the case that squarks are not kinematically favoured, the gluino can decay through $\tilde{g} \rightarrow g\chi^0$.

Squarks decay through $\tilde{q} \rightarrow q\bar{q}$ if it is kinematically allowed, otherwise they decay to charginos or neutralinos $\tilde{q} \rightarrow q^{(\prime)}\chi^{0/(\pm)}$. A direct decay to the lightest neutralino χ_1^0 is kinematically preferred.

Sleptons usually decay to charginos or neutralinos and a lepton $\tilde{l} \rightarrow l\chi^0$, $\tilde{l} \rightarrow \nu\chi^\pm$ and $\tilde{\nu} \rightarrow \nu\chi^0$, $\tilde{\nu} \rightarrow l\chi^\pm$. Both squark and slepton decays are sensitive to the chirality of the particle which stems from the amount of Bino and Wino mixture in right-handed and left-handed particles respectively, changing the decay preference depending on the handedness.

Neutralinos and Charginos are mixtures of gauginos and higgsinos as mentioned earlier. This allows for a variety of mass scale dependent decays

which are heavily dependent on the SUSY scenario [73].

In general the richness of the combined SUSY and SM particle spectrum allows for quite complex event topologies where jets, missing energy and an assortment of leptons are produced in cascade decays. In SUSY configurations where decay modes are suppressed to restrain a sparticle from decaying, LLPs will be introduced into these topologies as well. Such LLP searches with associated cascade decays are typically explored within RPV-SUSY. In the scenario pursued in this thesis we avoid the rest of SUSY phenomenology by exclusively looking for LLPs, but naturally more involved searches can be performed based on these techniques.

3.2.5 Choosing the right scenario

Even with only a handful of MSSM scenarios⁴ the choice of input parameters is daunting. The search strategy chosen by the LHC experiments mainly focus on jets and missing energy signatures. The assumption is that these signatures are pronounced in most scenarios and hence most widely tests a broad range of SUSY parameter-space. By comparing regions of CMSSM excluded by ATLAS [31], with roughly 71k model points they found that this search strategy was mostly a sound approach with good coverage. What they also found was that the regions with the weakest sensitivity were the areas where long-lived particles were produced. This study provides a great incentive to further develop the methods for LLP searches in the context of SUSY. In Table 3.2 they show that hundreds of model points yield LLPs.

\tilde{x}	10^{-15}	10^{-16}	10^{-17}	10^{-18}	10^{-19}
$\tilde{\chi}_1^\pm$	9853	9728	8642	7683	6658
$\tilde{\tau}_1$	179	179	179	179	179
\tilde{t}_1	67	66	66	65	65
\tilde{c}_R	49	49	49	49	49
$\tilde{\chi}_2^0$	78	40	19	11	4
$\tilde{\mu}_R$	17	17	17	17	17
\tilde{b}_1	12	12	11	9	9
\tilde{c}_L	8	8	8	8	8
\tilde{s}_R	8	8	8	8	8
\tilde{g}	17	10	5	2	0

Coloured sparticles with widths $\Gamma < \Lambda_{\text{QCD}}$ can hadronise into bound states with SM quarks, called *R-Hadrons*. These particles are the main benchmark object of this thesis and the study shows that thousands of model points allow for these objects (Table 3.3).

The general search for LLPs is even within generic SUSY scenarios well motivated but other more specific models within SUSY predict LLPs, one which has served as the benchmark for phenomenologists and experimentalists alike is called *split supersymmetry*.

⁴ Note that MSSM is followed by NMSSM, the next to minimal supersymmetric Standard Model, and after that the NNMSSM and so on. SUSY in any meaningful sense is a mathematical framework where the actual implementation in general must be chosen based on the principle of 'least action', meaning the simplest model fitting observation.

Table 3.2: The number of models in the model-space described in [31] that for a specific sparticle has a width less than indicated in the header (in GeV). Here 10^{-17} GeV corresponds to a mean $c\tau \sim 20\text{m}$, Ref. [31].

Table 3.3: The number of coloured sparticles with widths < 100 MeV in the model-point space investigated in [31]. These numbers reflect all types with widths larger than the hadronisation scale and not necessarily long-lived particles, Ref. [31].

Particle	Models
\tilde{g}	12598
\tilde{u}_L	9628
\tilde{c}_L	9629
\tilde{u}_R	22667
\tilde{c}_R	22668
\tilde{d}_L	13595
\tilde{s}_L	13595
\tilde{d}_R	27996
\tilde{s}_R	27998
\tilde{b}_1	13355
\tilde{b}_2	431
\tilde{t}_1	5695
\tilde{t}_2	1

3.3 Split-Supersymmetry

One of the leading motivations behind the previously mentioned SUSY scenarios is the curing of the Hierarchy problem (Sec. 3.1) in a natural way. It has been argued [10, 9] that naturalness as an argument for selecting certain models is somewhat excessive in the light of the cosmological constant that requires a much greater level of fine-tuning in any of the known theories enacting electroweak symmetry breaking. Based on this level of reasoning *naturalness* becomes less relevant and is effectively left to the anthropic principle by the authors of a new theory called *Split Supersymmetry* (SSUSY). Instead the theory's main focus is to avoid proton decay, support a Higgs particle with mass larger than the LEP limit⁵ of $114 \text{ GeV}/c^2$ and providing a realistic dark matter candidate. SSUSY accomplishes this by replacing low energy SUSY with a two new mass scales. All the supersymmetric scalars (squarks, sleptons) are placed at a high mass scale m_S , except the Higgs boson which can be accommodated in the mass region where it has been found in 2012. All the SUSY fermions (charginos, neutralinos, gluino) are allowed to be relatively light.

⁵And now consistent with a $m_H = 125 \text{ GeV}/c^2$.

A side-effect of this theory is that the decay of gluinos to squarks ($\tilde{g} \rightarrow q\tilde{q}$) is suppressed by the large mass difference between the two mass scales. Due to this decay suppression the life-time of the gluino is effectively coupled to the mass scale difference

$$\tau_{\tilde{g}} = 4\text{s} \left(\frac{\text{TeV}/c^2}{m_{\tilde{g}}} \right)^5 \left(\frac{m_S}{10^9 \text{ GeV}/c^2} \right)^4 \quad (3.6)$$

A typical value for m_S is $> 10^{10} \text{ GeV}/c^2$ which makes the lifetime of the gluino $\tau \sim \mathcal{O}(1 \text{ s})$. The mass of the Higgs particle is closely linked with the mass scale m_S in SSUSY. The recent discovery of a Higgs particle effectively limits the value of the mass scale below 10^7 GeV as can be seen in Figure 3.3. Thus the Higgs discovery has large ramifications for the search for SSUSY as it limits the lifetime of the gluino dramatically. The SSUSY sensitivity at ATLAS and the LHC given this constraint is explored in Chapter 10.

3.4 Other models with LLPs

GMSB provides justification [52] for searching for long-lived staus. In specific cases the gravitino is the LSP and the stau is the NLSP. This leads to a

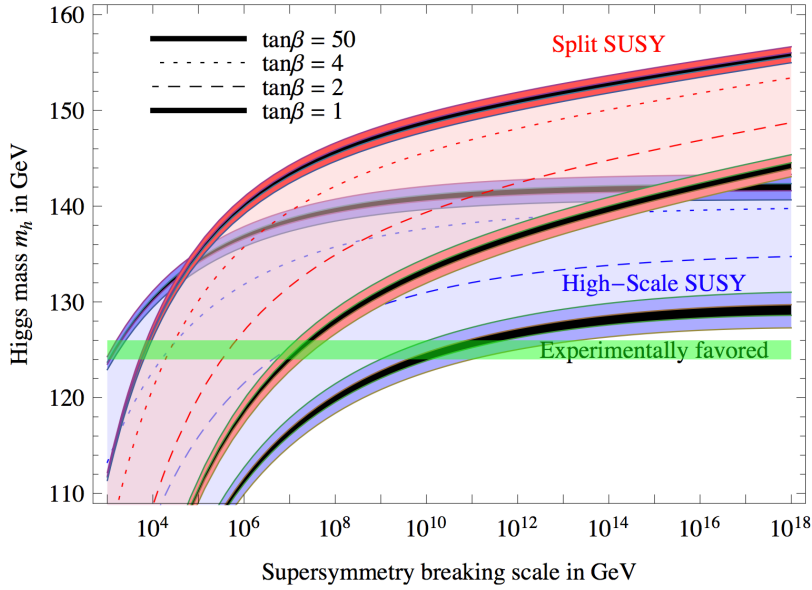


Figure 3.3: Next-to-leading order prediction for the Higgs mass m_h in High-Scale Supersymmetry (blue, lower) and Split Supersymmetry (red, upper) for $\tan\beta = \{1, 2, 4, 50\}$ Ref. [53].

lifetime of

$$c\tau_{NLSP} = 0.1 \text{ mm} \times \left(\frac{100 \text{ GeV}/c^2}{m_{NLSP}} \right)^5 \times \left(\frac{m_{\tilde{G}}}{2.4 \text{ eV}/c^2} \right) \quad (3.7)$$

where \tilde{G} is the mass of the Gravitino.

SUSY scenarios provide a plethora of LLPs as was found in Sec. 3.2.5 and it is easy to forget that other BSM theories such as Universal Extra Dimensions [11] and Minimal Walking Technicolor [49] also predicts such particles.

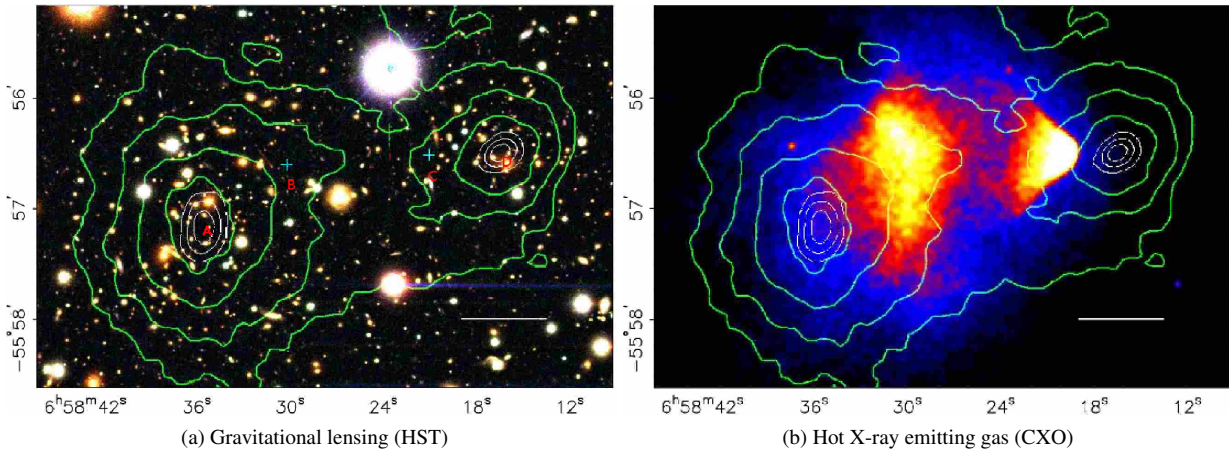


Figure 3.4: The Bullet cluster. In both figures, green contours are the reconstructed gravitational distribution from weak lensing. The white line corresponds to 200 kpc. Ref. [29].

⁶ Much like W. Pauli’s neutrino was a ‘dark particle’ until its actual discovery.

⁷ One could imagine other concepts such as a hidden ‘substrate’, extra dimensions, super-long-range forces and other global constructions that could cause such observations, as the scales are so alien to our normal concepts of natural, but so far matter is the only direct handle we have on gravity.

⁸ The Virial theorem, frequently used in astrophysics relates the average kinetic energy (T) of a gravitationally bound system to its gravitational potential (W)

$$\langle T \rangle = -\frac{1}{2} \langle W \rangle.$$

From that, masses can be estimated based on the doppler shifts of orbiting stars.

3.5 Dark matter

Dark matter (DM) was proposed in the early thirties as a placeholder substance⁶ to account for orbital velocities which are much higher than expected in the halo regions of galaxies, if only visible matter contributed gravitationally [77, 138]. The problem is, based on our current understanding of the universe, either that some unseen mass must be distributed in the universe, *or* that the laws of gravitation are inaccurate⁷.

3.5.1 Galactic rotation curves

An object in a stable Keplerian orbit with radius r should move with a rotational velocity $v \sim \sqrt{M(r)/r}$ where $M(r)$ is the integrated mass within the orbit. If the object lies outside the visible part of the galaxy we should expect the velocity to drop off Newtonian $v(r) \sim 1/\sqrt{r}$, assuming the observation of light emitted by orbiting structure to be correlated with mass⁸. Instead of the expected drop-off, the velocity flattens to a constant value out at the largest radii observed (for our galaxy: $v \sim 240$ km/s [125]). If we assume Newtonian gravity is correct, the velocity would imply a ‘dark halo’-contribution surrounding and pervading the galaxies with a mass density $\rho(r) \sim 1/r^2$ or: $M(r) \sim r$. If the galaxies are not floating in a common dark matter ‘pudding’, we must assume that the halo drops off at some point, but it is not yet clear where. As we don’t know where the dark halo mass contribution actually ends, a lower bound on the galactic DM density is found to be $\Omega_{DM} \gtrsim 0.1$ with $\Omega_X \equiv \rho_X / \rho_{crit}$ where for a flat universe the total density is $\Omega_{tot} = 1$.

The Bullet cluster A (seemingly) strong argument for particle dark matter is the observation of the ‘Bullet’ cluster (1E0657-558) shown in Figure 3.4. In the figure an overlay of the gravitational field extracted from weak gravitational lensing observations with the Hubble Space Telescope (HST) is shown on top of an x-ray photograph from the Chandra X-Ray Observatory (CXO). If only the visible matter contributed to the gravitational potential deflecting light from the galaxies behind, then the overlay and the hot gas in Figure 3.4b would match up. This is not the case, and it has been taken as evidence for

dark matter found outside the zone of x-ray emitting gas. It should also be noted that due to the very asymmetrical configuration (thought to arise from an earlier collision with another galaxy cluster) it is also unlikely that modified Newtonian gravity (MOND) can account for the offset. It is therefore – based on this and similar observations inferred that DM is particle-like in nature [19].

3.5.2 *Dark matter particle candidates*

Cosmology disfavours electric and colour-charged DM, but allows for weak interactions. If dark matter is connected to the SM in any way (anthropically speaking) we can produce it with colliders and observe it and it is likely a Weakly Interacting Massive Particle (WIMP). Non-WIMP long-lived particles have strongly constrained lifetimes, masses and charges [45]. This is due to the effect on the expansion history of the universe. If a massive particle was produced with any significant abundance, it would change the energy density and hence the overall metric of the universe, leading to disagreement with observation. Another constraint comes from the LLP decaying and offsetting the relative abundance of light elements or be directly visible today as red-shifted gamma-rays. Also any large abundance of charged massive particles would likely have been found in isotope [7, 5, 134, 15, 96, 95, 37] or magnetic monopole searches [8].

In addition, if DM has particle-nature⁹, it must be subjected to certain constraints imposed from the CMB, relic abundance and ability to stay ‘dark’ in observations of light emission. In simple terms, DM must adhere to the following criteria [19]:

- Non-relativistic at the formation phase of galaxies
- Stable at cosmological time-scales
- Very weak interaction with electromagnetic radiation
- Relic density matching observations from CMB.

Many models exist that predicts particles with these characteristics: Kaluza-Klein B(1) particles [88], Sterile neutrinos [38], Axions [33], T-Photons [21], Q-balls [50, 68], Mirror baryons [60], D-Matter [89], Self-interacting dark matter [98], Cryptons [41], Super-WIMPs [47], 4-gen. fermions [136], technibaryons [76], Primordial black holes [54] and Supersymmetric weakly interacting massive particles (WIMPs) to mention some of all the creative names out there (see [125, 45, 19] for excellent reviews).

What all these models have in common (except for black holes) are their WIMP-like signatures. The most common WIMP model today is Supersymmetry (SUSY) with R-parity conservation. SUSY as we shall see, can manifest a DM candidate in multiple ways but in general the lightest mass state, or lightest supersymmetric partner (LSP) is conserved by the introduction of a conserved quantum number *R* in SUSY (Sec. 3.2.2). An interesting possibility within SUSY is the presence of quasi-stable particles that later decay to the LSP. This opens up for coloured and charged LLPs with lifetimes short enough to avoid some of the constraints that the real dark matter (the LSP) is bounded by.

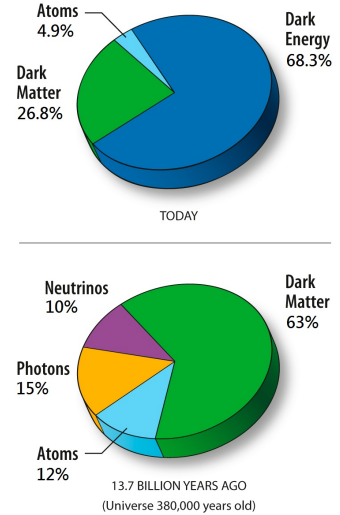


Figure 3.5: Matter densities in the universe today and at the time of the cosmic background radiation release [126].

⁹ That all DM is contained in a single particle type is rather unlikely, at least we know that neutrinos contribute to the mass density, and nothing hinders a complex particle hierarchy in describing the ‘dark sector’.

3.6 Previous searches

The wide implications of a new type of massive long-lived particle is reflected in the variety of techniques applied in the search for them. The scope of this thesis is searches at colliders (Table 9) but out of general interest some of the nowadays less conventional searches are reported here as well.

Searches are conducted under a wide range of assumptions and sensitivity ranges that merits further categorisation beyond simply stating that particles are long-lived.

Following the classifications in [45] we divide the searches into three classes

1. General searches for LLPs, without any additional assumptions on the LLP beyond a charge or mass sensitivity range. Limits are placed on the production cross section.
2. Quantum number constrained searches, minimal model assumptions such as possible loop corrections from additional particles in the BSM model. Production cross sections serve as upper limits but mass exclusion limits can be placed as well.
3. Model specific searches, where the full parameter space of a specific model is applied to constrain the particle hypothesis.

The categories are in practice somewhere blurred as a general search might be severely limited by detector sensitivity that implicitly limits the generality of the result, while a model specific search might place limits on a specific hypothesis while the selection could be open to alternative interpretations given broad detection sensitivity within the hypothesis space. The latter case is illustrated by the search for long-lived super-symmetrical particles at the LHC. These searches are, as we shall see in later chapters based very loosely on SUSY assumptions, and can be reinterpreted to encompass searches for multi-charged particles, universal extra dimensions and various other models detectable by slow-moving charged particles. It can be quite a headache to unfold assumptions and constraints from both assumed theories

Table 3.4: Selected searches for SMPs at colliders.

^a These searches are part of the study presented in Chapter 9, but are shown here as they represent the latest results from ATLAS at the time of writing.

^b The mass range between 100 and 500 have slightly worse limits.

\sqrt{s} [TeV]	$\int L dt$ [fb ⁻¹]	Exp.	Mass [GeV/c ²]	Charge [e]	Cross section limit [pb]	Model	Ref.
7, pp	4.7	ATLAS	300 – 1500	± 1	$\mathcal{O}(0.008)$ ^a	gluino $\tilde{g}g = 10\%$, Tracker+TOF	[111]
7, pp	4.7		200 – 1000	± 1	$\mathcal{O}(0.005)$ ^a	stop, Tracker+TOF	[111]
7, pp	4.7		200 – 1000	± 1	$\mathcal{O}(0.009)$ ^a	sbottom, Tracker+TOF	[111]
7, pp	4.7		200 – 500	± 1	$\min \mathcal{O}(0.002)$ ^a	stau, Tracker+TOF	[111]
7, pp	5.0	CMS	300 – 1500	± 1	$\mathcal{O}(0.009)$	gluino $\tilde{g}g = 10\%$, Tracker+TOF	[114]
7, pp	5.0		200 – 1000	± 1	$\mathcal{O}(0.005)$	stop, Tracker+TOF	[114]
7, pp	5.0		100 – 600	± 1	$\min \mathcal{O}(0.001)$	stau, Tracker+TOF	[114]
8, pp	18.8		300 – 1500	± 1	$\mathcal{O}(0.001)$	gluino $\tilde{g}g = 10\%$, Tracker+TOF	[114]
8, pp	18.8		200 – 1000	± 1	$0.01 - 0.001$ ^b	stop, Tracker+TOF	[114]
8, pp	18.8		100 – 600	± 1	$\min \mathcal{O}(0.0005)$	stau (and $ q = 1$ DY), Tracker+TOF	[114]
1.96, $p\bar{p}$	1.0	CDF	100 – 260	± 1	$\mathcal{O}(0.09)$	stop, Tracker+TOF	[112]
1.96, $p\bar{p}$	6.3	D0	100 – 300	± 1	$\mathcal{O}(0.02)$	stau, Tracker+TOF	[115]
1.96, $p\bar{p}$	6.3		100 – 300	± 1	$\mathcal{O}(0.01)$	Gaugino, Tracker+TOF	[115]
0.3, $e\bar{p}$	0.06	H1	< 100	± 1	190	Tracker	[117]

and the detector sensitivity. Hence, care must be taken when attempting such reinterpretations.

Nevertheless the most basic properties will be listed in the following tables and the reader should carefully consult the reference for further assumptions on the basis of the individual analysis.

If SMPs are produced in nature then depending on the abundance we would be able to find them in our local environment. Electrically charged particles with large masses may bind to other particles forming heavy hydrogen or anomalous molecules. Coloured SMPs may be found in nuclides where they contribute as either charged or neutral components. These ‘R-hadronides’ can be looked for with mass spectrometry where the mass-to-charge ratio is abnormally large. Table 3.5 summaries single charged ‘heavy hydrogen’ searched, performed by analysing sea water. Table 3.6 lists searches for neutral strongly interacting particles embedded into known nuclei.

The possible concentration of low- Z heavy nuclei in water is dependent on the depth of sea¹⁰. During the eighties and nineties surveys in three regions have been undertaken.

¹⁰ Based on the delusion of heavy water in water a fall rate is found to be $v_{fall} \sim MgD/kT$ where $D = 1.4 \times 10^{-5} \text{cm}^2 \text{s}^{-1}$.

Concentration X/H	Charge [e]	Mass [GeV/c^2]	CL	Comment	Ref
$< 4 \times 10^{-17}$	1	5 – 1600	95%	0.25 l deep sea water, $d = 4000$ m	[135]
$< 6 \times 10^{-15}$	1	$10^5 - 3 \times 10^6$	95%	8.8l sea water $d = 2800$ m	[130]
$< 3 \times 10^{-20}$	1	$10^3 - \times 10^4$	90%	sea water	[59]
$< 10^{-28}$	1	10 – 1000	–	16 μ l enriched $\text{D}_2\text{O} \sim 1.2 \times 10^8$ l H_2O , $d \sim \mathcal{O}(0\text{m})$	[96]

Table 3.5: Upper limits on concentration of stable charged particles in matter Ref. [125].

Searches for neutral coloured SMPs have been conducted by mass spectrometry analysis of Au, Fe and C. The samples have been collected under various circumstances and some exposed to space while others to heavy ion beams. The table below illustrates some of these searches see e.g. [125] for a complete summary.

Concentration X/N	Charge [e]	Mass [GeV/c^2]	CL	Comment	Ref
$< 4 \times 10^{-20}$	1	100	90%	Embedded in: C	[59]
$< 8 \times 10^{-20}$	1	1000	90%	Embedded in: C	[59]
$< 2 \times 10^{-16}$	1	10000	90%	Embedded in: C	[59]
$< 6 \times 10^{-13}$	1	1000	90%	Embedded in: Li	[59]
$< 1 \times 10^{-11}$	1	1000	90%	Embedded in: Be	[59]
$< 6 \times 10^{-14}$	1	1000	90%	Embedded in: B	[59]
$< 4 \times 10^{-17}$	1	1000	90%	Embedded in: O	[59]
$< 4 \times 10^{-15}$	1	1000	90%	Embedded in: F	[59]

Table 3.6: Upper limits on concentration of stable neutral particles embedded in nuclei Ref. [125].

3.7 Conclusion

From a theoretical point of view, long-lived particles are well motivated. SUSY with its wide parameter-space hosts thousands of model points which imply LLPs. Dark matter poses an observational enigma that in many ways are bound to LLPs. It is possible that they are in fact WIMPs and can be described by SUSY. It can also be something else, and while people are quick to rule out CHAMPs or Charged Massive Particles as DM candidates, on various grounds, it is still too early to say anything with complete certainty.

Previous searches for charged LLPs have indeed come up empty, so it is clear that whatever is out there, is less obvious than we have hoped. Even if the theoretical motivations outline here were not sufficient to convince the reader, the access to new collider energies, at high intensities is sufficient motivation for a search for LLPs, given the history of particle discovery in the twentieth century.



*Principles of particle
detection*

4 *Particle detection and identification*

The basic design principle in modern particle detectors relies on the ionisation or excitation of atoms in detector material. This chiefly allows for the study of charged particles that through Coulomb interactions with either atomic electrons or nuclei deposit energy that can be collected by counting photons from excitations or electrons from ionisation. While the actual techniques differ depending on the particle of interest and whether the objective is trajectory determination, particle identification or calorimetric energy measurements, the basic principles are the same. Hadrons have the additional possibility of nuclear scattering whereby they fragment to form new particles. This process is extremely relevant to the search for coloured long-lived particles as it gives rise to a characteristic phenomena we call ‘charge-flipping’. In this chapter these principles will be reviewed as the future chapters rely on them.

The main sources for this chapter are [87, 125, 91, 56] where nothing else is mentioned.

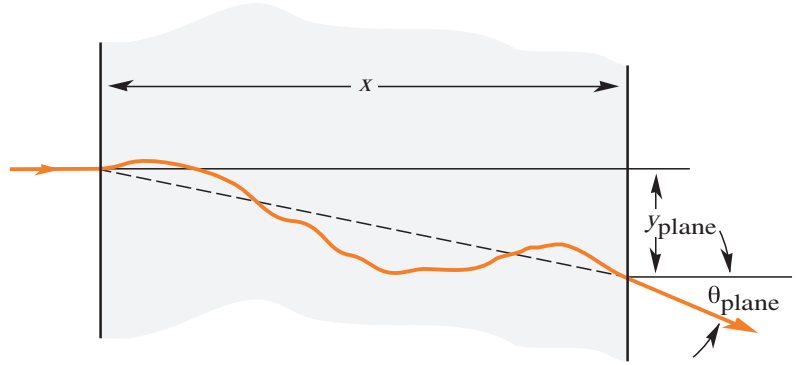
4.1 *Electromagnetic interactions*

Charged particles passing through matter have a chance of momentum transfer (Sec. 4.1.2) and deflection (Sec. 4.1.1) when passing near an atom. The momentum transfer can lead to the excitation of electrons with subsequent release of light or ionisation where the free electrons can be collected by an anode and amplified as a signal. Electrons and positrons suffers additional effects due to their lightness (and their shared identity with atomic electrons). The primary source of energy loss for electrons and positrons is bremsstrahlung (Sec. 4.1.3) where energy is radiated in the form of photons, from the electron as it is deflected (and decelerated) in the presence of a nucleus. High energy photons typically interact with nuclei by pair-production of electron-positron pairs. The production of photons due to bremsstrahlung, combined with the pair-production from photons can lead to an electromagnetic cascade (Sec. 4.1.5) where the energy of an incoming photon or electron is dissipated in the medium by successive photon and pair production.

4.1.1 *Electromagnetic multiple scattering*

When a charged particle traverses a medium it is susceptible to deflection through Coulomb interactions with atomic nuclei. For small angles θ_0 the

Figure 4.1: Illustration of multiple scattering. Adapted from Ref. [125].



average multiple scattering (MS) is approximately gaussian with an angular distribution width as a function of the thickness of the medium x given by

$$\theta_0 = \frac{13.6 \text{ MeV}}{\beta c p} z \sqrt{x/X_0} [1 + 0.038 \ln(x/X_0)]. \quad (4.1)$$

With βc , p and z being the velocity, momentum and charge of the incoming particle respectively. X_0 is called the radiation length (Sec. 4.1.3) and is given in units of g cm^{-2} and is proportional to the distance a high energy electron will travel before having lost a significant amount of its energy. (4.1) captures the central 98% of the distribution. Figure 4.1 illustrates how (4.1) relates to the deflection y_{plane} after traversing a distance x . From (4.1) it is clear that the scattering chiefly affects low-energy particles or particles with a large effective charge z .

With Monte Carlo simulation, an easy way to calculate θ_{plane} and y_{plane} is to produce two gaussian random numbers r_1 and r_2 and calculate,

$$y_{\text{plane}} = r_1 x \theta_0 \sqrt{12} + r_2 x \theta_0 / 2 \quad (4.2)$$

$$\theta_{\text{plane}} = r_2 \theta_0 \quad (4.3)$$

Where the first term in (4.2) handles the correlation between the two variables. Multiple scattering as described here, accounts for a 2-dimensional scattering plane, but since MS can be assumed to be independent in both directions, a 3-d estimate can be found by applying (4.2) and (4.3) twice one time for each component [125, chap. 31]

$$\theta_0 = \theta_{\text{plane}}^{\text{rms}} = \frac{1}{\sqrt{2}} \theta_{\text{space}}^{\text{rms}}. \quad (4.4)$$

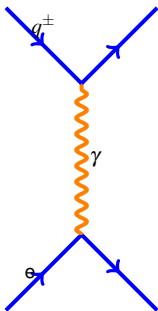


Figure 4.2: Coulomb interaction

4.1.2 Electromagnetic ionisation loss

Charged particles can lose energy through multiple processes. for massive particles with mass $M c^2 \gg m_e c^2$ energy loss through ionisation of atoms in the medium is a dominant contribution. The ionisation happens via elastic Coulomb interactions with atomic electrons illustrated in Figure 4.2.

From a statistical point of view, the mean energy loss per distance $\langle dE/dx \rangle$ is a sum of individual energy contributions from all the electron interactions happening during the traversal dx of the incident particle,

$$\Delta E = \sum_{n=1}^N \delta E_n. \quad (4.5)$$

The individual contribution ΔE is quite complex especially at low energy, so we will limit ourselves to the mean energy loss that when treated statistically is called *straggling*. In semi-classical terms (developed by N. Bohr [23, 24]) we consider the interaction of a massive particle with a single electron as a function of the impact parameter b (Figure 4.3) then the momentum transfer due to the Coulomb force is

$$\Delta p = \int F dt = \int F \frac{1}{v} dx = \frac{2ze^2}{bv}, \quad (4.6)$$

and the single energy transfer is

$$\Delta E(b) = \frac{\Delta p^2}{2m_e} = \frac{2z^2 e^4}{m_e b^2 v^2}. \quad (4.7)$$

The barrel in Figure 4.4 is assumed to contain $N_e = n(2\pi b)dbdx$ electrons where n is the electron density¹.

We find that:

$$-dE(b) = \frac{\Delta p^2}{2m_e} 2\pi n b db dx = \frac{4\pi n z^2 e^4}{m_e v^2} \frac{db}{b} dx \quad (4.9)$$

If we integrate over the impact parameter db we see a divergence as $b \rightarrow 0$ as we would expect due to the inverse square law. Instead we constrain the integration to a range $[b_{min}, b_{max}]$:

$$-\frac{dE}{dx} = \frac{4\pi n z^2 e^4}{m_e v^2} \int_{b_{min}}^{b_{max}} \frac{db}{b} = \frac{4\pi z^2 e^4}{m_e v^2} \ln \left(\frac{b_{max}}{b_{min}} \right). \quad (4.10)$$

Selecting the integration range in a meaningful way can be done setting the minimum distance b_{min} to the radius of the electron by saying that it should be located within its de Broglie wavelength,

$$b_{min} = \lambda_e = \frac{h}{p} = \frac{2\pi\hbar}{\gamma m_e v}. \quad (4.11)$$

The outer range b_{max} is limited by the assumption that the electron is fixed in space relative to the incoming particles (as it is found in a region bound by the location of the nucleus). That is to say, we place a limit on the interaction time (b/v) which is shorter than the electron revolution time (γ/v_e):

$$b_{max} = \frac{\gamma v}{\langle v_e \rangle}. \quad (4.12)$$

Putting it all together and we arrive at the Bohr equation:

$$-\left\langle \frac{dE}{dx} \right\rangle = \frac{4\pi z^2 e^4}{m_e c^2 \beta^2} n \ln \frac{m_e c^2 \beta^2 \gamma^2}{2\pi\hbar \langle v_e \rangle}. \quad (4.13)$$

The general form of the curve in Figure 4.5 can be understood by a kinematical drop that happens when the incident particles pass the electrons faster. i.e. they have less time to interact with the individual electrons the faster they move. The minimum at $\beta\gamma \sim 3 - 4$ is called the minimum ionising region. For particles with $\beta\gamma > 4$, relativistic effects Lorentz transforms ($E_y \rightarrow \gamma E_y$) the electric field, increasing the interaction cross section and leading to a 'relativistic raise' of the curve.

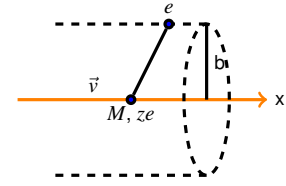


Figure 4.3: Coulomb interaction between an incoming particle with mass M , velocity \vec{v} and charge ze and an electron at rest (e). b is the impact parameter.

¹ Electron density:

$$n = N_A Z / A \quad (4.8)$$

where $N_A = 6.022 \times 10^{23} \text{ mol}^{-1}$ is Avogadro's constant, Z is the atomic number and A the mass number of the material.

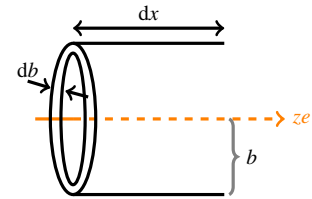


Figure 4.4: Barrel with N_e electrons.

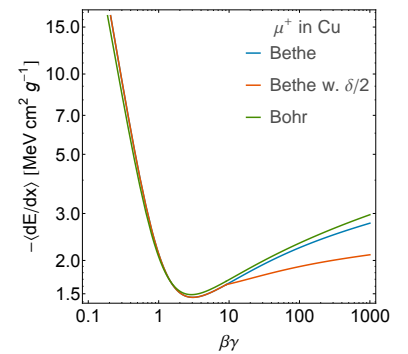


Figure 4.5: dE/dx for muons in copper. The lines show the Bohr equation (4.13) and the complete Bethe-Bloch equation (4.14) with and without the density correction at high energies as a function of speed.

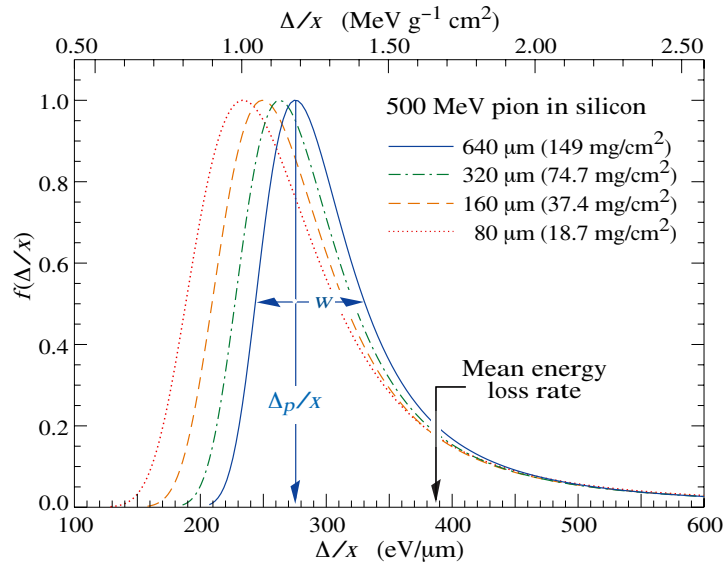
Bethe-Bloch formula Bohr developed his stopping formula (4.13) in 1913, it has later been revised with a quantum mechanical treatment and the more full formula is:

$$-\left\langle \frac{dE}{dx} \right\rangle = Kz^2 \frac{Z}{A} \frac{1}{\beta^2} \left[\frac{1}{2} \ln \frac{2m_e c^2 \beta^2 \gamma^2 T_{\max}}{I^2} - \beta^2 - \frac{\delta(\beta\gamma)}{2} \right] \quad (4.14)$$

Where $K = 4\pi N_A r_e^2 m_e c^2 = 0.307 \text{ MeV g}^{-1} \text{ cm}^2$ and $T_{\max} = \frac{2m_e c^2 \beta^2 \gamma^2}{1 + 2\gamma m_e/M + (m_e/M)^2}$ is the *maximum energy transfer* in a single collision and $\delta(\beta\gamma)$ is a *density correction* due to polarisation of the medium that reduces long range contributions by shielding the particle from far away charges. In addition to the density correction a small *shell correction* at low velocities is added to account for particles moving at intra-atomic speeds (Figure 4.5).

The Bethe-Bloch equation in its full form is mainly depending on the medium and the velocity of the incoming particle. This makes it an excellent estimator for particle velocity as long as we know if the particle is in the kinematical or the relativistic regime. If it is further combined with a momentum measurement we can calculate the rest mass. One thing we must consider is that the Bethe-Bloch equation gives us a *mean value* of what is in fact a sum of highly complex interactions. The actual interactions are found to obey a Landau distribution which is a highly asymmetrical distribution with a long tail toward high energies.

Figure 4.6: Landau distributions [125] for various thicknesses of silicon. For reference the ATLAS pixel sensors are $250 \mu\text{m}$ thick.



The Landau-Vavilov equation From the Landau distribution in Figure 4.6 we can see that for moderately thick mediums (often found in particle detectors), the Most Probable Value (MPV) is much lower than the mean value expected from (4.14). In practice the Vavilov equation is much more appropriate:

$$\Delta_p = \xi \left[\ln \frac{2m_e c^2 \beta^2 \gamma^2}{I} + \ln \frac{\xi}{I} + j - \beta^2 - \delta(\beta\gamma) \right]. \quad (4.15)$$

Where $\xi = (K/2) \langle Z/A \rangle (x/\beta^2) \text{ MeV}$, $j = 0.200$.

The form of the Landau distribution is not easily parameterisable, but it is approximated with a MPV from (4.15) and a width $w = 4\xi$ as

$$f(\Delta/x) = \frac{1}{\sqrt{2\pi}} \exp \left[-\frac{1}{2} \left(\frac{\Delta/x - a(\Delta/x)_{mp}}{\xi} \right)^2 + e^{-\left(\frac{\Delta/x - a(\Delta/x)_{mp}}{\xi} \right)} \right]. \quad (4.16)$$

These considerations are naturally of theoretical nature and is mainly important to us during simulations as the actual measurement is smeared and distorted by detector effects. In practice we develop an empirical model specifically for our instruments when using energy loss as a β estimator.

4.1.3 Bremsstrahlung

Charged particles with sufficient energy can interact electrically with the Coulomb field of atomic nuclei. This type of interaction is called bremsstrahlung (Figure 4.7) and is mainly relevant for electrons and positrons as the energy loss is proportional to $1/m^2$:

$$\frac{dE}{dx} = 4\alpha N_A \frac{z^2 Z^2}{A} \left(\frac{1}{4\pi\epsilon_0} \frac{e^2}{mc^2} \right)^2 E \ln \frac{183}{Z^{1/3}} \sim \frac{E}{m^2} \quad (4.17)$$

For highly energetic muons like the ones we can measure with IceCube the same effect can be observed when E is sufficiently high in proportion to $1/m^2$.

Radiation Length For electrons bremsstrahlung is such a dominant effect that it is customary to write eq (4.17) in terms of a radiation length X_0 , the length in a given material it takes a traversing electron to radiate all but $1/e$ of its energy:

$$\frac{dE}{dx} = 4\alpha N_A \frac{z^2 Z^2}{A} r_e^2 E \ln \frac{183}{Z^{1/3}} \quad ((4.17) \text{ for electrons}) \quad (4.18)$$

$$\frac{dE}{dx} = \frac{E}{X_0} \quad \text{where} \quad X_0 = \frac{A}{4\alpha N_A Z^2 r_e^2 \ln \frac{183}{Z^{1/3}}}. \quad (4.19)$$

If we ignore the possible emission of low energy ($k = E_\gamma$) photons ($y = k/E \rightarrow 0$, at the infrared limit) and very high energy photons $y \rightarrow 1$ where screen becomes a problem, then the differential cross section is,

$$\frac{d\sigma}{dk} = \frac{1}{k} \frac{A}{X_0 N_A} \left(\frac{4}{3} - \frac{4}{3}y + y^2 \right). \quad (4.20)$$

The number of photons with energies between k_{min} and k_{max} emitted from an electron traveling a distance $x \ll X_0$ is

$$N_\gamma = \frac{x}{X_0} \left[\frac{4}{3} \ln \left(\frac{k_{max}}{k_{min}} \right) - \frac{4(k_{max} - k_{min})}{3E} + \frac{k_{max}^2 - k_{min}^2}{2E^2} \right]. \quad (4.21)$$

At a certain point ionisation losses are more dominant than bremsstrahlung losses. This *critical energy*

$$E_c = \frac{610 \text{ MeV}}{Z + 1.24} \text{ (Solids and liquids)}, \quad E_c = \frac{710 \text{ MeV}}{Z + 0.92} \text{ (Gasses)} \quad (4.22)$$

is the point at which an electromagnetic shower (Sec. 4.1.5) will terminate.

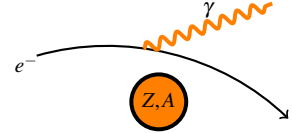
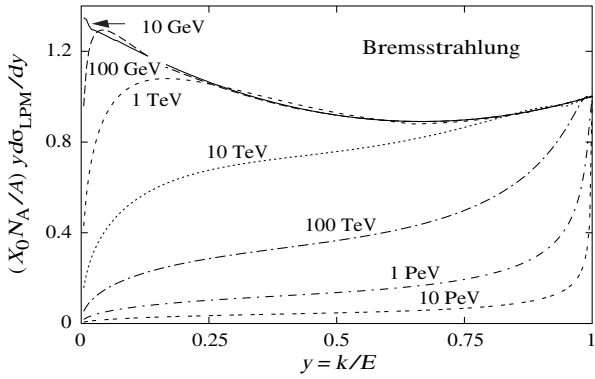
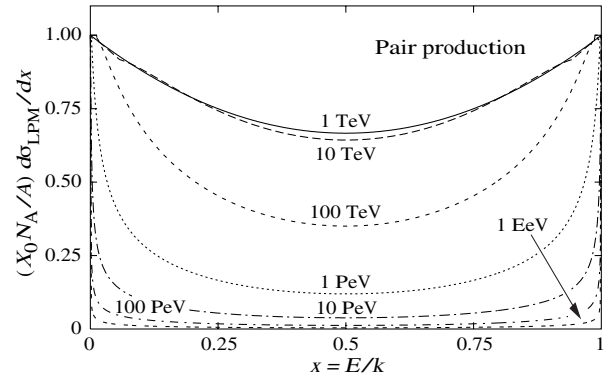


Figure 4.7: Photon emission by bremsstrahlung from an electron.



(a) Normalised bremsstrahlung spectrum. The horizontal axis shows the energy fraction $y = k/E$ transferred from the electron to the photon. The vertical axis is in numbers of photons per radiation length X_0 .



(b) Pair production cross section. x is the fractional energy transferred from the photon to the e^+e^- pair.

Figure 4.8: Bremsstrahlung and Pair production cross sections.

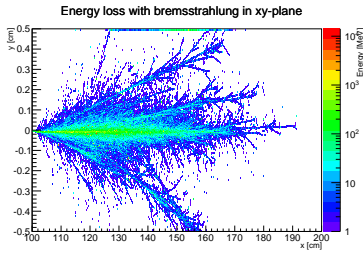


Figure 4.9: Computer simulation of Electromagnetic cascade, Ref. [28].

4.1.4 Photon pair production

The ‘inverse’ of bremsstrahlung is pair production. When photons are sufficiently energetic ($E_\gamma \gg m_e c^2$) they are able to produce electron-positron pairs. At $E_\gamma \sim 2m_e c^2(1 + m_e/m_n)$ pair production starts to become significant. The differential cross section for pair-production is similar to (4.20),

$$\frac{d\sigma}{dx} = \frac{A}{X_0 N_A} \left[1 - \frac{4}{3}x(1-x) \right], \quad (4.23)$$

where $x = E/k$ is the fractional energy transferred to the e^+e^- pair.

4.1.5 Electromagnetic cascades

Electromagnetic cascades (Figure 4.9) happens when a high energy electron or photon encounter dense matter. As mentioned in the introduction, it starts either as a bremsstrahlung interaction of an incident electron or as pair production from a photon. The subsequent creation of pairs and photons continues until all photons and electron/positrons have energies below their production threshold (4.22).

The overall profile of the cascade (or shower) can be described in terms of the depth of the medium and the energy fraction (Figure 4.8) in terms of the critical energy

$$t = x/X_0, \quad y = E/E_c. \quad (4.24)$$

The development of the shower can be seen as a geometric (or recursive) series, where the total particle multiplicity (electrons, positron and photons) at depth t is

$$N(t) = 2^t, \quad (4.25)$$

and the energy of the individual particles generated at t is

$$E(t) = E_0 \cdot 2^{-t}. \quad (4.26)$$

The multiplicative growth continues until $E_0/N \leq E_c$. After which point low-energy processes² will absorb the energy. The point where the critical

² Ionisation, Compton scattering, photoelectric effects...

energy is reached is called the maximum multiplication step

$$E_c = E_0 \cdot 2^{-t_{max}}. \quad (4.27)$$

Which is then

$$t_{max} = \frac{\ln(E_0/E_c)}{\ln 2} \sim \ln(E_0/E_c). \quad (4.28)$$

This is all based on a ridiculous simple model but illustrates the nature of electromagnetic cascades. The concept of cascades are further explained in [56, 125].

4.1.6 Cherenkov radiation

Compared to the energy loss described in the previous sections, emission of Cherenkov light by charged particles is insignificant. Nevertheless it is important for detection of particles in massive ice and water neutrino detectors. It also serves a role in particle identification in collider experiments, which on its own makes it relevant for long-lived charged particle searches.

A charged particle that moves at a speed faster than the phase speed of light in a medium it traverses, emits light

$$v \geq \frac{c_{vac}}{n_{medium}}. \quad (4.29)$$

This means that the effect has an onset for speeds

$$\beta \geq \frac{1}{n}. \quad (4.30)$$

The emission is caused by the atoms in the medium becoming polarised as the charged particle moves by. When the polarisation is relaxed light is emitted by the atoms. Due to the high velocity of the charged particle the emitted radiation interferes constructively and forms a wavefront that sideslips along the particle trajectory. The wavefront has a characteristic angle relative to the particle trajectory, this Cherenkov angle

$$\cos \theta_c = (1/n\beta) \quad \text{or} \quad \tan \theta_c = \sqrt{\beta^2 n^2 - 1} \quad (4.31)$$

effectively forms a light cone around the trajectory that radiates outwards with an angle θ_c . By inserting (4.30) into $E = \gamma m$ we find the minimum total energy a charged particle must have to radiate Cherenkov radiation

$$E_{min} = \frac{m}{\sqrt{1 - \frac{1}{n^2}}}. \quad (4.32)$$

The number of photons N with wave length λ radiated per path length x is expressed by

$$\frac{d^2 N}{dx d\lambda} = \frac{2\pi\alpha z^2}{\lambda^2} \left(1 - \frac{1}{\beta^2 n^2(\lambda)} \right) \quad (4.33)$$

where $\alpha = 1/137$ and the refraction index $n(\lambda)$ is given as a function of wavelength [81]. For ice the number of photons in the visible range is plotted in Figure 4.10 and Figure 4.12, where $n(\lambda)$ is

$$n(\lambda) = 1.55749 - 1.57988\lambda + 3.99993\lambda^2 - 4.68271\lambda^3 + 2.09354\lambda^4. \quad (4.34)$$

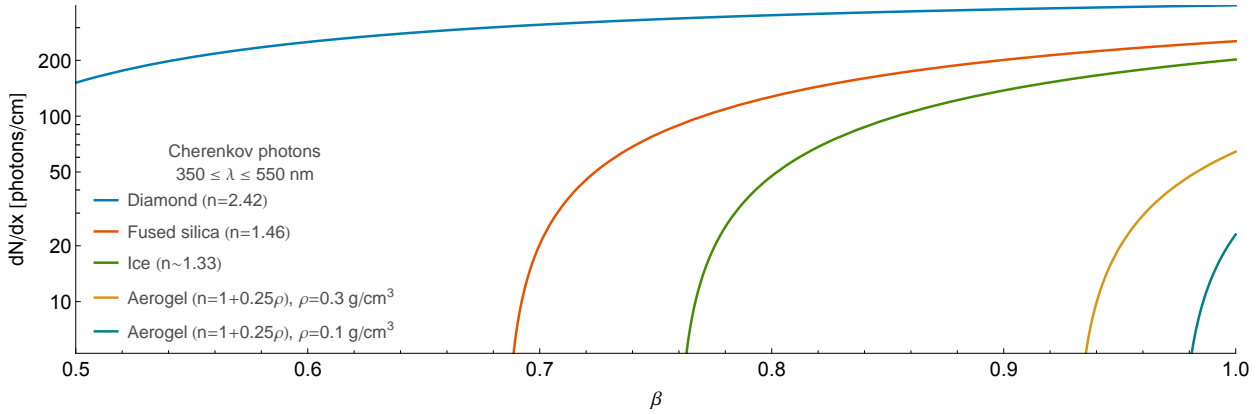


Figure 4.10: Equation (4.33) integrated from $350 < \lambda < 550$ nm in photon wavelength. Where the index of refraction for ice is determined from (4.34)

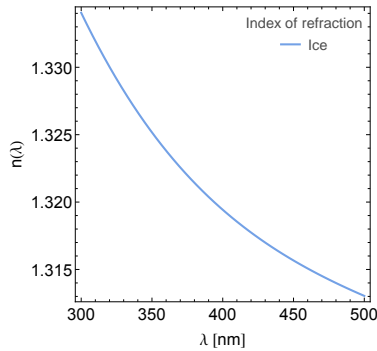


Figure 4.11: Index of refraction in ice.

4.1.7 Transition radiation

Like Cherenkov radiation, Transition Radiation (TR) is an electromagnetic effect that happens when a charged particle traverses dielectric materials. Cherenkov radiation is caused by a polarising effect in a dielectric medium. TR on the other hand is an effect of the charged particle moving from one medium to another with a different dielectric constant. Intuitively the effect of TR can be understood by analogy [39]. Radiation from a uniformly moving charge in a composite medium of changing dielectric constants is analogous to radiation from a particle in non-uniform motion (undergoing acceleration). In the case of the uniformly moving particle in changing medium the phase velocity of the medium changes, while in the case of the accelerated charged particle the velocity of the particle changes relative to the reference.

The light emitted by TR is usually in the X-ray range and unlike Cherenkov radiation depends on the Lorentz factor γ and not the speed (β) of the particle itself. This makes the effect particularly useful for particle identification of electrons at high energies. In ATLAS one of the tracking systems (Sec.6.2.3) is surrounded by material that allows the detector to serve a dual purpose as an electron-pion separator as well as tracker.

4.2 Hadronic interactions

Besides the electromagnetic interactions affecting charged particles, hadrons also have a chance interacting via the strong force. Of interest to particle detection (and LLPs) is mainly inelastic collisions where secondary hadrons are produced in the collision with nuclei in the medium.

Like the radiation length (X_0) for electrons characterises the interaction probability of charged particles, so does the average hadronic interaction length λ_I describe the absorption probability in matter:

$$N = N_0 e^{-x/\lambda_I} \tag{4.35}$$

For a medium with atomic number A and density ρ the hadronic interaction

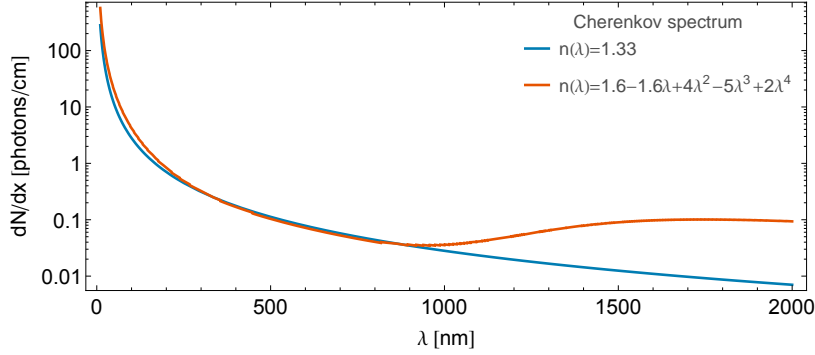


Figure 4.12: Cherenkov spectrum for ice.

length is given by

$$\lambda_I = \frac{A}{N_A \rho \sigma_{inel}}, \quad (4.36)$$

where N_A is Avogadro's constant.

The hadronic cross section

$$\sigma_{total} = \sigma_{el} + \sigma_{inel} \quad (4.37)$$

is for energies above the hadronisation threshold more or less constant with energy (Figure 4.13) and the inelastic component σ_{inel} dominates as

$$\sigma_{el} \approx \mathcal{O}(10) \text{ mb} \quad (4.38)$$

$$\sigma_{inel} \sim A^{2/3} \text{ mb}. \quad (4.39)$$

As for electromagnetic showers, the production of new hadrons that can again interact leads to a hadronic cascade,

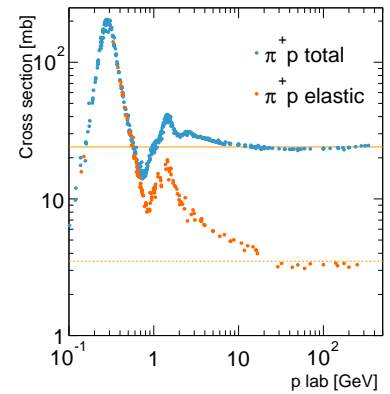
$$t = \frac{x}{\lambda_I}, \quad y = E/E_C \quad (4.40)$$

where $E_c = 290 \text{ MeV}$ enough for pair-producing pions π^\pm . With t and y the formulae in Electromagnetic cascades are identical. In general λ_I is much longer than X_0 so it takes more matter to contain a hadronic shower than an electromagnetic one.

4.3 Particle identification

Now that the common processes have been introduced we can summarise the principles in detecting long-lived particles. To identify a long-lived particle we need to find its rest mass m_0 and charge z . These quantities can be determined by combining multiple measurements. From *track reconstruction* we can find the momentum and $\text{sign}(z)$ from measuring the radius R of the curvature of the particle in a magnetic field (4.46). If the distances and time resolution allows it, the speed can be measured based on the particle time-of-flight (4.50). We also noted in Section 4.1.2, that electromagnetic energy loss is related to the speed by the Bethe-Bloch formula (4.14). If it is possible to stop the particle in a calorimeter, the kinetic energy is also available

$$E_{kin} = (\gamma - 1)m_0c^2. \quad (4.41)$$


 Figure 4.13: Total and Elastic cross sections for $\pi^+ p$ interactions, Ref. [125].

Another part of long-lived particle phenomenology is obviously the lifetime itself. In most cases a direct lifetime measurement requires the particle to decay somewhere within the volume of the detector and potentially within the event's time-frame. Specific searches for stopped particles that decay out-of-time with the event have been performed [110]. The case in-between, where the LLP is not stopped and lives longer than the detector range ($\tau_0 > \frac{r_{det}}{\beta\gamma c}$), the lifetime is usually unconstrained.

4.3.1 Momentum measurement

A charged particle moving in a magnetic field is subjected to the Lorentz force³

$$\vec{F} = z(\vec{E} + \vec{v} \times \vec{B}). \quad (4.42)$$

³ \vec{F} is the force vector affecting the z -charged particle when subjected to the accelerating electric field \vec{E} and the deflecting magnetic field \vec{B} .

⁴ κ is a constant that depends on the units of the \vec{B} -field and c .

That means that the propagation of the particle is governed by⁴

$$\frac{d\vec{p}}{dt} = \frac{d(m\gamma dx/dt)}{dt} = c^2 \kappa z \vec{v}(t) \times \vec{B}(\vec{x}(t)). \quad (4.43)$$

Assuming no energy loss (i.e. constant velocity), we can express the particle trajectory $\vec{r}(s)$ as a function of path length s along the track

$$\frac{d^2\vec{r}(s)}{ds^2} = \frac{z}{p} \frac{d\vec{r}(s)}{ds} \times \vec{B}(s). \quad (4.44)$$

In a cylindrical detector (like ATLAS) a solenoidal magnetic field will deflect the particles produced at the centre in the $x-y \sim (\rho - \phi)$ plane, that is to say along the circular curvature of the cylinder (ρ is the radial component, ϕ the azimuth angle, and z would be the cylindrical depth).

The curvature is measured at multiple tracking planes situated at different ρ . By fitting a helix equation, radius R of the curvature can be related to the momentum

$$p_T = 0.3BR. \quad (4.45)$$

The total momentum requires information on the $\rho - z$ dip angle λ and momentum is thus

$$p = \frac{p_T}{\cos \lambda} = \frac{0.3BR}{\cos \lambda}. \quad (4.46)$$

The error on the momentum is

$$\left(\frac{\Delta p}{p}\right)^2 = \left(\frac{\Delta R}{R}\right)^2 + (\tan \lambda \Delta \lambda)^2. \quad (4.47)$$

The error is important as it influences our mass measurement directly, and is the only factor in the estimation process that scales with the rest mass of the particle (time-of-flight and dE/dx only become better and better while the stiffer the track, the worse the momentum). Another thing to note, at hadron colliders one is usually interested in the transverse component only, as momentum conservation is 'broken' in the event due to the compositeness of the colliding particles. For long-lived particles the mass estimate is not calculated based on the invariant mass of the collision but for each individual particle candidate, that is why the total momentum is important.

The sign of the charge is limited by the track arm-length (L), the detector resolution (σ_y) and number of measurements (C_N) [82]

$$p < \frac{0.3BL^2}{3\sqrt{4C_N\sigma_y}}. \quad (4.48)$$

The inequality assumes a 3 standard deviation separation between the signs. For ATLAS, a momentum larger than 800 GeV will lead to sign confusion if measured only by the inner detector system (depending on the actual number of measurements C_N).

4.3.2 Identification by energy loss

The average ionisation energy loss depends on the energy of the particle. In Figure 4.14 the energy loss is plotted for electrons, muons, pions, kaons and protons in the 0.1 to 100 GeV momentum range. Since the energy loss is mass dependent, together with a momentum measurement we can distinguish the rest mass by inverting the Bethe-Bloch equation and finding $\beta\gamma$:

$$m = \frac{p}{\beta\gamma}. \quad (4.49)$$

The actual formula is not injective due to the kinematic falling slope and the relativistic rise. In practice we can choose to focus on one region, typically the kinematic slope and assume that every dE/dx measurement above the MIP region is lying on that slope. Looking at Figure 4.14 this may seem a bit optimistic, but the density effect is not applied here (See instead Figure 4.5) that flattens the relativistic rise dramatically.

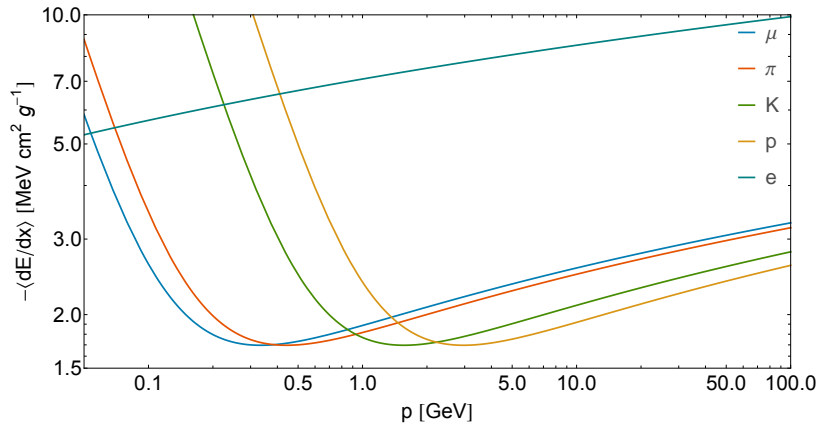
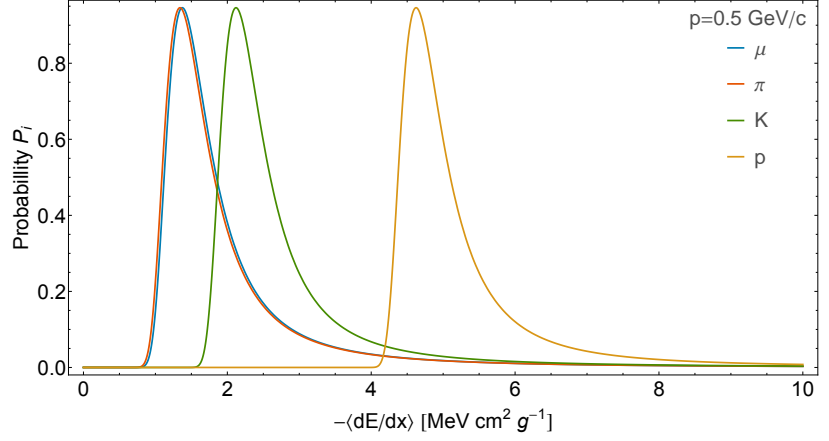


Figure 4.14: Average energy loss for long-lived Standard Model particles, (in Silicon, without density corrections).

Truncated mean One factor that is important is the possibility of large fluctuations in energy deposition (Figure 4.15). We know that the Landau distribution is not at all symmetric about the average energy loss, so how do we measure the average? Instead of combining all dE/dx measurement along a track we can use the *truncated mean*, where we remove the largest 20% – 50% of the measurements and average the rest. The actual percentage depends on the number of samplings available. With many samplings the smallest 5% – 10% can be removed as well to arrive at a more gaussian distribution as illustrated in Figure 4.16.

Figure 4.15: Specific energy loss at $p = 500 \text{ MeV}/c$.

4.3.3 Identification by time-of-flight

Mass can be measured by combining a precise Time-of-Flight (ToF) estimate with a momentum estimate:

$$\beta = \frac{L}{c \Delta t}, \quad p = c\beta\gamma m \quad (4.50)$$

$$\text{Setting } c = 1 \rightarrow \beta = \frac{L}{\Delta t}, p = \beta\gamma m$$

$$m^2 = p^2 \left(\frac{1}{\beta^2} - 1 \right) = p^2 \left(\frac{\Delta t^2}{L^2} - 1 \right) \quad (4.51)$$

Where $\Delta t = t_1 - t_0$ is the time difference between two detectors and L is the distance between them. The mass uncertainty is then [87]:

$$\sigma(m^2) = 2 \left[m^4 \left(\frac{\sigma_p}{p} \right)^2 + E^4 \left(\frac{\sigma_{\Delta t}}{\Delta t} \right)^2 + E^4 \left(\frac{\sigma_L}{L} \right)^2 \right]^{1/2}, \quad (4.52)$$

where E is the total energy of the particle: $E^2 = m^2 + p^2 = \frac{p^2 \Delta t^2}{L^2}$.

The actual measured time is a sum of multiple contributions

$$t = t_0 + t_{TOF} + t_{drift} + t_{electronics} + t_{DAQ} \quad (4.53)$$

each with its own uncertainties. t_0 is the trigger time offset from the actual interaction. In ATLAS it is the bunch crossing time, in IceCube (Chap. 11) it is the offset from when the interaction happened to when the first photomultiplier tube was struck. t_{TOF} itself is also not as uncomplicated as a straight line, bending in the magnetic field, breaking in material and so on modifies the assumed Δt . Depending on the detector itself the signal formation time in the detector adds an appreciable delay. In IceCube the time from when a photon hits the PMT to the signal is formed roughly 4 ns [121]. Electronic readout also contributes jitter and shaping to the signal, that again takes a finite time to arrive at the signal collecting station (t_{DAQ}).

In general ToF is dependent on the length of the flight path, the detector time resolution and the number of independent measurements available ($\sigma_{\Delta t} = \sigma_{t_{det}} / \sqrt{N_{meas}}$).

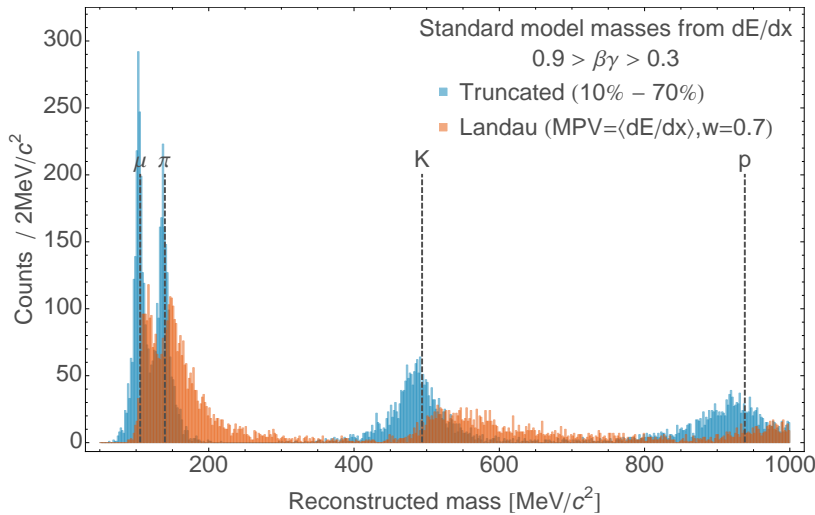


Figure 4.16: Example of how truncation 'gaussifies' the Landau fluctuations and shapes the reconstructed mass distribution found by extracting β inverting the Bethe-Bloch equation ($m = p / (\beta\gamma)$).

4.4 Summary

This chapter has served as an atomic interlude that will provide the experimental basis for the rest of the thesis. With the knowledge of how matter will behave when subjected to highly energetic charged particles we can now continue with a practical introduction on how to measure these signatures with the systems in ATLAS. In summary, the key findings in this chapter are:

- Charged particles lose energy in a medium depending on the particle velocity and charge, when they interact with atomic electrons, either exciting or ejecting them from their atoms.
- Coulomb interactions deflect the trajectory of slow and light particles in a medium. The cumulative change in path is called *multiple scattering*.
- Coulomb interactions with the nucleus of an atom leads to bremsstrahlung, where the incoming charged particle is deflected and hence decelerated enough to emit a high-energy photon.
- High energy photons can in the presence of a nucleus convert to an electron-positron pair. At lower energies Compton scattering and photo-electric emission dominates.
- High energy electrons and photons can start a cascade of pair-production and photon emission called an electromagnetic shower.
- Charged particles that move faster than the phase velocity (c/n) in a medium cause polarisation of the atoms in the medium. When the atoms relax their polarisation state they emit coherent light forming a wavefront called Cherenkov radiation at a specific angle relative to the particle trajectory.
- Hadrons can interact strongly with nuclei creating new hadrons at lower energies. This can lead to a cascade of particles like for electrons, but with a somewhat longer interaction length (λ_I).

- Long-lived particles can be identified by their speed in combination with their momentum.
- Momentum is measured as a function of the curvature of a charged particle in a magnetic field.
- Specific energy loss can provide the speed estimate ($\langle dE/dx \rangle \sim 1/\beta^2$). The method gives a more stable result if multiple measurements are ‘truncated’ hence removing Landau long-tail contributions.
- A direct time-of-flight measurement also provides a speed measurement.

5 The Large Hadron Collider

5.1 Hadron Colliders

At its roots particle physics aims to study nature by observing how subatomic particles interact. Observing what comes out when a target is bombarded with a specific particle at a specific kinetic energy has led to great revelations about how our universe is structured. These interactions can be caused by numerous means; naturally occurring radioactive processes and cosmic rays where some of the early sources. With the advent of particle accelerators a more systematic study has been possible, and quickly it was realised that the available kinetic energy in the collision meant opening up to new regions of physics, with new particles and new dynamics. Shooting a beam at a fixed target yields [125, chap. 45],

$$E_{cm} = (m_1^2 + m_2^2 + 2E_{1,lab} m_2)^{1/2}, \quad (5.1)$$

compared to,

$$E_{cm} = [(E_1 + E_2)^2 - (\vec{p}_1 + \vec{p}_2)^2]^{1/2} \quad (5.2)$$

if colliding two beams with each other. In Figure 5.1 we can see the difference.

It was thus a major breakthrough when the Intersecting Storage Rings (ISR) collided the first hadron beams in 1971 and allowed for nearly double the centre of mass energy. Ultimately the ISR reached a centre of mass energy of 63 GeV [64], which by (5.1) would have required a 2 TeV fixed-target accelerator. The ISR was not the first particle collider, but the use of hadrons made it possible to reach much higher collision energies and discover new heavier particles. The ISR also made it possible to upgrade the already running fixed-target SPS to a 540 GeV proton-anti-proton collider the Sp \bar{p} S that allowed the UA1 and UA2 collaborations to discover the W^\pm and the Z^0 bosons in 1983. A few years later in 1986 the American Tevatron collided its first protons with anti-protons that culminated with the discovery of the top quark in 1995 with a centre of mass energy of 1.96 TeV.

The use of hadrons instead of electrons creates a much more complicated collision environment due to the compositeness of the colliding particles. The reason why hadrons are collided at the high-energy accelerators is due to the emission of synchrotron radiation by accelerating charged particles. At the TeV scale the energy loss of electrons circulating a 27 km storage ring would be in the PeV range. An alternative would be linear colliders like the proposed International Linear Collider (ILC) that would be roughly 30 km long in order to reach 1 TeV. For discovering new physics at unknown

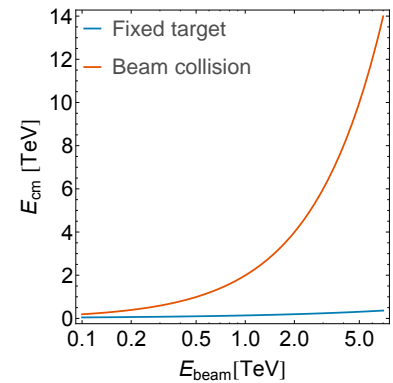
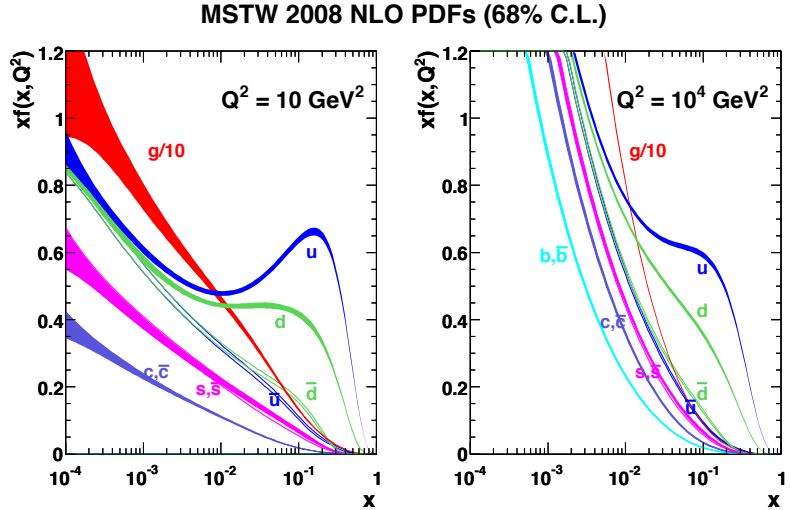


Figure 5.1: Beam colliders gain an enormous boost in centre of mass energy compared to fixed target. In both cases protons are colliding.

Figure 5.2: PDFs $f_i^A(x, Q^2)$ from the MSTW group. [72]

energies hadrons are more economical and that is why all 4 massive Standard Model particles discovered after 1980 have been found at hadron colliders.

5.1.1 Parton Distributions

Protons and other hadrons are not simply valence quarks in a brown paper bag, due to radiative production of quark-antiquark pairs by the gluons holding the valance quarks together an additional ‘sea’ of possible quarks are present inside the hadron.

By Deep Inelastic Scattering (DIS) information about the composition of hadrons have been obtained and turned into scale dependent parameterisations. Multiple collaborations produce these Parton Distribution Functions (PDF) that effectively assigns an interaction probability $f_i^A(x, Q^2)$ to each parton i in the hadron of type A to partake in a given scattering process,

$$\sigma_{A,B \rightarrow X} = \sum_{i,j} \int \int f_i^A(x_1, Q^2) \cdot f_j^B(x_2, Q^2) \cdot \hat{\sigma}_{i,j \rightarrow X} dx_1 dx_2. \quad (5.3)$$

Q^2 is the overall energy scale defined by the incoming particles momentum. x is the momentum fraction. $f_i^A(x, Q^2)$ is then the probability that the parton i at the energy scale Q^2 carries away a momentum fraction x of the hadron’s total momentum.

In Figure 5.2 the PDF of a proton at two different energy scales are shown. Notice that at high Q^2 the sea and gluon components have a high probability of carrying a significant fraction of the hadron momenta. This is in fact why colliding protons with protons is sensible as the valence quarks play a fairly small role and gluons are dominating, saving us from charge conservation.

5.2 The CERN Accelerator Complex

The accelerator facility CERN houses numerous experiments that all need accelerated particle beams. With advances in acceleration technology CERNs

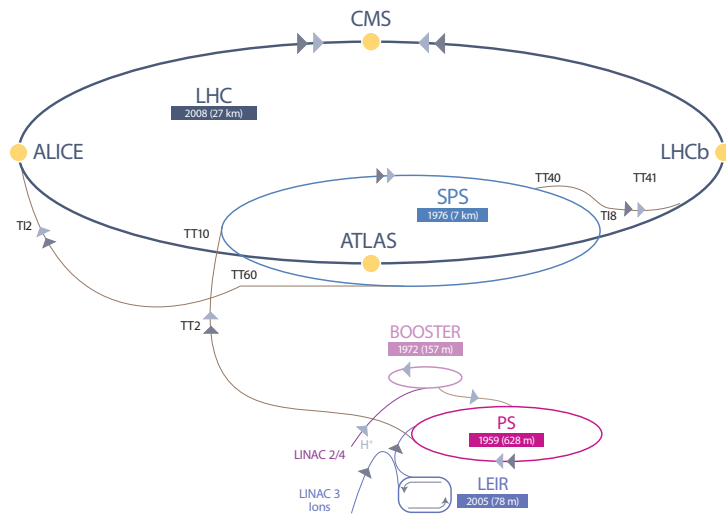


Figure 5.3: The LHC accelerator chain

portfolio of available beam types and energy has steadily increased. CERN mainly supply high energy and high intensity beams, at levels where national facilities have a hard time competing. Low energy at CERN starts at around 25 GeV which is the maximum energy of the Positron Synchrotron (PS). By injecting the PS beam into the SPS, a factor of 20 times the beam energy is created with a maximum energy of 450 GeV. Both storage rings deliver beams to fixed-target experiments, the PS serves the original CERN compound in Meyrin, Switzerland, where for instance the on-line isotope mass separator (ISOLDE) can produce nearly any isotope in the periodic system based on the PS beam. At the ‘North Area’ in Prévessin, France, beams are extracted from the SPS that can either be used at full energy or converted by targets to other particles such as high energy electrons and pions, that has been used as test-beams in the study of particle interactions in the LHC detectors.

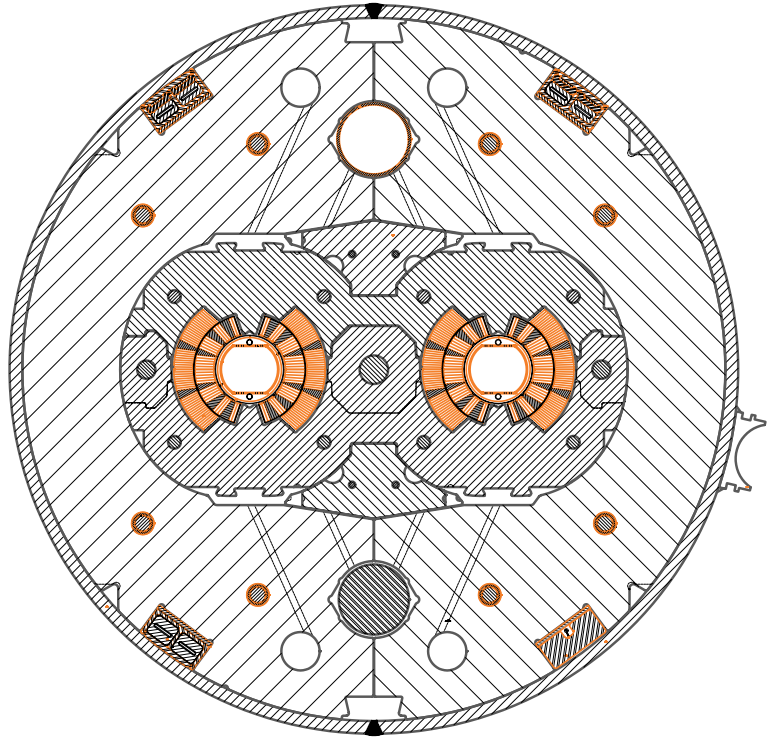
The Large Hadron Collider (LHC) is also fed by this chain of accelerators. In Figure 5.3 the chain of accelerators leading to the LHC is sketched. Beams are extracted from the SPS at 450 GeV and injected into the LHC in each direction. Here they are ramped to a maximum energy of 7 TeV. Unlike the other accelerators, the LHC does not provide any fixed-target services it is currently dedicated to beam collisions at the four interaction points also illustrated in Figure 5.3.

	LEP	Tevatron	LHC
Beam type	e^+, e^-	p^+, p^-	p^+, p^+
Beam energy [GeV]	45 – 104	900, 1000	3500, 4000, 6500, 7000
Circumference [km]	26.7	6.85	26.7
Years of operation	1989-2000	1986-2011	2008-
Luminosity [$\text{cm}^{-2}\text{s}^{-1}$]	$\sim 10^{30}$	10^{32}	$10^{33}, 10^{34}, 10^{34}$
\sqrt{s} [GeV]	161 – 207	1960	7000, 8000, 13000, 14000
Total statistics [pb^{-1}]	110, 300, 500	12000	5000, 20000, ?, ?

Table 5.1: Colliders

The LHC is placed in a 26.7 km tunnel constructed for the Large Electron-Positron collider (LEP). This tunnel was originally designed to facilitate a

Figure 5.4: A cross sectional view of one of the LHC dipole bending magnets. [43]



future hadron collider as well as the lepton collider, yet during the planning of the LHC the option to keep the LEP inside the tunnel was abandoned. The diameter of the tunnel is 3.7 m which would leave little space for two superconducting rings, instead the LHC magnets are designed with two bores sharing the same cryostat and magnet assembly as can be seen from Figure 5.4.

Compared to LEP, the underground facility shown in Figure 5.5 has been expanded with two new caverns housing the ATLAS detector (Sec. 6) and the CMS detector. A comparison with LEP and the Tevatron can be found in table 5.1.

In the years from 2010 until 2012 the LHC was in a commissioning phase (Table 5.2), where the beam energy was only half of the design energy. The decision to run at 3.5 TeV and later in 2012 at 4.0 TeV was due to a design error in the copper interconnects between the super-conducting bending magnets. The error was disastrously discovered in 2008 shortly after the initial run, where a magnet quench led to explosive decompression of the confined helium destroying several magnets. During the following year, the sector was repaired and quench monitoring systems were installed. Running resumed in Nov. 2009 at $\sqrt{s} = 900$ GeV with impressive strides in luminosity and beam optimisation.

5.3 Luminosity

From table 5.2 we see that the instantaneous luminosity of the LHC was around $L = 10^{33} \text{ cm}^{-2} \text{ s}^{-1}$ during the 2011 run, which is loosely calculated

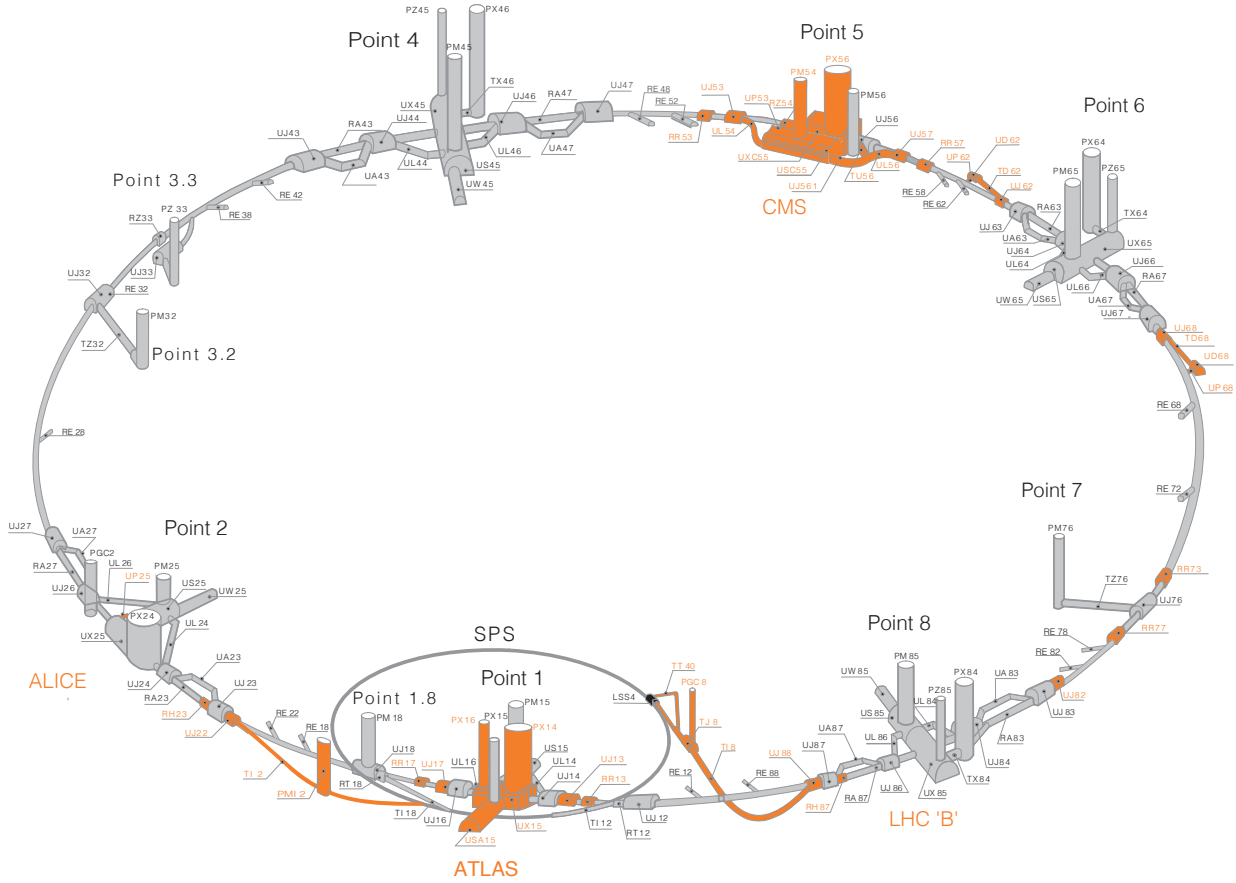


Figure 5.5: A schematic of the underground LHC facilities. The grey areas are pre-existing structures from the LEP accelerator complex, the orange areas are new infrastructure built for the LHC.

	Nominal	(late) 2011 Run
Beam energy [TeV]	7.0	3.5
Peak luminosity [$L=10^{33} \text{cm}^{-2} \text{s}^{-1}$]	10	3.5
Stored beam energy [MJ]	361.7	112.0
Bunch Intensity [$10^{10} p$]	11.5	14.5
Number of bunches per beam	2808	1380
Bunch Spacing [ns]	25	50
Colliding bunch pairs in ATLAS	2808	1331
Normalised transverse emittance [μm]	3.5	2.4
β^* at collision in ATLAS [m]	0.55	1.0
Average number of processes per crossing $\langle \mu \rangle$	25.60	~ 9.1

Table 5.2: LHC parameters at nominal operation and during the commissioning in 2011, Ref. [44].

by,

$$L = f \frac{n_1 n_2}{4\pi\sigma_x\sigma_y} \quad (5.4)$$

where f is the collision frequency of two bunches with n_1 and n_2 protons. σ_x and σ_y describe the gaussian beam width and height. It is common to measure the amount of accumulated statistics in integrated luminosity $\int L dt$ with the unit of inverse-barn. fb^{-1} for instance, corresponds to 70×10^{12} collisions. In terms of beam parameters (Table 5.2) the instantaneous luminosity can be expressed as

$$L = \frac{N_b^2 n_b f_{rev} \gamma_r}{4\pi\epsilon_n \beta^*} F, \quad (5.5)$$

where N_b is the number of particles per bunch, n_b is the number of bunches per beam, f_{rev} the revolution frequency, γ_r is the relativistic gamma factor,

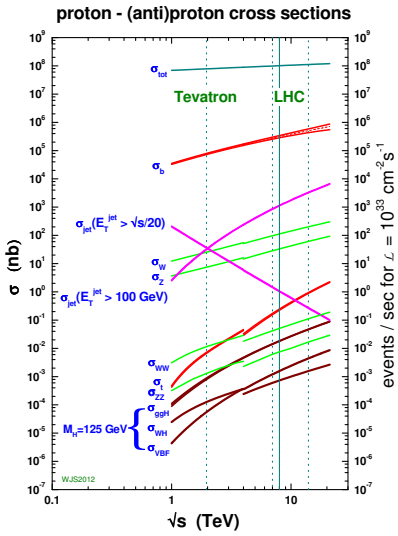


Figure 5.6: Interaction cross sections at the LHC Ref. [99]

Figure 5.7: Average simultaneous interactions per bunch-crossing in ATLAS, in 2011 and 2012 Ref. [103].

ϵ_n is the transverse beam emittance, β^* is the beta function at the collision point and F is a geometrical reduction factor due to the introduced crossing angle at the interaction points.

To give some idea about what that means in terms of production rate for common processes,

$$r_{process} = L\sigma_{process}, \tag{5.6}$$

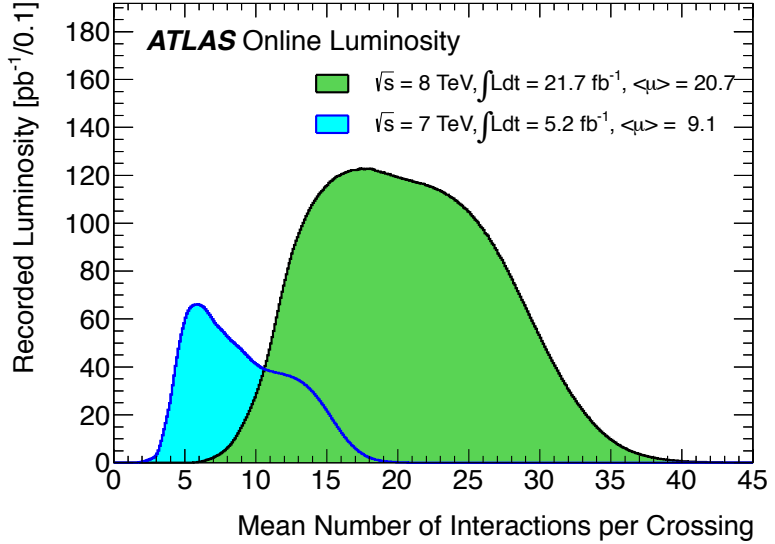
where $\sigma_{process}$ is the cross section of the specific process and L is the instantaneous luminosity, we see from Figure 5.6 that for instance Z-bosons are produced at a rate around 40 Hz and nearly a million b -pairs are produced per second.

To estimate the accumulated number event produced we can calculate,

$$N = \sigma_{process} \int L dt \tag{5.7}$$

5.3.1 Pile-up

The high collision rate comes at a price, pile-up, multiple interactions happening at the same time is a serious issue at the LHC. With 10^{11} protons per bunch colliding in a tightly squeezed region around 9.1 collisions happened per bunch-crossing inside ATLAS in 2011. This overlap leaves a challenge to the reconstruction algorithms where finding the correct vertex for each secondary particle is crucial when estimating missing energy and invariant masses.



6 The ATLAS detector

The LHC hosts four main experiments, one of these are ATLAS (A Toroidal LHC Apparatus), a general purpose detector designed to study a wide spectrum of particle interactions at the full beam intensity of the collider. The LHC is sized to allow for the production of TeV scale objects at low cross sections. The ATLAS detector is designed with these processes in mind. It has in particular been designed to cover every possible Higgs mass scenario ranging from $114 \text{ GeV}/c^2$ to $1000 \text{ GeV}/c^2$. The coupling of the Higgs particle to every other SM particle means that the possible production and decay modes varies widely as a function of Higgs mass (Figure 6.1).

This wide range of possible dominant decay modes made it necessary to have good photon reconstruction if $m_H < 2m_Z$, good lepton reconstruction in particular of muons and electrons if $m_H > 130 \text{ GeV}/c^2$, but also excellent jet and missing energy reconstruction if $m_H > 200 \text{ GeV}/c^2$ where WW and ZZ decays would be the primary decay modes. Models predicting new physics was also part of the benchmarks for ATLAS design performance. Heavy gauge bosons W' and Z' with rest masses up to $6 \text{ TeV}/c^2$ can be produced at the LHC. The study of their leptonic decays requires high-resolution lepton measurements, charge identification and transverse momentum resolution in the multi $p_T \sim \text{TeV}/c$ range. The breaking of the SM in $B_s^0 \rightarrow \mu\mu$ and other b -physics channels requires excellent primary and secondary vertex resolution, as does distinguishing one interesting interaction from the on average 23 simultaneous inelastic collisions that happens due to pile-up in ATLAS at every bunch-crossing. The search for MSSM Supersymmetry relies on missing transverse energy signatures from the weakly interacting LSP slipping away. This means that the calorimetry must have excellent hermeticity to estimate the total visible energy. Pile-up is not the only multiplicity challenge. ATLAS is also capable of reconstructing heavy ion collisions with thousands of charged particles being produced per collision. The intensity of the LHC collisions also puts requirements on radiation tolerance, fast readout times and high bandwidth data acquisition and fast trigger decisions.

This diverse set of challenges has lead to the construction of a detector-stack with multiple systems redundancy and design requirements found in Table 6.1.

A rendition of the final design is shown in Figure 6.2. The detector design is forward-backward symmetric around the interaction point (IP) and near-axial symmetric in acceptance around the beam-pipe. The general layout follows most general purpose detectors with the non-destructive tracking and vertex system close to the IP embedded in a solenoidal magnetic field, followed by an electromagnetic and hadronic calorimeter. The muon spec-

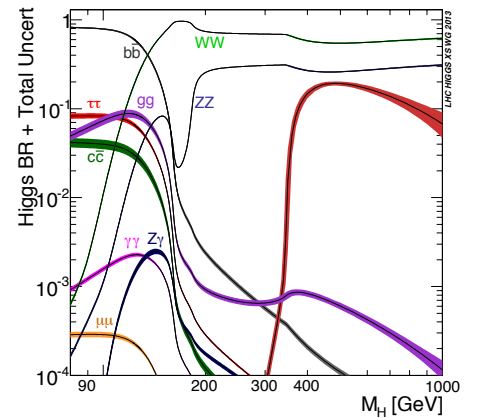


Figure 6.1: Higgs branching ratios [70].

Table 6.1: Performance goals for the ATLAS detector. Muon performance at high- p_T is quoted independent of the inner trackers and is the momentum resolution for muon segments alone, Ref [102].

Detector component	Required resolution	η coverage	
		Measurement	Trigger
Tracking	$\sigma_{p_T} / p_T = 0.05\% p_T \oplus 1\%$	± 2.5	
EM calorimetry	$\sigma_E / E = 10\% / \sqrt{E} \oplus 0.7\%$	± 3.2	± 2.5
Hadronic calorimetry (jets)			
barrel and end-cap	$\sigma_E / E = 50\% / \sqrt{E} \oplus 3\%$	± 3.2	± 3.2
forward	$\sigma_E / E = 100\% / \sqrt{E} \oplus 10\%$	$3.1 < \eta < 4.9$	$3.1 < \eta < 4.9$
Muon spectrometer	$\sigma_{p_T} / p_T = 10\%$ at $p_T = 1 \text{ TeV}/c$	± 2.7	± 2.4

trometer envelopes the calorimeters and a toroidal magnetic field allows for charge and momentum reconstruction of muons with $p_T > 1 \text{ TeV}/c$. The cylindrical design separates the detector stations into a barrel region and two end-cap regions. Tracking is available in the central region with $|\eta| < 2.5$ while calorimetry extends to $|\eta| < 4.9$. To allow for a consistent reference to activities in the detector we will define a general coordinate system and some of the frequently mentioned sizes.

6.0.2 *Coordinates*

ATLAS is situated at Point-1 (Figure 5.5). A right-handed coordinate system can be placed with the origin at the middle of the detector (the nominal interaction point) the z -axis then points along the beam-pipe, the x -axis towards the centre of the LHC ring (north) and the y -axis points upwards (Figure 6.3). Due to the geometrical symmetries it is useful to define a spherical coordinate system as well, with the azimuthal angle ϕ in the transverse $x - y$ plane, and the polar angle θ with respect to the positive z -axis. Polar angle θ is

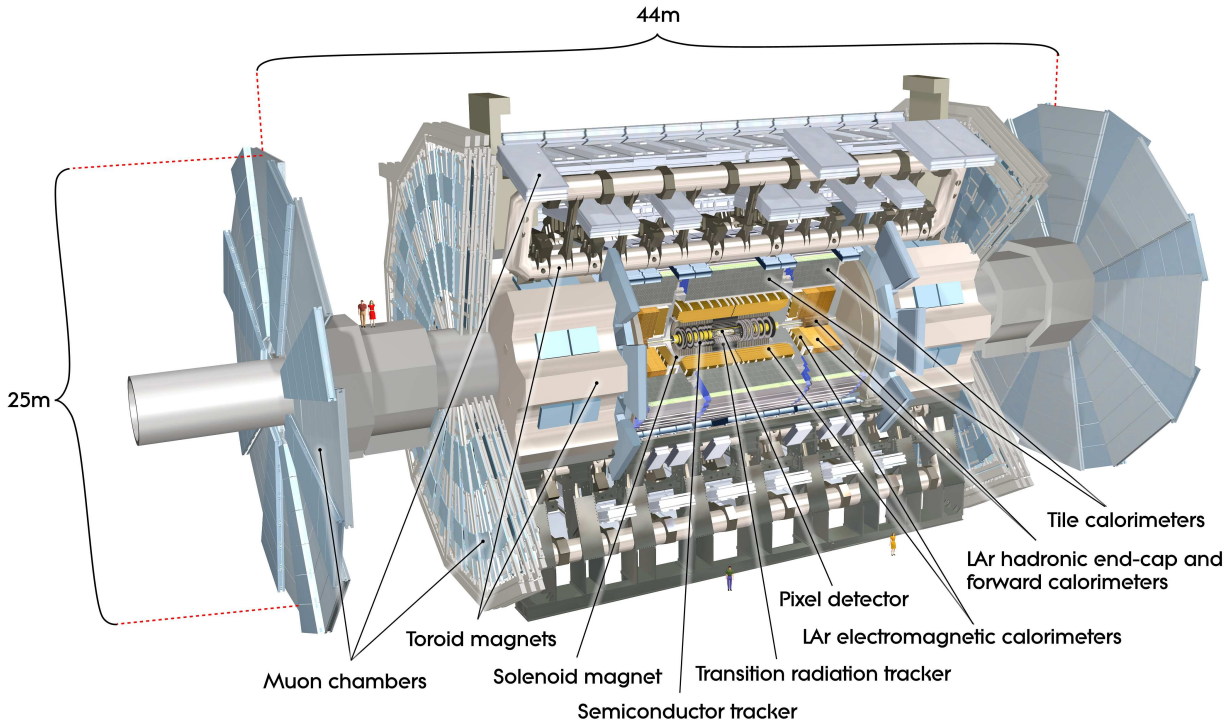


Figure 6.2: The ATLAS detector, Ref.[102].

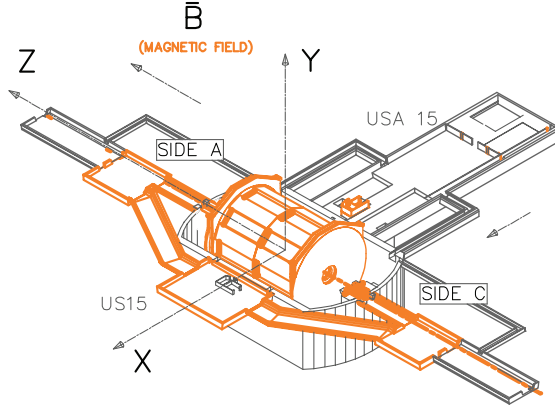


Figure 6.3: Coordinates relative to the ATLAS cavern.

usually expressed in terms of pseudorapidity

$$\eta = -\ln \left(\tan \frac{\theta}{2} \right). \quad (6.1)$$

In parton collisions the initial longitudinal momentum component is unknown due to compositeness of the parent hadrons. This restricts assumptions on energy and momentum conservation to the transverse plane, and common observables such as rapidity

$$y = \frac{1}{2} \ln \frac{E + p_z}{E - p_z} \quad (6.2)$$

are less used. For massless particles pseudorapidity is equivalent to rapidity. Differences in pseudorapidity are invariant under boosts along the z -axis making it easy to compare the relative distance between them

$$\Delta R = \sqrt{\Delta\eta^2 + \Delta\phi^2} \quad (6.3)$$

even if the longitudinal boost is unknown.

The lack of knowledge regarding the longitudinal momentum component makes it necessary to work in the transverse plane when requiring momentum conservation. We therefore introduce a set of transverse observables,

$$p_T = \sqrt{p_x^2 + p_y^2} = p \sin \theta \leftrightarrow |p| = p_T \cosh \eta \quad (6.4)$$

$$E_T = \sqrt{m^2 + p_T^2} \quad (6.5)$$

$$E_T^{miss} = -\sum p_T. \quad (6.6)$$

6.1 The Magnet system

To allow accurate momentum determination within the tracking volumes of ATLAS, four large super-conducting magnets are placed around the interaction region as can be seen in Figure 6.4. The system is comprised of a thin 2 T axial aligned solenoid magnet around the inner tracking region and three toroid magnet systems for the muon spectrometers - one for each end-cap and a central barrel magnet, their peak field strength is around 3.9 T.

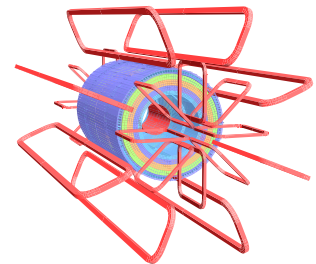


Figure 6.4: The magnet system is comprised of the inner solenoid magnet (the barrel structure in red), and the outer toroid magnets

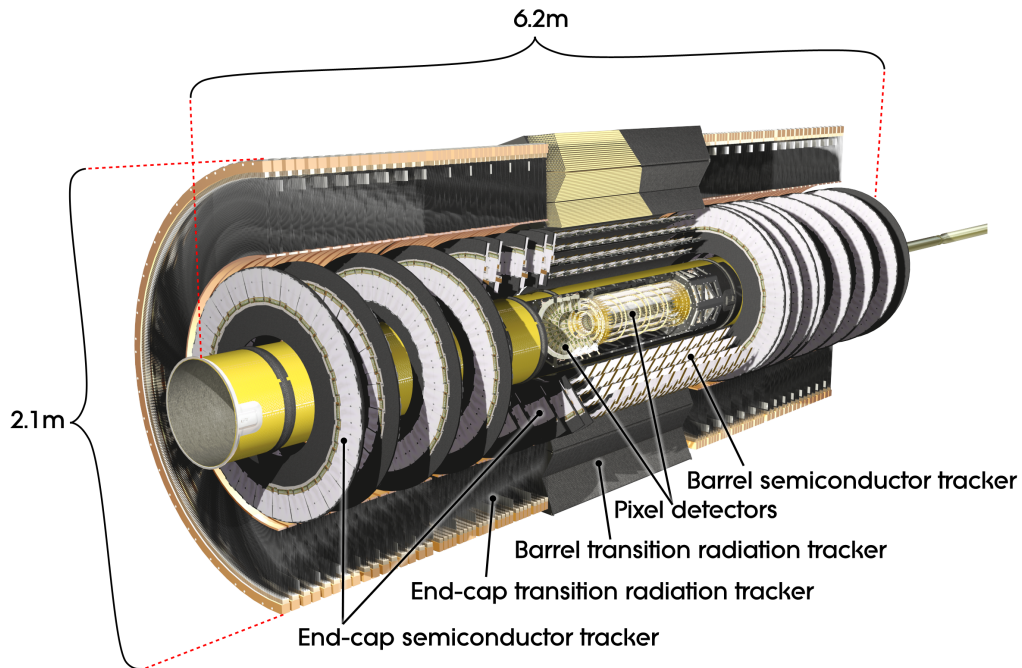


Figure 6.5: A cutaway of the inner detector.

6.1.1 Central solenoid magnet

The central solenoid is placed after the last tracking system and before the electromagnetic calorimeter. Due to its placement before the calorimeter, it has been an important design decision to bring down the material budget as much as possible. To minimise the material, the solenoid and the calorimeter share the same vacuum vessel, reducing the material budget due to the magnet to 0.66 radiation lengths. The magnet is 5.8 m long and has an inner diameter of 2.46 m.

6.1.2 The toroid magnets

The nearly iconic toroid magnets in ATLAS are shaped like eight race-track loops that each are 25.3 m in length and have an inner (outer) diameter of 9.4 m (20.1 m).

6.2 Tracking system

The inner tracking system in ATLAS is comprised of three distinct sub-systems, a silicon pixel tracker (PIX), a silicon strip detector (SCT) and a straw-based transition radiation detector (TRT). The trackers have been designed to endure the high intensity of the LHC, with radiation hard designs and fast readout technology. The tracking system is designed to allow for precise primary and secondary vertex estimation, excellent momentum resolution, charge determination and in case of the TRT also electron identification by transition radiation (Sec. 4.1.7). The overall dimensions of the system are shown in Figure 6.5.

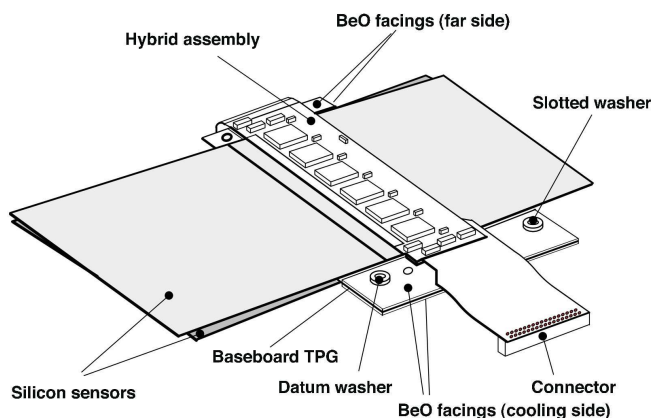
6.2.1 Silicon pixel detector

The silicon pixel detector consists of a barrel region ($|\eta| < 1.7$) with three concentric layers around the IP and 2x3 end-cap layers covering the region $2.5 > |\eta| > 1.7$. The combined pixel layers extends radially from 5.05 to 14.96 cm and a length of 130 cm. The detector layers consist of 1744 identical sensor modules with dimensions $19 \times 63 \text{ mm}^2$. Each module has 46080 active pixels with a nominal pixel size of $50 \times 400 \mu\text{m}^2$ and a thickness of $250 \mu\text{m}$. The chips are designed to be very resilient to radiation while maintaining good charge collection efficiency over long exposure times. The general principle of a semiconductor detector is that when a charged particle traverses a pixel area ionisation produces electron-hole pairs which can be collected as a signal when an electric field is applied. The intrinsic accuracy of the pixel layers are $10 \mu\text{m}$ in $xy - \phi$ and $115 \mu\text{m}$ in the z -direction. The average number of Pixel hits for a track within the acceptance is 3. Radiation tolerance is achieved by constructing the sensor on an n-bulk with n+ implants on the read-out side and p+ on the back-side forming a p-n junction [101]. At some point radiation will invert the n-bulk and the sensor will function as a p-type semiconductor. The pixel detectors basically forms segmented solid-state ionisation chambers where each pixel is defined by they n-type implants on the readout side with each that have the pixel dimensions.

A central concept in this design is ‘bump-bonding’ where direct connections between each pixel and its corresponding readout electronic is provided by small solder point spaced with a $50 \mu\text{m}$ pitch (Figure 6.7).

6.2.2 The semiconductor tracker

The SCT is a silicon strip detector which consists of four layers in the barrel region and nine layers in each end-cap. The radial dimensions spans 29.9 to 56.0 cm. And the total length of the detector is 272 cm. To give a space-point each module have two strip sensors glued together at a slight angle (40 mrad) relative to one another.



The average strip pitch is $80 \mu\text{m}$, two sensors are daisy chained in such a way that each effective strip is $\sim 12 \text{ cm}$ in length. The intrinsic resolution of the SCT is $17 \mu\text{m}$ in the $xy - \phi$ direction and $580 \mu\text{m}$ in z . The average number of SCT space-points for a track within the $|\eta| < 2.5$ acceptance is 8.

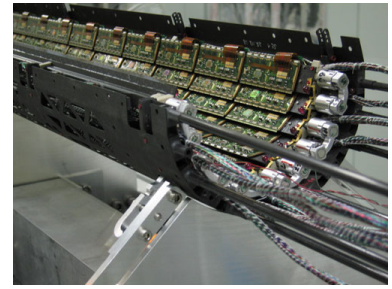


Figure 6.6: One of the two pixel barrel halves. Notice the overlapping modules and the carbon fibre support structure. <http://www.atlas.ch/news/2006/pixels-last.html>

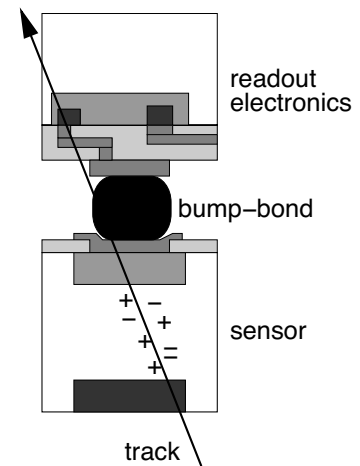


Figure 6.7: Bump-bonded silicon pixel die soldered to the front-end readout board.

Figure 6.8: A barrel SCT module. Notice the two sensors rotated relative to each other.



Figure 6.9: A layer of the TRT end-cap being assembled <http://www.hep.upenn.edu/atlas/trt/>.

6.2.3 Transition radiation tracker

The Transition Radiation Tracker (TRT) is a large straw-drift chamber situated beyond the SCT. It consists of 294304 drift tubes each 2 mm in radius. These tubes are configured in horizontal groupings in the barrel region and circular planes in the end-cap regions (see Figure 6.5). The overall dimensions spans a radius between 55.4 and 108.2 cm for the barrel and 61.5 to 110.6 cm for the end-caps.

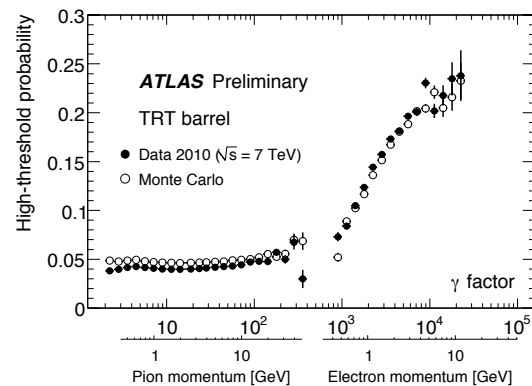
The barrel is 156 cm long and each end-cap is 191.7 cm in length. The single straw position resolution is $130 \mu\text{m}$ and a track is on average associated with 30 TRT measurements. The acceptance of the TRT is slightly smaller than the other two tracking systems only reaching $|\eta| < 2.0$.

Each straw is a thin drift chamber made by winding two $35 \mu\text{m}$ films around a hot mandrel fusing them into a straw. Each film is composed of $25 \mu\text{m}$ polyimide coated with $0.2 \mu\text{m}$ aluminium cathode on one side which is protected by a $5 \mu\text{m}$ layer of graphite-polyimide. The other side of the film is coated by a $5 \mu\text{m}$ layer of polyurethane layer that when heated melts the two film together around the mandrel. Each straw is further stabilised by carbon fibres wound around the tube. At the centre of each straw is an anode made by a $31 \mu\text{m}$ diameter tungsten wire coated by $0.6 \mu\text{m}$ gold. The attenuation length of a signal on the wire is $\sim 4\text{m}$, and the propagation time is $\sim 4\text{ns/m}$. The barrel straws are 144 cm in length but read out in each end, making the signal propagation length 71.2 cm. The endcap straws are 37cm long each.

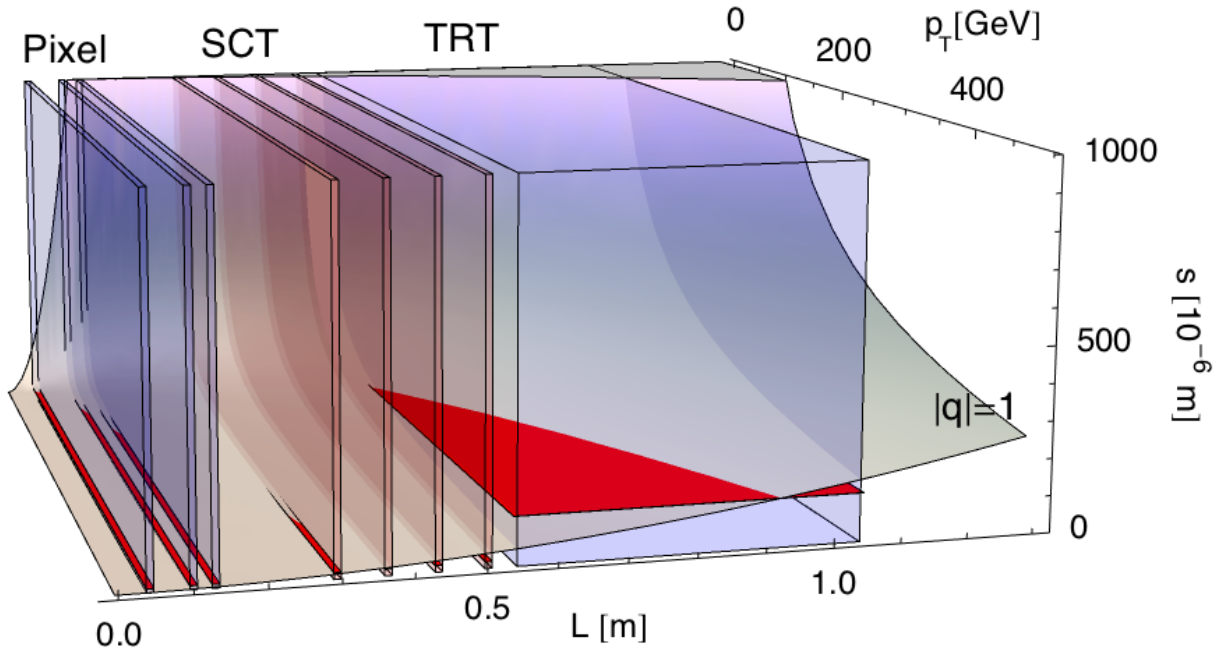
The straws are filled with a gas mixture comprised of 70% Xe, 27%CO₂ and 3%O₂. The gas mixture is optimised for the time requirements imposed by the bunch crossing rates, with a maximum electron collection time of $\sim 48\text{ns}$. The Xenon component also serves as X-ray absorber for photons emitted as transition radiation.

The straws are embedded in a matrix of thin polypropylene fibres that serves as transition radiators, that when crossed by a highly boosted particle will cause additional X-ray emission as described in Section 4.1.7. This feature of the TRT allows for electron-pion separation independent of the calorimeter systems as is illustrated in Figure 6.10 for the barrel region.

Figure 6.10: Transition radiation based particle identification in the TRT.



Due to the high number of channels and relatively long signal time, a full ADC readout is not feasible. Instead each straw readout is digitalised as a 24



bit value spanning 75 ns. Each bit represent a 3.125 ns time bin. When a bit is set to 1 it signifies that the signal has crossed a minimum ionisation threshold (300 eV). For every 25 ns interval a single bit represent a high-threshold value (6 KeV) that is set to 1 if transition radiation caused additional ionisation. Even with this relatively sparse information it is possible to estimate dE/dx based on multi-hit averaging [137].

6.2.4 Momentum resolution

As mentioned in the previous section, the magnetic field in the tracking region is around 2 T, which for hard tracks (TeV-range) leaves a very small sagitta,

$$R = \frac{p_T}{0.3B} \quad (6.7)$$

$$s = R(1 - \cos(L/R)) \quad (6.8)$$

$$s \sim 75 \times 10^{-6} \text{ m} |_{(p_T=1 \text{ TeV}/c, B=2 \text{ T})}. \quad (6.9)$$

On Figure 6.11 the sagitta at each detector plane is drawn with red planes illustrating the individual detector resolution. It is clear from the figure that all three sub-systems must work in unison to achieve decent momentum resolution in our region of interest around the TeV.

6.3 Calorimeters

The calorimeter systems in ATLAS are presented in Figure 6.12. All the systems are sampling based with independent absorber and active material. The total coverage is $|\eta| < 4.9$ and the total thickness is on average 11λ interaction lengths for hadronic showers and more than $22X_0$ radiation lengths for

Figure 6.11: Comparison of the intrinsic hit resolution (in the $xy - \phi$ -plane) in each tracker in the barrel region with the track sagitta (s) caused by a 2 T solenoid magnetic field. The grey surface illustrates the sagitta for a track bending in the magnetic field. The two additional axes are transverse momentum of the particle (p_T) and distance from the interaction point (L) respectively. The red horizontal planes are each detector's intrinsic resolution. When the red planes are visible it means that the intrinsic resolution of each detector is coarser than the sagitta bending distance at the specific length. A 100 GeV/ c track has a sagitta around 0.75 mm at the distance of the TRT. A track fit relies on the combination of all detectors, but it is worth noting that the individual detector resolution scales well with the sagitta. We also see that the primary function of the pixel detector is to provide directional and positional information whereas the SCT and the TRT are far enough from the IP to provide momentum and charge determination.

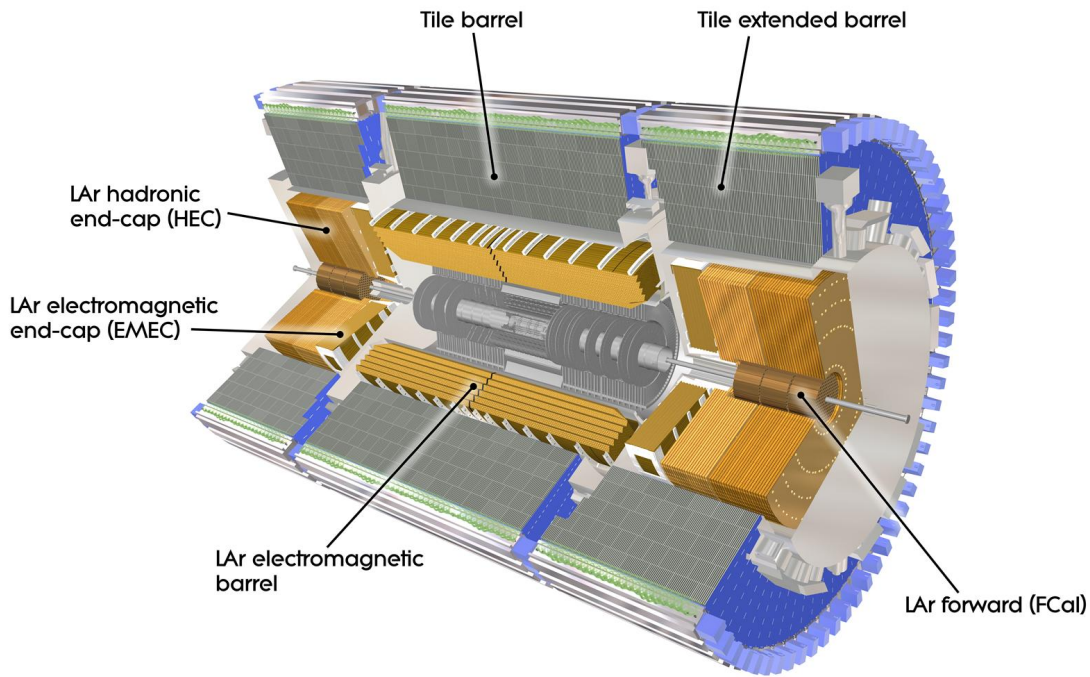


Figure 6.12: The combined calorimetry system in ATLAS.

electromagnetic showers. In total the calorimeter system provide good coverage both for electromagnetic and hadronic showers, limiting punch through to the muon spectrometer situated further away from the IP.

6.3.1 Electromagnetic calorimeters

The Electromagnetic calorimeters is a Lead-LAr detector where lead plates act as absorbers, liquid argon as active medium and electrodes made of kapton. The geometry of the electrodes are shaped as accordions allowing a ϕ symmetrical stacking that completely encloses the tracker along the azimuthal. The barrel region is highly granular with $\Delta\eta$ down to 0.02518 in the first radial layer and $\Delta\eta \leq 0.015$ for the second layer, to allow good electron and photon reconstruction with excellent directional pointing of photons. Radially it is comprised of four layers including a 1.1 cm presampler that compensates for energy loss in the tracking volume.

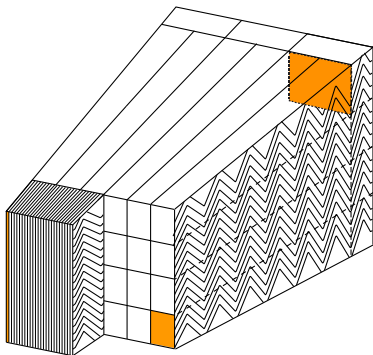


Figure 6.13: LAr barrel accordion structure. The orange surfaces corresponds to the granularity in each of the three layers (presampler excluded).

6.3.2 Hadronic calorimeters

Outside the electromagnetic calorimeter at $|\eta| < 1.7$ is the hadronic barrel calorimeter. It is a steel-absorber plastic-scintillator sampling calorimeter divided into a central ($|\eta| < 1.0$) and two extended $0.7 < |\eta| < 1.7$ barrels. The calorimeters extends radially from 2.28 m to 4.25 m and are divided into 64 modules in the azimuthal plane. It is segmented into three layers in depth with 1.5, 4.1 and 1.8 λ in the central barrel, and 1.5, 4.1 and 1.8 λ in the extended barrels. The scintillating tiles are read out by two independent PMTs one at high and one at low gain. The readouts are grouped into pseudo-projective blocks as we will see later in Section 8.

6.3.3 Hadronic end-cap calorimeter

The hadronic end-cap calorimeters (HEC) are based on LAr like the EM Calorimeter but with copper absorbers instead of lead. It extends from $|\eta| = 1.5$ to $|\eta| = 3.2$ overlapping with both the extended barrel calorimeter and the LAr forward calorimeter.

6.3.4 LAr forward calorimeter

At the extreme the LAr forward calorimeter (FCal) extends all the way to $|\eta| = 4.9$. It is three modules in depth with a total interaction depth of 10λ . The first module is made with copper absorber mainly for EM showering while the last two are made with tungsten to provide high density for hadronic showers.

6.4 Muon system

The Muon Spectrometer (MS) is situated around the calorimeter volumes and can in many ways act independently of the rest of the detector. Large superconducting air-toroid magnets provides deflection for momentum measurements independent of the inner detector. The MS is comprised of both trigger and tracking detectors. The main design goal for the MS is a stand-alone transverse momentum resolution of 10% for 1 TeV/ c tracks. With the magnetic field strength described in Sec. 6.1 the sagitta (6.8) is around $500 \mu\text{m}$, requiring a measurement resolution around $50 \mu\text{m}$. Muons with momenta less than $\sim 3 \text{ GeV}/c$ stops in the calorimeter but otherwise the MS is designed to allow momentum and charge determination for muons in the range 3 – 3000 GeV/ c . The MS is structured as three concentric cylindrical layers around the barrel region ($|\eta| < 2.0$) with radii 5 m, 7.5 m and 10 m, which approximately is also the radial extremes of the barrel toroid magnets. In the end-cap regions two large wheels are serviced by their own end-cap toroid magnets. The total acceptance is $|\eta| < 2.7$ for tracking and $|\eta| < 2.4$ for muon triggering. Four types of detectors are utilised in the MS, two precision tracking systems for sagitta measurements and two fast trigger systems that also provides a secondary coordinate in the non-bending plane for tracking. The main precision detectors are Monitored Drift Tubes (MDT) which covers $|\eta| < 2.7$ except at the innermost plane where radiation hardness is an issue for the drift tubes and Multi-Wire Proportional chambers (MWPC) are used instead. These MWPCs are specifically Cathode Strip Chambers (CSC) with the cathodes segmented into strips to provide a full 3D space point. The trigger system relies on two different technologies: in the barrel region Resistive Plate Chambers (RPCs) are used and in the end-cap region Thin Gap Chambers (TGCs). The MS envelopes 16000 m^3 and spans the full ATLAS length of nearly 40 m. Precision measurements with $50 \mu\text{m}$ resolution in such a large structure requires perfect alignment, and both gravitational fatigue and thermal effects significantly displaces the sensitive detectors. Alignment is done both optically and with high- p_T tracks.

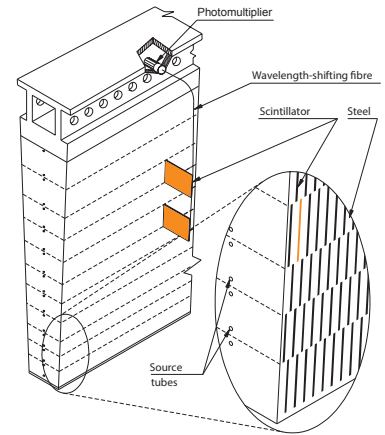
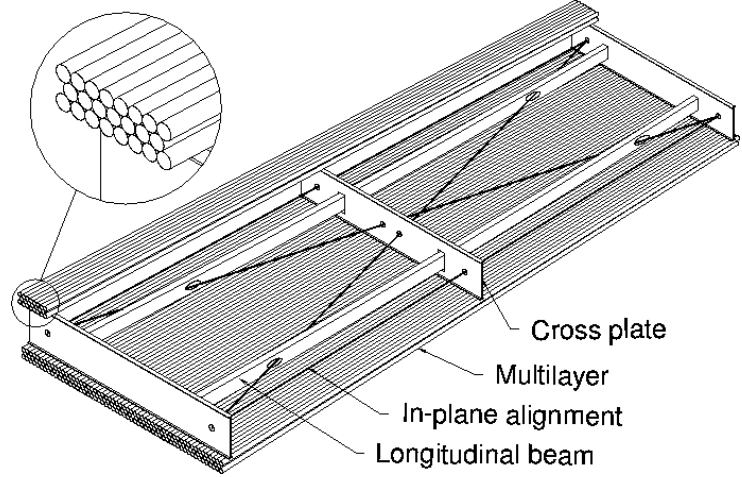


Figure 6.14: A tile calorimeter module with interchanging steel and scintillator plates.

6.4.1 Monitored Drift Tubes

The Monitored drift tube chambers are comprised of 2×3 layers of drift tubes. Each layer consists of between 16 and 72 tubes that are 3 cm in diameter. The chambers length along the z -direction is then $3 \text{ cm} \times n_{\text{tubes}}$ where the width along the ϕ direction can be between 2 and 5 m.

Figure 6.15: Monitored Drift Tube Chamber.



The individual straws are similar to the TRT straws but scaled in size. The tubes themselves are made of aluminium with a $50 \mu\text{m}$ gold-plated tungsten-rhenium wire as anode. The gas in the tube is a mixture of 93% argon, 7% CO_2 and trace amounts of water. The pressure is kept at 3 bar and with a nominal wire potential at 3080 V the maximum drift time is $\sim 700 \text{ ns}$. The average tube resolution is $80 \mu\text{m}$ and a full chamber yields a point resolution of $35 \mu\text{m}$. Combining hits from three MDT stations gives a resolution on the sagitta of $\Delta s = 45 \mu\text{m}$ corresponding to a momentum resolution of

$$\delta p/p = \frac{\Delta s p}{500 \mu\text{m}} \quad (6.10)$$

with p in units of TeV.

6.4.2 Cathode Strip Chambers

Beyond $|\eta| > 2$ the operational limit of the MDTs are reached (with rates in excess of 150 Hz/cm^2). This region corresponds to the first muon layer in the end-cap region. Here MDTs are replaced with Cathode Strip Chambers which are segmented MWPC that are capable of handling counting rates up to 1 kHz/cm^2 , enough to cover up to $|\eta| < 2.7$. A CSC works on the same principle as a multi wire proportional chamber but the cathode is segmented into strips that gives positional information on the orthogonal axes relative to the anode wires.

The CSCs consists of two wheels with eight small and eight large chambers positioned as shown in Figure 6.16. Each chamber contains four CSC planes. The anode wires are radially aligned and one set of cathodes orthogonal to the anodes provide one precision coordinate. Another set of cathodes parallel to the anodes provide a low resolution transverse coordinate. In the bending plane the per-plane resolution is $60 \mu\text{m}$ but 5mm in the non-bending

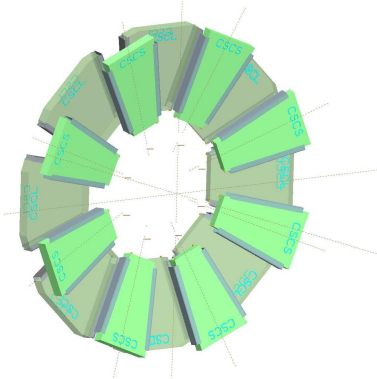


Figure 6.16: CSC Wheel

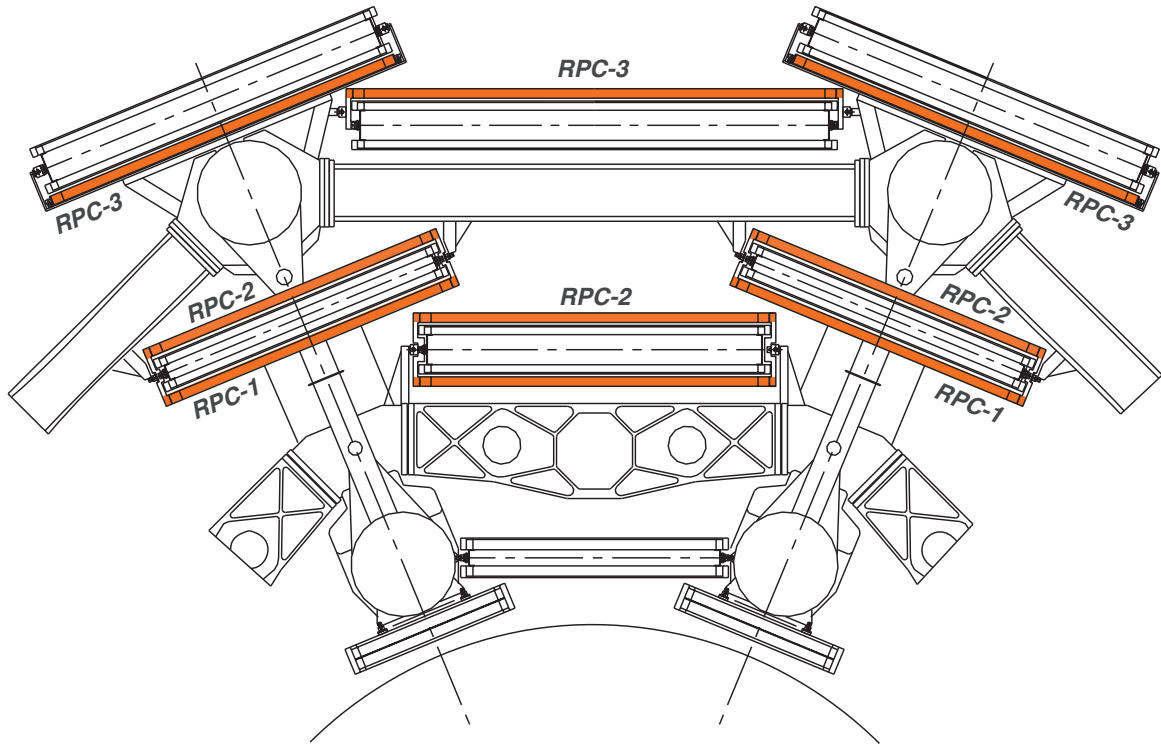


Figure 6.17: A cross-section of the barrel region showing the RPCs. The non-coloured chambers are MDTs, and the round structures are cross-sectional views of two air-toroid coils.

plane. Apart from good tracking in the intense environment 7 m away from the IP and 90 cm from the beam-line, the CSC also provides a 7ns time resolution per plane. The CSCs are filled with an Argon/CO₂ as the MDTs and operates at a potential of 1900 V.

6.4.3 Resistive Plate Chambers

The RPCs are designed to provide a fast but spatially coarse trigger response for the MS. The RPC stations consist of two units each with two layers one for each direction (η, ϕ). The positioning of the stations seen in Figure 6.17 allows for effective triggering on both low- p_T (6 – 9 GeV/ c) and high- p_T (9 – 35 GeV/ c) tracks. The two layers RPC1 and RPC2 sitting close together nearest the IP allows for efficient identification of low- p_T tracks while the addition of the longer lever-arm out to RPC3 provides a high- p_T trigger signal when combined with one or two closer stations. The RPCs are constructed by spacing two resistive plates by a 2 mm gas filled volume. The gas is a mixture of C₂H₂F₂/Iso – C₄H₁₀/SF₆. The RPC are operated in avalanche mode with a field gradient of 4.9 kV/mm which provides rate-independent time resolution and higher restitution rates compared with streamer operation. The RPCs are read out capacitively by metallic strips glued to the outer surfaces of the resistive plates. The strips are around 3 cm wide separated by a 2mm gap to provide positional information.

6.4.4 Thin gap chambers

TGCs serve as trigger planes in the end-cap regions. They also provide the end-cap MDTs with an azimuthal component to compliment the radial component measured by the drift chambers. The TGCs are basically MWPCs where the wire spacing is larger than the cathode-wire distance. This allows for a quasi-saturated operation with a voltage of 2.9 kV and a gas mixture of CO₂ and n-pentane which makes for very fast operation and a time resolution around 4ns. The TGC is planar like the CSC with segmented anodes and cathodes. The spatial resolution is 2 – 6mm in the xy -plane and 3 – 7mm in the ϕ -plane.

6.5 Speed estimation in ATLAS

All systems in ATLAS are capable of measuring particle speeds ($\beta = v/c$) in Table 6.2 the systems are listed with references to studies of the specific method. In the 2011 search for coloured long-lived particles presented in Chapter 9 a combination of estimators are utilised.

Table 6.2: Methods of $\beta/\beta\gamma$ -estimation in ATLAS.

Sub detector	Method	Reference
Pixel Tracker	dE/dx	[12]
SCT	dE/dx	[108]
TRT	Transition radiation	[104]
	dE/dx	[137]
	Time-of-Flight	not published
Calorimeters	Time-of-Flight	[69]
	dE/dx	[63]
Muon Spectrometer	Time-of-Flight	[27]
	dE/dx	[13]

Specifically the Pixel tracker which will be further introduced as a $\beta\gamma$ -estimator in Chapter 7 is used due to both high acceptance and β resolution. The TRT and the SCT have been found capable of estimating dE/dx but at relatively modest resolutions due to the readout format. The SCT provides three bits to describe Time-over-Threshold (ToT) which allows for a rudimentary dE/dx estimate. The TRT provides more measurements per track than the SCT and more ToT bits (including High-Threshold bits enabled if transition radiation is observed) but similarly to the SCT suffers from the lack of full ADC readout. Compared to the other systems in ATLAS they were found not to provide a significant improvement in our search and were left for cross checks. The calorimeters provides both dE/dx and ToF based β estimation for penetrating particles. The latter method which is presented and expanded in Chapter 8 was also applied in the 2011 search. The muon spectrometer with its fast trigger stations and precision drift tubes is capable of measuring ToF and dE/dx for charged particles that survives to these outer systems within the readout window. In our 2011 search any R-Hadron candidates found to match a muon track will be ascribed a combined β estimate based on calorimeter and MS measurements if found to be compatible (Sec. 9.4.1).



*Searches for long-lived
particles with ATLAS at the
LHC*

The pixel detector in ATLAS is capable of measuring the energy deposited by a charged track traversing its pixels. This chapter describes the development of a mass/ $\beta\gamma$ estimator that utilises this possibility. The method described there differs from the one used in our 2011 analysis and is presented as a stand-alone study exploring a new and improved avenue in the development of empirical parameterisations called genetic algebraic regression.

7.1 dE/dx from the pixel detector

Charged particles at even low momentum are expected to pass through the thin pixel detectors in ATLAS leaving behind energy in the form of specific energy loss following a Landau distribution (4.16) with a most-probable-value set by the Vavilov equation (4.15). For highly relativistic particles the density correction in the Vavilov equation reaches a ‘Fermi plateau’ and flattens to a constant energy loss. Figure 7.1 shows the difference between a Bethe-Bloch mean energy loss and the MPV energy loss for the Vavilov formula. This moderation in energy loss at high- $\beta\gamma$ allow us to distinguish between the low- $\beta\gamma$ rise and this ‘extended’ MIP-region stretching until electron-pair production sets in at $\beta\gamma \sim 1000$.

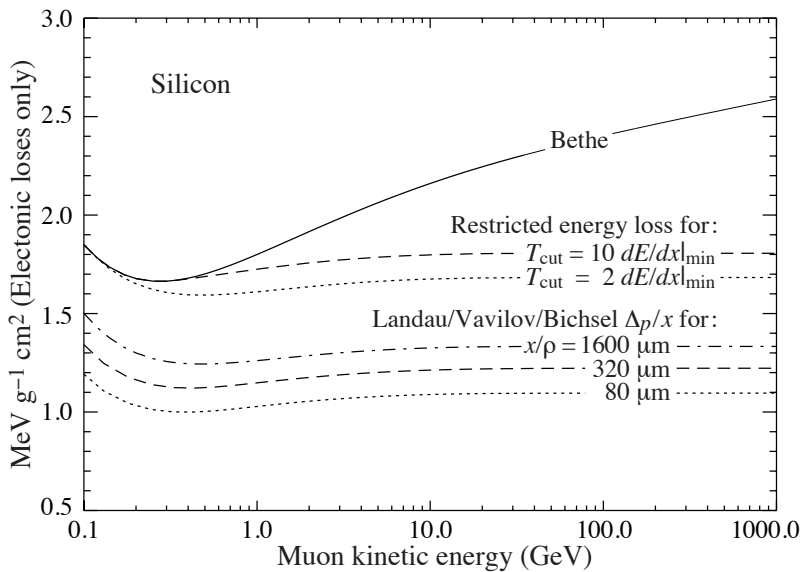


Figure 7.1: Energy loss in silicon [125]. The pixel sensors in ATLAS are 250 μm thick which gives a MIP loss $\sim 1.1 \text{ MeVg}^{-1}\text{cm}^2$.

If we can measure $\langle \frac{dE}{dx} \rangle$ it will allow us to determine $\beta\gamma$ by inverting (4.14). Combining the $\beta\gamma$ -estimate with the particles momentum and we

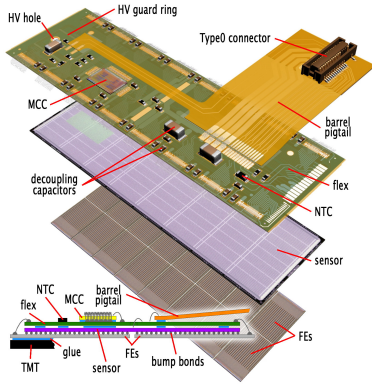


Figure 7.2: A pixel sensor with its three component layers exposed.

have a mass estimate. First we have to estimate the actual charge deposited in the detector for a given track.

7.1.1 Pixel charge estimation

In the pixel sensors (Figure 7.2) each pixel diode is connected to a read-out cell on the front-end board that contains an analogue charge-sensitive preamplifier. The preamp is designed to emit a discriminator pulse with a pulse width proportional with the input charge. This signal called Time-Over-Threshold (ToT) is measured by counting the number of cycles of a 40 MHz master clock passing for the duration of the emitted pulse. The number of cycles is then digitised into two 8-bit timestamps one called the Leading-Edge (LE) and the other the Trailing Edge (TE). The threshold is adjustable but has been set to $3.5ke$. The number of liberated electrons from a MIP particle traversing the $250 \mu\text{m}$ silicon is roughly

$$N_e = \left\langle \frac{dE}{dx} \right\rangle x_{thickness} / I_{Si} = 106 \text{ KeV} / 3.6 \text{ eV} \approx 29ke \quad (7.1)$$

based on (4.14). The MPV of electrons assuming a Landau distribution is closer to $20ke$ for a MIP moving with a normal incidence to the sensor plane. This is equivalent to a MIP giving an ADC value of 30. At 8 bit resolution this gives a maximum readout of 255 corresponding to ~ 8.5 MIPs or $170ke$. This upper limit on the dynamic range consequently means that energy deposited by highly ionising particles with $dE/dx > 8.5$ MIP will be discarded and not read out, not even an overflow signal is saved.

In Figure 7.3 the linear relationship between ToT and injected charge is shown. The overall readout ranges are listed in table 7.1.

Figure 7.3: Relationship between time-over-threshold and charge deposition for the pixel detector.

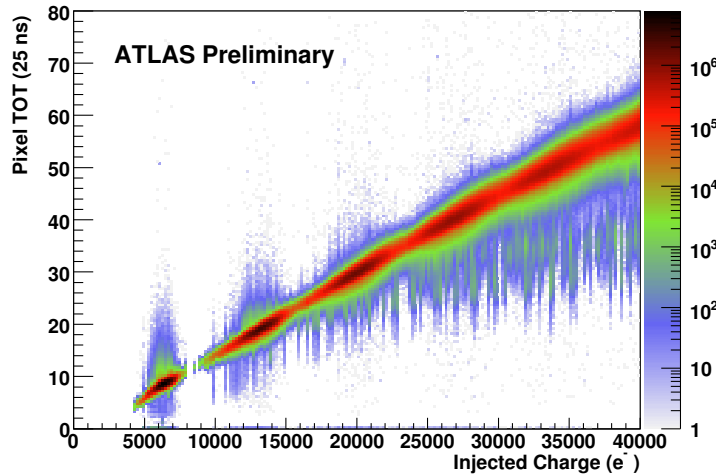


Table 7.1: Data ranges for charge readout on individual pixel diodes.

	Charge [ke]	ADC value [$counts$]
	$\Delta_Q: 0.66ke$	$\Delta_{ADC}: 1$
Minimum charge	3.5	1
Minimum ionising particle	20	30
Maximum charge	170	255

The charge response is regularly calibrated and kept normalised across the pixel diodes to within 2% variation, making it reasonable to combine multiple measurements in a combined $\langle \frac{dE}{dx} \rangle$ for all hits along a track in the pixel detector.

7.1.2 Truncated dE/dx estimation

A charged particle intersecting a pixel sensor is rarely confined to a single pixel and clusters of pixel hits are produced by grouping charge depositions in the vicinity of a track into a pixel cluster.

The combined charge in a pixel cluster can be biased due to the limited dynamic range and the charge threshold described in the earlier section but also due to variations in the physical regions on the silicon die. To keep the dE/dx estimator relatively simple any complicated regions are discarded. In practice outliers close to the sensor edge and ‘ganged’ pixels are discarded. Ganged pixels are pixel diodes placed between two readout chips in a region where bump-bonding is impossible. Instead they share a readout channel with pixels under the front-end board by local connections shown in Figure 7.4 as black lines.

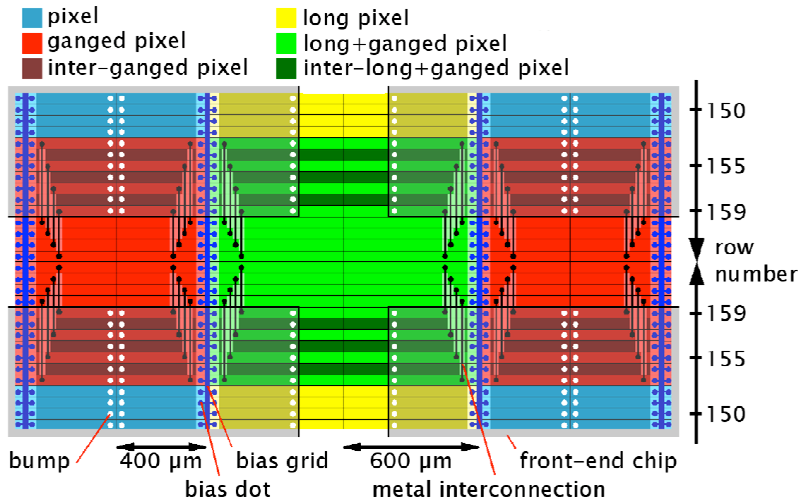


Figure 7.4: Pixel layout. The white points are bump bonding connectors. The black lines illustrates how pixels are ganged together to allow readout of the pixels outside the covered region of the readout chips [101].

A veto is done by excluding the region where the track trajectory intersects the non-greyed region in the subfigure in Figure 7.5. For each cluster that passes these quality requirements the specific energy loss is calculated

$$\left\langle \frac{dE}{dx} \right\rangle = \frac{QW \cos \alpha}{epd} \quad (7.2)$$

Here Q is the cluster charge, $W = 3.68 \pm 0.2 \text{ eV/pair}$ is the energy required to create a e-h pair in silicon, $d = 250 \mu\text{m}$ is the thickness of the sensor and $\cos \alpha$ is the incident angle of the track relative to the sensor surface. Shallow tracks with $\cos \alpha < 0.16$ are discarded as the relation no longer holds (they make up 0.4% of associated clusters).

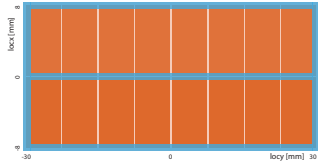
The deposited charge in a single pixel follows a Landau distribution (see Figure 4.6). Multiple measurements allow us to calculate a mean value that asymptotically is related to (4.14). With only 3 layer hits on average a single high energy deposit can throw off the mean value enough to make $\beta\gamma$

estimation impossible. To alleviate this problem, the truncated mean method introduced in section 4.3.2 is used. To give a general overview the algorithm for estimating the truncated pixel-dE/dx is shown in Figure 7.5.

Figure 7.5: Truncated dE/dx estimate from ATLAS Pixel detector

```

1: function GETPIXELDEDX(track)
2:    $q_{total} \leftarrow 0$  ▷ Total collected charge
3:    $nHits \leftarrow 0$  ▷ Total measurements used
4:    $\vec{q}_\mu \leftarrow null$  ▷ Empty vector for charges
5:   for all pixel surfaces along the track trajectory do
6:      $pix_{cluster} \leftarrow$  Pixel cluster intersected by track on surface
7:      $loc_x \leftarrow$  location of  $pix_{cluster}$  on sensor x-axis
8:      $loc_y \leftarrow$  location of  $pix_{cluster}$  on sensor y-axis

9:     if  $\{loc_x, loc_y\}$  inside orange regions in  then
10:        $\cos \alpha \leftarrow \vec{p}_{trk} \cdot \hat{n}_{surface}$  ▷ Track angle wrt. surface
11:       if  $|\cos \alpha| < 0.16$  then continue with next surface
12:       end if
13:        $q \leftarrow TotalCharge(pix_{cluster}) \times \cos \alpha$ 
14:        $q_{total} \leftarrow q_{total} + q$ 
15:        $\vec{q}_{\mu+1} \leftarrow q$ 
16:        $nHits \leftarrow nHits + 1$ 
17:     end if
18:   end for
19:    $\vec{q}_{vec} \leftarrow$  sorted( $\vec{q}_{vec}$ ) by value
20:    $q_{avg} \leftarrow 0$ 
21:   if  $nHits \geq 1$  then
22:     if  $nHits = 1$  then ▷ No truncation if only 1 hit.
23:        $q_{avg} \leftarrow q_{total}$ 
24:     else if  $nHits < 5$  then ▷ Truncate the largest value if nHits < 5.
25:        $q_{total} \leftarrow q_{total} - \vec{q}_{nHits-1}$ 
26:        $q_{avg} \leftarrow q_{total} / (nHits - 1)$ 
27:     else ▷ If more than 5 hits, truncate at the second-largest.
28:        $q_{total} \leftarrow q_{total} - \vec{q}_{nHits-1}$ 
29:        $q_{total} \leftarrow q_{total} - \vec{q}_{nHits-2}$ 
30:        $q_{avg} \leftarrow q_{total} / (nHits - 2)$ 
31:     end if
32:   end if
33:   return  $q_{avg} \times I_{Si} / (\rho_{Si} d)$  ▷ Scale to  $MeVg^{-1}cm^2$ .
34: end function

```

The $\langle \frac{dE}{dx} \rangle$ algorithm requires access to pixel clusters. These are in general not stored after reconstruction in upstream data formats. Because of that the estimator runs as part of official ATLAS reconstruction and this study has been done on this information produced in central reconstruction on Monte Carlo samples.

In Figure 7.6a the ATLAS dE/dx ‘propaganda plot’ is shown as a function of track momentum for low- p Standard Model particles. From the figure we can see that there is promising separation between each particle type, but more importantly between the MIP band and low- $\beta\gamma$ particles. Compatibility between Monte Carlo simulation and data is also fairly good. In Figure 7.6b simulated minimum bias events ($p > 3 \text{ GeV}/c$) are compared with recorded events from 2010. The peak in Figure 7.6b is clearly defined with only a slight asymmetric tail but otherwise the long Landau tail is removed by truncation.

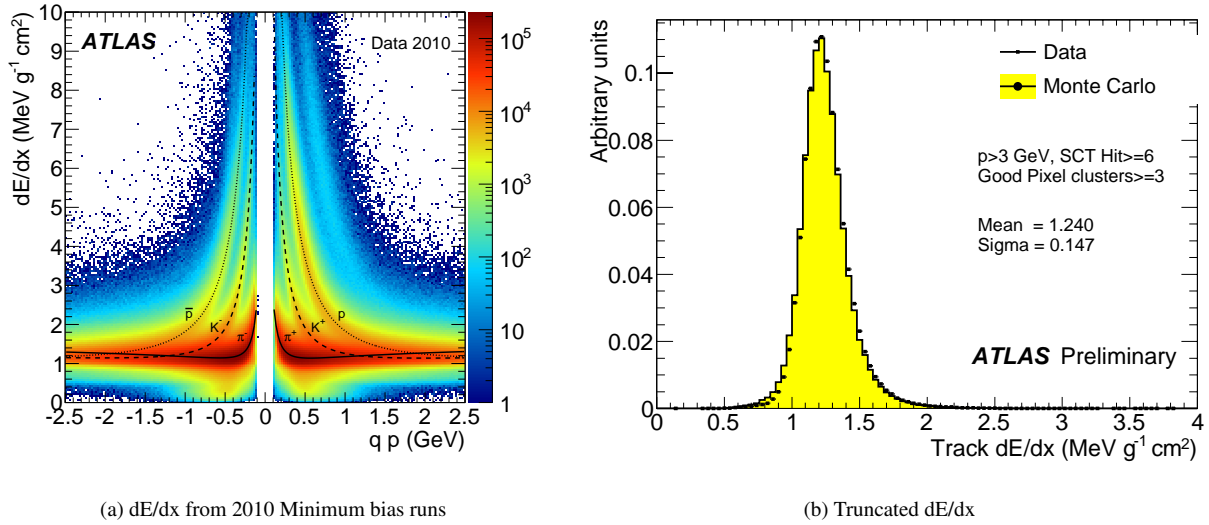


Figure 7.6: dE/dx from 2010 Minimum bias runs

7.1.3 dE/dx from LLPs in ATLAS

Before we continue developing the mass estimator we shall first take a quick look at how our signal samples behave to understand the situation. In Figure 7.7 muons with $\beta\gamma \gg 4$ show clear separation from the slower R-Hadrons with $\beta\gamma < 4$.

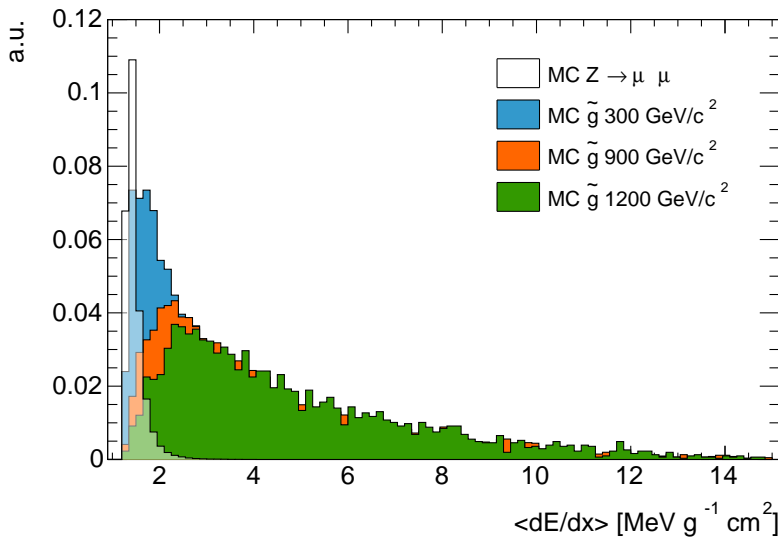
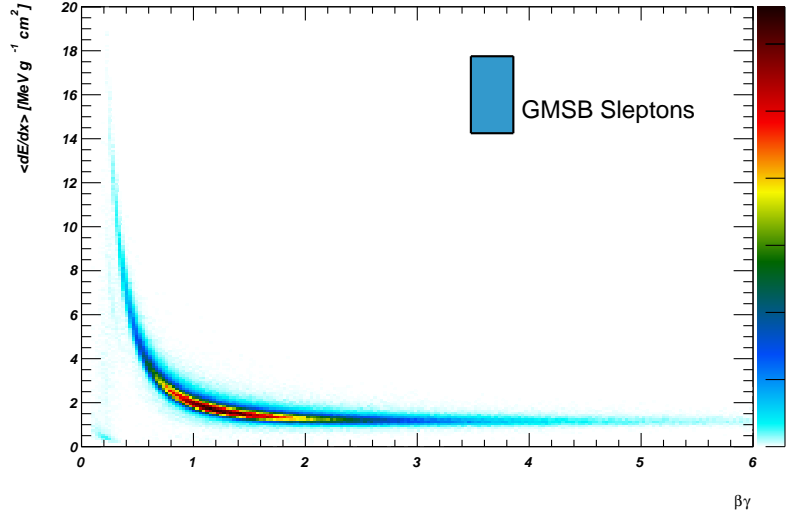


Figure 7.7: dE/dx for select R-Hadron \tilde{g} samples (w. $\beta\gamma < 4$) and muons (w. $\beta\gamma \gg 4$) from a $Z \rightarrow \mu\mu$ MC sample.

Figure 7.8 illustrates how energy deposition of slow particles follows (4.14), (4.15) and (4.16). The figure is the result of plotting the dE/dx estimate from the track reconstruction against the particles speed. The histogram is filled by multiple slepton ($\tilde{\tau}$) samples with a variety masses but as all particles with charge $|q| = 1$ follows this exact curve it only serves to increase the statistics. The dripping peak at $\beta\gamma \sim 0.2$ is due to the limited dynamic range of the ADC. It can be seen from Figure 7.8 that the distribution flattens out at the MIP minimum around $\beta\gamma \sim 2.5$

Figure 7.8: Ionisation loss dE/dx in the ATLAS pixel detector for simulated long-lived $\tilde{\tau}$ sleptons produced in $\sqrt{s} = 7$ TeV pp -collisions.



7.1.4 Number of good dE/dx hits dependence

The dE/dx estimate depends on the number of good pixel clusters available (Table 7.2) which again depends on whether the track crosses the barrel, the end-cap region or both. This point is illustrated in Figure 7.9 where the number of pixel clusters per dE/dx is plotted as a function of pseudorapidity. After $|\eta| > 2$ the barrel overlaps with the end-cap region.

Figure 7.9: Number of good hits in the acceptance region

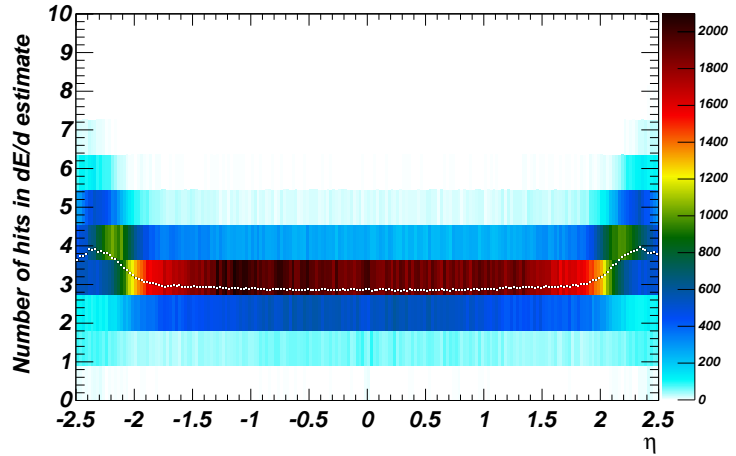


Table 7.2: dE/dx truncation factors and the effect on the mean value of MIPs.

Number of clusters	number excluded	$\langle dE/dx \rangle$ [MeVg ⁻¹ cm ²]	σ [MeVg ⁻¹ cm ²]
1	0	1.354 ± 0.003	0.239 ± 0.003
2	0	1.212 ± 0.001	0.185 ± 0.001
3	1	1.255 ± 0.000	0.163 ± 0.000
4	1	1.287 ± 0.001	0.153 ± 0.001
5	2	1.226 ± 0.001	0.129 ± 0.001
6	2	1.250 ± 0.002	0.119 ± 0.002
7	2	1.252 ± 0.006	0.120 ± 0.005
8	2	1.259 ± 0.057	0.175 ± 0.088

7.2 Pseudorapidity correction

Figure 7.10 illustrates the phase-space variation of muons from a $Z \rightarrow \mu\mu$ MC sample. We clearly see the expected dependence on boost in pseudorapidity. To verify whether the detector geometry has any influence on the average dE/dx we shall make sure that any variation in $|\eta|$ is not simply due to $\beta\gamma$ variation in our MIP sample.

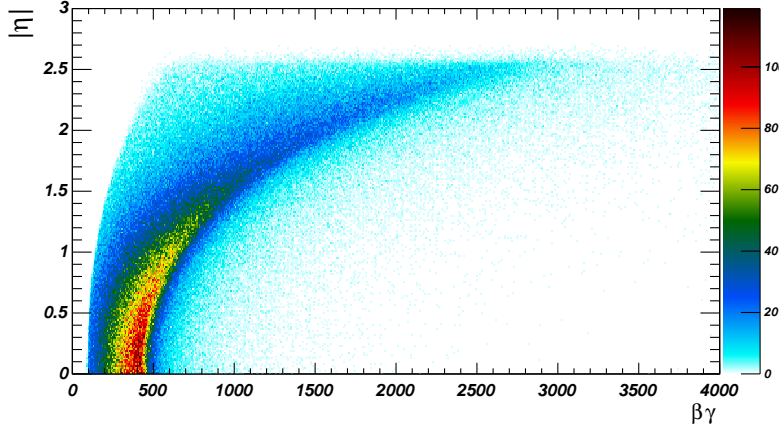


Figure 7.10: Phase-space of muons from $Z \rightarrow \mu\mu$ simulations.

Figure 7.11 show $dE/dx(\beta\gamma)$ of the $Z \rightarrow \mu\mu$ sample. From the figure a slight rise is noticeable but the sample has already reached the Fermi plateau if we look at the dashed black line representing the high- $\beta\gamma$ limit of the Vavilov equation¹

$$\Delta_p \frac{\xi}{\beta\gamma \gtrsim 100} \rightarrow \left[\ln \frac{2mc^2\xi}{(\hbar\omega_p)^2} + j \right] \quad (7.3)$$

¹ where ξ, j are defined together with the full Vavilov equation in section 4.1.2, $\hbar\omega_p$ is the plasma energy replacing the mean excitation energy I at high velocities.

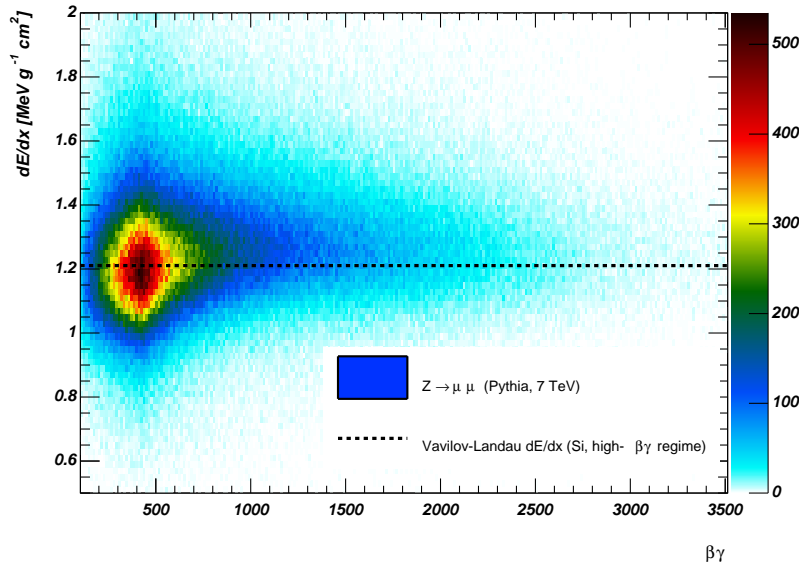


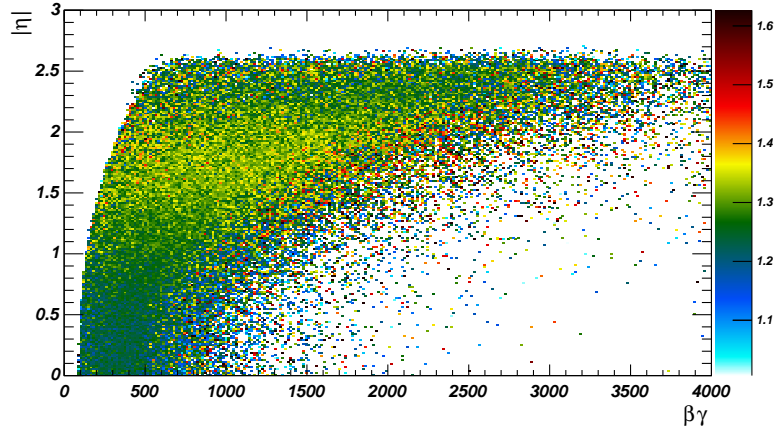
Figure 7.11: dE/dx of muons from $Z \rightarrow \mu\mu$ simulations.

The variation in the sample is then more likely caused by the phase-space

“pushing” the sample out into a non-linear region of the detector rather than an expected increase in dE/dx due to added speed.

Figure 7.12 gives us a further clue. Here each point in $\{\beta\gamma, |\eta|\}$ -space is the mean dE/dx in that particular point. The yellow band of increased dE/dx in $1.5 < |\eta| < 2.0$ is independent of $\beta\gamma$ and likely a detector effect we can correct.

Figure 7.12: Mean dE/dx variation in $Z \rightarrow \mu\mu$ -muons phase-space in the sample.



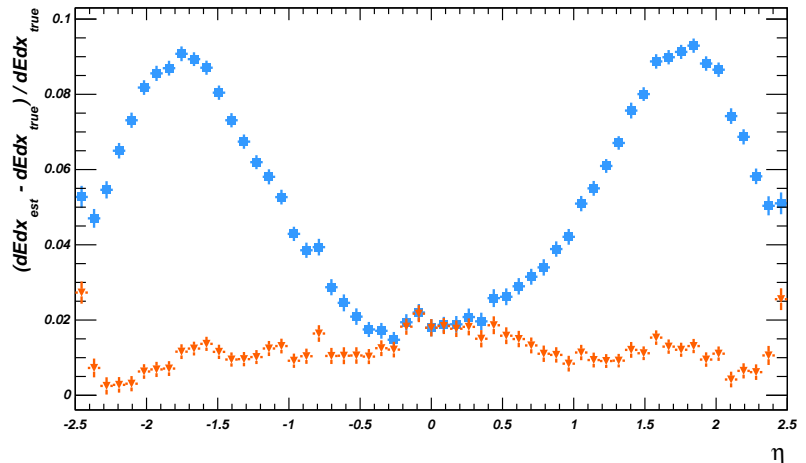
To make the variations clear we can use the difference between the estimate and (4.15),

$$\delta(dE/dx) = \frac{dE/dx_{est} - dE/dx_{Vavilov}}{dE/dx_{Vavilov}}, \tag{7.4}$$

to show which regions vary from the nominal.

In Figure 7.13 the deviation from theory is shown, and as we expected from Figure 7.12 the geometry is attributable to a 10% variation.

Figure 7.13: Variation in dE/dx due to geometrical effects. The Blue points are the uncorrected relative variation from expectation. The orange points are the same dataset after applying (7.5).



7.2.1 Correction

The usual way of finding an equation that matches data is either reverting to fundamental principles and geometry or guessing the equation based on trial-and-error and experience. In this case I knew the underlying equation but not the accumulated responses from ATLAS due to geometry, electronics and reconstruction. Instead of guessing, I decided to use *Eureqa* [86] a computer program that based on genetic algorithms fits a symbolic expression to many-dimensional data. *Eureqa* works by letting the user specify basic mathematical building blocks and accompanying ‘complexity weights’ for instance $+$, 1 , $*$, 2 , $Gauss(x)$, 10 and so on. When started the program combines these building blocks and fits the dataset with the combination. Based on the fit *Eureqa* does Pareto optimisation on the complexity of the expression and the fit quality letting expressions evolve that are both simple and precise. Genetic algorithms emulates the biological process of evolution by mating, mutating and terminating expressions. As the method relies on stochastic processes one can be lucky and find a good expression within the first few minutes on a single system but usually the result especially for complicated datasets with large non-linear variations takes time to converge. The input for the *Eureqa* run was monte carlo simulated muons with $\beta\gamma > 50$, which we expect to be flat in η with an average value close to the MIP value. A few results from the search is listed in Table 7.3.

Size	Fitness	Equation
11	0.0187	$dE/dx _{MIP}(\eta) = 1.218 + 0.097 \sin(0.468\eta^2)$
13	0.0186	$dE/dx _{MIP}(\eta) = 1.257 + 0.059 \sin(0.665\eta^2 - 0.665)$
15	0.0185	$dE/dx _{MIP}(\eta) = 1.229 + 0.115\eta \sin(\eta) - 0.065 \eta $
17	0.0184	$dE/dx _{MIP}(\eta) = 1.229 + 0.112\eta \sin(\eta - 0.0321) - 0.062 \eta $
19	0.0184	$dE/dx _{MIP}(\eta) = 1.229 + 0.112\eta \sin(\eta - 0.0270) - 0.063 \eta - 0.0271 $
9	0.0197	$dE/dx _{MIP}(\eta) = 1.276 - 0.047 \cos(\eta^2)$
7	0.0265	$dE/dx _{MIP}(\eta) = (3.617 + \eta ^{0.150})$
1	0.0364	$dE/dx _{MIP}(\eta) = 1.264$
5	0.0362	$dE/dx _{MIP}(\eta) = 1.263 + 0.002\eta$

Table 7.3: Search results for an expression fitting $dE/dx=f(\eta)$ Coefficients are truncated for visibility. Execution time: 8 hours on 40 CPU cores, resulting in 5.21×10^{11} evaluations.

All the results in Table 7.3 holds similar compatibility with the dataset, so I chose the first function on the list. Rewriting to subtract the variation gives a corrected dE/dx ,

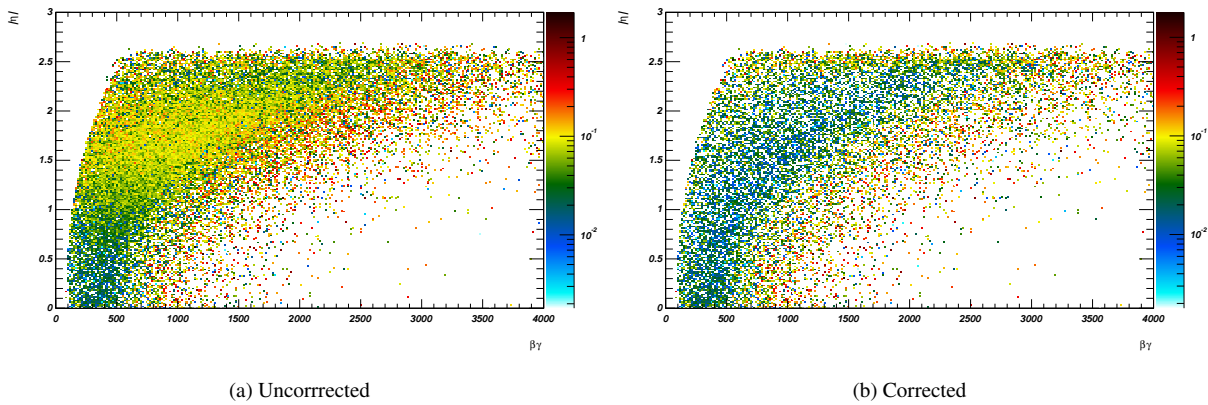
$$dE/dx(\eta)_{corr} = dE/dx_{est} - 0.09676 \sin(0.4675\eta^2). \quad (7.5)$$

Applying (7.5) to the $Z \rightarrow \mu\mu$ sample yields the result shown in Figure 7.14 where the plot to the left is how the sample differed from (4.15) before the correction and the right plot shows the corrected distribution.

7.3 Mass estimation

To create a mass estimate we must find an expression $\beta\gamma(\langle \frac{dE}{dx} \rangle)$ that follows the low- $\beta\gamma$ rise but stops when the MIP minimum is reached.

The quality of a statistical estimator can be summarised by the following qualities [62]:

Figure 7.14: η -corrected muons.

- The estimator must be consistent and converge towards the true value.
- Unbiased.
- Have the least amount of variance .
- Retain maximum information.
- Be as simple as possible.
- Computable.
- User-friendly.

The aim is thus to create an estimator that is precise, unbiased analytically invertible and relatively uncomplicated. The natural parameterisation is either Bethe-Bloch or the Vavilov equation simplified and fitted to data. The problem with these equations is that they lack the convolution of ATLAS detector and DAQ response and contain non-invertible parts. Instead of trying to make them fit an empirical distribution not well-described in the first place (see [63, 12] for attempts) we will apply another method to arrive at a more precise expression.

- Generate a $dE/dx(\beta\gamma)$ histogram (i.e. Figure 7.8).
- Slice the histogram along the $\beta\gamma$ -axis.
- Fit each individual slice with a gaussian shape to extract the mean value and spread of dE/dx .
- Create a dataset with $\{\beta\gamma, dE/dx, \sigma_{dE/dx}\}$ in the range $1 < \beta\gamma < 6$ to capture both the rise and enough of the MIP band to allow the fit a well defined asymptote towards high- $\beta\gamma$.
- Fit the dataset with Eureqa, a machine learning tool that generates an algebraic formula based on symbolic regression.

7.3.1 Symbolic regression fit

The primary motivation for this study is the estimation of masses of new massive long-lived particles. Because dE/dx is dependent on $\beta\gamma$ for slow

particles (section 4.1.2) a mass can be estimated by combination with an independent momentum measurement.

$$m = p/(\beta\gamma) \quad (7.6)$$

The Bethe-Bloch formula describes this relationship for various materials, but due to the complexity of the ATLAS detector it is impractical to analytically estimate the relation. Instead it is possible to find a parametrisation by fitting low momentum Standard Model data where protons, kaons and pions give distinct bands for momenta lower than 1 GeV/c.

In 2011 the default track reconstruction skipped tracks with momenta below 1 GeV/c, requiring custom performance data files for this study. To illustrate the method I have performed the fit on simulated events. The input is SUSY $\tilde{\tau}$ with varying masses².

Selection The input data has been selected by requiring an inner detector reconstructed track, at least two hits in the pixel detector, zero shared pixel clusters between tracks, isolation from tracks and jets $\sqrt{\Delta\eta^2 + \Delta\phi^2} > 0.3$. In order to estimate the $\beta\gamma$ value all tracks are matched to ‘truth’ information from the event generation step.

Each track matching the above criteria is saved in a 2D histogram with the following geometry: x-axis: 500 bins between 0.1 and 10 $\beta\gamma$, y-axis: 500 bins between 0 and 20 dE/dx.

To estimate the mean dE/dx value as a function of $\beta\gamma$ the 2D histogram is sliced by projecting along the y-axis. Each slice is fitted with a Gaussian function and the resulting mean value with statistical errors saved in a 1D histogram. The standard variation for each Gaussian fit is also saved in a separate histogram.

Parametrisation The histogram with mean values are then fitted with Eureka. The figure below shows the input 2D histogram as well as the (black) dots from the slice fits. The red and blue lines are the currently best and second best fit function respectively.

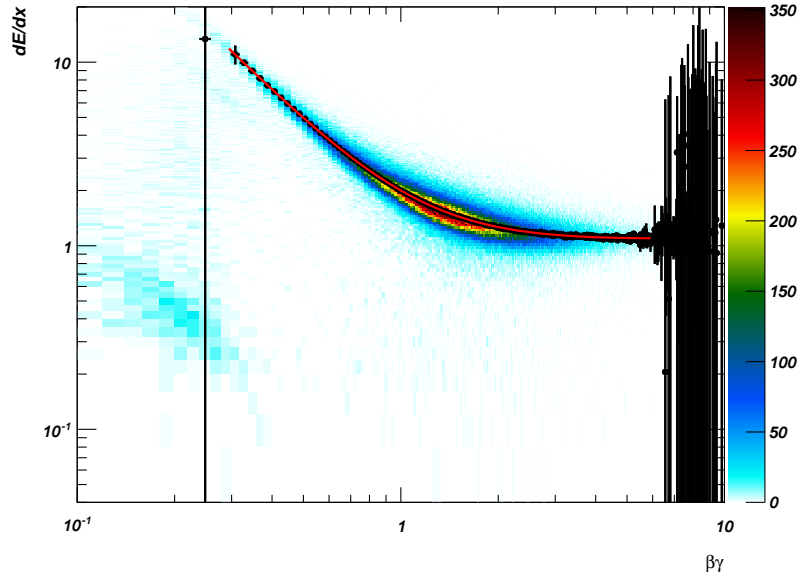
Size:	Fitness:	Equation:
15	0.0135497	$dE/dx(\beta\gamma) = (1.175/\beta\gamma + \beta\gamma - 0.231)/(0.080 + 0.892\beta\gamma)$
14	0.0138698	$dE/dx(\beta\gamma) = 1.184 + (1.376 - 0.554\beta\gamma)/\beta\gamma^{1.785}$
19	0.0135428	$dE/dx(\beta\gamma) = (\beta\gamma^{1.006} + 1.180/\beta\gamma - 0.211)/(0.079 + 0.905\beta\gamma)$
13	0.0142499	$dE/dx(\beta\gamma) = 1.102 + 0.906\beta\gamma^{-0.290\beta\gamma - 1.947}$
11	0.0147863	$dE/dx(\beta\gamma) = 1.072 + 1.156(0.099 + \beta\gamma)^{-2.385}$
9	0.0210256	$dE/dx(\beta\gamma) = 1.057 + (0.030 + \beta\gamma)^{-2.132}$
8	0.0257238	$dE/dx(\beta\gamma) = 1.040 + 0.970/\beta\gamma^2$
7	0.0276055	$dE/dx(\beta\gamma) = 1.027 + \beta\gamma^{-1.968}$
6	0.163132	$dE/dx(\beta\gamma) = \exp(0.763/\beta\gamma)$
4	0.427812	$dE/dx(\beta\gamma) = 2.508/\beta\gamma$
1	1.01597	$dE/dx(\beta\gamma) = 1.535$

² $\tilde{\tau}$ s are excellent particles for this study as they behave like heavy muons, whereas R-Hadrons would add complexity due to fluctuating charge and hadronic interactions.

Table 7.4: Results from fitting $dE/dx = f(\beta\gamma)$. Execution time: 8 hours on 40 cores, 283063 generations, 10^{11} evaluations

$$\left\langle \frac{dE}{dx} \right\rangle(\beta\gamma) = \frac{\beta\gamma + \frac{1.1751}{\beta\gamma} - 0.2306}{0.8924\beta\gamma + 0.0797} \quad (7.7)$$

$$\Rightarrow \left\langle \frac{dE}{dx} \right\rangle(\beta\gamma) = \frac{a + b\beta\gamma + (\beta\gamma)^2}{\beta\gamma(c + d\beta\gamma)} \quad (7.8)$$

Figure 7.15: Fit of dE/dx for long-lived GMSB $\tilde{\tau}$.

Inverting

$$\beta\gamma\left(\left\langle\frac{dE}{dx}\right\rangle\right)=\frac{\sqrt{4\alpha(\kappa\left\langle\frac{dE}{dx}\right\rangle-1)+(\omega\left\langle\frac{dE}{dx}\right\rangle-\rho)^2}+\rho-\omega\left\langle\frac{dE}{dx}\right\rangle}{2(\kappa\left\langle\frac{dE}{dx}\right\rangle-1)} \quad (7.9)$$

Which finally gives a mass estimate,

$$m\left(\left\langle\frac{dE}{dx}\right\rangle,p\right)=\frac{2(\kappa\left\langle\frac{dE}{dx}\right\rangle-1)p}{\rho-\omega\left\langle\frac{dE}{dx}\right\rangle+\sqrt{(\rho-\omega\left\langle\frac{dE}{dx}\right\rangle)^2+4\alpha(\kappa\left\langle\frac{dE}{dx}\right\rangle-1)}}. \quad (7.10)$$

where $\alpha = 1.175$, $\rho = -0.231$, $\omega = 0.080$, $\kappa = 0.892$.

7.4 Results

The mass estimator developed in this chapter is not the only one in use in ATLAS. In fact the previous searches for R-Hadrons (including the one in this thesis) all used a different method developed by the ATLAS pixel performance group. The results presented here are compared with this estimator. The Eureka-method is called the ‘NBI-estimator’ in the following plots. The results are presented using the ‘true’ particle momentum from event generation.

7.4.1 ATLAS default method

The ‘default’ mass estimator[12] is based on numerically inverting a parametric Bethe-Bloch function,

$$\frac{dE}{dx} = \frac{p_1}{\beta^{p_3}} \log(1 + (|p_2| \beta \gamma)^{p_5}) - p_4. \quad (7.11)$$

The free parameters p_n are found by fitting the pion, kaon and proton bands in Figure 7.6. The method can be summarised as

- Generate n 1D histograms by slicing Figure 7.6 with $\beta\gamma$ instead of p along the horizontal axis.
- For each histogram $i \in n$ fit a three Crystal ball functions to the peaks of each particle type

$$f(x; \alpha, n, \bar{x}, \sigma) = N \cdot \begin{cases} \exp\left(-\frac{(x-\bar{x})^2}{2\sigma^2}\right), & \text{for } \frac{x-\bar{x}}{\sigma} > -\alpha \\ A \cdot \left(B - \frac{x-\bar{x}}{\sigma}\right)^{-n}, & \text{for } \frac{x-\bar{x}}{\sigma} \leq -\alpha \end{cases} \quad (7.12)$$

Where $A = \left(\frac{n}{|\alpha|}\right)^n \cdot \exp\left(-\frac{|\alpha|^2}{2}\right)$, $B = \frac{n}{|\alpha|} - |\alpha|$, N is a normalisation factor and α , n , \bar{x} and σ are parameters which are fitted with the data. The crystal ball function has the advantage that it has a controllable tail emulating the Landau tail and otherwise easy to fit.

- The MPV from each peak in slice i is plotted on a graph with the corresponding $\beta\gamma$ value of the histogram.
- When all slices have been fitted individually, eq (7.11) is fitted to the $\beta\gamma$ -MPV graph to obtain the free parameters p_n .
- We are interested in $\beta\gamma$ based on dE/dx and must invert (7.11) to obtain the relativistic speed. It is not possible to invert the function algebraically so the function is numerically inverted based on the specific dE/dx value.

A good argument for using this estimator is that it is fitted on both data (minimum bias data from 2010) and Monte Carlo and is as such very well-calibrated. In later runs the track multiplicity in most events required us to only reconstruct tracks with a minimum $p_T = 1 \text{ GeV}/c$ effectively removing the non-mip Standard Model region.

7.4.2 Mass estimation performance for R-Hadrons

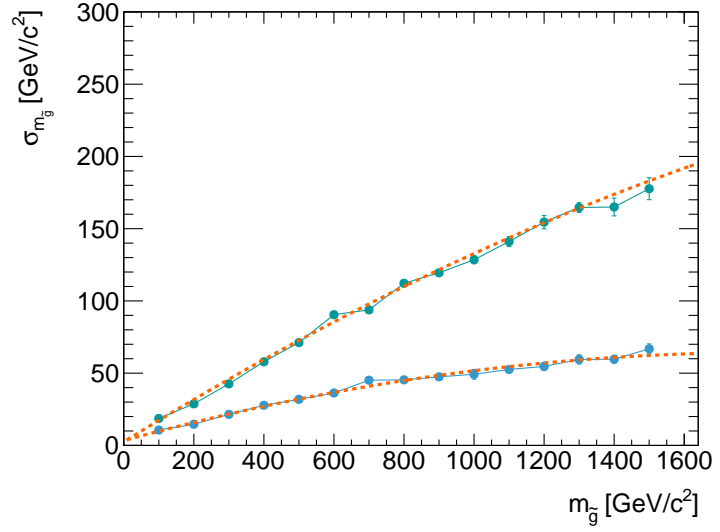
To estimate how well the mass estimators perform the following comparison is made

$$\delta(\text{mass}) = \frac{\text{mass}_{\text{est}} - \text{mass}_{\text{true}}}{\text{mass}_{\text{true}}} \quad (7.13)$$

Mass resolution The spread of this distribution is the mass resolution (Figure 7.16) which tells us how much the mass estimate varies from the true value.

Fitting a second degree polynomial to the graphs we find the following relationships,

Figure 7.16: Mass resolution. The blue dots are the NBI estimator and the green dots the ATLAS-default estimator.



$$\sigma_{NBI} = 3.324 + 0.067m - 1.816 \times 10^{-5}m^2 \quad (7.14)$$

$$\sigma_{Default} = 2.478 + 0.150m - 1.999 \times 10^{-5}m^2. \quad (7.15)$$

The resolution divided with the corresponding mass gives us the relative spread (Figure 7.17).

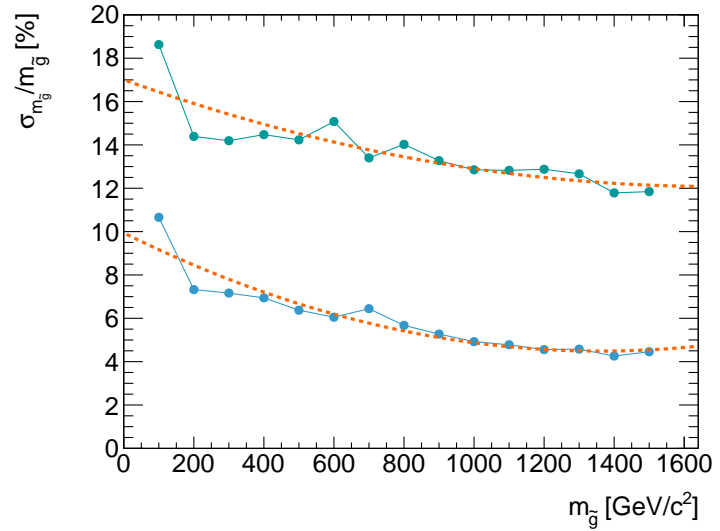


Figure 7.17: Relative mass resolution for the NBI estimator (blue) and the Default estimator (green).

$$\sigma_{NBI}/m = 9.939 - 0.008m + 2.939 \times 10^{-6}m^2 \quad (7.16)$$

$$\sigma_{Default}/m = 17.007 - 0.006m + 1.722 \times 10^{-6}m^2 \quad (7.17)$$

Bias An important feature of any statistical estimator is a small bias, or systematic deviation from the true value.

$$mass_{bias} = mass_{est} - mass_{true} \quad (7.18)$$

In Figure 7.18 the NBI estimator stays unbiased for all mass points while the default method drifts towards higher estimated masses.

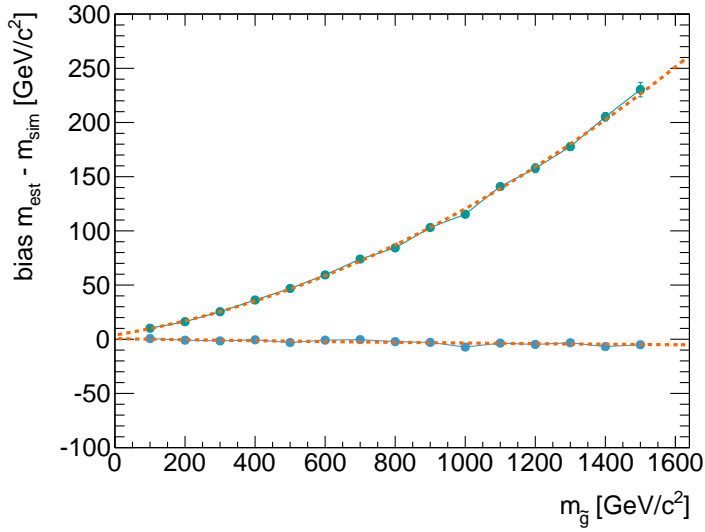


Figure 7.18: Bias. Deviation from the true mass shown for the NBI estimator (blue) and the Default estimator (green).

The polynomials below show this tendency quite clearly

$$bias_{NBI} = 0.51 - 0.005m + 8.87 \times 10^{-7}m^2 \quad (7.19)$$

$$bias_{Default} = 3.85 + 0.053m + 6.339 \times 10^{-5}m^2. \quad (7.20)$$

Comparisons One of the features of the NBI estimator is that it is analytically invertible. This also means it is not describing any effects after the MIP minimum. In Figure 7.19 The expression is compared to both Bethe-Bloch that shows a very clear rise and the Vavilov equation that more closely resembled by the expression.

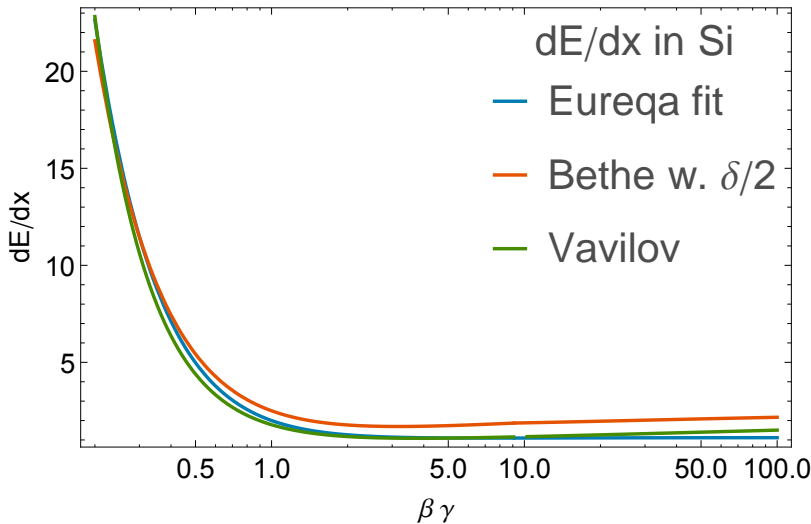


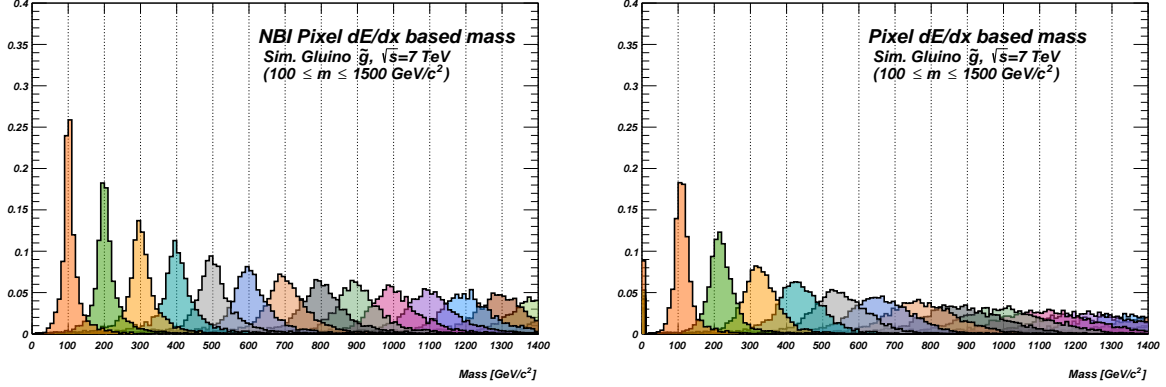
Figure 7.19: Comparison between the Eureqa expression in (7.7). The Bethe-Bloch equation (4.14) and the Vavilov equation (4.15) for Silicon. The three functions follow each other in the low- $\beta\gamma$ regime, but the Eureqa expression flattens out at the MIP level and never rises.

While both (4.14) and (4.15) diverges the expression converge at,

$$\lim_{\beta\gamma \rightarrow \infty} \rightarrow 1.121 \text{ MeVg}^{-1}\text{cm}^2. \quad (7.21)$$

The minimum is found at $dE/dx_{min}(\beta\gamma) = dE/dx_{min}(7.39) = 1.096 \text{ MeVg}^{-1}\text{cm}^2$ compared to $dE/dx_{Vavilov,min}(\beta\gamma) = dE/dx_{min}(3.77) = 1.086 \text{ MeVg}^{-1}\text{cm}^2$ and $dE/dx_{Bethe,min}(\beta\gamma) = dE/dx_{min}(3.17) = 1.694 \text{ MeVg}^{-1}\text{cm}^2$.

To give a qualitative impression of the difference between the two estimators all the signal samples available have been plotted in the same histogram (Figure 7.20).



(a) The new method developed here.

(b) The default method.

Figure 7.20: A qualitative comparison of the two estimators. Both distributions contain R-Hadron gluino samples with masses at $100 \text{ GeV}/c^2$ intervals between 100 and $1400 \text{ GeV}/c^2$. In both figures the momentum is taken from the event generation stage (truth information).

7.5 Conclusion

This chapter reviewed the ATLAS Pixel dE/dx estimator. A geometrical dependence was discovered by studying the interaction of MIP particles in the tracker. A correctional expression has been developed based on symbolic regression and is likely to be applicable to the data if refitted (a lower mean dE/dx is expected due to radiation damage not accounted for in the simulation). A new mass estimator based on Pixel dE/dx has been developed, also based on symbolic regression. It has been shown that the mass resolution of this new estimator is superior to the current estimator for simulated events and using ideal momentum. Further studies are needed to validate its performance based on collision data.

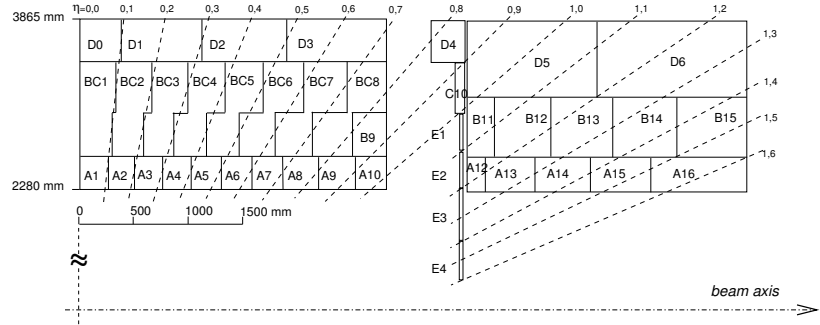
LLPs produced at the LHC will be slow ($\beta \ll 1$) yet penetrating like muons, allowing detection by time-of-flight measurements in calorimeter systems. The Tile Calorimeter (TileCal) in ATLAS is well suited for this kind of measurement with a time resolution $\sigma_t \sim 1\text{ns}$ which is sufficient for detecting slow particles at the distance of the calorimeter cells. In [58, 69] a Tile calorimeter based ToF method for the ATLAS hadronic calorimeter was introduced. This chapter presents an updated study on how to gain additional β -resolution by correcting the time-response in the non-linear regime beyond 25ns as well as η -dependence introduced by the non-projective square calorimeter modules in the other part of the Tile calorimeter. These enhancements stems from the previous assumption that all calorimeter cells are infinitely small and located at the exact centre of the cell coordinate. For the Liquid Argon Calorimeter (LArCalo) with its projective geometry this can be assumed to be true but for the semi-projective geometry of the TileCal it is no longer a fitting assumption as we will discuss later in this note. A correction scheme is devised that allows for a more precise determination of the actual travel length. Another correction will be discussed later as well, relating to the time response of particles with $\beta < 0.4$ which typically have a $t > 20\text{ns}$ relative to a particle arriving at the speed of light. In this time region the $r-t$ relationship is no longer linear and a direct ToF estimate is no longer valid leading to abnormally low β -estimates. A relationship that corrects for this non-linear response is presented here. In the last section the performance of these corrections is measured relative to the *vanilla* algorithm found in earlier reports.

8.1 The Tile calorimeter

The Hadronic Tile Calorimeter is a non-compensating sampling calorimeter where tiles of steel is interleaved plastic scintillators acting as absorber and active detector layers respectively. The Tile calorimeter is divided into a central barrel region ($|\eta| < 1$) with two partitions (around $\eta = 0$), the Long Barrel A (LBA) and Long Barrel C (LBC). On each side of these are two extended barrel partitions EBA and EBC that cover $0.8 < |\eta| < 1.7$. The partitions are segmented into 64 azimuthal (ϕ) wedge modules providing a near-uniform coverage in the azimuthal direction. The active scintillators are grouped into readout cells giving rise to three radial layers and a semi-projective segmentation along the beam-axis makes the detector response

approximately flat in η . Each cell is connected to two photomultiplier tubes (PMTs) by bundles wavelength-shifting fibres connected to the scintillators from the side of the modules. The two PMTs have a gain difference of 64 extending the dynamic range of the output signal to cover both low and high energy depositions. The signal from the PMTs are digitalised by front-end electronics and transmitted to the Read Out Driver Boards (RODs) through optical fibres for further processing.

Figure 8.1: The readout cell geometry. The modules in Figure 6.14 are connected to form readout cells in three layers A, BC and D. The readout cells are structured to be approximately linear in η .



8.1.1 Signal processing

Each of the roughly 10000 readout cells are sampled 7 times during a readout window (Figure 8.2). The samples S_i are spaced by 25ns. From these samples the PMT pulse is reconstructed using the following function

$$f(t) = Ag(t_0 - t) + p, \quad (8.1)$$

where A is the amplitude, $g(t)$ is a normalised pulse shape function, p is the pedestal value and t is the peak position of the pulse at time t relative to a reference time t_0 . At a readout rate of roughly $1/10\mu\text{s}$ the RODs are processing $\sim 8.8\text{GB/s}$ severely restraining the allowed computing time for each pulse reconstruction. To fit (8.1) for all readout cells within the $10\mu\text{s}$ window a fast algorithm called Optimal Filtering (OF) is implemented in the ROD DSPs. The algorithm reconstructs the amplitude, time difference and pedestal from the seven samplings using a linear combination of the samples and coefficients a_i , b_i and c_i related to the target observables in (8.2), (8.3), (8.4), (8.5).

$$A = \sum_{i=1}^7 a_i S_i \quad (8.2)$$

$$At = \sum_{i=1}^7 b_i S_i \quad (8.3)$$

$$t = \frac{At}{A} \quad (8.4)$$

$$p = \sum_{i=1}^7 c_i S_i \quad (8.5)$$

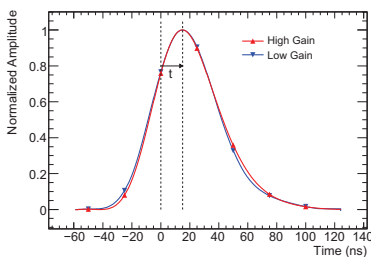


Figure 8.2: Illustration of a fitted Tile-Cal pulse. Notice the 7 sampling points, Ref. [58].

Most of the particles measured by ATLAS are expected to travel at close to the speed of light. To make the best use of a limited sampling window the readout time in all time sensitive detectors in ATLAS are centred around

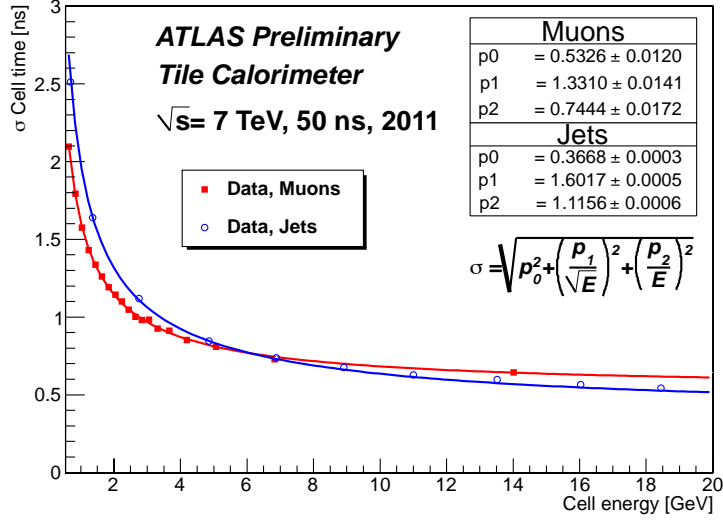


Figure 8.3: Cell time resolution as a function of cell energy in the 2011 collision data at $\sqrt{s} = 7$ TeV and 50 ns bunch spacing. The time of the cell has been corrected for its mean time. The resolution was parameterised with the function $\sigma = \sqrt{p_0^2 + \left(\frac{p_1}{\sqrt{E}}\right)^2 + \left(\frac{p_2}{E}\right)^2}$, describing well the data. Muons deposit only a small fraction of their energy, so only high-gain region is explored, which reaches up to 20 GeV. The time resolution is 0.5 – 0.6 ns for $E \sim 20$ GeV and 1.3 – 1.15 ns at ~ 2 GeV for jets and muons respectively.

the time a particle leaving the interaction point at the speed of light ($\beta = 1$) would arrive at the respective detector. This means that times measured in each TileCell is calculated relative to the time a massless particle would have arrived at the readout cell. The OF method is optimised to estimate t under the $t \sim 0$ assumption and the resolution is slightly degraded at later times.

8.1.2 Calorimeter time resolution

The time resolution of TileCal has been measured during collision runs in 2011 (Figure 8.3). The estimated time resolution for a readout cell i is parameterised by

$$\sigma = \sqrt{p_0^2 + \left(\frac{p_1}{\sqrt{E}}\right)^2 + \left(\frac{p_2}{E}\right)^2} \quad (8.6)$$

where $1/\sqrt{E}$ is the statistical uncertainty and $1/E$ a noise contribution. $p_0 = 0.533$, $p_1 = 1.331$ and $p_2 = 0.744$ a constants determined by the fit shown in Figure 8.3.

Based on (8.6) it is possible to determine if the TileCal provides sufficient resolution for LLP searches.

In Figure 8.4 the maximum speed allowed to distinguish it from $t = 0$ is plotted as a contour. LLPs produced in pairs at $\sqrt{s} = 7$ TeV have a mean velocity $\beta < 0.85c$ even at $m = 100$ GeV/ c^2 .

8.2 Simulation of signal samples

For this study a set of simulated samples were used. The production and simulation is described in Chapter 9 suffice to say that R-Hadron are generated with Pythia 6 and Slepton samples are generated with Herwig. R-Hadrons are produced by generating a gluino pair that is kept stable by decay suppression. The gluinos then hadronise with Standard Model quarks [67] into bound states called R-Hadrons. Sleptons are also kept stable and can be

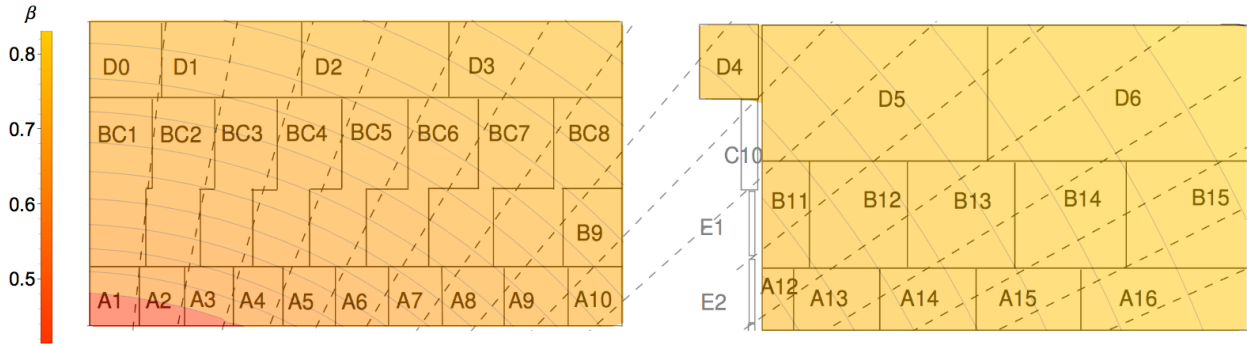


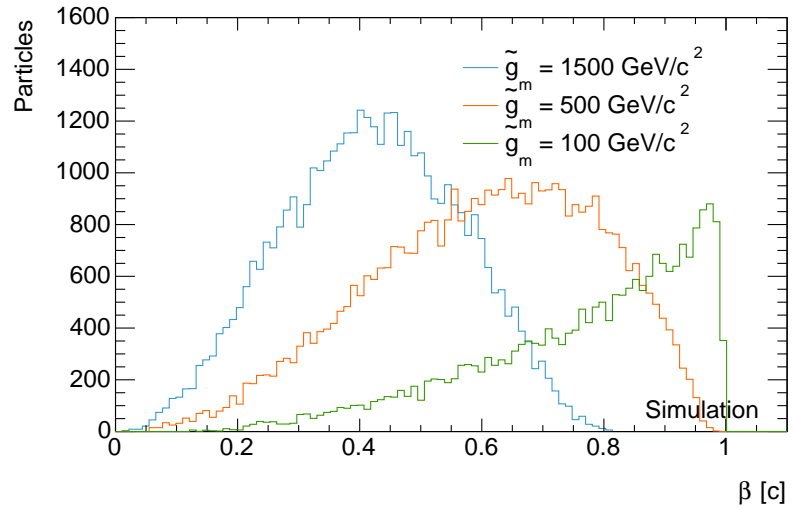
Figure 8.4: The contour overlay illustrates the speed β required to satisfy $3\sigma_t < \frac{\sqrt{z^2+p^2}}{\beta c} - \frac{\sqrt{z^2+p^2}}{c}$. A1, the cells closest to the interaction point, can only accurately separate a slow particle from a particle moving at the speed of flight if $\beta < 0.63c$. Contrary, the D6 cells is capable of estimating the time difference for $\beta < 0.82c$

perceived to be massive muons in their interactions. The generated events are simulated by the Geant 4 transport code where custom extensions handle the complicated hadronic interactions of R-Hadrons when interacting with matter. The Geant 4 simulation is done with the full ATLAS Geometry which is well validated against data.

8.3 Characteristic features of LLPs

New types of LLPs are massive and hence slow moving at the LHC. This is quickly accessed by plotting a few representative distributions (Figure 8.5).

Figure 8.5: Speed distributions of \tilde{g} R-Hadrons with $m = 100, 500, 1500 \text{ GeV}/c^2$ $\sqrt{s} = 7 \text{ TeV}$.



Comparing the upper limit on β estimation in Figure 8.4 with the β -spread in Figure 8.5 we see that at $m > 100 \text{ GeV}/c^2$ sufficient resolution is available in all of TileCal.

8.4 Calorimeter based time measurements for SMP detection

The utilisation of TileCal and the calorimeters as a whole for ToF estimation has already been established [69]. This note focuses on two enhancements

of the β -resolution by taking into account the point of the individual cells relative to the IP, as well as the overall linearity in timing. The study has been performed on nominal simulation samples emulating the run conditions throughout 2011. Compared to the previous study this allow us to compare the effects of the enhancement with a more realistic performance scenario.

8.4.1 Data objects

The method described requires access to individual CaloCells which are data object storing information from individual calorimeter readout channels. There are two ways of accessing these at post-reconstruction level. For muon tracks CaloCells in the vicinity of the track are saved to analysis data files (AODs) and can be accessed with ease. Alternatively special derived event summary data (dESDM) files can be constructed to contain CaloCells. This study relies on the latter approach and we use the RPVLL_DESDM files produced centrally in ATLAS for long-lived particle searches. To avoid complications arising with R-Hadrons due to their possible charge-flip properties we rely on inner detector tracks and track extrapolation to the calorimeter layers rather than muon tracks.

To associate tracks with crossed CaloCells a special filler module has been developed within the LongLivedParticleD3PD package that calls the AtlasExtrapolator package and adds any CaloCell to the resulting ntuple file that is crossed by a track. For a CaloCell to be accepted it must have an energy deposition above a noise threshold set individually for each cell by the CaloNoiseTool. The procedure is implemented in the TrackInCaloTools package. For each cell the centre position of the cell along with the arrival time and energy deposition is saved.

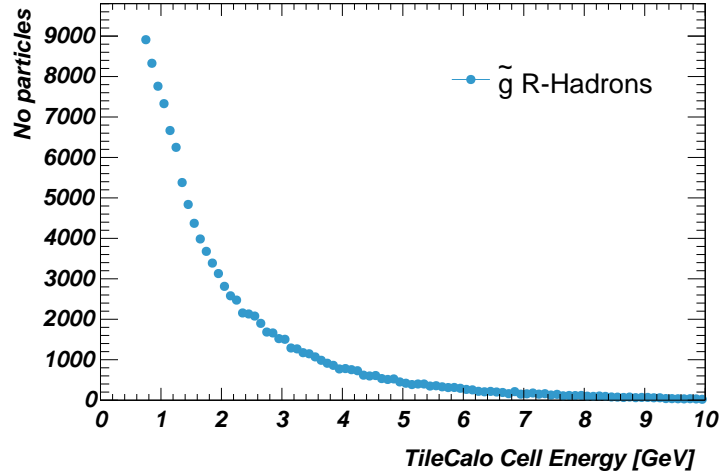
Furthermore another package CalodEdxTool has been developed to construct dE/dx estimates for calorimeter cells [63]. This package is based on the same tools as the CaloCell extractor but it calculates the expected track length within a given cell (dx) as well as the energy loss in the cell. Any CaloCells marked as ‘bad’ are discarded as well. A combined dE/dx estimate as well as the associated uncertainty $\sigma_{dE/dx}$ is calculated and filled for each track in the LongLivedParticle D3PD.

In previous studies only the first set of CaloCell information was available. With the CalodEdxTool it is possible to make intra-cell corrections correcting for time variations due to tracks grazing a cell or hitting it straight at the centre.

8.4.2 Energy deposition

LLPs deposit relatively small amounts of energy in the calorimeter cells compared to jets. The cell energy distributions in Figure 8.6 illustrates this for a number of R-Hadrons samples. The noise cuts is ~ 300 MeV as can be seen in the first bin on the histogram. Otherwise the bulk of the distribution is at $E \sim 1$ GeV. Comparing with Figure 8.4 we expect a time resolution between 1.5 and 1 ns for these particles.

Figure 8.6: Energy deposited in calorimeter cells for R-Hadrons of various masses.



8.4.3 A review of the current time-of-flight method

The time associated with each CaloCell is centred around 0 ns for signals arriving at $v \sim c$ relative to the trigger time. The actual time-of-flight t_{true} is thus related to the cell time t_{reco} by

$$t_{reco} = t_{true} - \frac{d_{cell}}{c} \tag{8.7}$$

where d_{cell} is the straight line distance from the IP to the cell centre, and c is the speed of light in vacuum. For relativistic particles a tight distribution around $t = 0$ ns is expected while LLPs are expected to have values $t > 0$. The range of t is limited to 75 ns. This causes a distance dependent drop in signal efficiency that for TileCal is happening $\beta \sim 0.4$.

Figure 8.7: CaloCell time for R-Hadrons (the blue cloud above $t = 0, p_T > 50$ GeV/c) and Standard Model particles (the asymptotic distribution at low pT).

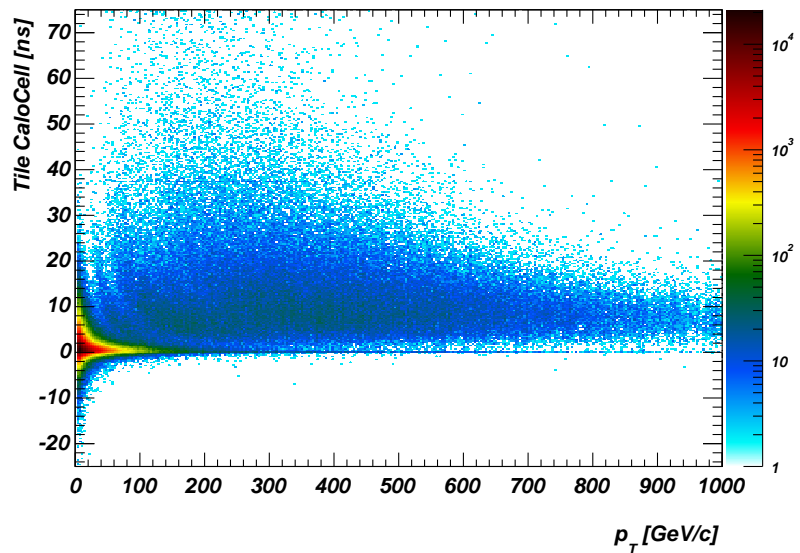


Figure 8.7 shows the spread in t of R-Hadrons (\tilde{g}) and associated SM particle in the events. The relationship between t and β is evident in the late arrival times of the massive particles. It is also worthwhile to note that

the d_{cell}/c normalisation removes the expected offset at progressively larger travel distances.

8.4.4 Determining β from t and distance

The CaloTime is by itself a relevant discriminator between MIP-like Standard Model particles and LLPs. By calculating the actual speed β a deeper connection to the underlying kinematics allows us to determine the particle mass which of course is the fundamental observable we are really trying to reconstruct.

The speed of a particle β is related to the time t it takes for it to traverse a distance d , which when accounting for (8.7) is expressed by

$$\beta_{cell} = \frac{v}{c} = \frac{d_{cell}}{t_{true} c} = \frac{d_{cell}}{\left(t_{reco} + \frac{d_{cell}}{c}\right) c} = \frac{d_{cell}}{t_{reco} c + d_{cell}}. \quad (8.8)$$

The chief objective of this study is to arrive at a precise β estimate for our signal region while preserving separation with relativistic particles. To gauge the effect of the corrections we study the β -resolution

$$\frac{\Delta\beta}{\beta} = \frac{\beta_{est} - \beta_{true}}{\beta_{true}}. \quad (8.9)$$

Speed estimates from individual cells are independently measured allowing for a combination by weighted average. The weights used in this study are the time uncertainty from (8.6)

$$w_i = \frac{1}{\sigma_t(E_i)^2}. \quad (8.10)$$

The weighted average is calculated as

$$\beta_{est} = \frac{\sum_{i=0}^n w_i \beta_i}{\sum_{i=0}^n w_i} \quad (8.11)$$

for all CaloCells i along a track.

8.5 Correction to CaloCell time

For relativistic particles extended CaloCell times are not expected, and the linearity of any deviation from $t = 0$ is of little importance. Luckily for LLP searches the time response is fairly linear at least up to $t \sim 25$ ns. Figure 8.8a illustrates this for a number of TileCal cells each corresponding to a distinct line on the scatter plot. The relationship between cell time and β is easier to see when we compare the estimated speed with the true particle speed in Figure 8.8b. The tail at $t > 25$ ns is responsible for the tail seen in the Figure 8.10a. To correct for this effect a parameterisation was developed by fitting Figure 8.8b and correcting for the variation from $\Delta\beta/\beta = 0$.

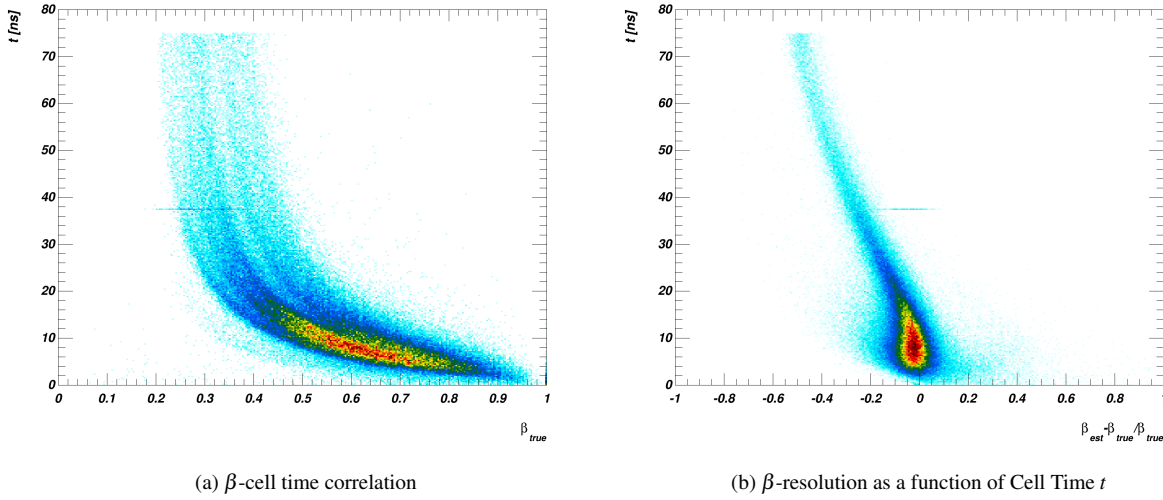


Figure 8.8: Cell time is highly dependent on the time-of-flight for slow particles. At times $t > 25$ ns the distance-time relationship is no longer linear as assumed by $\beta = d/v$.

Table 8.1: Results from fitting Figure 8.8b.

$\frac{\beta_{est} - \beta_{true}}{\beta_{true}}$	t ns	σ_t ns
-0.0314724	7.73333	0.0364489
-0.0341309	11.2	0.0342408
-0.050243	14.6667	0.031727
-0.0732759	18.1333	0.0307136
-0.103417	21.6	0.0282578
-0.136266	25.0667	0.0270231
-0.168793	28.5333	0.0260619
-0.202317	32	-0.0243261
-0.235523	35.4667	-0.023792
-0.264849	38.9333	-0.0249566
-0.295163	42.4	-0.0238266
-0.323435	45.8667	0.0232422
-0.348302	49.3333	0.0231769
-0.375721	52.8	0.0215777
-0.396387	56.2667	-0.0239718
-0.416147	59.7333	0.0229488
-0.439177	63.2	-0.0200229
-0.459816	66.6667	0.022856
-0.474327	70.1333	0.0211903
-0.483607	73.6	0.0193258

Table 8.2: Eureqa results from fitting the data in Table 8.1.

8.5.1 Input for fitting

The distribution in Figure 8.8b was generated based on 120000 R-Hadron events for all TileCal cells as they were shown to have a similar response. The histogram was first fitted in slices along the t -axis with a scalable Breit-Wigner (BW) shape

$$\sigma(E) = N \frac{\Gamma}{(2\pi)(E - E_0)^2 + (\Gamma/2)^2} \quad (8.12)$$

where E_0 in this fit, is the central $(\beta_{est} - \beta_{true})/\beta_{true}$ value for each Δt slice, and Γ is the width of the BW function. The scale constant N is introduced ad-hoc to ease the fit. The choice of the BW function is due to its sharply peaking shape, the situation obviously has nothing to do with decay-widths. As initial parameter guesses N is set to be the peak value of the slice, E_0 is set to be the Gaussian sample mean for the slice and Γ two times the root-mean-square (RMS). For each slice E_0 is saved as the Most Probable Value (MPV) with associated errors on the value set to be $\pm 0.5 \Gamma$. The resulting points are listed in Table 8.1. To find a parameterisation that expresses $f(t) = (\beta_{est} - \beta_{true})/\beta_{true}$ the dataset was fitted with Eureqa (Sec. 7.2.1). Four results that fits the dataset the best is presented in Table 8.2.

Size	Fit	Expression
46	0.005	$\frac{\Delta\beta}{\beta} = 70.05 + 9.87 \log(t) + 0.0016t\sqrt{t} + -45.91\sqrt{t}/t - 0.026t - 51.46\sqrt{\log t}$
30	0.005	$\frac{\Delta\beta}{\beta} = 0.014t + 23.80/t + 36.66\sqrt{\log t} - 35.49 - 9.85 \log t$
25	0.008	$\frac{\Delta\beta}{\beta} = 0.37\sqrt{t} + 0.020t^{1.28} - 0.496 - 0.107t$
22	0.008	$\frac{\Delta\beta}{\beta} = 0.41 + 9.50 \times 10^{-5}t^2 + -1.15 \log t/t - 0.018t$

From these results the second on the list was selected as a good compromise between fit quality and complexity. The resulting equation was solved for β_{true} to yield:

$$\beta_{corr} = \frac{\beta_{est} t}{p_0 t^2 + p_1 + p_2 t \sqrt{\log t} - p_3 t - p_4 t \log t + t} \quad (8.13)$$

where $p_0 = 0.01397$, $p_1 = 23.79640$, $p_2 = 36.65512$, $p_3 = 35.48987$, $p_4 = 9.85138$.

The correction is applied by computing (8.13) for the estimated cell β . The correction yields a much narrower distribution shown in Figure 8.9. From the figure it is clear that the correction isn't perfect and further work with Eureqa can possibly result in a better expression.

Nevertheless the result gives a significant improvement and the asymmetrical tail in Figure 8.10 is basically gone and traded for additional statistics around the true value.

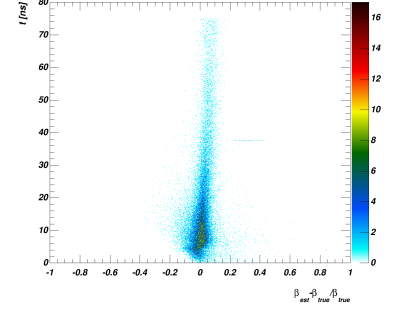


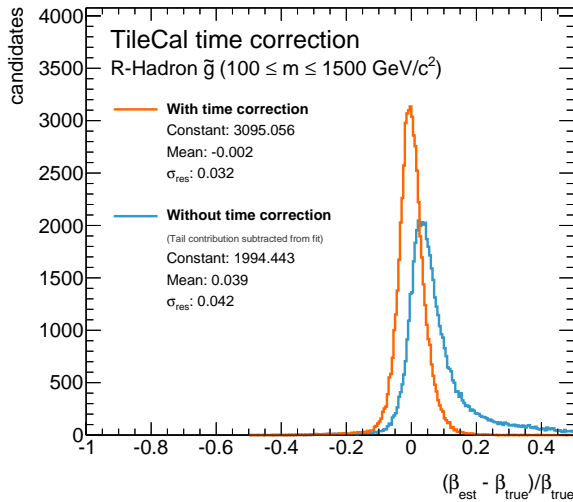
Figure 8.9: Corrected time for R-Hadrons

8.5.2 Timing correction result

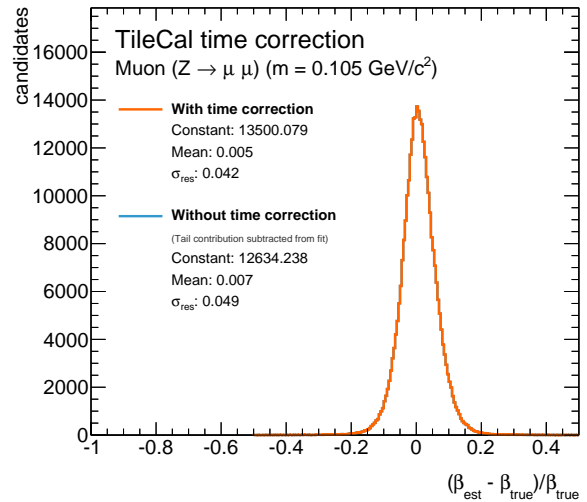
The time correction $f(\Delta\beta/\beta)$ when applied to R-Hadrons have a measurable effect in particular for high mass samples which can be seen in Figure 8.11 a and b.

The effect is more pronounced at high masses due to the longer ToF for heavier particles. For muons the effect of the correction is negligible as we would expect since the $t = 0$ region is well-calibrated already. Sleptons represent an intermediate case in the sense that their masses do not exceed $500 \text{ GeV}/c^2$ in our test samples. The β -dependent resolution is shown together with the relative bias in Figures 8.13ab. The correction is applicable to the full TileCal as all the cells have the same time response shown in Figure 8.8b.

Figure 8.10: The effect of the timing correction is clearly noticeable for slow particles (a) but relativistic particles are already centred around $t = 0$ and not affected by the correction at $t > 0$.



(a) β -resolution for \bar{g} ($m > 100 \text{ GeV}/c^2$).



(b) β -resolution for μ ($m = 0.105 \text{ GeV}/c^2$).

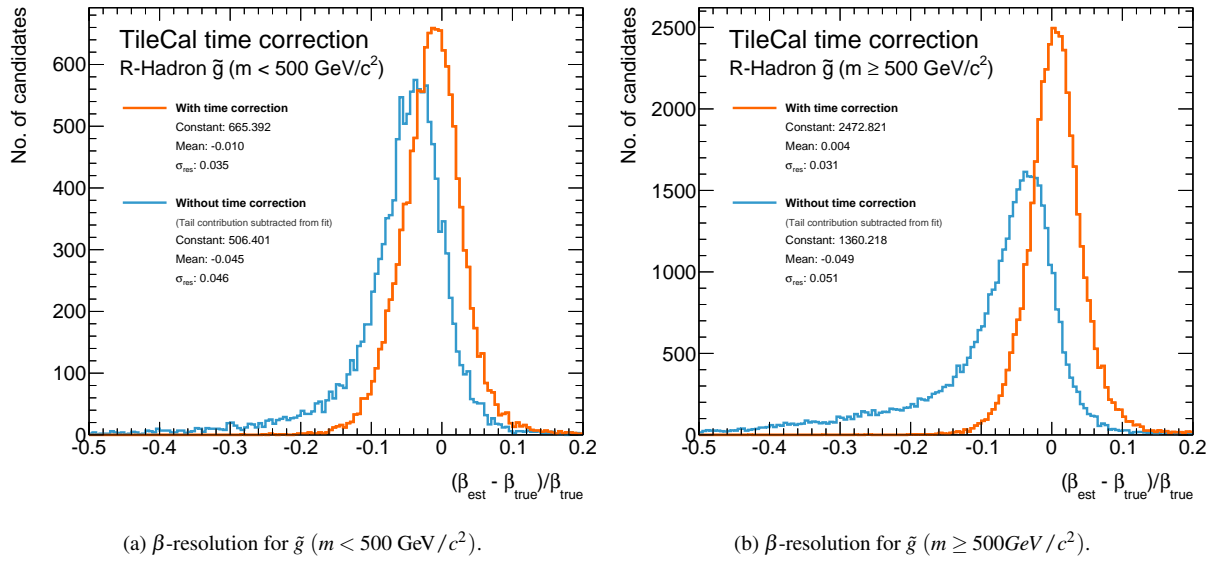
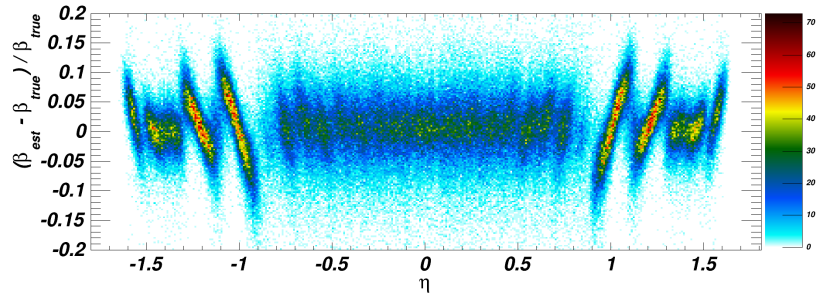


Figure 8.11: Effects from the time correction on \tilde{g} separated into two mass ranges at $500 \text{ GeV}/c^2$. The time correction is most noticeable for the heavier particles that in general arrives later than the lighter.

8.6 Projective correction for cubic calo cells

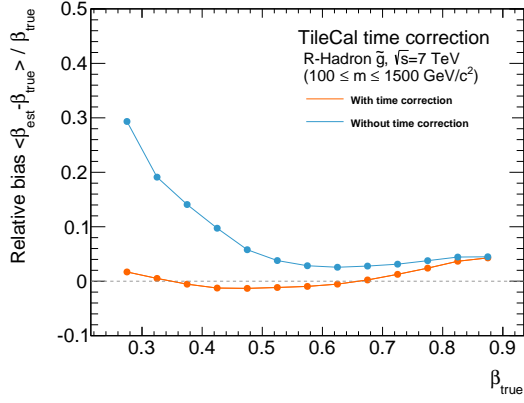
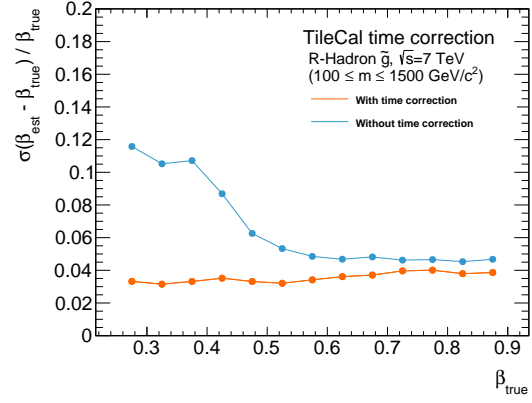
A track crossing one of the larger cubic calo cells in Figure 8.1 is assumed to have its time and distance measured relative to the cell centre as the smaller and projective cells. This introduces the visible systematic bias in Figure 8.12 when plotting the β -resolution as a function of the pseudorapidity for each cell.

Figure 8.12: Beta-resolution variation due to geometry (muons).



The variation shown in Figure 8.12 is around 10% for the largest cells. As with the time drift in the preview section, the cell size bias is correctable with a per-cell fit. To implement the correction, each individual cell in the $r - z$ plane is fitted by a polynomial that then supplies a correction to the nominal β estimate. The procedure is similar to the one introduced in the previous section. Each cell is slice-fitted with a Breit-Wigner function to reduce the 2D histogram to a set of data-points. As the cells gradually develops the bias, only cells with a linear correlation $\rho > 10\%$ between $(\beta_{est} - \beta_{true}) / \beta_{true}$ and η are fitted.

Figure 8.14 shows a cell fit. The resulting fit parameters along with a validity range defined by the RMS of the distribution is saved to a YAML lookup table that can be read by the analysis code. For a linear relationship


 (a) Relative bias in β .

 (b) Relative β -resolution.

the corrected β is then computed from the two fit parameters a and b

$$\beta_{\text{corr}} = \frac{b d_{\text{cell}}}{(-a + b + \eta)(c t + d_{\text{cell}})}. \quad (8.14)$$

For a second degree polynomial fit the resulting corrected β is

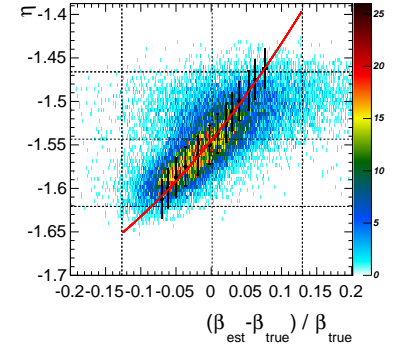
$$\beta_{\text{corr}} = \pm \frac{d_{\text{cell}} \left(\sqrt{4\eta k - 4ak + b^2} \mp b + 2k \right)}{2(ct + d_{\text{cell}})(\eta - a + b - k)} \quad (8.15)$$

where a , b and k are the three parameters.

8.6.1 η correction result

The η correction mainly affects the outer cells in the extended barrel. As $|\eta| \sim 1/m$ for heavy particles the massive R-Hadrons in this study tend to be detected in the central region. Staus and muons on the other hand receive a correction as their lower masses opens the phase space to the extended barrel. This means that muon-R-Hadrons separation is improved by the correction, while the effect on the R-Hadrons themselves are moderate. The effect of η correction on the overall $\Delta\beta/\beta_{\text{true}}$ resolution is plotted in Figure 8.18 for R-Hadrons and muons. The effect of fitting a 1 or 2-degree polynomial is studied to give a relative improvement on $\Delta\beta/\beta_{\text{true}}$ for muons of 10% for 2-degree relative to 1-degree fits.

Figure 8.13: Relative bias and resolution for the corrected and default estimators.


 Figure 8.14: A CaloCell in the process of being fitted. $\rho = -0.62$

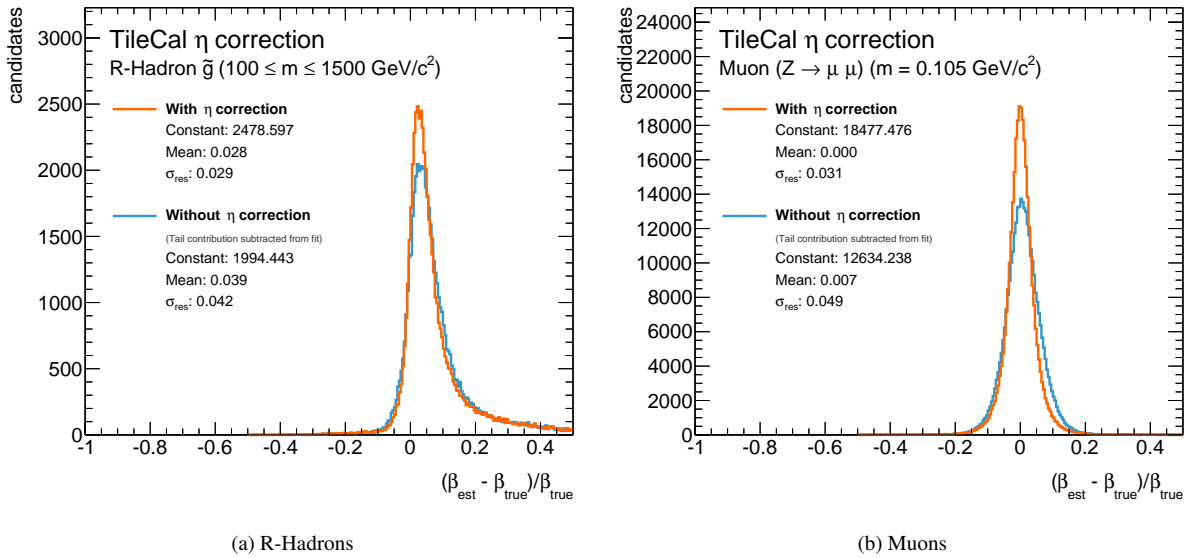


Figure 8.15: The result from the η correction in the inclusive case with both corrected and uncorrected cells contributing to the β -estimate.

The cells that benefits from the fitting procedure are all the ones that have an appreciable entry surface pointed towards the IP (Figure 8.16). The variability in η is proportional to a relative time offset compared with the trigger time. A way to quantify the need for correction is to look at the correlation between $\Delta\beta/\beta_{true}$ and η for the individual cells. Figure 8.19 show this correlation for cells in $z-r$ space. The cells in the central region of the detector are largely uncorrelated except for large cells in the outermost layer. The largest correlations are found in the extended barrel where some Calo-Cells have correlations $\rho > 80\%$. The two $\eta - \Delta\beta/\beta_{true}$ distributions in Figure 8.17 visually show the corrections applied, in this case to the muons in the $Z \rightarrow \mu\mu$ sample.

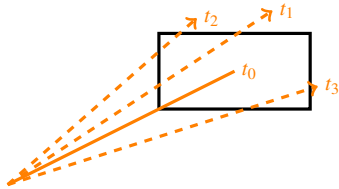
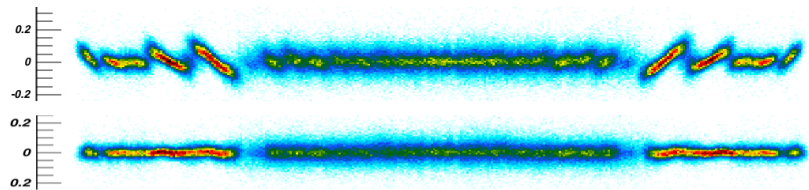


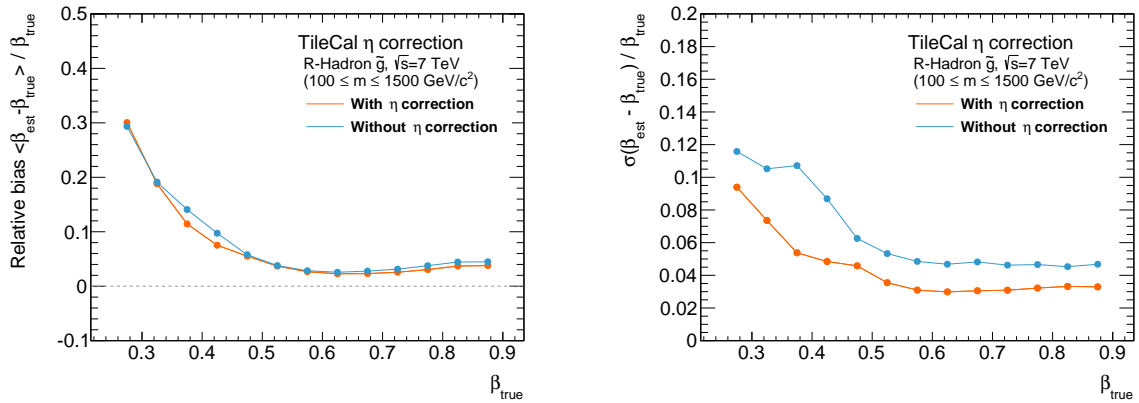
Figure 8.16: A calo cell with an extended area of entry will break with the assumption that the detection time is measured for a particle entering at the centre of the cell (t_0).

8.7 Combined result

The two corrections are complementary as the time corrections affects very slow particles that tend to be produced centrally while the η correction is mainly relevant in the forward regions where lighter and hence faster particles are detectable.

Figure 8.17: η correction. Before and after application. The plotted particles are muons from $Z \rightarrow \mu\mu$ simulations. The scale on the x-axis is pseudorapidity η and the y-axis is $(\beta_{est} - \beta_{true})/\beta_{true}$.





(a) Relative bias in β .

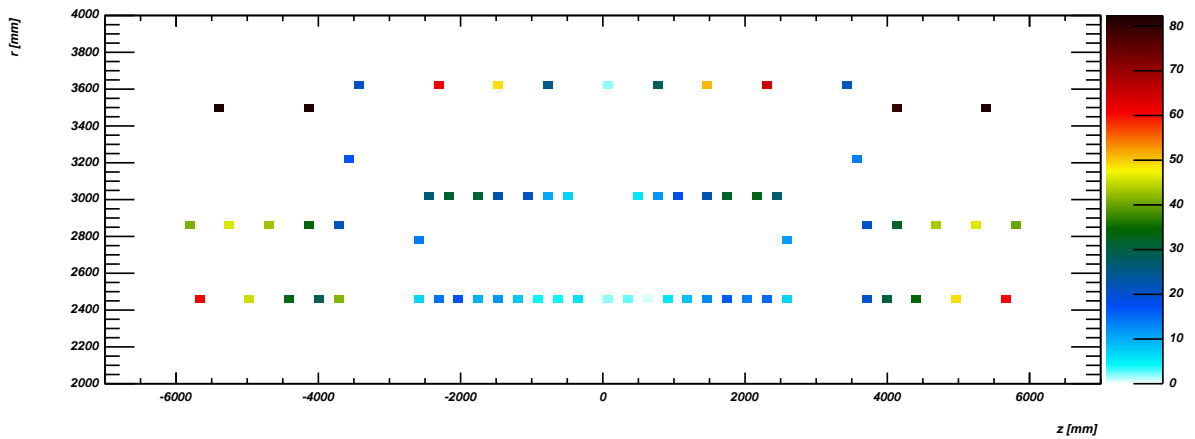
(b) Relative β -resolution.

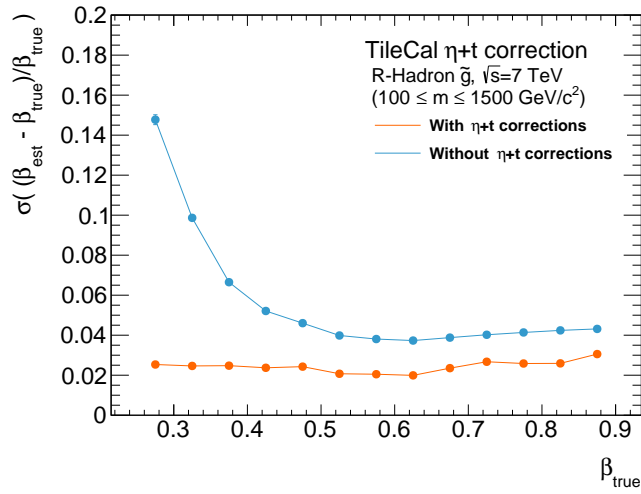
8.8 Summary

Two corrections to the Tile based ToF estimator has been introduced. The combined effect is illustrated by the resolution curves in figures 8.20. Overall β resolutions have in some cases improved by a factor of 2 or more. The time correction enables unbiased β estimates at $\beta \sim 0.2$ where up to 60% biases had been observed previously. The improvements have not been applied to any searches so far but could be applied to the 2012 run not yet published by ATLAS or future searches at nominal collision energies (Chap. 10).

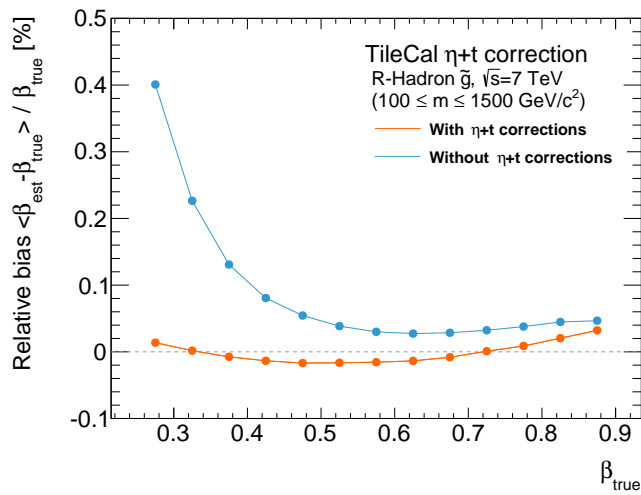
Figure 8.18: Relative bias and resolution for the corrected and default estimators.

Figure 8.19: Linear correlation coefficients (in per cent) for the TileCal. Note that all cells are anti-correlated but plotted as $|\rho| = |\text{corr}(\Delta\beta/\beta_{true}, \eta)|$ to give a sensible colour gradient.

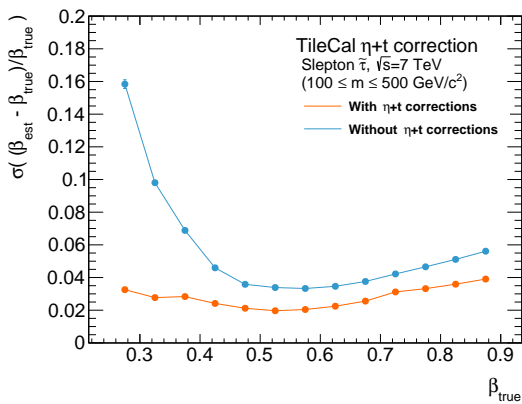




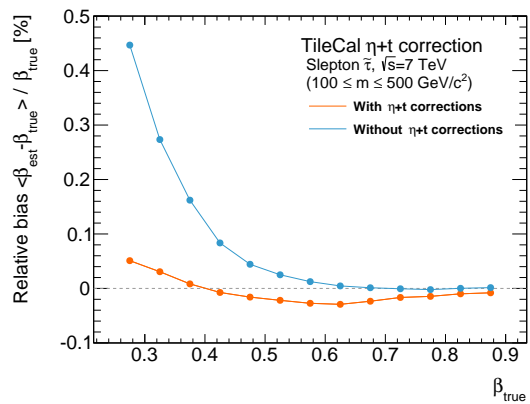
(a) R-Hadron β -resolution



(b) R-Hadron β -bias

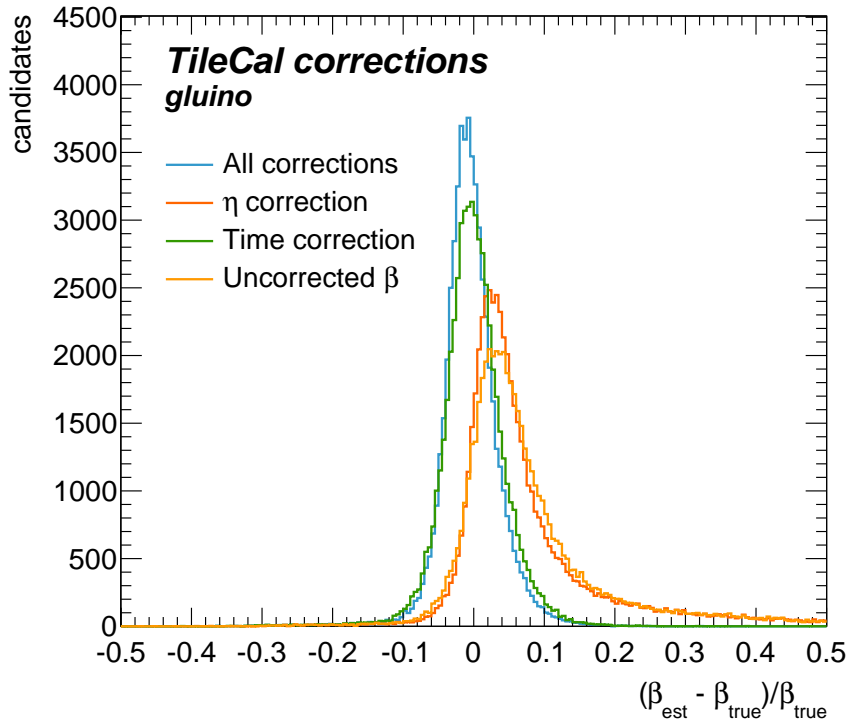


(c) Slepton β -resolution

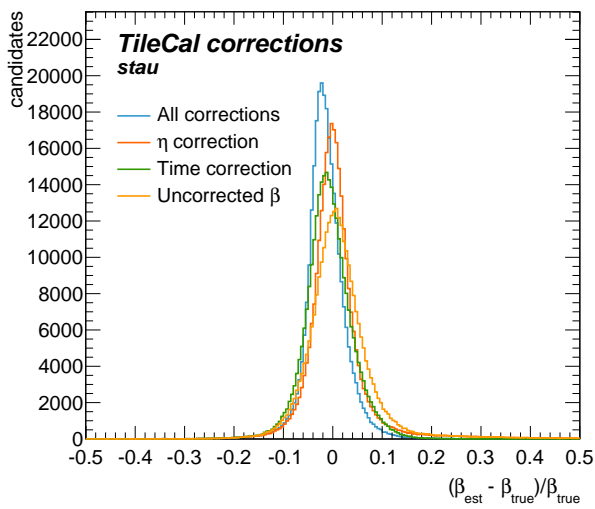


(d) Slepton β -bias

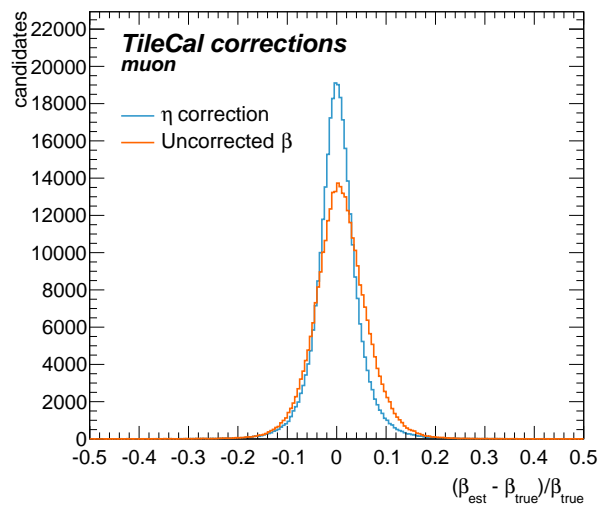
Figure 8.20: Combined correction result.



(a) R-Hadrons



(b) Sleptons



(c) Muons, showing only η -correction due to zero effect from the time correction.

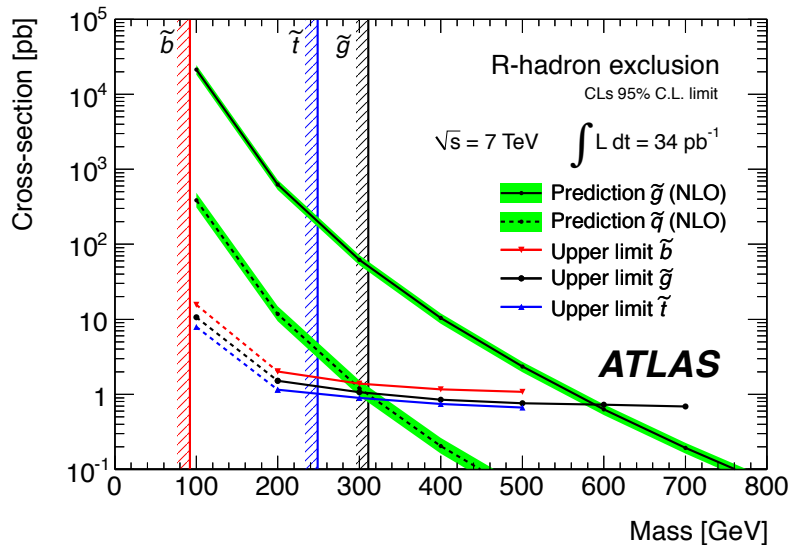
Figure 8.21: Effects of the corrections presented in this chapter on R-Hadrons, sleptons and muons.

9 *Search for long-lived coloured particles in ATLAS with 2011 LHC data*

This chapter describes the second search for coloured long-lived particles conducted with the ATLAS detector. Data-taking took place during 2011 where $\mathcal{L} = 4.7 \text{ fb}^{-1}$ proton-proton collisions were recorded at 7 TeV centre of mass energy. A general motivation for such a search is given in Section 3. Signal samples, background samples and collision datasets are listed in Section 9.2. The decision on physics trigger is explained in Section 9.3. The event selection is found in Section 9.4, a background estimation technique we used is explained in Section 9.5. Systematic uncertainties, statistical interpretation and Results from the event selection are found in Sections 9.6, 9.7 and 9.8 respectively. Finally the chapter is concluded in Section 9.9 where upper limits on production cross sections are found.

In Chapter 10 the result is presented in the context of ‘Split-Supersymmetry’ (SSUSY), where specifically Figure 10.7 summarises this work and show the future reach of ATLAS searches for SSUSY gluinos.

Figure 9.1: Previous ATLAS limits on long-lived coloured particles.



9.1 Introduction

Searching for coloured long-lived particles is a specific sub-set of searches for long-lived charged particles at colliders and elsewhere. Multiple models (Chap. 3) predict coloured LLPs and a search for such particles are especially motivated at the LHC as it is a hadron collider giving a great potential increase in production cross sections for such objects.

The search is an evolution of our previous search [105] with the first LHC dataset from 2010 conducted on $\mathcal{L} = 34 \text{ pb}^{-1}$ of data. The upper limits from that search are shown in Figure 9.1 at that time we found a lower limit on long-lived gluino production at $586 \text{ GeV}/c^2$. Searches for Supersymmetry are in general be defined by multiple parameters and two overall mass scales $m_{1/2} = \tilde{m}$, m_0 denoting sfermions and sbosons. Our search is vastly simplified, as we simply remove the possibility of particle decay, introduced in SUSY as having a mass scale for the possible decay products so far away in mass scale that the decay is effectively prohibited by limited phase-space. This means that the actual analysis is greatly simplified as we consider that primary LLP stable throughout the ATLAS volume. It also means that placing specific limits on SSUSY is complicated as we don't make a specific assumption on the high-mass scale that regulates the life-time of the gluino. In Chapter 10 I will nevertheless try to estimate an overall exclusion range for SSUSY based on our implicit assumptions and complementary results from the Higgs boson discovery. The effective model we use when generating Monte Carlo signal samples is based on the production of MSSM gluinos, but with a ad-hoc particle spectrum similar to the one in Figure 9.2 where the sfermions are prohibiting gluino decay.

After event generation the stable gluinos are propagated through ATLAS with a custom Geant 4 module that simulates how a massive coloured particle might hadronise into R-Hadrons and undergo hadronic interactions in dense material. The effect of having a penetrating particle akin to a muon but with much higher mass and colour leads to interesting consequences for track

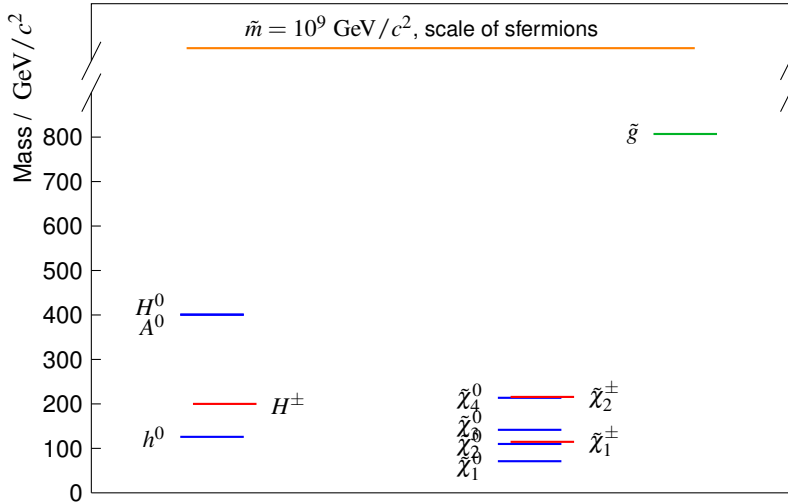


Figure 9.2: A Split-SUSY Spectrum with a Higgs at $125.9 \text{ GeV}/c^2$ and a gluino at $m = 800 \text{ GeV}/c^2$. All sfermions are retained at the GUT scale $\tilde{m} = m_{GUT}$. The gluino is long-lived in this model as its only decay mode is sfermionic which is kinematically prohibited by the large mass difference between $m_{\tilde{g}}$ and \tilde{m} .

reconstruction and specific energy loss estimates as the particle can turn neutral in mid-range, acquire double electric charge or simply flip the charge sign all due to colour conservation (see Sec. 2.3). Except for calorimeter dE/dx which is directly sensitive to these effects, it leads to momentum smearing and acceptance loss. The probability of hadronic interaction increases as the particle traverses the calorimeter systems, that is why we have three distinct search strategies which relies on progressively more of the outer ATLAS detector. The three strategies are termed: Inner detector only (ID-Only), ‘Muon Spectrometer Agnostic’ (MS-Agnostic) and ‘Full Detector’ (Full). The ID-Only analysis relies solely on the silicon trackers for momentum and particle identification, while the MS-Agnostic also includes Time-of-Flight from the calorimeter systems. The full detector search allows for muon-spectrometer reconstructed tracks as well which with its longer lever arm gives a better ToF estimate than the MS-Agnostic, but with higher probability of charge flip also further charge confusion for track and momentum reconstruction. My work has focused on the two inclusive searches involving the outer detectors systems as well as the inner trackers, and I will not describe the ID-Only search further, but the result is included in Figure 10.7.

The search for LLPs in ATLAS poses multiple challenges. The collision rate at the LHC defines the read-out rate of the detector systems which are tuned to measure highly relativistic particles within a collision frame of 25 ns. For a massive long-lived particle it takes a finite time ($t = \gamma d / (c\beta)$) to reach a detector system a distance d away, where t becomes longer the closer the particle mass approaches the centre of mass energy. In general ATLAS is not designed to do direct particle identification on other than Standard Model particles. That is why we have designed estimators ourselves based on low-level information from detector subsystems. As most of the reconstructed objects in ATLAS are calibrated at high-level, information such as raw timing from each calorimeter measurement is not very precise, and we have designed calibration routines for this kind of information. Also triggering on LLPs is a challenge as no tracking information is available at the trigger decision time. Instead we rely on indirect event topological information. Lastly tracking is in general difficult at very high momentum and the

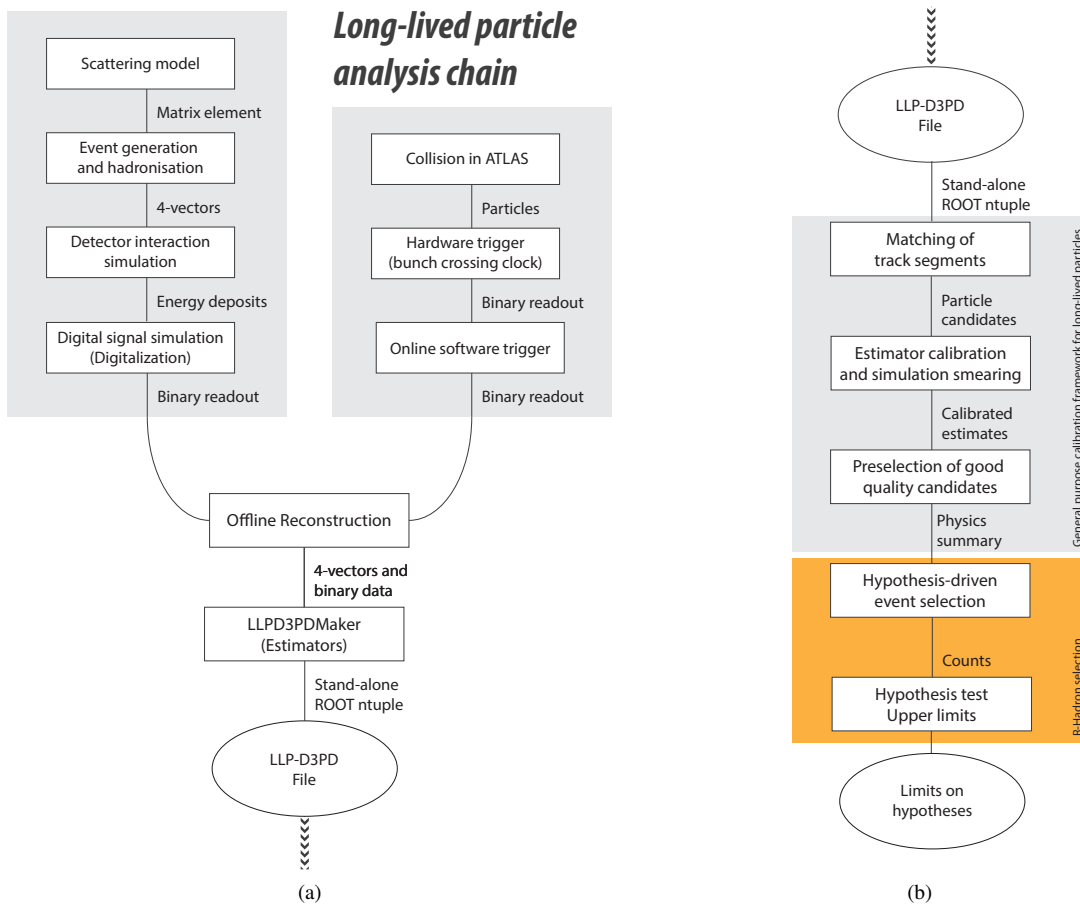


Figure 9.3: A schematical overview of the analysis procedure. Part (a) are produced within the ATLAS framework and part (b) is based on a standard-alone data format produced as the end product of (a).

possible charge flipping does not help in that matter either. As a result of these challenges much of the actual work happens before the final physics analysis, but when that finally takes place the only background is due to mis-reconstructed particles.

The direct signature of LLPs are either one or two particles with anomalously long ToF, high dE/dx and high momentum. In case of a discovery of a new massive LLP a further ‘quantum leap’ in dE/dx between measurements corresponding to the $dE/dx \sim q^2$ dependence on dE/dx in (4.14) would signify that it is a coloured LLP or *R-Hadron*. Besides the trigger selection our analysis strategy utilises precise dE/dx and ToF that will be developed in the coming sections.

As schematic overview of the entire analysis is shown in Figure 9.3.

9.2 Data and Simulated samples

9.2.1 Signal Samples

In SSUSY only the gluino is stable, but to allow for a wider search also samples of stable stops and sbottoms where produced. The production mechanism in all cases are based on SUSY MSSM where all particles except the one under study are decoupled by placing their masses at multiple TeVs, forcing the particle to be long-lived.

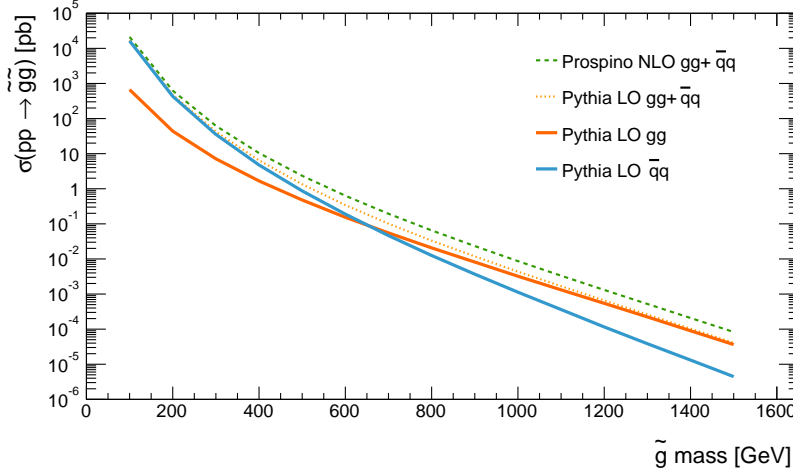


Figure 9.4: Gluino pair production cross section at $\sqrt{s} = 7$ TeV, notice the overlapping of gg and $q\bar{q}$ production around 600 GeV.

The underlying structure of protons (Sec. 5.1.1) complicates the production channels which for squarks and gluinos at leading order are [16]

$$\tilde{q}\tilde{q} \text{ production: } q_i + \bar{q}_j \rightarrow \tilde{q}_k + \tilde{q}_l \quad (9.1)$$

$$g + g \rightarrow \tilde{q}_i + \tilde{q}_i \quad (9.2)$$

$$\tilde{q}\tilde{q} \text{ production: } q_i + q_j \rightarrow \tilde{q}_i + \tilde{q}_j \quad \text{and c.c.} \quad (9.3)$$

$$\tilde{g}\tilde{g} \text{ production: } q_i + \bar{q}_j \rightarrow \tilde{g} + \tilde{g} \quad (9.4)$$

$$g + g \rightarrow \tilde{g} + \tilde{g} \quad (9.5)$$

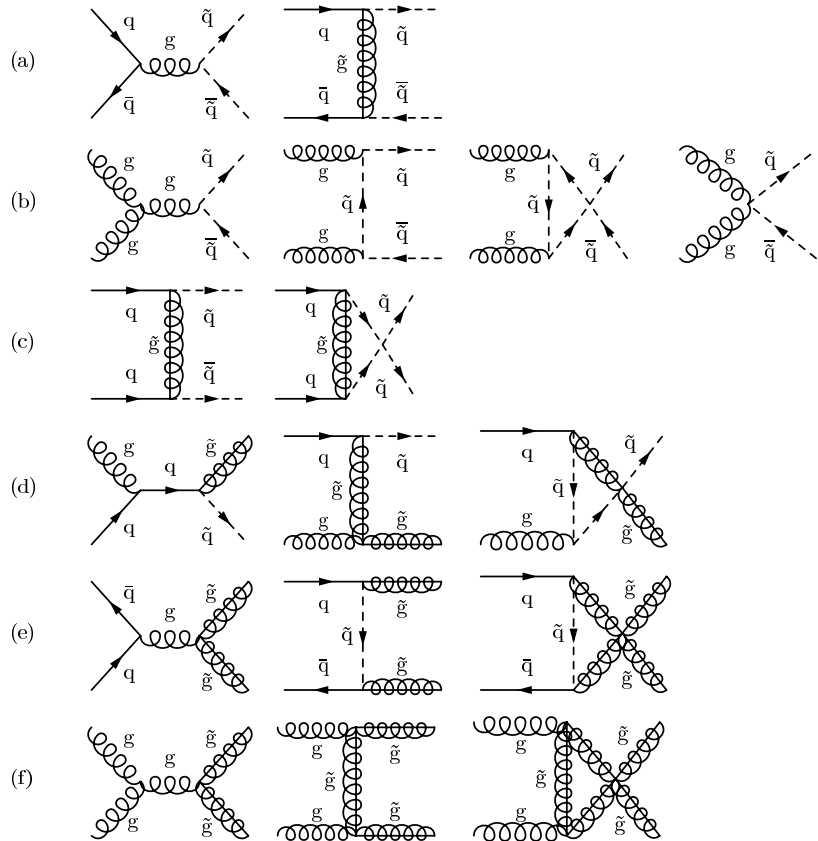
$$\tilde{q}\tilde{g} \text{ production: } q_i + g \rightarrow \tilde{q}_i + \tilde{g} \quad \text{and c.c.} \quad (9.6)$$

Both squarks and gluinos are produced in strong interactions with their production cross sections mainly depending on their masses (Figure 9.4). At high masses compared to the collision energy the momentum fraction needed to produce the particles is high and the production is most likely dominated by valence quark interactions. At lower masses and hence lower required momentum fraction the gluon density dominates the proton PDF and gluon fusion is the primary production mode. The $q\bar{q}$ production diagrams (e) in Figure 9.5 will increase the total cross section depending on the squark mass and are therefore very model dependent [66], due to this, the gluino samples are generated as two independent samples one with $q\bar{q} \rightarrow \tilde{g}\tilde{g}$ and one with $gg \rightarrow \tilde{g}\tilde{g}$ production, allowing us to study the contributions independently. We also ignored any single-particle production modes such as (9.6) and diagram d.3 in Figure 9.5 for the same reasons.

The production was done with Pythia 6.403 [93] integrated into the ATLAS production framework. The primary particles are kept stable artificially ‘by hand’ in Pythia and the remaining sparticles have their masses set at 4 TeV to avoid interference.

After the creation of the sparticles they are hadronised in Pythia allowing the formation of R -Hadrons comprised of the heavy sparton and a Light Quark System (LQS). The hadronic final-states in general takes the forms C_3qq , $C_3q\bar{q}$, C_8qqq , C_8g , where C_3 and C_8 represent a massive colour triplet or octet respectively [67]. Any other combination is excluded by QCD. The fraction of charge-neutral gluino-gluon bound states ($C_8g = \tilde{g}g$) is set as an

Figure 9.5: Quark and gluino production at the LHC. Squarks are produced in (a), (b), (c) and (d) and gluinos in (d), (e) and (f). In SSUSY only diagrams (e) and (f) are relevant. Sources: [67, 16].



ad hoc parameter, where we conservatively choose 10% based on advice from the author of PYTHIA [92]. This fraction is one of the underlying assumptions in this analysis as it translates into the probability of generating a neutral R-Hadron state undetectable with our search strategy.

9.2.2 Cross sections

The search for LLPs itself does not depend on specific production cross sections per se, but in order to gauge the sensitivity of the analysis and for further interpretation we have calculated MSSM cross sections assuming a decoupled mass scale with PROSPINO 2.1 [17] and FAST-NLL. PROSPINO is a next-to-leading-order (NLO) SUSY cross section calculator for hadron colliders. FAST-NLL is program that calculates supersymmetric QCD corrections and resummation of soft gluon emission at next-to-leading-logarithmic (NLL). Uncertainties on the total cross sections are calculated by prescription from the PDF4LHC group [26] and is done based on ATLAS SUSY Group recommendations. Two distinct PDF sets (CTEQ6.6AS and MSTW2008) are applied and varied. CTEQ is varied within its 1σ uncertainty to account for α_s -variations, and both PDFs are varied to account for renormalisation and factorisation scale uncertainties. The uncertainties due to these varia-

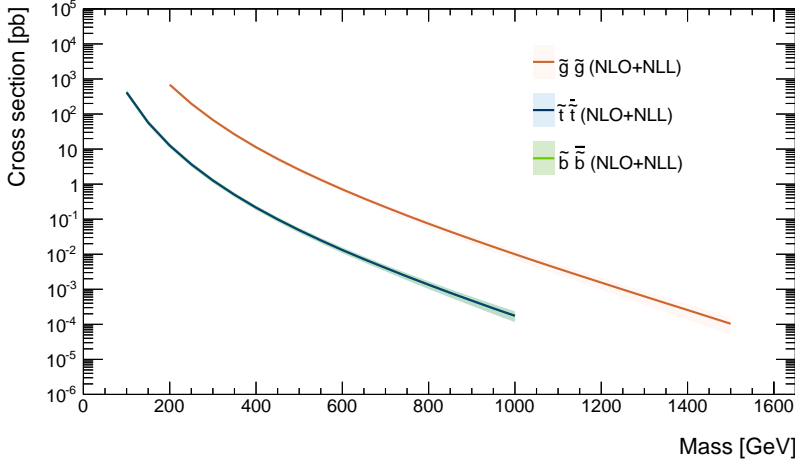


Figure 9.6: Production cross sections for $\tilde{g}\tilde{g}$ and $\tilde{q}\tilde{q}$ where \tilde{t} and \tilde{b} squarks are produced at virtually the same cross section. The cross sections are produced assuming MSSM with PROSPINO 2.1 at next-to-leading order, with soft gluon emission resummation at next-to-leading-log calculated with FAST-NLL. The uncertainties on the plot are calculated by varying the PDF, renormalisation and factorisation scales as described below.

tions are combined as

$$\begin{aligned}
 CTEQ_{error_{up}} &= \sqrt{cte q_{PDF_{up}}^2 + cte q_{scale_{up}}^2 + \alpha_{S_{up}}^2} \\
 CTEQ_{error_{down}} &= \sqrt{cte q_{PDF_{down}}^2 + cte q_{scale_{down}}^2 + \alpha_{S_{down}}^2} \\
 MSTW_{error_{up}} &= \sqrt{mstw_{PDF_{up}}^2 + mstw_{scale_{up}}^2} \\
 MSTW_{error_{down}} &= \sqrt{mstw_{PDF_{down}}^2 + mstw_{scale_{down}}^2} \\
 A &= \max(CTEQ + CTEQ_{error_{up}}, MSTW + MSTW_{error_{up}}) \\
 B &= \min(CTEQ - CTEQ_{error_{down}}, MSTW - MSTW_{error_{down}})
 \end{aligned}$$

And the cross section is then a midpoint average of the largest variations,

$$\sigma = 0.5(A + B) \pm (A - B)/(A + B) \text{ [pb]}. \quad (9.7)$$

The produced cross sections with uncertainties are shown in Figure 9.6.

9.2.3 Expected particle yield

From the cross sections in Figure 9.6 we can make an estimate of the event yield in our 2011 dataset shown in Table 9.1.

9.2.4 Detector simulation

After event generation the propagation of the R -Hadrons are simulated in Geant 4 with a special package designed to handle interactions of the Light Quark System (LQS) with matter. Depending on the LQS configuration the R -Hadron can be charged and will interact electromagnetically in the same manner as described in Sec. 4.1.2. Being a hadron the bound state can also undergo nuclear interaction that is modelled [71] by letting the LQS interact with a geometric cross section at similar scale as $\pi - p$ scattering (see Figure 4.13). The heavy sparton itself is ignored in these interactions as its de Broglie wavelength falls as $1/M^2$ and hence contributes negligible to the overall hadronic interaction cross section. Instead the sparton acts like a kinetic energy carrier for the R -hadron.

Table 9.1: Expected number of \tilde{g} R-Hadrons in the simulated signal samples in Table 9.2, based on the cross sections in Figure 9.6.

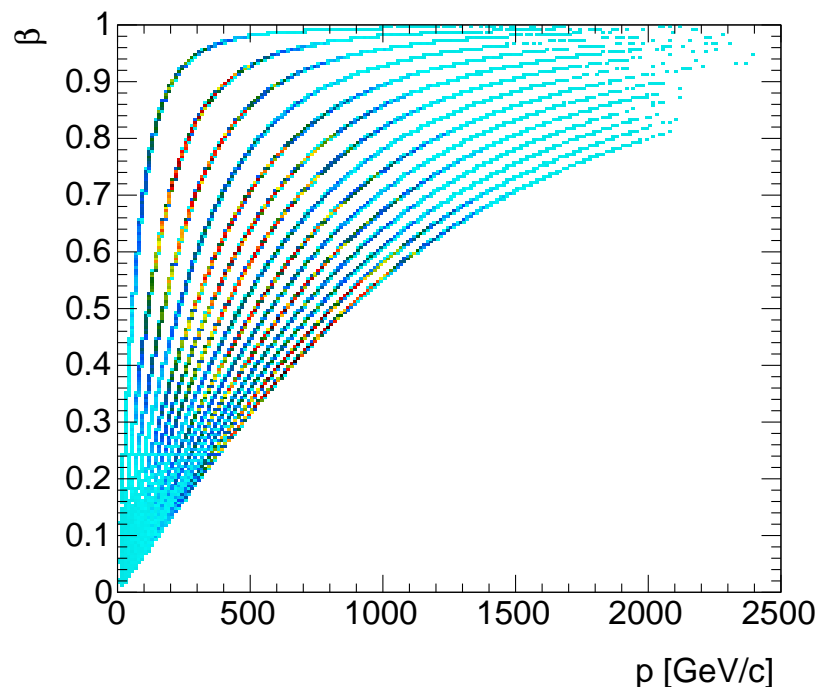
\tilde{g} Mass GeV/ c^2	σ [pb]	Events/ fb^{-1}	Events 2011 $\int L dt = 4.7fb^{-1}$	Equivalent integrated luminosity (gg) [fb^{-1}]	($q\bar{q}$) [fb^{-1}]
100	21200	2120000	9964000	0.000306753	0.00748963
200	625	625000	2937500	0.02323	0.114029
300	62.1	62100.	291870.	0.282667	0.701148
400	10.4	10400.	48880.	1.05041	2.99783
500	2.34	2340.	10998.	11.5174	10.4567
600	0.634	634.	2979.8	52.8274	32.4615
700	0.194	194.	911.8	215.878	90.7328
800	0.0651	65.1	305.97	398.341	241.611
900	0.0233	23.3	109.51	2713.17	612.626
1000	0.00867	8.67	40.749	4424.72	1553.68
1100	0.00333	3.33	15.651	27629.4	7587.25
1200	0.00131	1.31	6.157	43308.3	18404.
1300	0.000522	0.522	2.4534	129904.	44810.2
1400	0.000208	0.208	0.9776	760282.	111257.
1500	0.000083	0.083	0.3901	2.25232×10^6	274731.

9.2.5 Expectations from the signal samples

Based on the signal models alone we can make a series of preliminary observations not specific to ATLAS. One category concerns the purely kinematical distributions and another the underlying phenomenology due to nuclear interactions of the LQS, information on both can help guide our search strategy.

Kinematics The dominant signature of LLPs at colliders are their tendency to be moderately relativistic compared with the highly relativistic Standard Model secondaries otherwise observed directly.

Figure 9.7: Momentum for gluino masses ranging from 100 to 1500 GeV. We see that as the invariant mass increase, the phase space contracts. The lines are histograms where the colour scale indicates the probability density of each $\beta - p$ point in the signal samples (Table 9.2).



In figures 9.7 we see the relationship between momentum and speed at $\sqrt{s} = 7$ TeV for R-Hadrons produced with masses between 100 and 1500

GeV. As can be seen from the figures R-Hadrons with masses $m_{\tilde{g}} \sim 100 \text{ GeV}/c^2$ have enough phase space to be fairly relativistic with Lorentz factors up to $\gamma \sim 15 - 20$. As the mass approaches the production threshold for pair production the phase-space contracts and at $m_{\tilde{g}} \sim 1500 \text{ GeV}/c^2$ we seldom see boosts of more than $\gamma \sim 2$. These observations have consequences for our hope of utilising specific energy loss as a speed estimator, at $\gamma > 3$ we know from (4.14) that a particle is minimum ionising and we have lost our discrimination power against SM particles, which can also be seen in Figure 9.13 when looking at the $m_{\tilde{g}} = 100 \text{ GeV}/c^2$ mass bin.

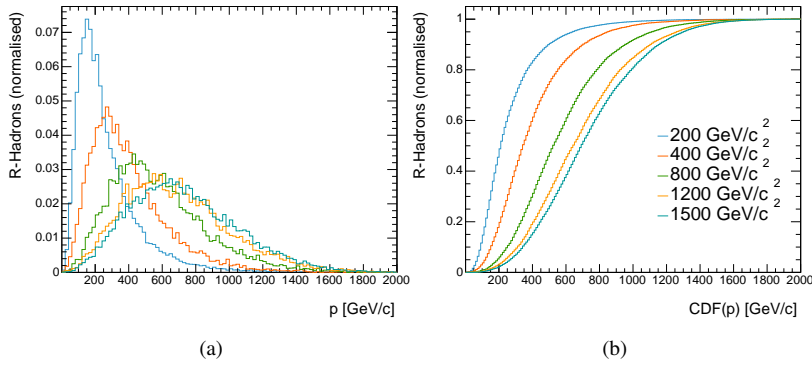


Figure 9.8: Momentum spectra for selected gluino samples.

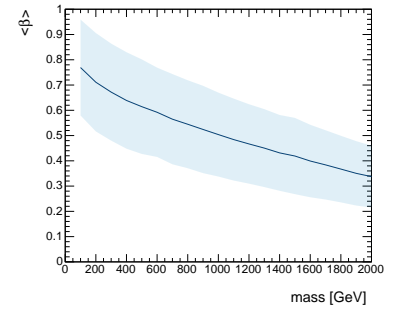


Figure 9.9: Average speeds at production for gluinos at $\sqrt{s} = 7 \text{ TeV}$. Produced with Pythia 8. The spread represents the RMS.

Luckily the low masses are extremes, as we can see in Figure 9.9 at masses larger than $m_{\tilde{g}} = 400 \text{ GeV}/c^2$ the speed is distinctly less than c even accounting for the kinematic spread shown as the shaded region. At low speeds we could worry that the acceptance in ATLAS is limited by the bunch spacing which leaves an event window between 50 and 25 ns for each collision, a $1 \text{ TeV}/c^2$ particle with an average speed of $\beta \sim 0.5$ will manage to move 4.3 m in 25 ns or twice that in 50 ns, enough to reach the calorimeters but not necessarily the muon spectrometer, if the particle is produced in a forward direction. That leads us to the production angles. As we would expect by the decreasing phase space at high masses, the production become gradually more central at high masses. In figures 9.10 we see that more than 90% of the events falls within the $|\eta| < 2.5$ tracking detector acceptance of ATLAS.

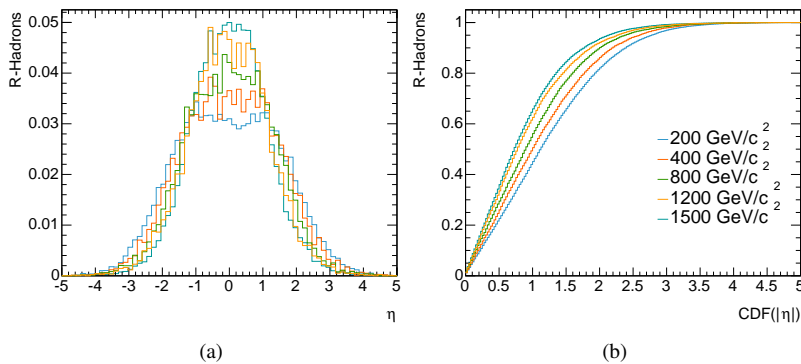


Figure 9.10: Pseudo-rapidity for a selected set of gluino samples.

'R-baryogenesis' Earlier studies [71] show some characteristic features of coloured massive particles with an additional conserved quantum number (R-parity, KK-parity). One interesting observation is that meson states have a chance of acquiring a baryon number. It was found that 90% of all meson- \tilde{g} states have converted to a baryon state after traversing 1 m of iron, Figure 9.11 shows the conversion fraction as a function of penetration depth. The reverse process of converting baryons into mesons is disfavoured based on the interaction probability and in general due to kinematics [67].

Figure 9.11: (a) Baryon fraction, (b) energy lost due to a single hadronic interaction for a $m = 300 \text{ GeV}/c^2$ gluino (solid line) and stop (dashed). The toy models are irrelevant in this context (Ref. [71]).

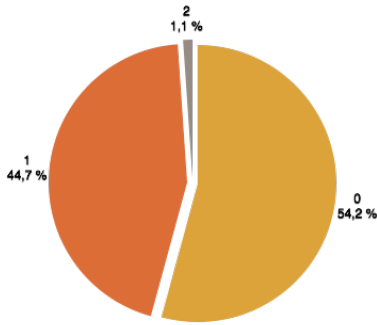
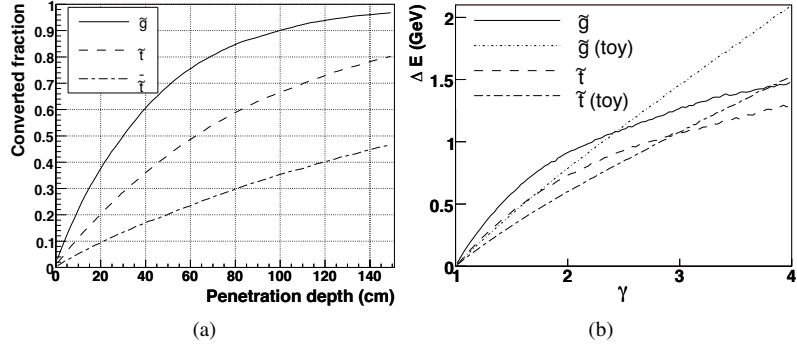


Figure 9.12: Charge distribution of R-Hadron final states

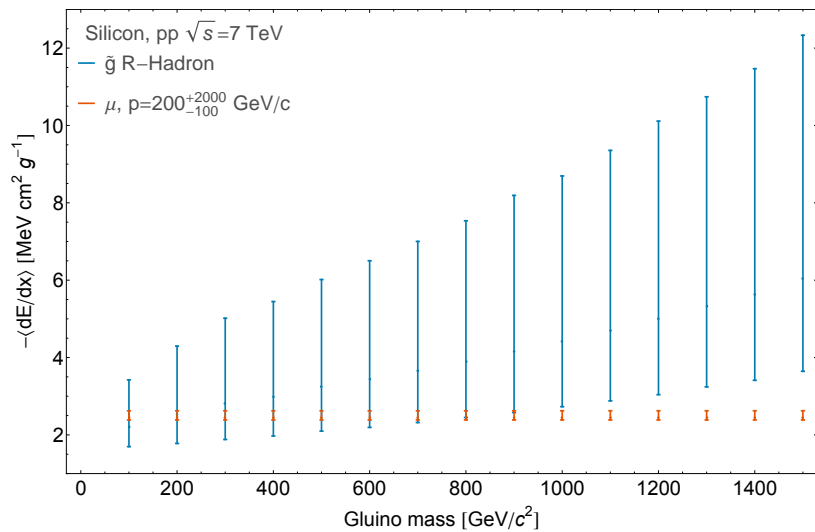


Apart from the baryophile tendencies of R-hadrons, we also note that a substantial fraction of the produced R-Hadrons are neutrals. The fraction found with Pythia 8 is summarised in Figure 9.12 for gluinos.

Hadronic energy loss During hadronic interaction the amount of deposited energy scale with the kinetic energy of the heavy sparton as can be seen from Figure 9.11b, at $\sqrt{s} = 7 \text{ TeV}$ the hadronic energy loss for $m > 500 \text{ GeV}$ is around 1 GeV per interaction.

Electromagnetic energy loss Ionisation loss is one of our primary identification methods. Based on the velocity profile in Figure 9.9 we expect a mean specific energy loss above the MIP level as illustrated in Figure 9.13.

Figure 9.13: Expected mean ionisation loss. Mean values are calculated with (4.14) with the density factor applied. Velocity of R-Hadrons are calculated with Pythia 6, and the error bars represent a 1σ spread in β for each mass point if produced at $\sqrt{s} = 7 \text{ TeV}$ (Effectively the width of the distributions in Figure 8.5 and similarly for the remaining mass points).



Tables of signal samples To summarise the Monte Carlo signal samples produced for this study the different samples have been listed in tables 9.2 and 9.3 below. The three scattering models: ‘generic’, ‘regge’ and ‘intermediate’ represent variations in how the R-Hadrons are thought to hadronically interact. The ID is an ATLAS specific label that is kept here for internal reference, it allows anybody to look up the actual generator configuration used to produce the sample through ¹.

¹<http://acode-browser2.usatlas.bnl.gov/lxr-rell16/source>

mass (GeV)		generic scattering		Regge scattering		intermediate scattering	
		ID	events	ID	events	ID	events
100	gg	114760	5k	114790	10k	114820	~10k
	$q\bar{q}$	118523	5k				
200	gg	114761	10k	114792	10k	114822	10k
	$q\bar{q}$	118524	~5k				
300	gg	114762	10k	114794	10k	114824	10k
	$q\bar{q}$	118525	5k				
400	gg	114763	5k	114796	5k	114826	10k
	$q\bar{q}$	118526	5k				
500	gg	114764	10k	114798	10k	114828	10k
	$q\bar{q}$	118527	5k				
600	gg	114765	10k	144235	10k	144240	10k
	$q\bar{q}$	118528	5k				
700	gg	114766	10k	144237	10k	144242	10k
	$q\bar{q}$	118529	5k				
800	gg	114767	5k	144239	10k	144244	~10k
	$q\bar{q}$	118530	5k				
900	gg	114768	10k	144240	10k	144241	10k
	$q\bar{q}$	118531	5k				
1000	gg	114769	5k	144241	10k	144242	10k
	$q\bar{q}$	118532	5k				
1100	gg	144215	10k	144242	10k	144243	5k
	$q\bar{q}$	144220	10k				
1200	gg	144216	5k	144243	10k	144244	~10k
	$q\bar{q}$	144221	10k				
1300	gg	144217	5k	144244	10k	144245	5k
	$q\bar{q}$	144222	10k				
1400	gg	144218	10k	144245	10k	144246	5k
	$q\bar{q}$	144223	5k				
1500	gg	144219	10k	144246	10k	144247	~10k
	$q\bar{q}$	144224	5k				

Table 9.2: Simulated gluino R-Hadron signal samples with a gluino-ball fraction of 10% and three different scattering models (generic, Regge, intermediate).

All samples have been fully simulated in Geant 4 with no fast parameterization applied due to the complicated detector response of these particles. After simulation a digitalisation process with little R-Hadron specific routines and general reconstruction was done. The output from reconstruction was further processed into the LLP3PD where low-level estimators such as Calorimeter ToF and dE/dx are calculated. The LLP3PD is a generic ROOT ntuple that allows us to run analysis on machines without our somewhat resource demanding ATLAS framework.

Table 9.3: Simulated stop and sbottom R -hadron signal samples for two different scattering models (generic, Regge).

mass (GeV)	stop		sbottom	
	generic scattering ID	events	Regge scattering ID	events
100	114850	10k	114860	20k
200	114851	10k	114861	20k
300	114852	10k	114862	20k
400	114853	10k	114863	20k
500	114854	10k	114864	20k
600			114865	10k
700			114866	10k
800			114867	~10k
900			114868	10k
1000			114869	10k

9.2.6 Background Samples

The considered background MC samples include di-jet and $W \rightarrow \mu\nu$ and $Z \rightarrow \mu\mu$ events generated with PYTHIA as well as (semi)leptonic $t\bar{t}$ and various single-top events generated with MC@NLO [51] + HERWIG/JIMMY [32]. An overview on the theoretical cross sections and the available statistics is given in Table 9.4. Note that the background estimation is completely data driven and does not rely on these samples.

Table 9.4: Simulated background samples used in this analysis.

sample	ID	events	xsec	lumi
QCD di-jets J0 (PYTHIA)	105009	446997	9.860 mb	4.533 μb^{-1}
QCD di-jets J1 (PYTHIA)	105010	314998	678.14 μb	0.464 nb^{-1}
QCD di-jets J2 (PYTHIA)	105011	336000	40.981 μb	8.198 nb^{-1}
QCD di-jets J3 (PYTHIA)	105012	129999	2.1931 μb	0.059 pb^{-1}
QCD di-jets J4 (PYTHIA)	105013	180999	87.707 nb	2.064 pb^{-1}
QCD di-jets J5 (PYTHIA)	105014	227996	2.3502 nb	97.01 pb^{-1}
QCD di-jets J6 (PYTHIA)	105015	99996	33.618 pb	2.974 fb^{-1}
QCD di-jets J7 (PYTHIA)	105016	167993	137.44 fb	1.222 ab^{-1}
QCD di-jets J8 (PYTHIA)	105017	269984	6.0987 ab	44.26 zb^{-1}
$W \rightarrow \mu\nu$ (PYTHIA)	106044	1600996	8937.9 pb	0.179 fb^{-1}
$Z \rightarrow \mu\mu$ (PYTHIA)	106047	1401994	855.25 pb	1.639 fb^{-1}
$t\bar{t}$ (semi)leptonic (MC@NLO)	105200	3801970	80.107 pb	42.376 fb^{-1}

9.2.7 Data Sample

The presented analysis was done with data recorded during proton-proton runs in 2011 at $\sqrt{s} = 7$ TeV. The total delivered amount of integrated luminosity was 5.61 fb^{-1} of we managed to record 5.25 fb^{-1} with ATLAS. Since this was the second year of LHC operation the accelerator was still under commissioning that meant changing beam conditions throughout the season. The instantaneous luminosity was gradually increased and by the end of the year a peak luminosity was reached at $3.65 \times 10^{33} \text{cm}^{-2}\text{s}^{-1}$ or about half of the nominal value at 14 TeV. Table 9.5 summaries each individual run period that in general are distinguished by changes to the overall beam configuration. Two of the columns that are especially relevant for our

analysis are μ_{\max}^{avg} the average maximum number of simultaneous collisions per bunch-crossing, or *pile-up* and the bunch spacing Δt that is the amount of time between each collision. Pileup has detrimental effects on our PID estimators as low-level energy readings polluted by a stray particle crossing a calorimeter cell within the same readout window as a candidate track can increase dE/dx by a MIP or throw off the measurement time. This kind of contamination is avoided by discarding overlapping tracks, but it is potentially a problem if the pileup events are not reconstructed. The bunch spacing was mentioned in Sec. 9.2.5 and is one of our main motivations for a Muon spectrometer-‘agnostic’ search that avoid relying on the outer layers of ATLAS for triggering.

Period	Date Range	Run Range	Stable / Ready Lum [fb ⁻¹]	Max. Inst. Lum [10 ³⁰ cm ⁻² s ⁻¹]	μ_{\max}^{avg}	Fill Range	Bunch Count	Bunch Δt [ns]
A	Mar-13 - Mar-21	177531 - 177965	9 / 8.7 (97%)	158	7.3	1613 - 1640	3 - 138	75 - 2500
B	Mar-21 - Mar-24	177986 - 178109	18 / 18 (97%)	249	9.2	1642 - 1647	138 - 194	75
D	Apr-14 - Apr-29	179710 - 180481	188 / 185 (98%)	719	7.6	1710 - 1746	214 - 598	50
E	Apr-30 - May-03	180614 - 180776	54 / 52 (98%)	841	7.8	1748 - 1756	598 - 700	50
F	May-15 - May-25	182013 - 182519	162 / 158 (97%)	1113	8.1	1783 - 1807	14 - 874	50 - 1250
G	May-27 - Jun-14	182726 - 183462	580 / 572 (99%)	1278	8	1809 - 1868	874 - 1042	50
H	Jun-16 - Jun-28	183544 - 184169	291 / 286 (98%)	1278	6.9	1870 - 1902	1041 - 1318	50
I	Jul-13 - Jul-29	185353 - 186493	423 / 411 (97%)	1913	9.2	1936 - 1991	2 - 1331	50 - 2500
J	Jul-30 - Aug-04	186516 - 186755	244 / 240 (98%)	2023	9.8	1992 - 2002	1317	50
K	Aug-04 - Aug-22	186873 - 187815	695 / 684 (98%)	2356	11	2002 - 2040	1317	50
L	Sep-07 - Oct-05	188902 - 190343	1653 / 1621 (98%)	3295	16	2086 - 2183	250 - 1318	50
M	Oct-06 - Oct-30	190503 - 191933	1202 / 1174 (98%)	3896	19	2185 - 2268	2 - 138	25 - 8000
Total	Mar-13 - Oct-30	177531 - 191933	5521 / 5408 (98%)	3896	19	1613 - 2268	2 - 1380	25 - 5000

The LHC was not the only part of the experiment that changed during the year. ATLAS itself being a complex system also had varying efficiencies as subsystems failed and where repaired. To account for changing detector conditions a system was introduced to make it easier to quantify defects and define periods where data was of ‘analysis grade’, depending on what systems where required by a specific analysis. The ATLAS Data Quality team compiles all defects reported by the individual sub system’s experts and generates a ‘good run list’ (GRL), that specifies in 2 minute intervals when the detector delivered reliable data.

This list is in XML format (Figure 9.14) that can then be read during analysis to skip events if flagged as bad. Another use of these GRLs is to

Table 9.5: Generously lifted from Mortiz Backes 2013

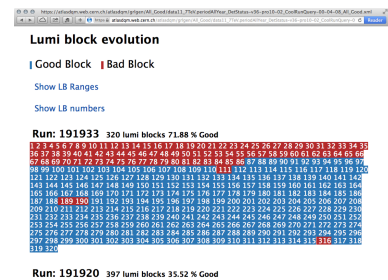


Figure 9.14: Visual representation of an XML ‘Good Run List’. Any given run is divided into Lumi Blocks 2 minutes in duration. Based on detector conditions, each block can be flagged as either fit or unfit for analysis use. The view was made with Javascript and XSLT by the author.

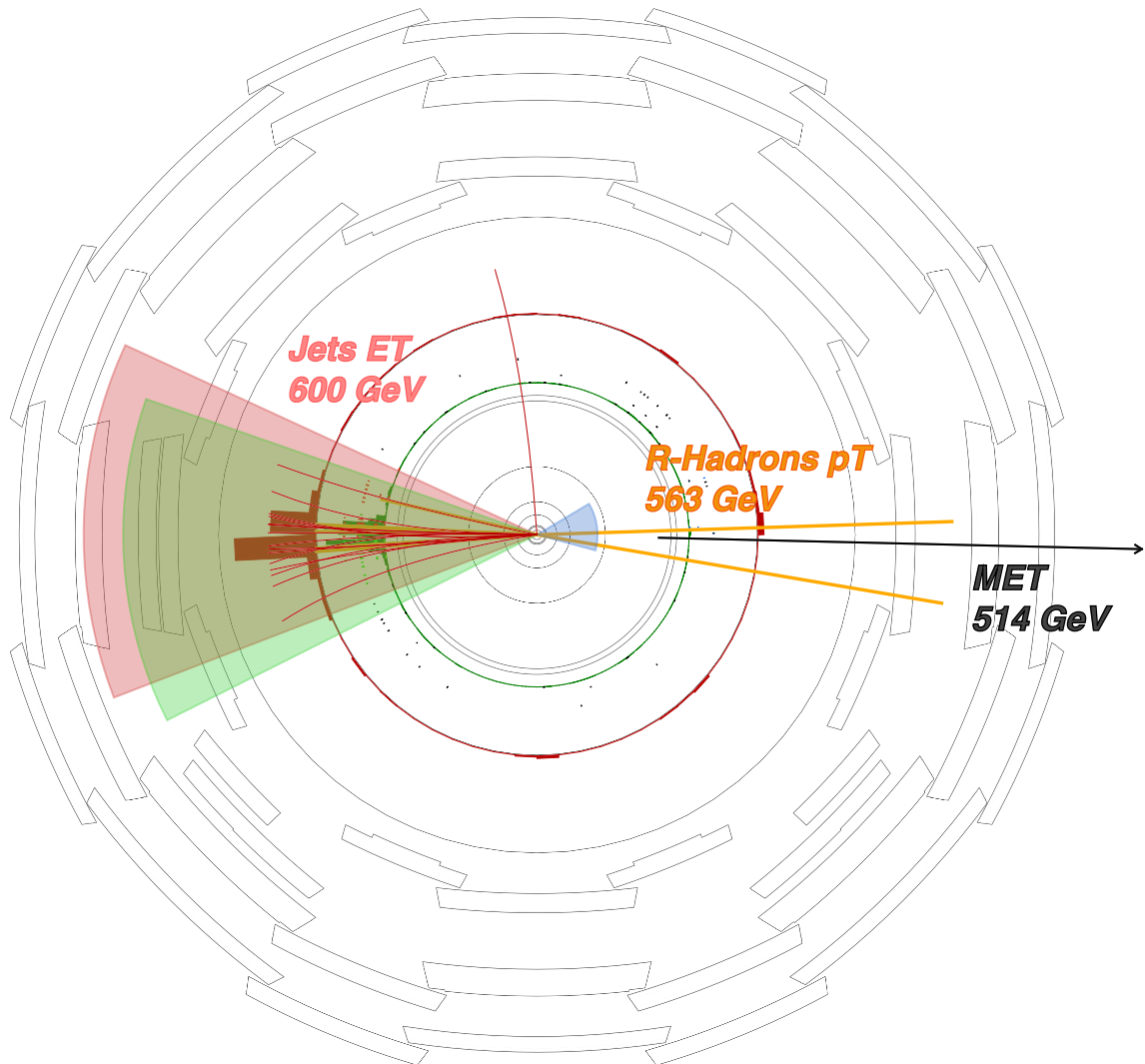


Figure 9.15: Any associated remnants from the strong production of the coloured LLP pair will likely be heavily boosted by the recoil of the two massive particles. The LLPs themselves leave the calorimeter system unscathed, only depositing a small fraction of their energy. From the transverse energy imbalance in the event it is then inferred that a large portion of the total energy must be missing. We exploit this when using a ‘missing energy trigger’ with no muon energy compensation.

estimate the integrated luminosity for the data samples used in a specific analysis. With specific triggers the actual integrated luminosity in a sample depends on whether the triggers required were online and if pre-scaled to what extent a single event represents multiple events statistically.

9.3 Trigger Selection

To trigger on R-Hadrons we principally rely on missing energy triggers, as no track-based triggers were available in 2011 and Muon triggers fail to serve due to the low chance of R-Hadrons being charged and arriving within a bunch crossing at the Muon system.

The most direct way to trigger on LLPs are simply reconstructing their momenta and their speeds. Due to the high collision rate at the LHC it has so far not been feasible to read out the tracking system and reconstruct particles at trigger time. Instead we could rely on the muon system where the particle multiplicity and detector technology allows for a fast momentum estimate of

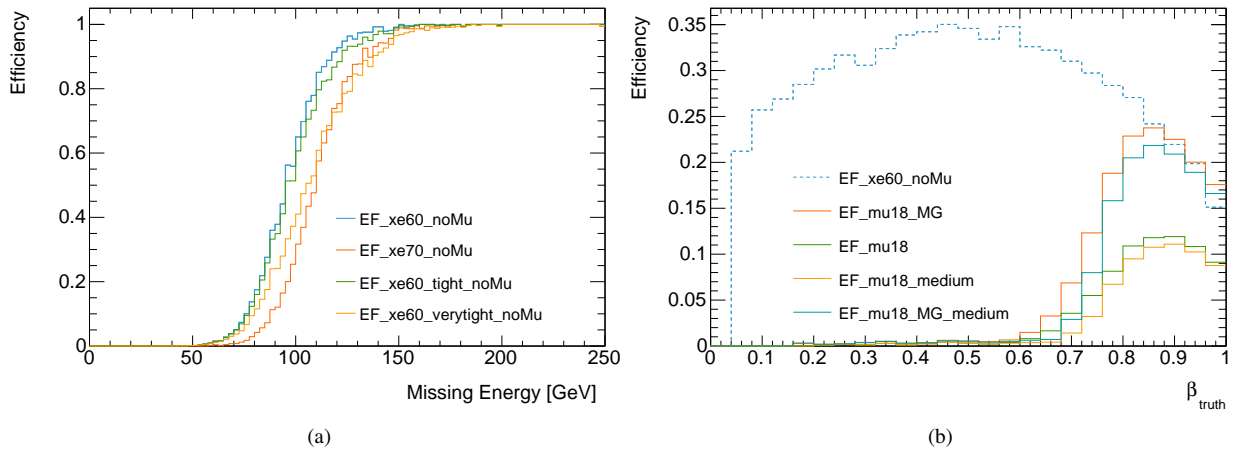


Figure 9.16: Figure (a) show missing energy turn-on curves for missing energy, figure (b) show that muon triggers requires a particle speed of $v > c0.7$ to be efficient while the missing energy triggers are much less sensitive to the particle speed. Both figures are based on simulated R-Hadron response.

penetrating particles. Here the problem again arises that the time frame in which an event is assumed to be correlated with detector responses is on the order of 50 ns as mentioned earlier. This leads to a minimum time of arrival at the trigger stations in the muon spectrometer effectively excluding slow particles. The effect on our lowest unpre-scaled muon triggers in 2011 is seen in Figure 9.16(b).

To regain some trigger efficiency within ATLAS we instead rely on the recoil from the LLPs onto initial state radiation. In Figure 9.15 the event displayed shows two R-hadrons with rest masses of $700 \text{ GeV}/c^2$ and a summed p_T in excess of 560 GeV moving to the right. Momentum conservation forces the ISR remnants to the left giving rise to a proportional energy deposition in the calorimeter system. As the R-Hadrons themselves don't deposit their full energy (only $10 - 30 \text{ GeV}$) in the detector it escapes ATLAS and the energy balance is skewed registering as missing transverse energy (MET). Quite substantial amounts of energy is lost in this manner and we can use MET as a trigger quantity. In Figure 9.16(a) the turn-on curves for the selected triggers are shown. The internal ATLAS notation implies that an EF_xe60_noMu trigger is a trigger with at least 60 GeV of MET based only on the energy deposited in the calorimeters without any muon spectrometer contributions.

As we are *searching* for new hypothetical particles, pre-scaled triggers are of little interest, even if they have lower trigger thresholds. Combined with the increasing beam intensity, this meant that the available un-pre-scaled triggers during 2011 had progressively higher trigger thresholds. In table 9.6 the lowest unpre-scaled missing energy triggers are listed for each data period. To attain the highest trigger efficiency possible we combined both muon triggers and MET triggers in our search as they were shown to be decorrelated at high- β . The muon triggers in general requires $p_T > 18 \text{ GeV}/c$ as is noted in the naming scheme for the muon triggers.

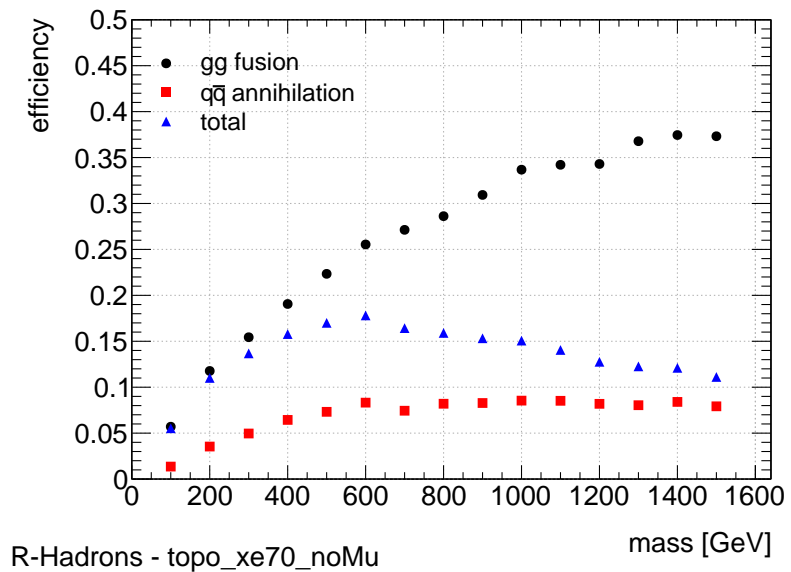
An overall trigger efficiency can be seen in Figure 9.17. We can also see that the amount of ISR in the event becomes increasingly relevant as $q\bar{q}$ production begins to dominate at high masses where less are produced.

The overall trigger efficiency is between 10 and 30% depending on the hypothesis mass.

Table 9.6: Trigger chains utilised in this analysis along with an indication in which data taking periods these were un-pre-scaled on all three trigger levels. The orange dots where actively used in the selection at the corresponding data period.

Trigger by period	D	E	F	G	H	I	J	K	L	M
EF_xe60_noMu	●	●	●	●	●	●				
EF_xe60_tight_noMu						●	●	●		
EF_xe60_verytight_noMu									●	●
EF_xe70_noMu	●	●	●	●	●	●	●	●	●	
EF_mu18	●	●	●	●	●	●				
EF_mu18_MG	●	●	●	●	●	●				
EF_mu18_medium							●	●	●	●
EF_mu18_MG_medium							●	●	●	●

Figure 9.17: Trigger efficiencies for a selected MET trigger with an onset at 70 GeV



9.3.1 Integrated luminosity

The integrated luminosity was calculated by summing the contributions of all data collection intervals marked as fit for physics by a good run list (Sec. 9.2.7) that required well functioning calorimetry. If for some reason the chosen triggers for each run period were offline at a specific interval it would be excluded. The overall estimate was computed by a tool internally available in ATLAS called the iLumiCalc tool. The luminosity estimate for the analysis is $\int \mathcal{L} dt = 4.7 \text{fb}^{-1}$

Pileup re-weighting For the R-Hadron search, attempts were made to align the running and detector conditions in MC with the actual conditions during data taking. For this the MC sample are divided into four different sets where each set represents a number of data taking periods. In each set the distribution of pileup events and the detector conditions were matched to the conditions in the represented periods. During data preparation, some data was not available to us in spite our best efforts. To make the MC sample represent the data that was actually available to our analysis, we re-weighted the MC periods to the fraction of data that they represent. The fractions of MC and data that fall into each period are shown in Table 9.7. The correction weights that can be derived from these fractions are also shown. We used the weights in all cut-flows. This explains the fractional number of signal events

data periods	fraction of MC	\mathcal{L} [pb ⁻¹]	fraction of Data	correcting weight
B-D	3.2%	166.65	3.5%	1.106
E-H	17.4%	948.576	20.2%	1.158
I,J,K	25.8%	1154.3	24.6%	0.950
L,M	53.5%	2431.74	51.7%	0.965

Table 9.7: Fraction of data and corresponding MC for each data taking period.

in some cases.

9.4 Event Selection

The analysis described in this thesis is based on the assumption that the particle of interest is massive, long-lived and *charged*. The methodology does not concern itself with colour charge (see instead [97, 63, 71]), hence the analysis in general covers identification of any LLP with electric charge.

This choice imply that we in principle are conducting a statistical test on mass distributions defined by

$$m_i = \frac{p}{(\beta\gamma)_i} \quad (9.8)$$

where $\beta\gamma_i$ is one of the many previously introduced ways of estimating speed in ATLAS, and p is the momentum from the track that caused the estimator's signal.

Our analysis thus relies on the quality of the $\beta\gamma$ estimates and the momentum. This quality is assured by a series of cuts on the input variables we call a *preselection* (Sec. 9.4.2).

As we know that the chance of a hadronic interaction taking place increases proportionally with the amount of material the R-Hadron traverses, we chose to conduct two analysis scenarios one excluding the muon spectrometer (Called *MS-Agnostic* search) and one including β -measurements and trigger information from it (but relying on the inner detector for momentum due to the high probability of charge confusion after the R-Hadron has traversed the dense calorimeters).

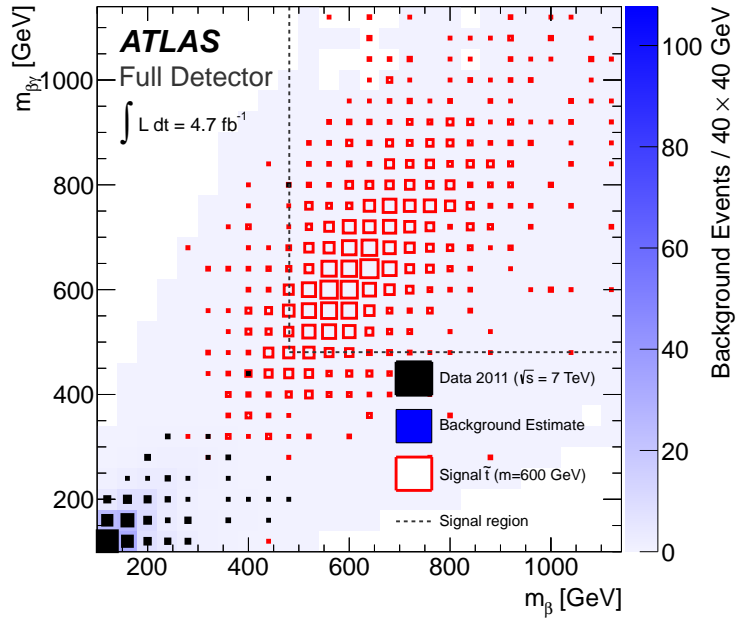
The calorimeter systems' (and in case of the 'full' detector search, also the MS') β -measurements are combined in a weighted average described in Section 9.4.1. The specific ionisation loss from the pixel system (Pixel- dE/dx) defines a second speed estimator that due to the technological 'orthogonality' with the ToF estimators are kept as a separate independent measurement.

The remaining dE/dx estimates was dropped as the pixel based estimate has superior β -resolution for R-Hadrons, leaving no incentive to add further complexity to the analysis by introducing dE/dx from the calorimeters (with charge flips).

We then have two speed estimators: Pixel- dE/dx based ' $\beta\gamma$ ' and ToF based ' β ' and the particle momentum as our three discriminating variables. Based on these, the final selection is done in a way that optimises the signal region for each specific R-Hadron hypothesis (Sec. 9.4.3).

The final result are three 2D histograms (one for signal, background and data) with β and $\beta\gamma$ -mass estimates in each respective dimension as shown in Figure 9.18.

Figure 9.18: Signal (red), background (blue) and data (black) on the mass plane for a 600 GeV/ c^2 stop (\tilde{t}) hypothesis.



A region on this *mass plane* is found that defines our counting window. All events in this window are summed. A statistically significant excess of measured events in the counting region compared with the expected number of Standard Model background events, constitutes a discovery. In case of a null result we can based on the signal expectation produce an upper limit estimate on the signal production cross section.

9.4.1 ToF β combination

The combination of β estimates from Calorimeters, MS MDT and RPC stations (Section 6.5) is done based on their underlying detector's time resolution and geometric acceptance. We combine these measurements as a weighted average with their individual measurement uncertainties as weights $1/\sigma_{err}$

$$\hat{\beta} = \frac{\sum_i \beta_i / \sigma_i^2}{\sum_i 1 / \sigma_i^2}, \quad \sigma_{\hat{\beta}}^2 = 1 / \sum_i \frac{1}{\sigma_i^2}. \quad (9.9)$$

The combination is based on the already combined calorimeter- β and the MS RPC and MDT β s. All of the inputs themselves are well calibrated and well determined (Chap. 8 and Ref. [111]) and each can stand on its own, only the best of these are added to the combination.

First the quality of the individual β -measurement must satisfy

$$0 < \beta_i < 2 \quad (9.10)$$

and the individual measurements at the sub-detector level must be compatible

$$Prob(\chi_i^2, ndof) > 0.0001 \quad (9.11)$$

Next all the available estimators must be compatible with we judge by the combined χ^2 here assuming all three estimates survived the individual qual-

ity cut:

$$\hat{\chi}^2 = \frac{(\hat{\beta} - \beta_{calo})^2}{\sigma_{calo}^2} + \frac{(\hat{\beta} - \beta_{MDT})^2}{\sigma_{MDT}^2} + \frac{(\hat{\beta} - \beta_{RPC})^2}{\sigma_{RPC}^2} \quad (9.12)$$

$$ndof = \text{Number of available estimators} - 1 \quad (9.13)$$

The p-value must satisfy $p(\hat{\chi}^2, ndof) > 0.0001$ and $\hat{\sigma} < 0.04$ otherwise we drop the event from the analysis. If only one estimator is available (or in case of the MS Agnostic search we only have the calorimeter based), then it must have $\sigma_i < 0.1$ to be included in the selection.

9.4.2 Preselection

The preselection is fundamentally divided into four categories

- Event quality
- Track quality
- Pixel dE/dx estimator quality
- Tof estimator quality

All four categories aim to discard the event based on badly measured quantities while retaining the actual hypothesis optimising cuts for later.

Event quality cuts concerns the overall run conditions and status of the detector. At this level the triggers in Section 9.3 are applied and a good run list (Sec. 9.2.7) based on standard quality criteria is consulted to discard events recorded during transient problems with needed sub-detector systems. The electromagnetic calorimeter some times suffered from noise bursts that we also veto due to the heavy reliance on it.

The data acquisition model in ATLAS split the output from trigger decisions into multiple output data streams to optimised readout-throughput. We are using data from multiple streams (JetEtMiss, Muon and debug streams) we also *remove identical overlapping events* that happened to be recorded by more than one stream. Events that fail to reconstruct within the processing window of the high-level software trigger are saved in a *debug* stream. R-Hadrons could conceivably be found in that stream and we therefore included it as well.

Track quality All tracks are associated with estimators based upon the hits along the track. For any measurement beyond the TRT that means we extrapolate the trajectory, into the calorimeters. If it matches a muon segment track the two are combined in a new fit and the object is called a *combined muon*. For R-Hadrons that have a tendency of flipping their charges this can have decremental effects in the combined momentum reconstruction, which is why we solely rely on the inner detector momentum even if the track is matched to a muon segment. To make sure the track is well determined even with abnormal ionisation in the trackers and possibly charge-flipping, we apply low-level quality cuts rather than overall track-fit quality requirements. Starting from the vertex, the candidate track must have impact parameters,

$$z_0 < 10 \text{ mm} \quad \text{and} \quad d_0 < 2 \text{ mm}, \quad (9.14)$$

where z_0 is the longitudinal and d_0 the transverse impact parameters respectively. This ensures we are dealing with a well determined track origin (and t_0) from a primary particle.

Next comes the **silicon pixel tracker**, which our 2-fold interest both for tracking and dE/dx leads us to require,

$$N_{\text{Pixel}}^{dE/dx} > 1 \quad (9.15)$$

- or at least two pixel hits that also have been used to determine the dE/dx value on the track (see requirements in Sec. 7.1.2).

The **silicon strip tracker** is the primary tracking system for our search as it is not responsible for any β -estimators and have a good detector resolution and sufficient distance from the vertex to give an adequate momentum estimate even at high momentum (see Figure 6.11). We require,

$$N_{SCT}^{\text{hits}} + N_{SCT}^{\text{dead sensors}} > 5 \quad (9.16)$$

where by dead sensors it is meant that if the sensor was alive it was within acceptance to contribute a hit to the track.

In addition to the two silicon trackers the **straw-based TRT** must have at least,

$$N_{\text{RT}}^{\text{hits}} > 6 \quad \text{if } |\eta| < 1.9. \quad (9.17)$$

The **transverse momentum** must be

$$p_T > 10 \text{ GeV}/c^2 \quad (9.18)$$

and the **momentum** must be within

$$20 \text{ GeV}/c < p < 3.5 \text{ TeV}/c. \quad (9.19)$$

These cuts gives a decent momentum side-band for data-driven background estimation (Sec. 9.5). The track must be well within the tracking volume with a **pseudo-rapidity**,

$$|\eta| < 2.0 \quad (9.20)$$

to avoid non-linear responses from tracking and estimators.

Pixel dE/dx estimator quality At high track multiplicity there is a chance of multiple particles crossing the same pixel cell, giving rise to higher levels of ionisation ($\sim 2 \geq$ MIPs) faking a signal. To avoid this, we disallow **shared pixel hits**, and set a minimum distance to all other tracks in the event,

$$N_{\text{pixel}}^{\text{shared}} = 0, \quad \Delta R_{\text{Tracks}_{p_T > 10 \text{ GeV}/c}} > 0.25. \quad (9.21)$$

A pixel dE/dx measurement must be present

$$0 < dE/dx < 20 \text{ MeV g}^{-1} \text{ cm}^2 \quad (9.22)$$

and the associated $\beta\gamma$ estimate must be

$$0 < \beta\gamma < 10. \quad (9.23)$$

The calorimeter-based ToF β estimate requires good isolation from other activity in the calorimeter and we place a jet-isolation cut at

$$\Delta R_{\text{Jet}_{E_T > 40 \text{ GeV}/c}} > 0.3. \quad (9.24)$$

In case of the MS Agnostic search we only require ToF from the calorimeter, where we demand

$$\sigma_{\beta_{\text{calo}}} < 0.1, \quad p(\chi^2, \text{ndof}) > 0.001 \text{ and } 0 < \beta_{\text{calo}} < 2 \quad (9.25)$$

For the full detector search we use the combination described in Sec. 9.4.1 where,

$$0 < \beta_{\text{calo}} < 2 \quad \text{OR} \quad 0 < \beta_{\text{MDT}} < 2 \quad \text{OR} \quad 0 < \beta_{\text{RPC}} < 2 \quad (9.26)$$

$$\sigma_{\hat{\beta}} < 0.04 \quad \text{and} \quad p(\chi^2, \text{ndof}) > 0.0001. \quad (9.27)$$

To avoid anomalous time measurements due to cosmic rays a cut is applied to the full detector search that requires any other track to either have a different charge or be at a different angle wrt. the interaction point,

$$|\eta_i + \eta_j| > 0.005 \quad \text{OR} \quad |\phi_i + \phi_j - \pi| > 0.005 \quad \text{OR} \quad q_i \neq q_j. \quad (9.28)$$

After the preselection a small ntuple is produced and passed to the final event selection described in the next sub section.

9.4.3 Signal Region Optimisation

The goal of the final selection is to count how many new particles have been produced if they exist. This count is conducted in such a way that the signal sensitivity is maximised, that is, the signal to noise ratio is as large as possible. This optimisation is done under the assumption that the signal is rare compared to background processes and so to enhance the probability of detection the particle if it exists we must find a region in observable-space that favours the signal hypothesis.

As have been described in earlier chapters, massive long-lived particles can be discriminated against known SM particles due to their relative speed and ionisation when produced at the LHC². After combining all ToF estimators (Sec. 9.4.1) into one (called β henceforth), we also chose to use specific energy loss (dE/dx) from the pixel detector to estimate speed in an uncorrelated way (we call this estimator $\beta\gamma$ to distinguish it from the ToF estimator),. The last component needed to discriminate against SM background in the track momentum p .

The final hypothesis-dependent selection is done solely in an observable-space spanned by these three variables $\beta, \beta\gamma, p$.

The selection is designed to accommodate the decreasing momentum resolution as the hypothesis rest mass increases and also the relative difference in β resolution of the two estimators.

In summary the selection proceed along the following steps:

- $\beta, \beta\gamma$ plane is scanned to find the optimal cut values.
- Background distribution is estimated in a data-driven way.
- An optimal mass cut is found in the $m_\beta - m_{\beta\gamma}$ -plane.

² As the momentum fraction transferred to the rest masses rather than their kinetic energies, the particles then become slow moving.

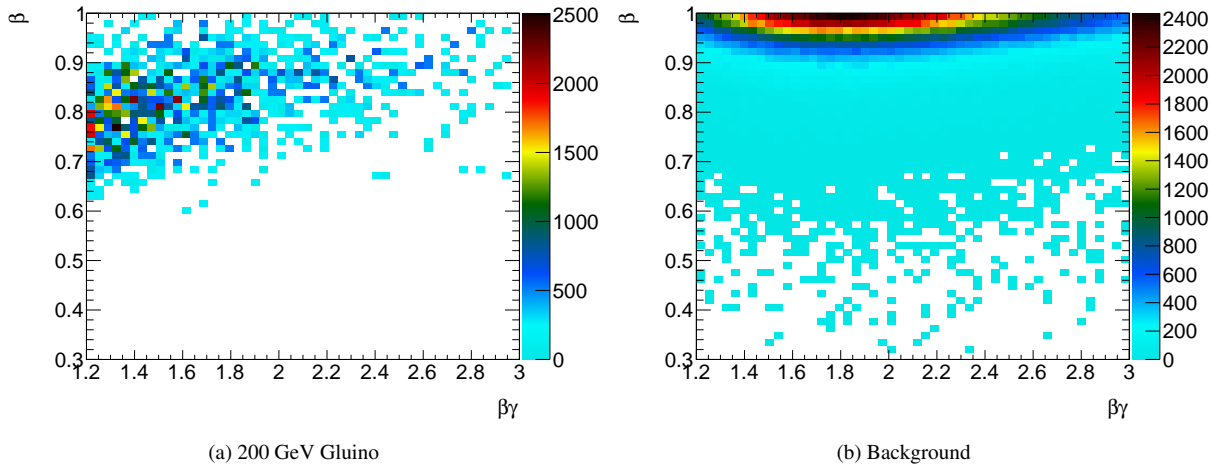


Figure 9.19: Input samples for cut optimisation

- The number of events with at least one candidate particles is counted for data and background. Signal efficiency is estimated.

This structure was found most suitable when requiring a data-driven approach to background estimation.

Each of these steps are described in detail below.

$\beta - \beta\gamma$ cut optimisation The background estimation method (Sec. 9.5) combines β , $\beta\gamma$ and p to form mass estimates. Before this is done no expectation on the rate of background is available, any cuts on β , $\beta\gamma$ after the background is generated will change and render the distribution false.

β and $\beta\gamma$ by themselves provides excellent discrimination power that would be smeared by the momentum in the mass estimates, I decided to cut on them before the background estimate was calculated.

This cut was found by defining a momentum side-band below 140 GeV/ c where most of the signal hypotheses didn't go. This allows collision data with $p < 140$ GeV to serve the role of background in the cut optimisation under the assumption that $\beta - \beta\gamma$ are independent of momentum for Standard Model background (Sec. 9.5). The optimisation was done by producing two 2D histograms one for data in the sideband and one for a specific signal hypothesis where the dimensions on the axes are β and $\beta\gamma$. Both observables are optimised simultaneously as they are correlated in signal and the approach allows for an implicit handling of their relative resolutions.

The Figures 9.19a and b show the regions for signal and background respectively. To find a region in the $\beta - \beta\gamma$ -plane that retains the maximum amount of signal (S) while removed the most background (B) a signal significance plane was computed by summing all entries from $\beta_0, \beta\gamma_0$ to $\beta_{cut}, \beta\gamma_{cut}$ for each bin

$$S = \sum_{i,j=0}^{cut} entry_{i,j}, \quad B = \sum_{i,j=0}^{cut} entry_{i,j}. \quad (9.29)$$

The sums were then applied to compute the signal sensitivity [35]

$$\text{med}[Z_W] = \sqrt{2((S+B) \ln(1+S/B) - S)} \quad (9.30)$$

which is an approximation of the poissonian likelihood ratio between signal and background. In the small signal limit $S \ll B$ it turns into

$$\text{med}[Z_W] \approx \frac{S}{\sqrt{B}}. \quad (9.31)$$

For the planes in Figure 9.19, equation (9.30) results in a sensitivity profile shown in Figure 9.20.

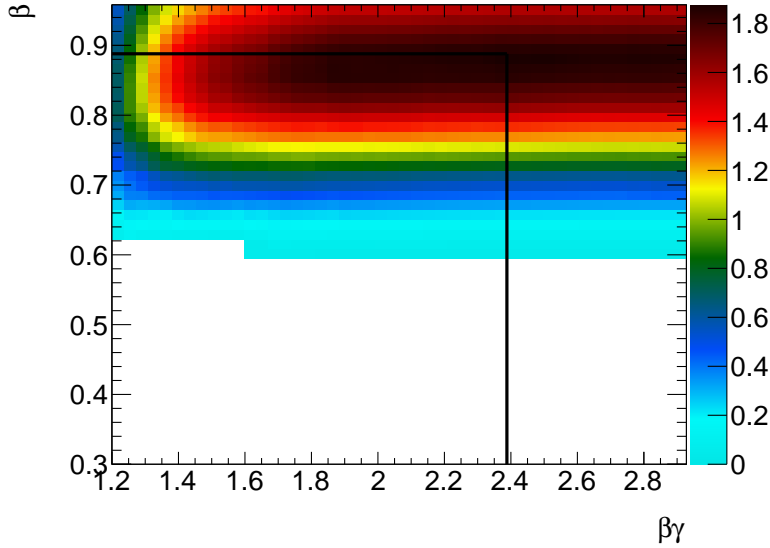


Figure 9.20: Sensitivity profile

On this plane the maximum value indicates the boundary with the optimal cuts. The resulting $[\beta, \beta\gamma]_{cut}$ values are then applied to data, signal and the background estimator input (Figure 9.21).

Mass cut optimisation With the background expectation normalised to data, and the signal sample ready, the final selection cut can be applied.

The cut is a mass window around the expected signal region. One way to define this window would be to reapply (9.30) this time to the mass plane. As the method is very sensitive to the amount of background (and signal) we found that the resulting mass window was too restrictive. Instead we went with a more fixed definition where 90% of the signal should be conserved after the cut was applied. The boundary was found by assuming the signal mass peak is Gaussian, where only the lower mass side was constrained by the window. The solution is then given by the cumulative distribution function (cdf)

$$90\% = 1 - \text{cdf}(\mathcal{N}(\mu, \sigma), x) \quad (9.32)$$

$$= 1 - \frac{1}{2} \text{erfc}\left(\frac{\mu - x}{\sqrt{2}\sigma}\right) \quad (9.33)$$

where $\mathcal{N}(\mu, \sigma)$ is a Gaussian PDF, with mean μ and standard deviation σ and x is the cumulative boundary we want to find. The solution is

$$x = \mu - 1.28155\sigma \quad (9.34)$$

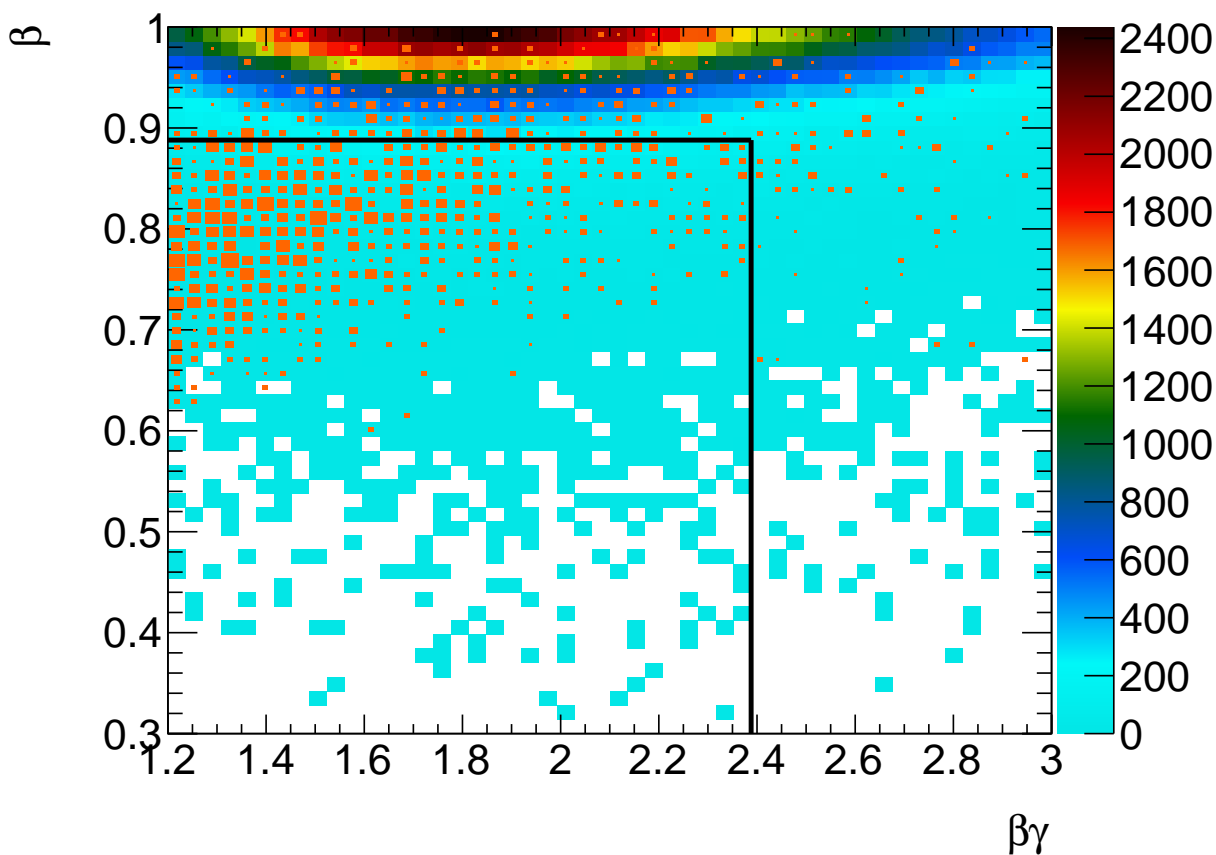


Figure 9.21: The cut region found by optimising the S/B ratio. The orange squares represent a $200 \text{ GeV}/c^2$ R-Hadron \tilde{g} sample.

Which then is our lower boundary for each mass dimension. μ and σ are found by fitting the 1D mass distributions for each signal hypothesis after applying $\beta - \beta\gamma$ cuts (Figure 9.22).

³We introduced a mass cutoff in case erroneous momentum reconstruction created high momentum outliers.

With the mass window defined by x and up to a cutoff³ of 3 TeV, the 2D histograms for data, background and signal is integrated to find the number

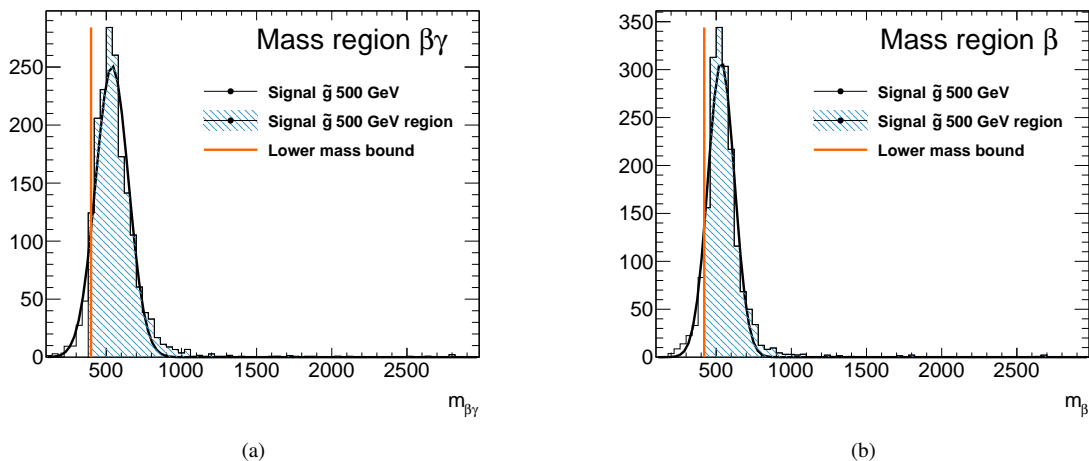


Figure 9.22: $500 > p > 100$ Joint PDFs

of candidate in the data sample. As the models we are testing assumes pair produced LLPs we only count the candidate with the highest p_T in each event. The absolute amount of signal events passing the selection holds no intrinsic value as we don't test a specific cross section hypothesis. Instead the signal observation efficiency is calculated as $\varepsilon = N_{obs}/N_{gen}$ where N_{gen} is the number of generated events after luminosity and pile-up corrections are applied.

The final cut windows found by applying the methods described in this chapter is found in the following tables (Table 9.8, 9.9 and 9.10).

	β cut	$\beta\gamma$ cut	m_β lower cut (GeV)	m_β upper cut (GeV)	$m_{\beta\gamma}$ lower cut (GeV)	$m_{\beta\gamma}$ upper cut (TeV)
\tilde{g} 200 GeV	0.902	2.928	182.4 GeV	3.0 TeV	155.1 GeV	3.0 TeV
\tilde{g} 300 GeV	0.874	2.280	262.3 GeV	3.0 TeV	236.5 GeV	3.0 TeV
\tilde{g} 400 GeV	0.874	2.136	344.7 GeV	3.0 TeV	314.0 GeV	3.0 TeV
\tilde{g} 500 GeV	0.874	2.100	423.7 GeV	3.0 TeV	403.5 GeV	3.0 TeV
\tilde{g} 600 GeV	0.860	1.776	502.3 GeV	3.0 TeV	481.6 GeV	3.0 TeV
\tilde{g} 700 GeV	0.860	1.704	575.6 GeV	3.0 TeV	566.8 GeV	3.0 TeV
\tilde{g} 800 GeV	0.846	1.704	634.9 GeV	3.0 TeV	626.2 GeV	3.0 TeV
\tilde{g} 900 GeV	0.860	1.776	711.3 GeV	3.0 TeV	694.1 GeV	3.0 TeV
\tilde{g} 1000 GeV	0.832	1.632	785.2 GeV	3.0 TeV	817.3 GeV	3.0 TeV
\tilde{g} 1100 GeV	0.818	1.704	839.2 GeV	3.0 TeV	856.9 GeV	3.0 TeV
\tilde{g} 1200 GeV	0.832	1.632	896.4 GeV	3.0 TeV	864.8 GeV	3.0 TeV
\tilde{g} 1300 GeV	0.818	1.524	999.8 GeV	3.0 TeV	995.3 GeV	3.0 TeV
\tilde{g} 1400 GeV	0.804	1.740	1050.1 GeV	3.0 TeV	1123.0 GeV	3.0 TeV

Table 9.8: Counts for gluinos - Full detector

	β cut	$\beta\gamma$ cut	m_β lower cut (GeV)	m_β upper cut (GeV)	$m_{\beta\gamma}$ lower cut (GeV)	$m_{\beta\gamma}$ upper cut (TeV)
\tilde{t} 200 GeV	0.902	2.568	172.4 GeV	3.0 TeV	161.9 GeV	3.0 TeV
\tilde{t} 300 GeV	0.888	2.352	255.4 GeV	3.0 TeV	242.1 GeV	3.0 TeV
\tilde{t} 400 GeV	0.874	1.920	331.2 GeV	3.0 TeV	327.0 GeV	3.0 TeV
\tilde{t} 500 GeV	0.874	2.064	407.2 GeV	3.0 TeV	395.4 GeV	3.0 TeV
\tilde{t} 600 GeV	0.860	1.776	481.1 GeV	3.0 TeV	480.7 GeV	3.0 TeV
\tilde{t} 700 GeV	0.860	1.848	541.5 GeV	3.0 TeV	546.2 GeV	3.0 TeV
\tilde{t} 800 GeV	0.860	1.812	626.8 GeV	3.0 TeV	600.8 GeV	3.0 TeV
\tilde{t} 900 GeV	0.860	1.920	674.9 GeV	3.0 TeV	671.4 GeV	3.0 TeV

Table 9.9: Counts for stops - Full detector

	β cut	$\beta\gamma$ cut	m_β lower cut (GeV)	m_β upper cut (GeV)	$m_{\beta\gamma}$ lower cut (GeV)	$m_{\beta\gamma}$ upper cut (TeV)
\tilde{b} 200 GeV	0.888	2.136	172.7 GeV	3.0 TeV	166.3 GeV	3.0 TeV
\tilde{b} 300 GeV	0.888	2.424	252.0 GeV	3.0 TeV	246.0 GeV	3.0 TeV
\tilde{b} 400 GeV	0.888	2.208	329.1 GeV	3.0 TeV	326.8 GeV	3.0 TeV
\tilde{b} 500 GeV	0.860	1.776	409.5 GeV	3.0 TeV	407.2 GeV	3.0 TeV
\tilde{b} 600 GeV	0.874	1.920	479.6 GeV	3.0 TeV	478.4 GeV	3.0 TeV
\tilde{b} 700 GeV	0.860	1.704	554.1 GeV	3.0 TeV	555.3 GeV	3.0 TeV
\tilde{b} 800 GeV	0.874	1.740	630.0 GeV	3.0 TeV	624.2 GeV	3.0 TeV
\tilde{b} 900 GeV	0.874	1.920	672.5 GeV	3.0 TeV	693.9 GeV	3.0 TeV

Table 9.10: Counts for sbottoms - Full detector

9.5 Background Estimation

Background estimation is necessary due to two things. The amount of monte carlo simulations needed to produce a satisfactory spectrum with the amount of statistics needed at the LHC is impractical to compute, especially QCD background. The other reason is that we rely on ‘fringe’ variables (timing varying from nominal expectation, energy loss in a tracking detector) the tails of which are not well simulated in the first place.

Luckily we can show that after our quality cuts, the main variables p, β and $\beta\gamma$ are not correlated for background processes in the momentum range of interest. The background is mainly due to mis-reconstructed time and ionisation estimates, therefore the background can be simulated by combining these uncorrelated variables to produce a mass spectrum that trivially follows from $m = p/\beta\gamma$.

To assure ourselves that this is a sound strategy we can measure the correlation between the variables, where we find an in general small linear correlation on the order of $\mathcal{O}(1\%)$. Because we cut on $\beta - \beta\gamma$ before generating the input histograms for the background estimator, fairly low statistics is available and we run a risk of oversampling. To avoid this we do not use fully orthogonal data samples where $\beta|_{p < 100 \text{ GeV}}^{<cut}$ and $p|_{\beta > 100 \text{ GeV}}^{>cut}$. Instead we sample the full $\beta|^{<cut}$ and $p|^{>100 \text{ GeV}}$ region.

We allow this as the p -spectrum effectively smears any low-lying β value. Also the final normalisation is done on a sideband below the signal region and not on the full spectrum, hereby avoiding any over estimation of the background at the potential cost of a signal hidden in the data.

Any way to show that p is independent of β and $\beta\gamma$ is by comparing the spectrum where $p < 100 \text{ GeV}$ but where $\beta|_{p > 100 \text{ GeV}}$ with a data spectrum with $p < 100 \text{ GeV}$ and $\beta|_{p < 100 \text{ GeV}}$. When normalised they should be identical if $p, \beta\gamma$ and β are independent. In Figure 9.23 we see these spectra.

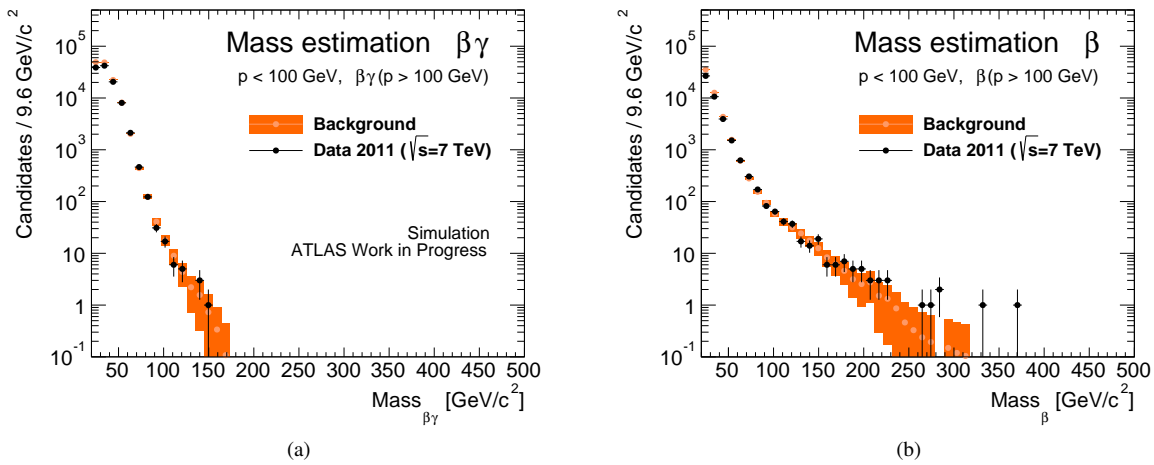
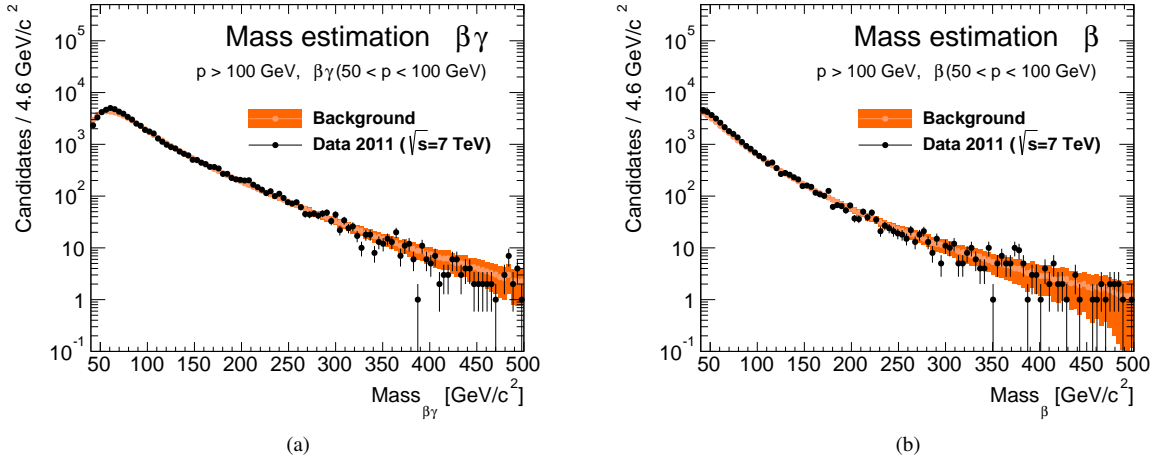


Figure 9.23: $p < 100$

Additionally we can produce the same spectra but for $p > 100 \text{ GeV}$ for data (with a blinding for $m > 500 \text{ GeV}$) where the input to the background is $p > 100 \text{ GeV}$ and $\beta|_{p < 100 \text{ GeV}}, \beta\gamma|_{p < 100 \text{ GeV}}$, as we can see in Figure 9.24, they match pretty well. The implementation of the background estimation is made in such a way that it takes an η -dependence into account. As input we produce three histograms, $p - \eta, \beta - \eta$ and $\beta\gamma - \eta$ shown in Figure 9.25.

The three histograms represents joint-pdfs, where for a set of mass estimates $\{m_\beta, m_{\beta\gamma}\}$ the $p - \eta$ distribution is sampled at random producing a joint estimate: (p, η) . The two estimator distributions are then profiled along η whereby a conditional pdf is produced for each variable, $p(\beta|\eta), p(\beta\gamma|\eta)$. These pdfs are then sampled to give estimates of β and $\beta\gamma$ that are



correlated in η but uncorrelated with p . The three estimates $p_e, \beta\gamma_e, \beta_e$ are then combined to form two mass estimates:

$$m_\beta = \frac{p_e}{\beta_e \sqrt{1 - \beta_e^2}}, \quad m_{\beta\gamma} = \frac{p_e}{\beta\gamma_e}. \quad (9.35)$$

The estimates are filled into a 2D-histogram, representing the joint pdf for the background (Figures 9.26).

The procedure is parallelised using Python multiprocessing libraries wrapping a C++ ROOT kernel to speed up the process, as roughly 3×10^7 samplings are need to produce a realistic tail at high mass.

A problem with this technique is that very aggressive cuts on the input distributions leads to ‘spikes’ in the 2D mass distribution. This can be potentially avoided by parameterising the distributions $f(\beta_{cut}, \beta\gamma_{cut}, N)$ with Eureqa or another symbolic regression package. We avoid the problem by only using the integral of the 2D histogram and not the actual differential spectrum.

Normalisation The output contains many millions of candidates, we therefore normalise the distribution to data before use. This is done by scaling a sideband region with $50 < m_x < 150$ GeV to data in the same mass range.

Injection test We can inject a signal sample into the input data to test if the background estimator is sensitive to possible ‘contamination’ from a signal. Injecting a gluino sample with $m = 300$ GeV and $\sigma_{NLO} = 62.1$ pb into all the above histograms shows that the method is not sensitive to a signal as

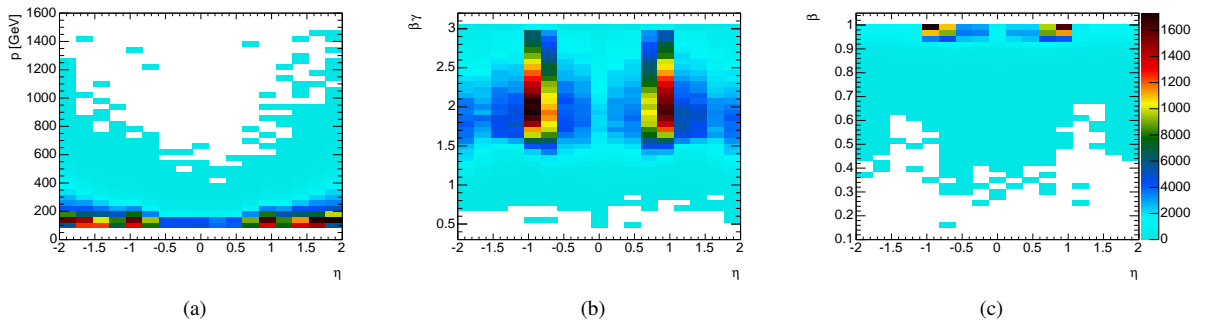
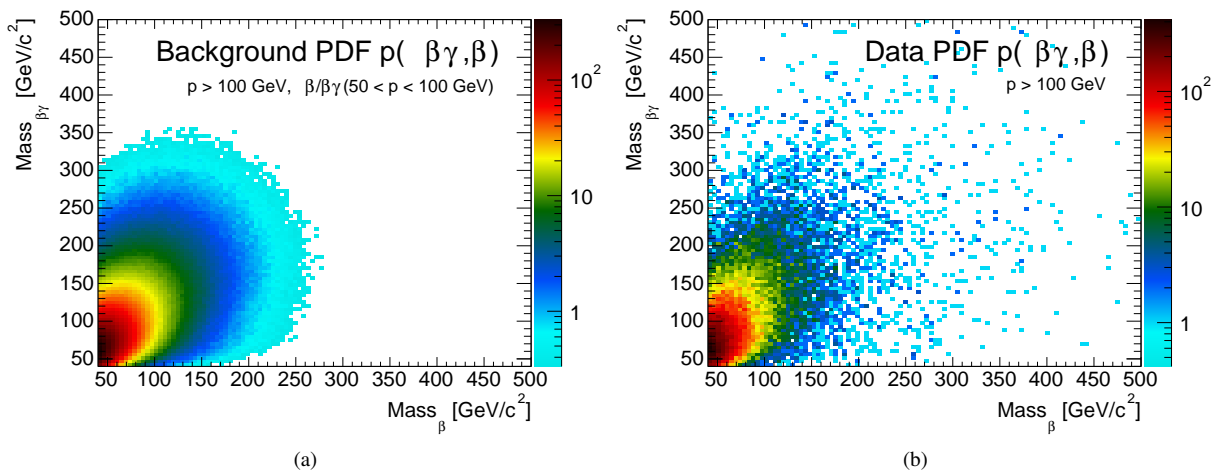


Figure 9.25: Inputs $500 > p > 100$

Figure 9.26: $500 > p > 100$ Joint PDFs

we would still have a very large deviation from the generated background expectation even if a signal was found within the sample (figs. 9.27).

9.6 Treatment of Systematic Uncertainties

Any results from a measurement must be viewed in light of its limitations. Our search had multiple sources of systematic uncertainty. They can be attributed to intrinsic sources such as the scale of QCD phenomena at the LHC (ISR, FSR) and the uncertainty on the amount of integrated luminosity, as we don't have an absolute luminosity measurement for ATLAS. The methodology applied in estimate speed from dE/dx and ToF also carries uncertainties and last the overall signal efficiency carries a large uncertainty due to the phenomenological nature of the model. The relative uncertainty on the background estimate, the signal efficiency and the integrated luminosity is found summarised in table 9.11.

Table 9.11: Systematic uncertainties on R-Hadrons in the 2011 ALTAS search. Ref. [111]

Source	Relative uncertainty %
Theoretical systematic uncertainty on signal cross section	15–30
Experimental uncertainty on signal efficiency	11.6
Signal trigger efficiency	4.5
QCD uncertainties (ISR, FSR)	8.5
Signal pre-selection efficiency	1.5
Momentum resolution	1.3
Pixel dE/dx calibration	5
Calo β timing calibration	1.0
MS β timing calibration	3.6
Offline E_T^{miss} scale	7.3–4.5
Luminosity	3.9
Experimental uncertainty on background estimate	15

9.6.1 Uncertainties in the theoretical cross section

The uncertainties on the theoretical cross section for MSSM SUSY production is calculated following the PDF4LHC recommendations outlined in Section 9.2.2. The uncertainty is 15% at masses around $100 \text{ GeV}/c^2$ increasing to roughly 30% for masses over $1 \text{ TeV}/c^2$.

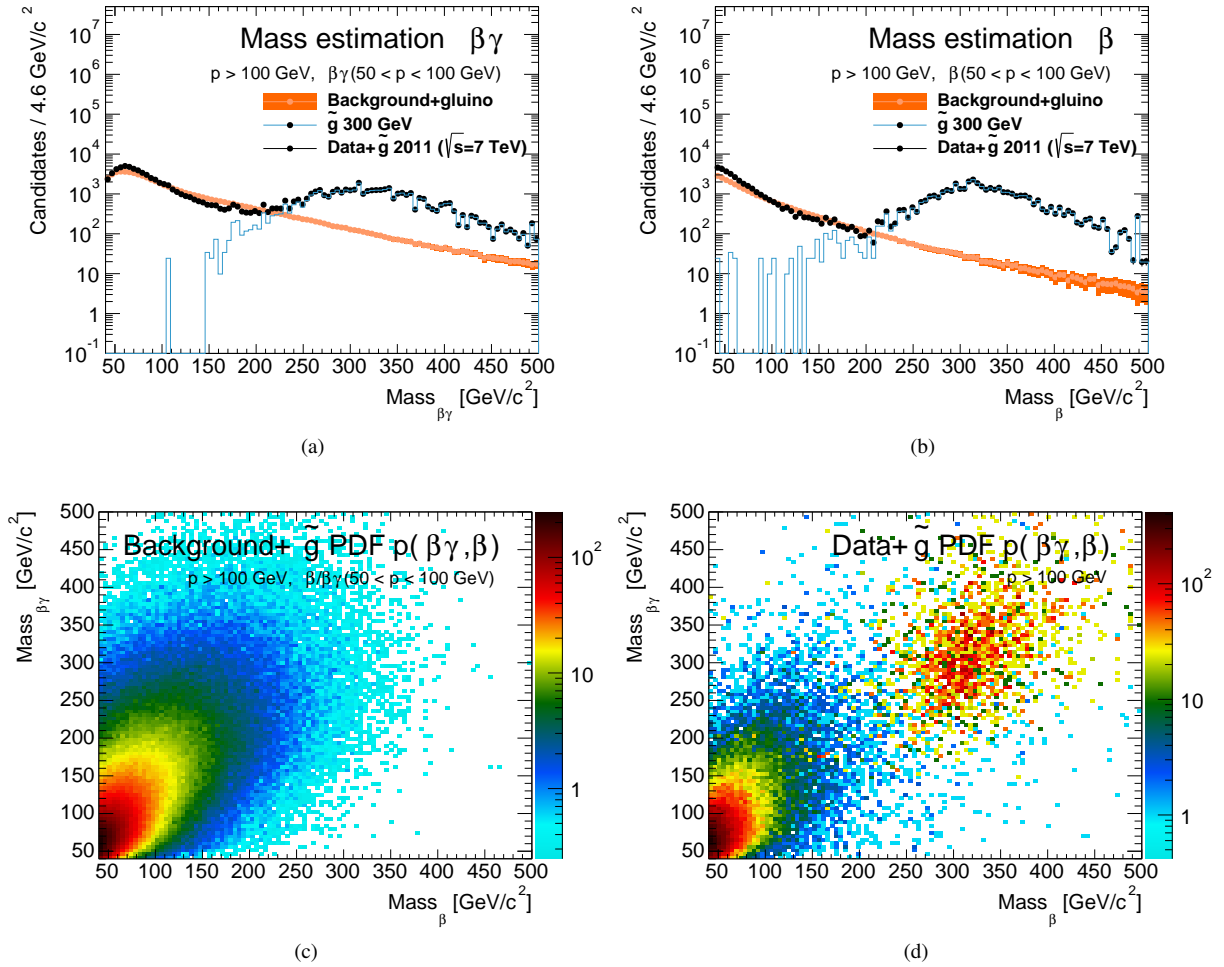


Figure 9.27: Distributions where a gluino sample has been injected.

9.6.2 Uncertainties in expected signal efficiency

The R-Hadrons signal efficiency had multiple sources of uncertainty. A systematic uncertainty attributable to a potential scale difference between the trigger efficiency for Monte Carlo simulation and data was studied by looking at the trigger onset curve (similar to Figure 9.16) for simulated and recorded $Z \rightarrow \mu\mu$ events. The trigger used ignores the muon spectrometer giving rise to a missing- E_T signature from the invisible muons. The trigger turn-on curve was multiplied bin-by-bin by the true missing- E_T to obtain the signal efficiency. The uncertainty was estimated by fitting the turn-on curve and varying the fitted parameters with $\pm 1\sigma$. The systematic uncertainty was found to be 4.5%.

The reliance on initial state and final state radiation in our trigger topology means that ISR and FSR is a source of uncertainty in a trigger context. To study the effect two R-Hadron \tilde{g} samples with $m = 1000 \text{ GeV}/c^2$ were produced, one with an elevated level of radiation and one with a decreased. By subjecting the resulting Missing- E_T spectrum for each of the samples to the trigger turn-on curve for our main trigger XE60_noMu a systematic uncertainty of 8.5% was found. The remaining signal uncertainties listed in Table 9.11 were found by comparing $Z \rightarrow \mu\mu$ MC to data.

9.6.3 *Uncertainties in background estimation*

To a large extent the uncertainties attributed to Monte Carlo based background estimation are automatically negated by the purely data-driven approach described in Section 9.5. The method itself did introduce other sources of uncertainty, in particular the binning of the input histograms, which were varied to see the effect and more adversely the lack of statistics in the same histograms when β and $\beta\gamma$ cuts had been applied. The total uncertainty was found to be 15%.

9.6.4 *Integrated luminosity*

The systematic uncertainty on integrated luminosity was estimated centrally by the ATLAS collaboration and was found to be 3.9% at the time of the analysis (it was later revised to 1.8% [109]).

9.7 *Statistical interpretation*

In our analysis we have designed the experiment with the number of observed events as our estimator. In practice we are interested in a cross section estimate on a specific particle mass hypothesis. If we had a specific theory in mind, we could based on the estimated cross section falsify the theory, if the cross section found by analysis is lower or higher than expected by the theory.

In the general case of LLPs we are less worried about specific model exclusion and separates our measurement into two cases based on the p-value for the background-only hypothesis. If we define a control region based on the statistical significance α , we say that the background-only hypothesis is excluded if $p < \alpha$, that is, we have a discovery.

Convention requires $p_{bkg} < 5.733 \times 10^{-7}$ to claim discovery of something in excess of the background only hypothesis in particle physics. On the other hand exclusion of a signal hypothesis requires a less stringent $p_{sig} < 0.05$ or what we call a 95% confidence level (CL) exclusion.

This brings us to the main topic of this chapter, namely how to interpret a model that has been excluded as $p_{sig} < \alpha$ where $\alpha = 0.05$. An exclusion at $\alpha = 0.05$ begs the question what is the largest possible cross section (or number of signal events) not excluded by the confidence level, this *upper limit* is the number we quote as the largest possible value given the pre-specified coverage of our test.

To find the upper limit on the cross section we must define a statistical model that represent our measurement along with its uncertainties. We model the expectation with a likelihood function that assumes a Poissonian probability on the number of observed events together with Gaussian distributions for each of the systematic uncertainties. To make the model as simple as possible we note that we have uncertainties on the signal efficiency (δ_ϵ) and background expectation (δ_b) together with a global uncertainty on the integrated luminosity (δ_L) from Sec. 9.6. The model is then defined by the

likelihood:

$$\mathcal{L}(\sigma; \delta_\varepsilon, \delta_b, \delta_L) = \quad (9.36)$$

$$\mathcal{L}(\sigma; \vec{\theta}(\sigma)) = \text{Pois}(n|\mu) \mathcal{N}\left(v_\varepsilon | \sqrt{\delta_\varepsilon^2 + \delta_L^2}\right) \mathcal{N}(v_b | \delta_b),$$

$$\text{where } \mu = \sigma L \varepsilon v_\varepsilon + b v_b.$$

In (9.36) $\vec{\theta}(\sigma)$ is the vector of nuisance parameters, n is the number of observed events, σ the effective cross section (in pb), L is the integrated luminosity (in pb⁻¹), ε is the signal efficiency and b is the number of expected background events.

If we express the background hypothesis as $L(0, \vec{\theta}(\sigma = 0))$ and the signal+background hypothesis as $L(\sigma, \vec{\theta}(\sigma))$, then the p -value is found by the following prescription.

A likelihood ratio $\lambda(\sigma)$ is defined as

$$\lambda(\sigma) = \frac{\mathcal{L}(\sigma, \hat{\hat{\theta}})}{\mathcal{L}(\hat{\sigma}, \hat{\hat{\theta}})} \quad (9.37)$$

The ‘hats’ $\hat{\hat{\theta}}$ denote that the nuisance parameters have been profiled⁴ $\hat{\hat{\theta}}$ are the Maximum Likelihood Estimate (MLE) fits that maximises \mathcal{L} for a given cross section σ , whereas $\hat{\sigma}$ and $\hat{\hat{\theta}}$ are the parameters that maximises the likelihood if σ is left as a free parameter. This construction, called a profile likelihood ratio is used as part of a test statistic defined as

$$t_\sigma = -2 \ln \lambda(\sigma) \quad (9.38)$$

The test statistic t_σ is a measure of the disagreement between the signal hypothesis and data (as $\lambda \rightarrow 1$ when $\hat{\sigma} \rightarrow \sigma$). t_σ is then sampled by generating toy Monte Carlo experiments with a specific cross section to form a pdf $f(q_\sigma | \sigma, \hat{\hat{\theta}}(\sigma, obs))$ where $\hat{\hat{\theta}}(\sigma, obs)$ is the conditional MLE assuming $n = obs$.

With $f(t_\sigma)$ we can calculate the p -value of the signal+background expectation

$$p_\sigma = \int_{t_{\sigma, obs}}^{\infty} f(q_\sigma | \sigma, \hat{\hat{\theta}}(\sigma, obs)) dt_\sigma. \quad (9.39)$$

To form an upper limit based on (9.39) we must find the cross section that satisfies $p_\sigma^{up} = 0.05$, this is usually done by scanning a region of expected cross sections (e.g. $[0, \frac{k(n-bkg)}{\varepsilon L}]$ with k as a fudge factor).

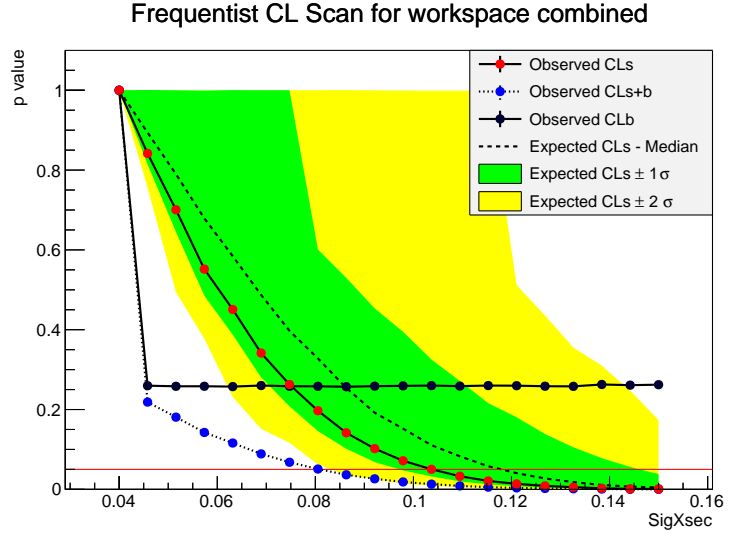
This limit is called CL_{s+b} as it is calculated for the combined expectation to both signal and background. In the eventuality that the background is much larger than the expected signal, an observed downward fluctuation in background can lead to excessively tight limits on the cross section. This means that an experiment can claim tighter upper limits than justified by the experimental sensitivity simply due to the combined s+b assumption in (9.39).

This effect is undesirable and to avoid it we can normalise with a background-only hypothesis p_b

$$p_b = 1 - \int_{t_{0, obs}}^{\infty} f(q_0 | 0, \hat{\hat{\theta}}(0, obs)) dt_0. \quad (9.40)$$

⁴ Profiling likelihoods essentially is a way to find the maximum likelihood of a multi-dimensional parameter space by reducing the number of parameters by fixing one parameter and integrating another assuming a conditional value for the fixed. The method is not as precise as a full maximum likelihood of all dimensions but is much faster i. e. practical.

Figure 9.28: CL_s upper limit on the cross section of a 200 GeV LLP gluino hypothesis. The red line at the bottom represents the 95% CL.



where the same test statistic is used but the cross section is $\sigma = 0$.

The effective p -value is then a ratio between the two

$$p'_\sigma = \frac{p_{s+b}}{1 - p_b} \quad (9.41)$$

which is scanned in the same manner as (9.39) to find the upper limit on the cross section given $p'_\sigma = 0.05$. This result is called the CL_s upper limit, and is in practice a more robust but also more conservative limit than the CL_{s+b} (see Figure 9.28 for a comparison).

9.8 Results

Applying the statistical method outlined in the previous chapter to the result from the analysis brings us to the concluding results. We found that in general the observed number of events were compatible with the expected background rate within uncertainties. Instead of quoting p -values we went on to set upper limits on the production cross section. This thesis has emphasised the gluino-induced R-Hadrons and Split-Supersymmetry but our result covered two additional R-Hadron configurations based on \tilde{t} and \tilde{b} squarks. The results are summarised in *limit plots* illustrating the upper limit on the production cross section for each of the tested mass hypotheses (Figures 9.29 and 9.30). Due to the cumulative chance of charge flips a search ignoring any muon spectrometer was designed as well as a search including muon spectrometer measurements if they were available. Both strategies have their advantages. The MS Agnostic search has poorer background rejection but better signal sensitivity while the opposite is true for the MS Inclusive search.

In Figure 9.32 and 9.31 the counting region for two of the tested signal hypotheses are shown. Summing all entries within the bounded region to the top right gives the number of observed events in the signal region.

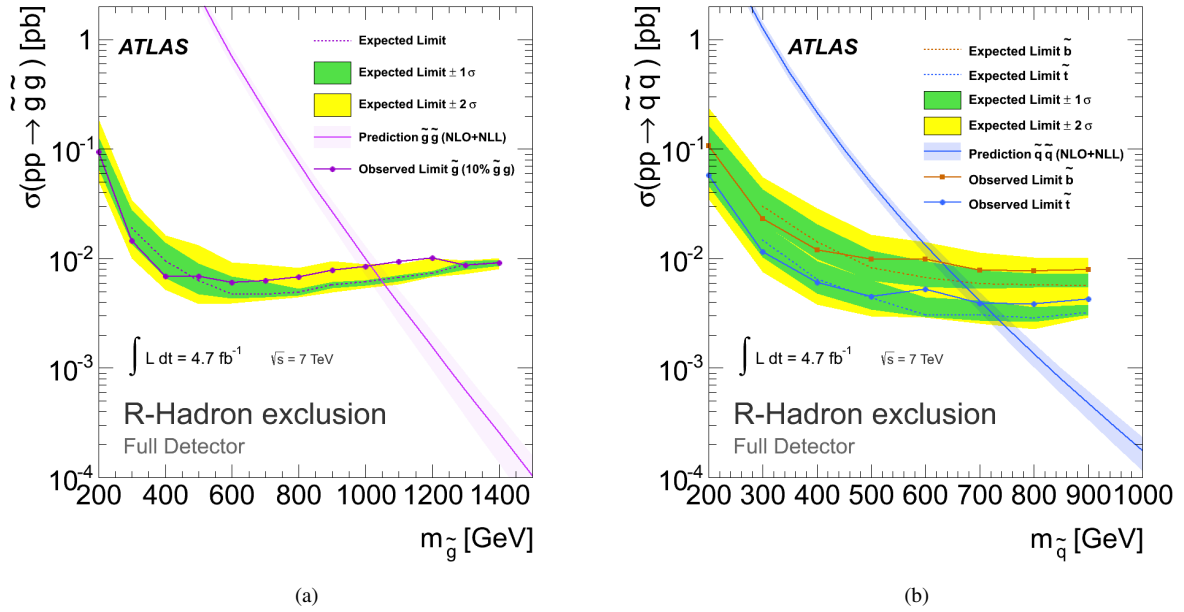


Figure 9.29: Limit on R-Hadrons based on the Muon Spectrometer inclusive strategy.

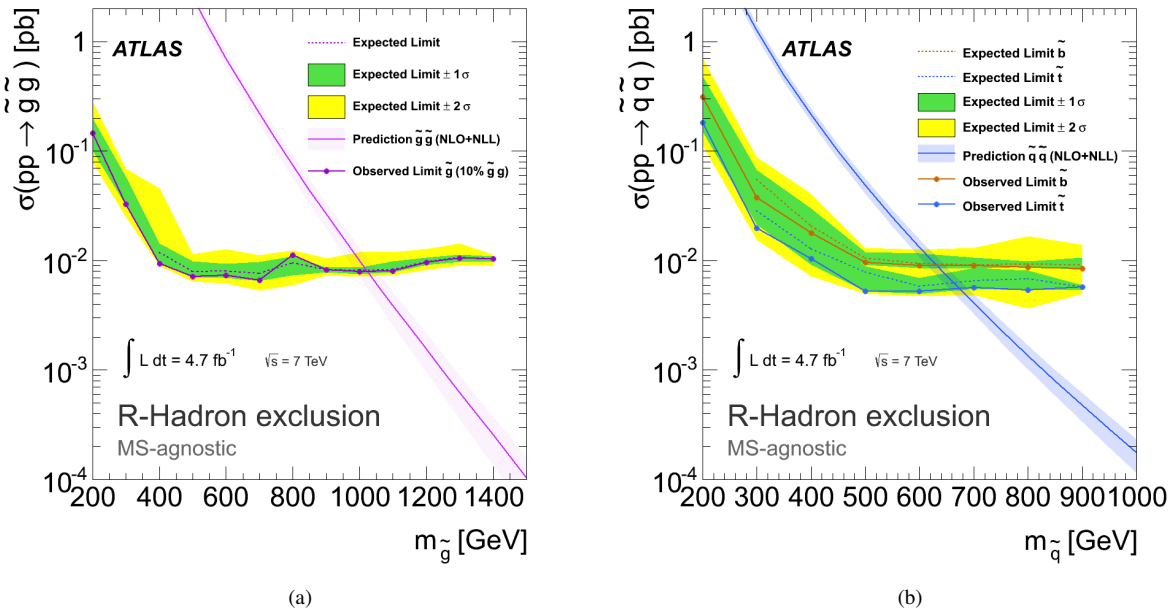


Figure 9.30: Limits on R-Hadrons based on the Calorimeter only strategy.

9.9 Conclusion

Comparing with the expected production cross section for decoupled gluinos in MSSM (which emulates SSUSY) it is possible to place a lower mass exclusion limit on long-lived particle pairs.

The overall upper limit on cross section is on the order of ~ 0.01 pb for all hypotheses. In comparison with a specific model prediction (PROSPINO, mass splitting scale 10 TeV) we can estimate lower limits on the mass of each hypothesis. The resulting limit on the gluino mass for the full (muon spectrometer agnostic) selection is approximately 985 GeV/c² (989 GeV/c²) at 95% C.L. as can be inferred from Figures 9.29a, 9.30a. For sbottoms the

Table 9.12: Counts for gluinos - Full detector

$m_{\tilde{g}}$ [GeV/ c^2]	Signal Eff.	Exp. Bkg	Obs. Data	Exp. Limit [pb]	+1 σ [pb]	-1 σ [pb]	Obs. Limit [pb]
200	0.113	131.183	135	0.089	0.128	0.065	0.094
300	0.126	18.691	15	0.019	0.028	0.014	0.015
400	0.138	5.178	3	0.010	0.014	0.007	0.007
500	0.144	1.751	2	0.006	0.009	0.005	0.007
600	0.136	0.557	1	0.005	0.007	0.004	0.006
700	0.134	0.294	1	0.005	0.006	0.004	0.006
800	0.126	0.148	1	0.005	0.005	0.005	0.007
900	0.109	0.165	1	0.006	0.006	0.005	0.008
1000	0.102	0.058	1	0.006	0.006	0.006	0.008
1100	0.093	0.036	1	0.007	0.007	0.006	0.009
1200	0.084	0.043	1	0.007	0.008	0.007	0.010
1300	0.069	0.020	0	0.009	0.009	0.008	0.009
1400	0.063	0.014	0	0.009	0.010	0.009	0.009

Table 9.13: Counts for stops - Full detector

$m_{\tilde{t}}$ [GeV/ c^2]	Signal Eff.	Exp. Bkg	Obs. Data	Exp. Limit [pb]	+1 σ [pb]	-1 σ [pb]	Obs. Limit [pb]
200	0.152	128.364	122	0.064	0.094	0.046	0.058
300	0.180	21.950	18	0.015	0.021	0.010	0.012
400	0.192	4.647	4	0.006	0.010	0.005	0.006
500	0.215	2.036	2	0.004	0.006	0.003	0.004
600	0.214	0.594	2	0.003	0.004	0.003	0.005
700	0.213	0.413	1	0.003	0.004	0.003	0.004
800	0.219	0.260	1	0.003	0.004	0.003	0.004
900	0.196	0.212	1	0.003	0.004	0.003	0.004

Table 9.14: Counts for sbottoms - Full detector

$m_{\tilde{b}}$ [GeV/ c^2]	Signal Eff.	Exp. Bkg	Obs. Data	Exp. Limit [pb]	+1 σ [pb]	-1 σ [pb]	Obs. Limit [pb]
200	0.068	97.112	94	0.114	0.164	0.080	0.107
300	0.089	21.978	18	0.030	0.043	0.021	0.023
400	0.101	6.295	5	0.014	0.020	0.010	0.012
500	0.102	1.405	2	0.008	0.012	0.006	0.010
600	0.110	0.860	2	0.007	0.010	0.006	0.010
700	0.108	0.320	1	0.006	0.008	0.005	0.008
800	0.109	0.265	1	0.006	0.007	0.005	0.008
900	0.108	0.250	1	0.006	0.007	0.005	0.008

Table 9.15: Counts for gluinos - Agnostic

$m_{\tilde{g}}$ [GeV/ c^2]	Signal Eff.	Exp. Bkg	Obs. Data	Exp. Limit [pb]	+1 σ [pb]	-1 σ [pb]	Obs. Limit [pb]
300	0.059	22.154	17	0.044	0.059	0.032	0.033
400	0.062	2.073	0	0.012	0.014	0.010	0.009
500	0.079	0.739	0	0.008	0.010	0.007	0.007
600	0.078	0.666	0	0.008	0.009	0.007	0.007
700	0.083	1.089	0	0.008	0.010	0.007	0.007
800	0.080	0.847	0	0.009	0.011	0.007	0.011
900	0.070	0.049	0	0.008	0.009	0.008	0.008
1000	0.073	0.200	0	0.008	0.009	0.008	0.008
1100	0.070	0.368	0	0.008	0.010	0.008	0.008
1200	0.061	0.200	0	0.010	0.011	0.009	0.010
1300	0.055	0.200	0	0.011	0.011	0.010	0.010
1400	0.053	0.008	0	0.010	0.011	0.010	0.010
1500	0.046	0.200	0	0.013	0.014	0.013	0.013

lower mass limit is 612 GeV/ c^2 (618 GeV/ c^2) and for stops: 683 GeV/ c^2 (657 GeV/ c^2) (Figure 9.29b, 9.30b)

These limits include the discussed systematic uncertainties on the signal cross section and efficiency ($\sim 14\%$ depending on mass point as described

$m_{\tilde{t}}$ [GeV/ c^2]	Signal Eff.	Exp. Bkg	Obs. Data	Exp. Limit [pb]	+1 σ [pb]	-1 σ [pb]	Obs. Limit [pb]
200	0.039	103.864	97	0.208	0.301	0.150	0.182
300	0.070	15.304	10	0.028	0.037	0.021	0.020
400	0.086	3.124	2	0.013	0.018	0.009	0.010
500	0.095	0.851	0	0.008	0.009	0.005	0.005
600	0.108	0.692	0	0.006	0.007	0.005	0.005
700	0.102	0.899	0	0.007	0.009	0.006	0.006
800	0.106	1.432	0	0.007	0.008	0.005	0.005
900	0.102	0.071	0	0.006	0.006	0.005	0.006
1000	0.100	0.728	0	0.006	0.009	0.006	0.006

Table 9.16: Counts for stops - Agnostic

$m_{\tilde{b}}$ [GeV/ c^2]	Signal Eff.	Exp. Bkg	Obs. Data	Exp. Limit [pb]	+1 σ [pb]	-1 σ [pb]	Obs. Limit [pb]
200	0.025	106.208	103	0.339	0.487	0.241	0.312
300	0.047	25.450	17	0.055	0.067	0.039	0.038
400	0.050	2.829	2	0.021	0.030	0.015	0.018
500	0.060	0.931	0	0.011	0.012	0.009	0.010
600	0.063	0.397	0	0.009	0.012	0.009	0.009
700	0.065	0.188	0	0.009	0.011	0.008	0.009
800	0.068	0.115	0	0.009	0.010	0.009	0.009
900	0.066	0.705	0	0.009	0.011	0.008	0.008
1000	0.068	0.039	0	0.008	0.009	0.008	0.008

Table 9.17: Counts for sbottoms - Agnostic

in section 9.6) as well as on the data-driven background estimate uncertainty (15%), as described above.

In the next chapter these results are compared with SSUSY to guide further searches at higher collision energies.

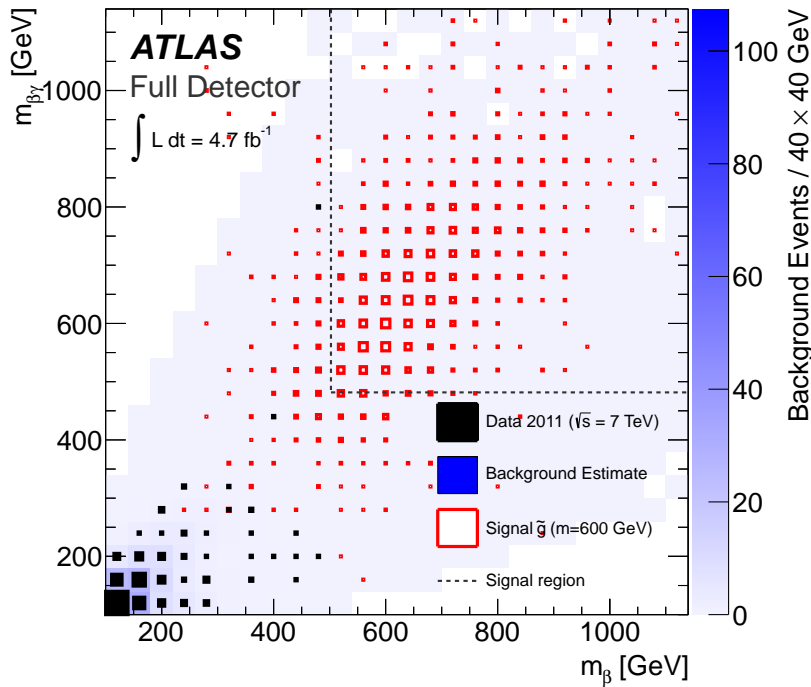


Figure 9.31: Final selection plane for a \tilde{g} with $m = 600 \text{ GeV}/c^2$. The axes are reconstructed mass based on Calorimeter and MS β along the x -axis and Pixel $\beta\gamma$ based mass along the y -axis. The dotted lines are the 90% signal coverage bounds, everything within that region is counted and listed in table 9.8.

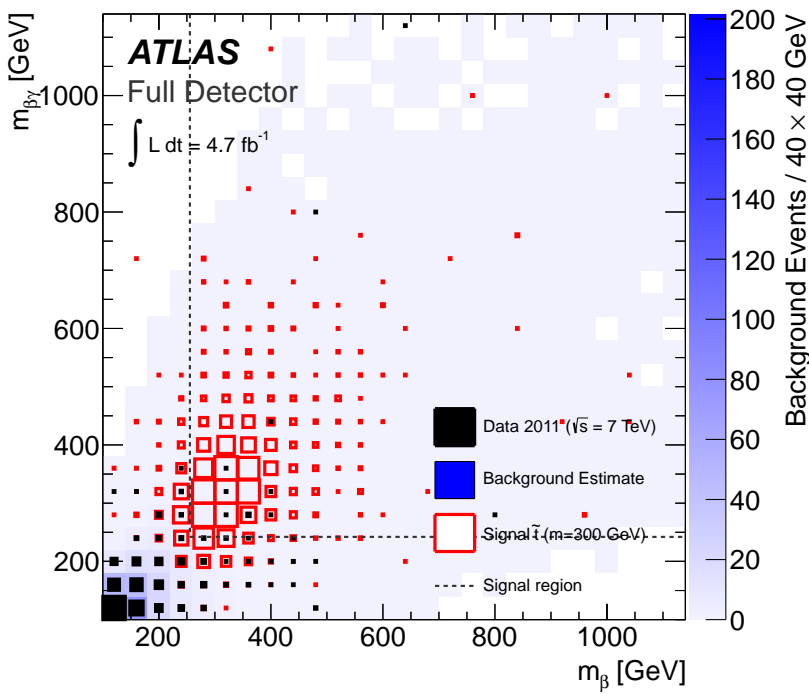


Figure 9.32: Final selection plane for a \tilde{t} with $m = 300 \text{ GeV}/c^2$. The axes are reconstructed mass based on Calorimeter and MS β along the x -axis and Pixel $\beta\gamma$ based mass along the y -axis. The dotted lines are the 90% signal coverage bounds, everything within that region is counted and listed in table 9.13.

IV *Prospects for future
searches with ATLAS at
the LHC*

10 *Future searches for Long-lived particles at the Large Hadron Collider*

This thesis documents searches performed with the LHC at its very first years of operation. This initial period has been exceptionally accommodating for orthogonal studies such as these that requires deep levels of access to sensor data and run conditions favouring long event windows. The design specifications for the LHC and its experiments define much tighter operations where the tolerances are tightened to maximise collision rates with the assumption that everything directly measurable with the detectors are relativistic SM remnants and not slow massive exotica. In this chapter I will explore the phenomenological side of the search for LLPs in particular SSUSY R-Hadrons, and let the technical challenges of this new mode of operation be left to future analysts. To set the scene the next section will sketch the changes awaiting us.

10.1 *The LHC in 2015*

During the runs in 2010-2012 the LHC was crippled due to misconnected superconducting splices between the bending magnets. With the first Long Shutdown (LS1) in 2013-2014 these connections will be repaired and the current expectations is to start collisions at $\sqrt{s} = 13$ TeV in April 2015. While the actual beam configuration is still being decided preliminary studies suggest the values listed in table 10.1. A key uncertainty is the bunch spacing. It has dramatic consequences for the experiments as well as the accelerator whether it will continue with 50 ns or be decreased to the design value of 25 ns. This naturally also have consequences for the time dependent search for slow moving LLPs.

	2011	2012	2015	Nominal
Beam energy [TeV]	3.5	4.0	6.5	7.0
Peak luminosity [$L=10^{33}\text{cm}^{-2}\text{s}^{-1}$]	3.5	6.6	16	10
Integrated luminosity per year	5	25	45	-
Bunch Intensity [10^{10}p]	14.5	15	11.5	11.5
Number of bunches per beam	1380	1380	2508	2808
Bunch Spacing [ns]	50	50	25	25
Normalised transverse emittance [μm]	2.4	2.4	1.9	3.5
β^* at collision in ATLAS [m]	1.0	0.6	0.5	0.55
Average number of processes per crossing [μ]	9.1	20.7	43	25.60

Table 10.1: LHC parameters. (Ref. [44, 25]).

The luminosity evolution is so far planned to add around 50 fb^{-1} a year (Figure 10.1). The plan is to collect around 300 fb^{-1} before the next shut-down LS2.

Figure 10.1: Planned baseline evolution for the LHC. We were in the LS1 period when this was written in the winter of 2014. Ref. [25].



10.1.1 ATLAS LS1 upgrades

The experiments are not waiting idle while the LHC is being repaired. Nearly all systems in ATLAS are being repaired and upgraded during the shutdown. Many of these changes have implications for the LLP searches as they are very dependent on subtle features of each detector. Any in-depth review is beyond the scope of this section but some of the major changes are

- **Beam pipes** are being replaced. This means that the study described in Section 10.3 can be started.
- **Insertable B-layer** A major upgrade is a new b -layer inserted around a smaller beam pipe. The IBL will at $r = 33 \text{ mm}$ sit inside the old pixel b -layer. This upgrade is likely going to improve dE/dx and give precise vertex determination.
- **Pixel** Recovery of sensors now 99% are back online from 95%.
- **SCT** Back end electronic now capable of handling up to 90 simultaneous pileup events.
- **TRT** leaks fixed, resuming operation with a xenon mixture (Sec. 6.2.3) enabling electron PID.
- **LAr Calorimeter** decreasing DAQ sampling from 5 to 4 samples per readout. This could affect the time and energy resolution for LAr ToF and dE/dx .
- **Muon Spectrometer** major repairs all around and new chambers increasing acceptance

To really gauge what consequences the LS1 has on LLP searches full simulations must be performed, but based on the figures in Chapters 8 and 7 the time window need not be must larger than the nominal for signals to be detected at $\beta < 1$.

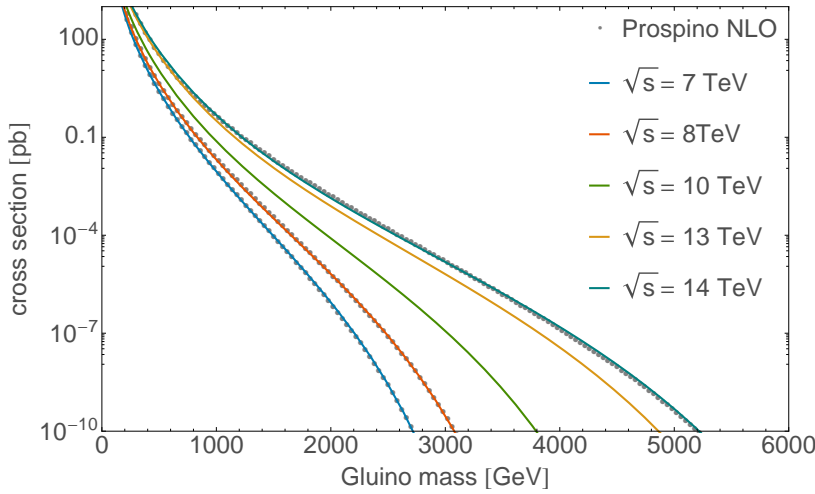
10.2 Future sensitivity to Split-Supersymmetry with ATLAS

The plans for the LHC assumes the production 45fb^{-1} at $\sqrt{s} = 13\text{ TeV}$ in 2015. The very preliminary plans also states that 300fb^{-1} should be collected before the next long shutdown LS3 in 2021. We hope that the energy will be ramped to the nominal 14 TeV in 2016 and onwards. These scenarios are the basic assumptions for the results in this section.

To estimate the gluino pair production at 13 TeV it was necessary to produce an approximate cross section function based on $7, 8$ and 14 TeV estimates, as 13 TeV was not yet an option available in the PROSPINO NLO programme used for such predictions. The function was found by producing between 100 and 200 cross section estimates for masses ranging from 100 to 7000 GeV for each of the three available collision energies. The data points were then extracted and a model was found by using the Eureka application for symbolic regression. The resulting function which is independent of m_s (see Figure 10.2) was found to be

$$\sigma(E_{cm}, m_{\tilde{g}}) = \exp\left(\frac{m_{\tilde{g}}(0.7E_{cm} - 13.7m_{\tilde{g}} + 5195)}{m_{\tilde{g}}(0.06E_{cm} + m_{\tilde{g}} + 636) - 28060} - \frac{16m_{\tilde{g}}}{E_{cm} - 1.6m_{\tilde{g}} + 113.5}\right). \quad (10.1)$$

The expression is valid until $-\frac{16m_{\tilde{g}}}{E_{cm} - 1.6m_{\tilde{g}} + 113.5} > 0$. The fit spans many orders of magnitude (Figure 10.3) but is fairly consistent with and captures 99.93% of the input ($R^2 = 0.9983$).



Based on this cross section estimate and the projected statistics it is possible to estimate how many gluino pairs will be produced in the datasets.

$$N = \int \mathcal{L} dt \sigma_{\tilde{g}} \epsilon \quad (10.2)$$

In Figure 10.4 the black horizontal line is the threshold for single-pair production. For 13 TeV this threshold is reached at $2738\text{ GeV}/c^2$. A likely signal efficiency ϵ is around 10% which lowers the threshold to $2253\text{ GeV}/c^2$.

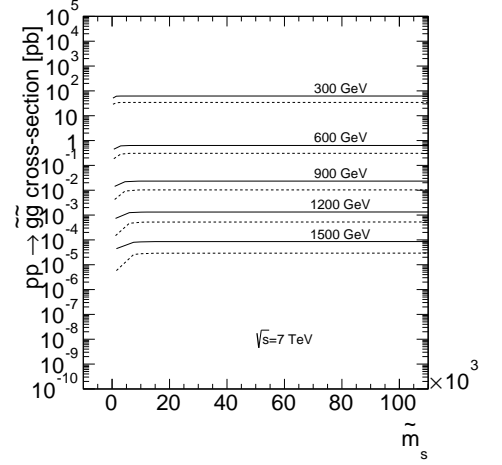
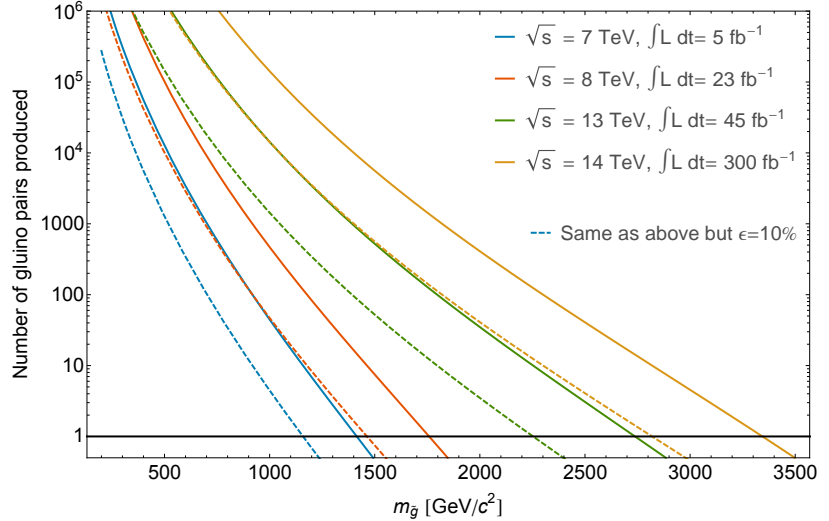


Figure 10.2: PROSPINO 2.1

Figure 10.3: Cross section estimates for pair produced gluinos at pp colliders with collision energies ranging from 7 to 14 TeV .

Figure 10.4: Expected number of gluino pairs produced in the various datasets produced and projected.



10.2.1 The high mass scale and gluino lifetimes

All searches to date have placed limits on gluino R-Hadron production in terms of their production cross section assuming the particles to be stable. Looking back at Figure 3.3 we note that the mass of the gluino is not the only constraining parameter of SSUSY. The mass scale m_S is with the discovery of the Higgs particle constrained to be $< 10^7 \text{ GeV}/c^2$. This limits the lifetime of the SSUSY gluino by remembering that the lifetime is related to the gluino mass and m_S by

$$\tau_{\tilde{g}} = \left(\frac{\text{TeV}/c^2}{m_{\tilde{g}}} \right)^5 \left(\frac{m_S}{10^9 \text{ GeV}/c^2} \right)^4 4s. \quad (10.3)$$

Depending on the size of m_S we will see different event signatures in ATLAS. By having searches that are sensitive to full detector-stable particles and gradually assumes stability at smaller radii we can exclude SSUSY m_S space by placing upper cross section limits on LLPs with a minimum assumed survival distance $\tau_{\tilde{g}} c \beta \gamma$.

From Figure 10.5 we see that for a gluino with a mass of $1 \text{ TeV}/c^2$ the life-time is less than a μs . To understand what that means in terms of travel length and hence detector acceptance in ATLAS, we can calculate the particles average decay-length as a function of the SUSY breaking scale

$$d = c\tau\beta\gamma \quad (10.4)$$

It is useful to define certain physics scenarios based on specific systems in ATLAS. In Table 10.2 six representative scenarios are listed that gradually requires the gluino to have track-like nature at longer and longer times. The invariant mass study effectively is a classic SUSY study where the decay modes are as described in Sec. 3.2.4. Displaced vertices can be found by the tracking systems from distances defined by the vertex resolution and out. The search strategy changes to a kinked-track search at moderate distances. The inner detector search is an implicit search in the sense that the gluino must be track-like throughout the tracking volume but no further assumptions

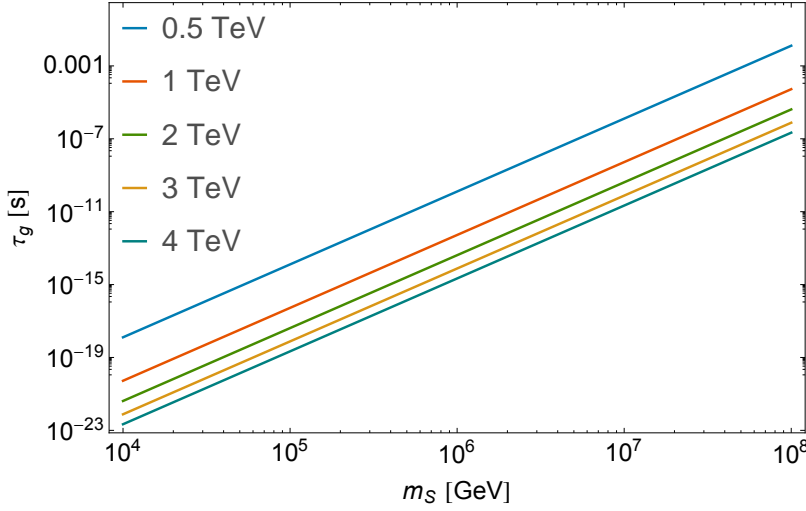


Figure 10.5: Average gluino lifetimes at $m_S < 10^8 \text{ GeV}/c^2$ calculated with (10.3).

are made about the tracks fate in the calorimeters and onwards. The same strategy is applied in the calorimeter range searches where the gluino must be track-like in the majority of the calorimeter volume as well as the inner tracker volume. The muon spectrometer search additionally requires a track in the muon spectrometer. The last case is particularly interesting in the case that the particle is stuck within the ATLAS detector and decays out of time with the ordinary events. A lifetime measurement in that case requires some correlation between the decay vertex and all former tracks extrapolated to that place, making the extraction of a lifetime very challenging data wise. In this study each of these searches have a defined radius where the system that must have a track signature is ending (Table 10.2).

Case	d [mm]	τ_{min} [μs] $d/\beta\gamma c \beta\gamma=3$	τ_{min} [μs] $d/\beta\gamma c \beta\gamma=0.1$
Invariant mass	0	—	—
Displaced vertex	$4 < r_{DV} < 180$	4.5×10^{-6}	0.0001
Inner detector range	1106	0.0012	0.0369
Hadronic calorimeter	4250	0.0047	0.1418
Muon spectrometer	10000	0.0112	0.3336
Trapped R-Hadron decays	≤ 10000	> 0	> 0

Table 10.2: Radial ranges for the search scenarios defined in this chapter. The two minimum mean lifetime τ_{min} columns represent the maximum and minimum reconstructable speeds of the methods in Chapter 7 and Chapter 8.

Particle identification is in general only possible if $0.1 < \beta\gamma < 3.0$ in the ATLAS detectors. This constrains the minimum mean lifetime to τ_{min} in table 10.2. By further combining the mean lifetimes with (10.3) and specific $\beta\gamma$ values for masses $m_{\tilde{g}}$ it is possible to estimate which regions of the detector is capable of excluding m_S ranges.

10.2.2 Gluino speeds at various production energies

As the LLPs travel significantly slower than the speed of light we should estimate what the average speeds of a gluino produced at a specific \sqrt{s} is likely to have, as this affects the travel distance before decay.

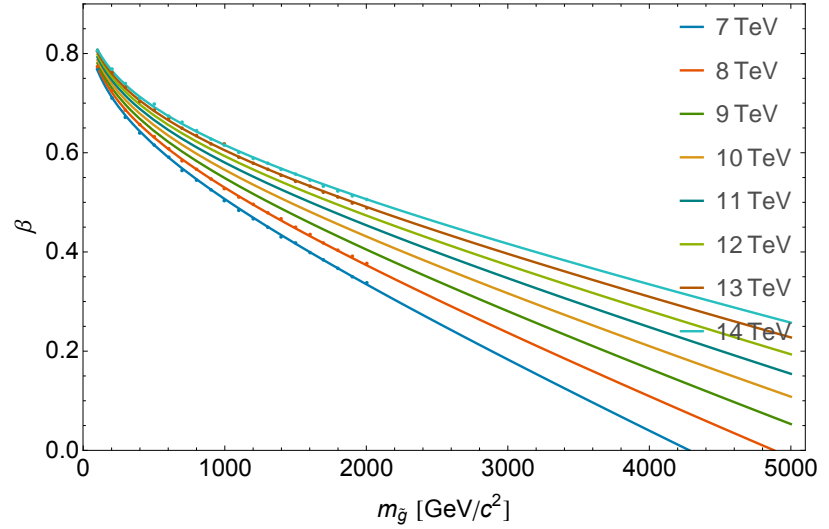
With the R-Hadron code in Pythia 8 20k events for 20 mass points between 100 and 2000 GeV where produced at $\sqrt{s} = 7, 8, 13, 14 \text{ TeV}$. The

mean β for these datasets where fitted with Eureka to produce a parameterisation

$$\beta(E_{cm}, m_{\tilde{g}}) = \frac{0.7787m_{\tilde{g}}}{E_{cm}} - 1.26\sqrt{\frac{m_{\tilde{g}}}{E_{cm} - m_{\tilde{g}}}} + 0.908. \quad (10.5)$$

The pythia results are plotted on top of the equation in Figure 10.6.

Figure 10.6: Mean β for pair produced gluinos at various centre of mass energies. The dots are Monte Carlo simulated with Pythia 8. The lines represent a parameterisation described in the text.



With the expected speed of the gluino and the expected lifetime at each gluino mass point, we can calculate an average travel distance for each mass hypothesis with (10.4).

The plot in Figure 10.7 above summaries the ATLAS analyses presented in this thesis. The overall axes are the gluino mass and the splitting mass scale with the contour lines being the average distance before decay of the gluino. The coloured regions represent the excluded areas where the upper limit on the cross section is smaller than the predicted gluino production cross section for that given mass. The lower bound on these regions comes implicitly from how far in ATLAS they must travel to be reconstructed as a long-lived particle. The 2011 analysis (the main subject of this thesis) is segmented into three areas, one where only the inner detector is utilised, one where only the ID and Calorimeters are used and lastly one where the muon spectrometer is included as well. The mass exclusion of the latter two are comparable but the squark mass exclusion gains a bit by the shorter distance to the calorimeter. For the inner detector background rejection is an issue, this can be seen on the slightly lower mass exclusion. The squark mass scale on the other hand is reduced significantly. The distances must be taken with a pinch of salt, as the detector geometry is not spherical around the interaction point, and the life-time is following an exponential rather than a Gaussian distribution, nevertheless the plot gives an idea about the true coverage of this kind of analysis. Cosmological constraints seems somewhat irrelevant now as the discovery of a Higgs around 125 GeV limits the life-time of the gluino to mere microseconds.

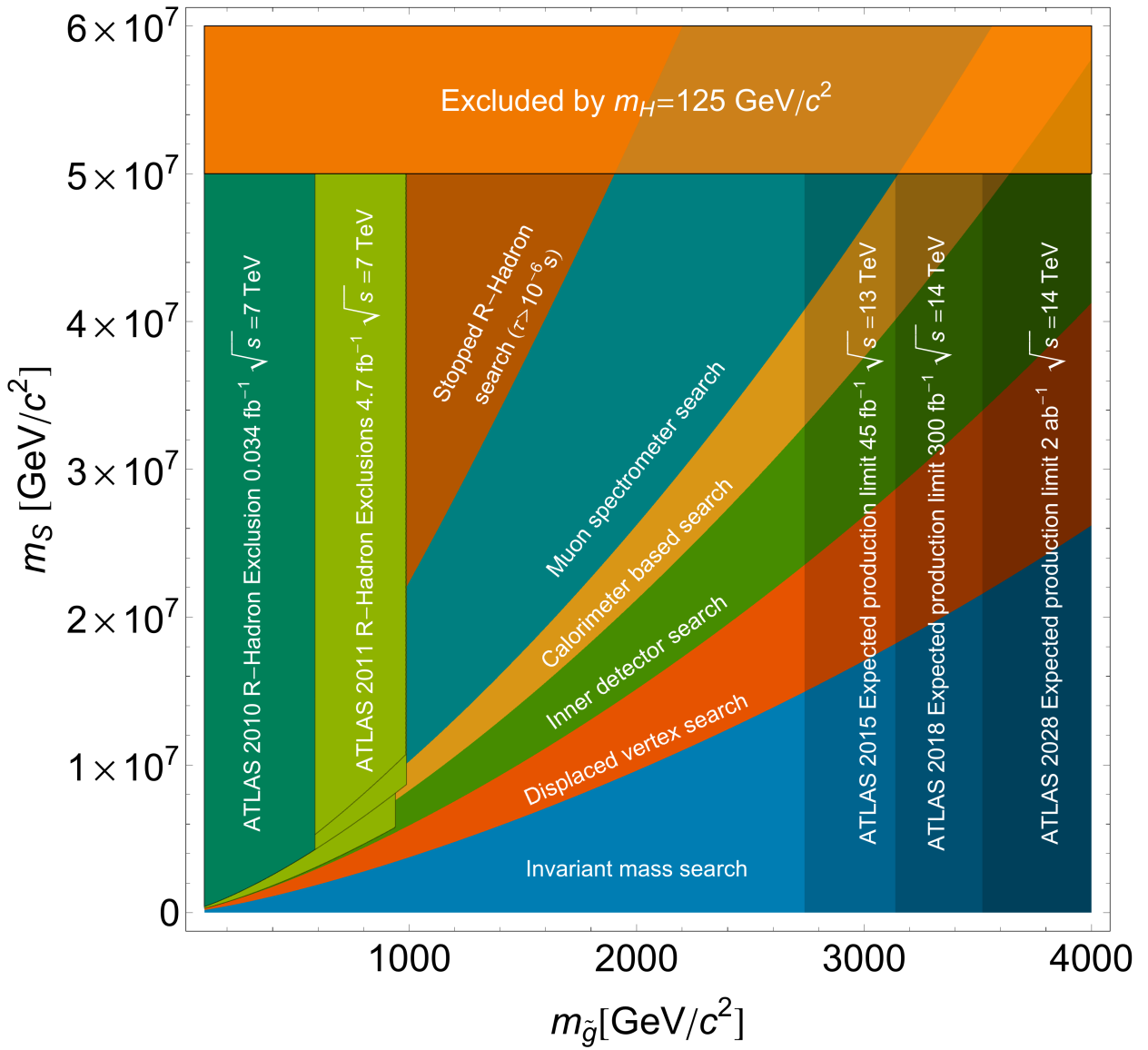


Figure 10.7: Current SSUSY limits and possible reach of the ATLAS detector at various statistics. The detector regions illustrates which analysis strategy matches a $\{m_s, m_{\tilde{g}}\}$ scenario. The 2011 search is divided into three independent analyses one relying on the inner detector only, one relying on the muons spectrometer and tracker only and a final analysis that also utilises possible matched tracks in the muon spectrometer. Only lifetimes are accounted for, not energy loss. The stopped R-Hadron search assumes that the R-Hadrons stops anywhere in the ATLAS volume and decays after 10^{-6} s, which is the lower acceptance in the search presented in [110].

10.3 Trapped monopoles

The problem of magnetic monopoles has deep roots in theoretical physics. It is one of the most glaringly obvious broken symmetries in our world, the asymmetry between magnetic and electric charges. Magnetic monopoles are predicted by numerous theories [90] and has continued to intrigue theoretical physicists and evade experimental physicists for nearly 100 years. It is not my intention to introduce nor motivate magnetic monopoles further, see the reference above for an introduction to the subject. The question is rather, if these monopoles exists and are produced at the LHC, where would we in all likelihood find them¹. Further, if they are sufficiently charged are there then a change that we would miss them with our detectors as the beam pipe itself would be opaque to them? This study is meant as a strategic pointer to where we would most economically collect samples of said beam pipe if it was available for analysis. The analysis itself can be carried out by scanning samples of the beam pipe material with a super conducting magnetometer as described in [83, 45]. The assumptions here are that the monopoles are effectively stable with lifetimes sufficient for sample accumulation during accelerator operation and proceeding analysis $\tau \sim 5s$. Earlier such works have been done in a more general context of the entire detectors at the LHC [84], this study is focusing on the beam-pipe itself as it is available for analysis after the LS1 where the installation of the IBL prompts a replacement of the beam-pipe with a smaller one.

¹ Conventional searches such as the LLP search in the earlier chapter can be sensitive to certain monopole hypotheses, but in general specialised search methods are employed in detector searches [107]

10.3.1 Simulating trapped magnetic monopoles

If magnetic monopoles exist with Dirac charges g_D it would mean that a unit of magnetic charge corresponds to an electric charge of $g_D = 137e/2$. The amount of energy loss due to ionisation in matter would be significantly larger [45] for such a particle than for particles with known electric charges $\mathcal{O}(1e)$.

$$-\left\langle \frac{dE}{dx} \right\rangle = K \frac{Z}{A} g^2 \left[\ln \frac{2m_e c^2 \beta^2 \gamma^2}{I_m} + \frac{K(|g|)}{2} - \frac{1}{2} - B(|g|) \right] \quad (10.6)$$

Here I_m is the mean ionisation potential which for magnetic monopoles can be expressed in terms of the usual I_e as $I_m = I_e \exp -D/2$, where $D(AI) = 0.056$. The charged dependent $K(|g|) = 0.406$ and $B(|g|) = 0.248$ for $g_D = 1$. The remaining terms have the same meaning as for the Bethe-Bloch formula in section 4.1.2.

Proportional energy loss as a function of the speed of the particle differs from the regular Bethe-Bloch formula by not scaling with $1/\beta^2$. This means that the ionisation loss is proportional to the speed of the particle, and highly energetic monopoles will lose the most energy per unit distance traverse in matter (Figure 10.8). A study done by [84] has found that for sufficiently energetic (or charged) magnetic monopoles even the beam pipe constitutes enough material to trap the particles.

Equations of motion The transport equation for magnetic monopoles requires a modification as the Lorentz force is acting inversely for magnetic

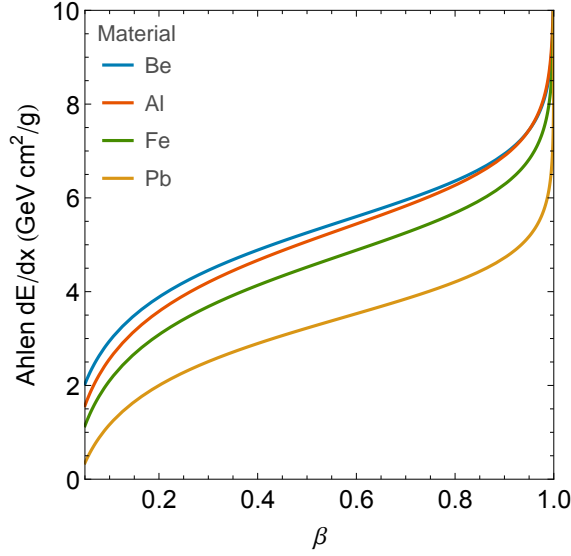


Figure 10.8: Energy loss of magnetic monopole. Notice the increase in energy loss as its velocity nears c .

charge [74]

$$\frac{d\vec{p}}{dt} = \vec{F} = q_e \left(\vec{E} + \frac{\vec{v}}{c} \times \vec{B} \right) + q_m \left(\vec{B} - \frac{\vec{v}}{c} \times \vec{E} \right). \quad (10.7)$$

An effect of this is that the solenoidal magnetic field immersing the inner detector will act as a longitudinal accelerator for any magnetically charged particles.

By applying the chain rule we can rephrase (10.7) in terms of trajectory length s instead of time t

$$\frac{d\vec{p}}{ds} = \frac{d\vec{p}}{dt} \frac{dt}{ds} = \frac{d\vec{p}}{ds} \frac{1}{v} = \frac{\vec{F}}{\vec{v}} \quad (10.8)$$

to obtain

$$d\vec{p} = \left[q_e \left(\vec{E} + \frac{\vec{v}}{c} \times \vec{B} \right) + q_m \left(\vec{B} - \frac{\vec{v}}{c} \times \vec{E} \right) \right] ds / \vec{v}. \quad (10.9)$$

$$(10.10)$$

which we for the individual components become

$$d\vec{p} = \frac{ds}{\vec{v}} \cdot \begin{pmatrix} q_e \left(\frac{B_z v_y}{c} - \frac{B_y v_z}{c} + E_x \right) + q_m \left(B_x + \frac{v_z E_y}{c} - \frac{v_y E_z}{c} \right) \\ q_e \left(-\frac{B_z v_x}{c} + \frac{B_x v_z}{c} + E_y \right) + q_m \left(B_y + \frac{v_x E_z}{c} - \frac{v_z E_x}{c} \right) \\ q_e \left(\frac{B_y v_x}{c} - \frac{B_x v_y}{c} + E_z \right) + q_m \left(B_z + \frac{v_y E_x}{c} - \frac{v_x E_y}{c} \right) \end{pmatrix} \quad (10.11)$$

By introducing $\hat{e} = \vec{v}/|\vec{v}| = \vec{p}/|\vec{p}|$ we get the classic representation,

$$d\vec{e} = \begin{pmatrix} \frac{q_e}{cp} (B_z e_y - B_y e_z) + B_x q_m + \frac{q_m}{cp} (E_y e_z - E_z e_y) + E_x q_e \\ \frac{q_e}{cp} (B_x e_z - B_z e_x) + B_y q_m + \frac{q_m}{cp} (E_z e_x - E_x e_z) + E_y q_e \\ \frac{q_e}{cp} (B_y e_x - B_x e_y) + B_z q_m + \frac{q_m}{cp} (E_x e_y - E_y e_x) + E_z q_e \end{pmatrix} \cdot ds \quad (10.12)$$

If no electric fields are present the equations reduces to

$$d\vec{e} = \begin{pmatrix} \frac{q_e}{cp} (B_z e_y - B_y e_z) + q_m B_x \\ \frac{q_e}{cp} (B_x e_z - B_z e_x) + q_m B_y \\ \frac{q_e}{cp} (B_y e_x - B_x e_y) + q_m B_z \end{pmatrix} \cdot ds. \quad (10.13)$$

These equations allow us to implement a transport code that simulates the behaviour of a magnetically charged particle in a magnetic field. Together with (10.6) this serves as the dynamics of a toy-Monte Carlo implemented to estimate where monopoles could be trapped in the beam pipe.

Implementing a monopole simulator The actual implementation is done in python with PyROOT as visualisation backend for effective debugging. The algorithm works as follows.

- A point in phase-space is emulated by sampling a point in a $\{\eta, p_T\}$ distribution generated based on the R-Hadron phase space for the specific mass of the monopole.
- The monopole is now defined by $\{g, q, mass, \eta, p_T\}$ and ejected from coordinate $\{0, 0, 0\}$.
- To propagate the monopole (10.13) is solved by the Runge-Kutta-Fehlberg method [46] which adaptively changes the step size ds depending on the error between a Runge-Kutta $\mathcal{O}(4)$ and RK $\mathcal{O}(5)$ estimate. The relative error must not exceed 10^{-5} if that happens the step size ds is decreased to a minimum of $ds_{min} = 10^{-10}$ mm.
- For each step (10.13) is calculated if the particle is within the volume of the solenoidal field of ATLAS defined to be $|z| < 2.65$ m, $\sqrt{x^2 + y^2} \leq 2.46$ m. Within the volume the field is 2 T.
- If the monopole is within the material of the beam pipe $34.3 \text{ mm} \geq \sqrt{x^2 + y^2} \geq 29 \text{ mm}$ then the momentum change is corrected by (10.6). If the monopole is a ‘Dyon’ carrying electric charge as well the Vavilov dE/dx is subtracted (4.1.2).
- The result is returned to the RK solver as a dp/ds estimate which is then applied to update $\{g, q, mass, \eta, p_T\}_i$.
- if the maximum propagation length of 50 m is reached, or the speed of the particle is less than $\beta < 0.02$ then the simulation is terminated.
- The output is all iteration steps along with current momentum and time.

Figure 10.9 is a visualisation produced from the simulation. The white lines are independent tracks produced by $g = 15g_D$ monopoles. The coloured dots are points where $dE/dx > 10$ MeV, the colour is proportional to the speed of the particle where **red** means $\beta \sim 0$ and **blue** is $\beta \sim 1$.

The simulation is limited by assuming the beam-pipe to be a simple tube, the magnetic field to be ideal and uniform and not least the energy depositions to be the mean value rather than Landau distributed. The phase space of the monopoles is also a source of uncertainty. With these caveats the results are but an illustration of the method and further studies can and should be undertaken to validate the claims below.

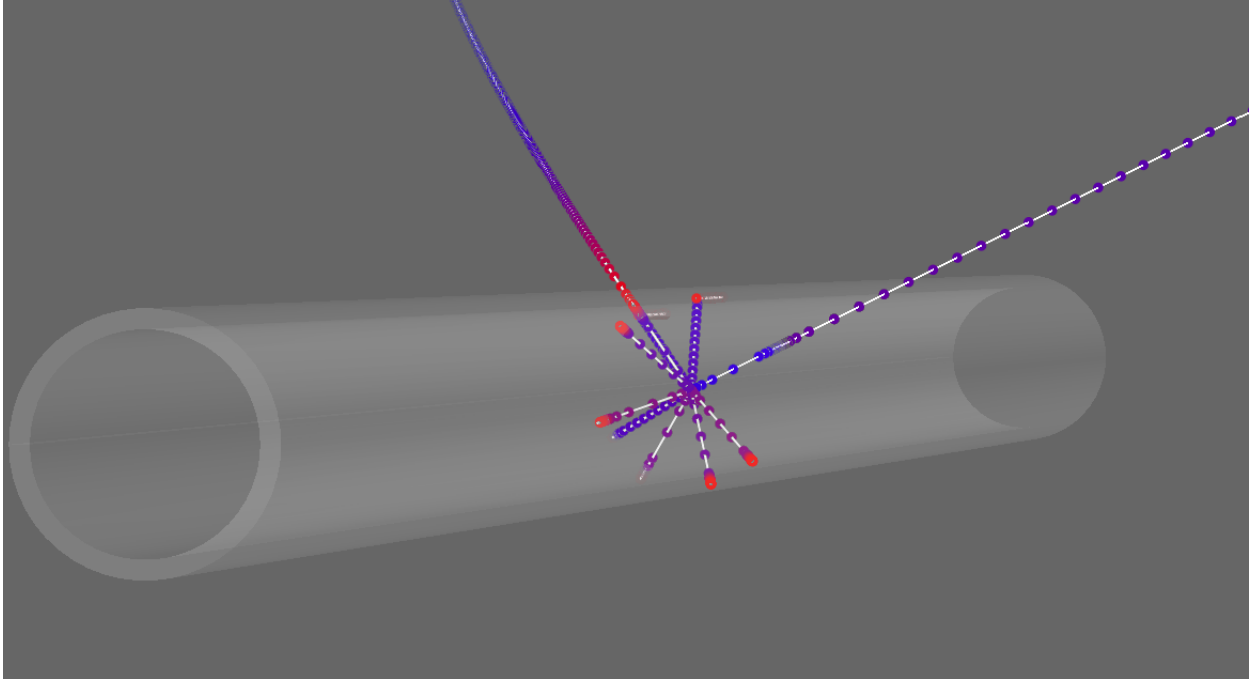


Figure 10.9: Snapshot of 10 simulated magnetic monopoles with $g = 15g_D$ and mass $600\text{GeV}/c^2$.

10.3.2 Most probable positions of trapped monopoles

The results in table 10.3 is produced by varying the charge $g = ng_D$ and the mass at each charge point. 5000 particles were simulated at each mass-charge point. The result is measured by counting all particles that stopped in the beam-pipe region due to energy loss.

Mass [GeV/c^2]	Magnetic charge [g_D]					
	1	5	10	15	20	30
600	0.0	0.0266	0.3042	0.8872	0.8172	0.88
1000	0.0004	0.0092	0.1252	0.223	0.8498	0.9614
1500	0.0006	0.0078	0.0594	0.3214	0.573	0.8102

Table 10.3: Fraction of magnetic monopoles stuck in the beam pipe in the simulation.

Table 10.3 show that the relationship between mass and charge is not trivial. We expect the range to be shorter in matter for particles with large charge. We would also expect that particles with large charges and smaller masses to be deflected more strongly in the magnetic field. In Figure 10.10 we see that high-charge samples do in fact ‘range out’ before the ones with less charge. The strict ordering comes from applying only the mean value (10.6) and not stochastic energy losses, this is illustrative when we want to study the basic trend.

The question raised in the beginning of this section was, where along the beam-pipe it would be the most relevant to analyse. In Figure 10.11 we see that in general the region around the interaction point is the most sensible place to start. Another feature in Figure 10.11 is the two edge bins at $|z| = 2.65\text{ m}$ which are the edges of the magnetic field. It was found that this effect arises when a monopole is trapped in the beam-pipe and *dragged* by the magnetic field outwards by studying the individual events with the event viewer. This effect is likely not found in a more realistic approach where nuclear binding and other effects are included.

Figure 10.10: Final position where monopoles are found at two mass points for charges $g_D > 4$.

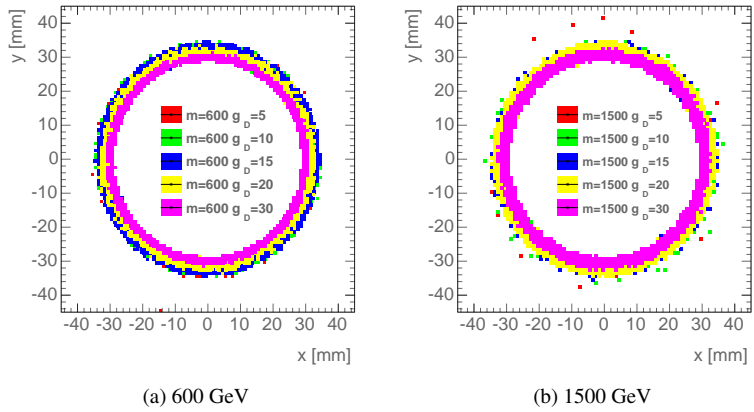
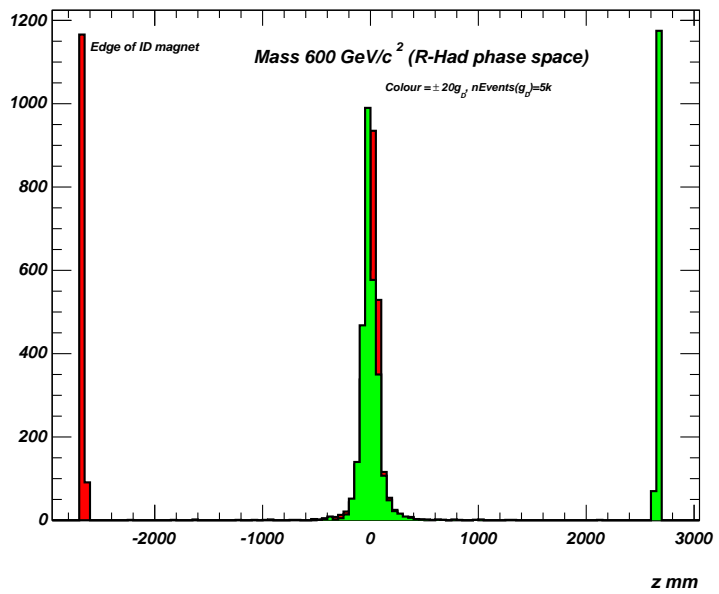


Figure 10.11: The final stopping points for magnetic monopoles with $g_D = 20$ and a mass of $600 \text{ GeV}/c^2$. The colours represent charge parity.



10.4 Conclusion

The hope for Split-Supersymmetry seems less bright with the discovery of the Higgs boson. Figure 10.7 show that the possible evolution of searches similar to the one in this thesis must be complemented by searches requiring the LLP to stay track-like if tighter constraints are to be placed on SSUSY. The balance between the Higgs limit on m_S , the overall sensitivity of ATLAS to LLPs and the realistic maximum amount of statistics generated over the lifetime of the experiment allows for only a narrow exclusion plane. At the time of writing the beam pipe in ATLAS is being replaced. The part of the old beam pipe that was situated around the interaction point seems to be an excellent place to begin a serious search programme for trapped magnetic monopoles at the LHC.

A famous dane once said that ‘it is hard to predict, especially the future’ it is no different when it comes to the future of particle physics. With the possibility of future precision colliders such as the International Linear Collider

(ILC) or TLEP with its 80 km circumference perhaps the future searches will be done indirectly by measuring deviations from the Standard Model rather than searching directly for new particles. The closure of the Standard Model prediction now makes the most economical strategy simply to disprove it by falsifying its predictions.

V

*Low mass dark matter
detection with IceCube*

Neutrinos interact solely through the weak and gravitational forces making them invisible to direct observation at the LHC due to the small associated scattering cross section. To study them in detail, dedicated neutrino experiments rely on either large volumes to increase the interaction probability or high intensity neutrino beams and dense stacks of detectors. Neutrinos are commonly involved in Standard Model processes and are therefore produced naturally in radioactive decay, atmospheric cosmic ray interactions and nuclear processes in the Sun, as well as more exotic astrophysical sources. The IceCube observatory at the South Pole is designed to study high-energy neutrinos of celestial origins with energies spanning 50 GeV to multiple PeVs [118]. Dark matter can be indirectly detected by IceCube by searching for neutrinos produced as secondary particles in dark matter self-annihilation processes. Weakly Interacting Massive Particles (WIMPs) are from an experimental point of view an interesting dark matter candidate (Sec. 3.5) as it is inert enough to serve as dark matter but still processes a detectable particle signature in the form of weak interactions. Supersymmetry (Sec. 3.2) provides WIMPs in the form of neutralinos (χ) enabling us to form predictions based on its phenomenology.

WIMPs could be captured by a massive object (stars, planets) after having scattered off nuclei leading them to accumulate in the gravitational potential within the object. The accumulation increases the rate of self-annihilation where the byproducts would be Standard Model particle pairs such as $\tau^+\tau^-$

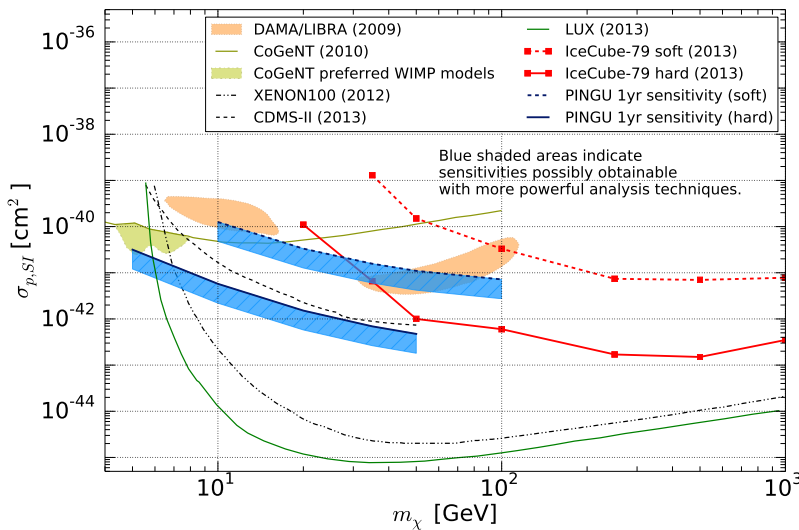


Figure 11.1: Spin independent WIMP sensitivity of PINGU with 40 detector strings. The dark blue regions mark possible improvements in sensitivity due to more optimised methods Ref. [61].

or $b\bar{b}$ [61]. The actual decay product and annihilation rate is model dependent. Previous IceCube searches [3] have shown sensitivity down to 20 GeV. The DAMA/LIBRA [18, 85], CDMS-II [4] and CoGeNT [2, 1] experiments all report possibility of anomalous signals in dark matter mass regions below 20 GeV. It has been proposed to upgrade IceCube with a low-energy infill that would increase the neutrino energy range down to 1 – 2 GeV, to allow the determination of the neutrino mass hierarchy (Sec. 2.5.4). The interest in this upgrade has increased significantly with the discovery of a non-zero θ_{13} (Sec. 2.5.3) mixing angle. This upgrade called the Precision IceCube Next Generation Upgrade (PINGU) [61] will also increase the sensitivity to indirect low-mass dark matter searches within the region of the anomalous results from the above experiments illustrated by the blue lines in Figure 11.1.

The studies presented in this section are focused on the development of novel ways to reconstruct neutrino events at these low energies, motivated by future indirect dark matter searches. In Chapter 12 a technique for reconstructing the interaction vertex, direction and energy of incoming neutrinos is presented. In Chapter 13 methods for identifying neutrino flavour is explored. These studies are by no means complete and they as the general design of the PINGU detector is still in development as of writing. The rest of this chapter provides a short introduction to the detectors in IceCube-PINGU, detailed references include [61, 120, 42].

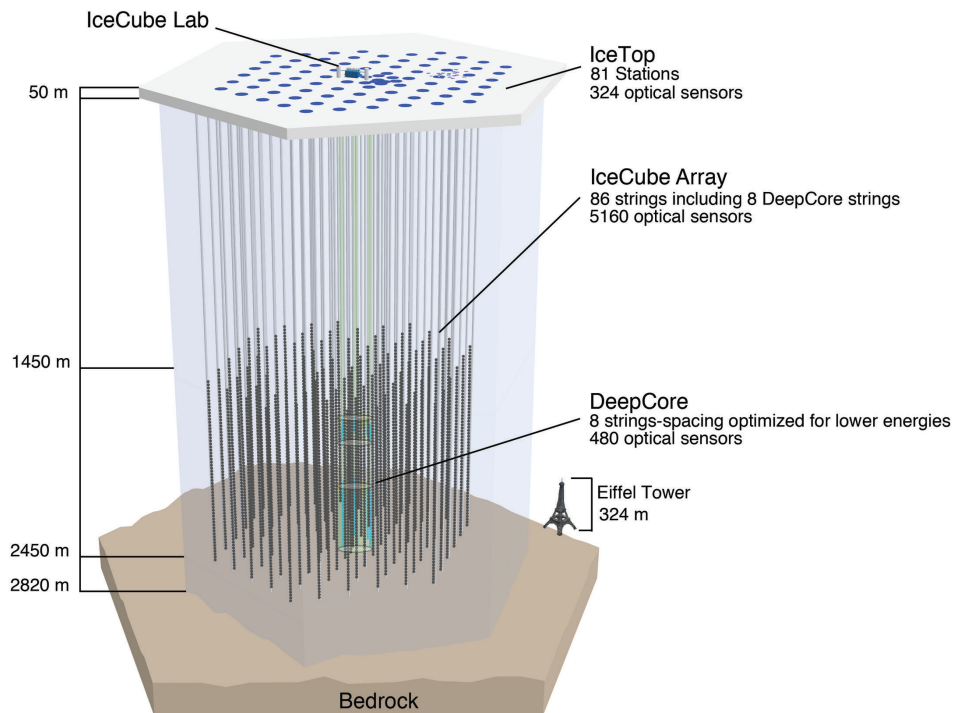


Figure 11.2: The IceCube Neutrino Observatory. The PINGU infill is to be situated within the DeepCore volume.

11.1 Detectors

The IceCube detector spans a cubic kilometre of ice at depths ranging from 1.45 to 2.45 km below surface level. It is located at the geographical South Pole in connection with the Amundsen-Scott South Pole Station. The detector is constructed as an array of Digital Optical Modules (DOMs) located on strings that are lowered into holes drilled in the ice (Figure 11.2). In the original IceCube geometry 78 strings are positioned in a hexagonal pattern with an inter-string distance of 125 m. Each string holds 60 DOMs that are positioned with a vertical spacing of 17 m. In total 5160 DOMs cover the 1km^3 volume. The distance between each string corresponds roughly to the attenuation length of photons in ice. This limits the directional sensitivity to muons coming from CC ν_μ interactions to energies where the range of the muon is roughly that distance. Neutrinos with energies below 100 GeV can be detected in the vicinity of the DeepCore infill which are 8 additional strings with a vertical DOM spacing of 7 m and at the centre of the IceCube array (Fig 11.2).

The detection principle is that secondary charged particles resulting from neutrino-nuclei scattering will be relativistic and emit Cherenkov photons (Sec. 4.1.6) in the detector volume. The photons propagate through the clear ice and is detected by the DOMs. Each DOM measures the number of photoelectrons (PE) produced as well as the precise time of arrival. These two measurements can be combined from all DOMs in the array to reconstruct the initial point of interaction as well as the direction and energy of the incoming neutrino.

11.1.1 Digital Optical Modules

Each DOM consist of a hemispherical 10-stage photo multiplier tube (PMT) 25.4 cm in diameter produced by Hamamatsu¹. The single photon time resolution for these PMTs is 2 ns [121] and their spectral acceptance lies within 350 to 650 nm with a peak sensitivity ~ 390 nm. At the peak sensitivity the Quantum Efficiency (QE) is 25% for the regular IceCube PMTs and 35% for the PMTs used in DeepCore. The PMT is housed in a spherical pressure vessel made of glass with a transparent gel interfacing the PMT and the sphere. Inside the sphere the PMTs are pointing downwards but the geometry of the PMT gives a roughly linear acceptance in $\cos\theta$ measured from downward vertical. Onboard the DOM is three Analog to Digital Converters (ADC) with complimentary readout thresholds allowing the reconstructing of pulses with μs durations at coarse time resolution (25 ns) and shorter pulses < 422 ns with 3.3 ns time resolution. The signals are unfolded into Photo Electron (PE) hits offline. In addition 12 LEDs are positioned on each DOM for calibration and determination of ice properties.

¹ Hamamatsu R7081-02

11.2 PINGU

The current PINGU proposal added an additional 20 or 40 strings to the centre of IceCube, each with 60 DOMs.

The DOM will slightly modified based on previous experiences the over-

Table 11.1: Two suggested geometries. The 20 geometry has proved insufficient for the neutrino mass hierarchy measurement, an is currently only investigated for supernova detection Ref. [61].

Number of Strings	Average Inter-string Spacing	Number of DOMs/String	Inter-DOM Spacing
20	26 m	60	5 m
40	20 m	60	5 m

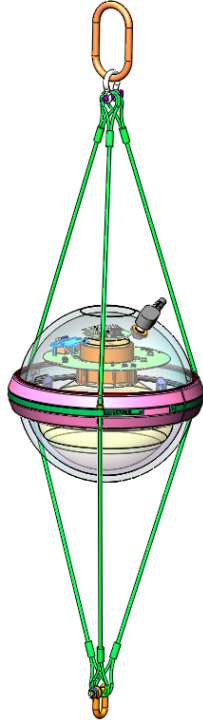


Figure 11.3: The proposed PINGU DOM Ref. [61].

all QE is expected to be comparable to the DeepCore DOMs. Due to the compact vertical spacing of the PINGU DOMs (PDOMs) a harness is proposed where the PDOMs are connected by carabiners (Figure 11.3) to inter-spacing steel wire allowing for quick deployment.

The placement of each string within IceCube is shown in Figure 11.4. Figure 11.4 is also available in Appendix A as a whole page.

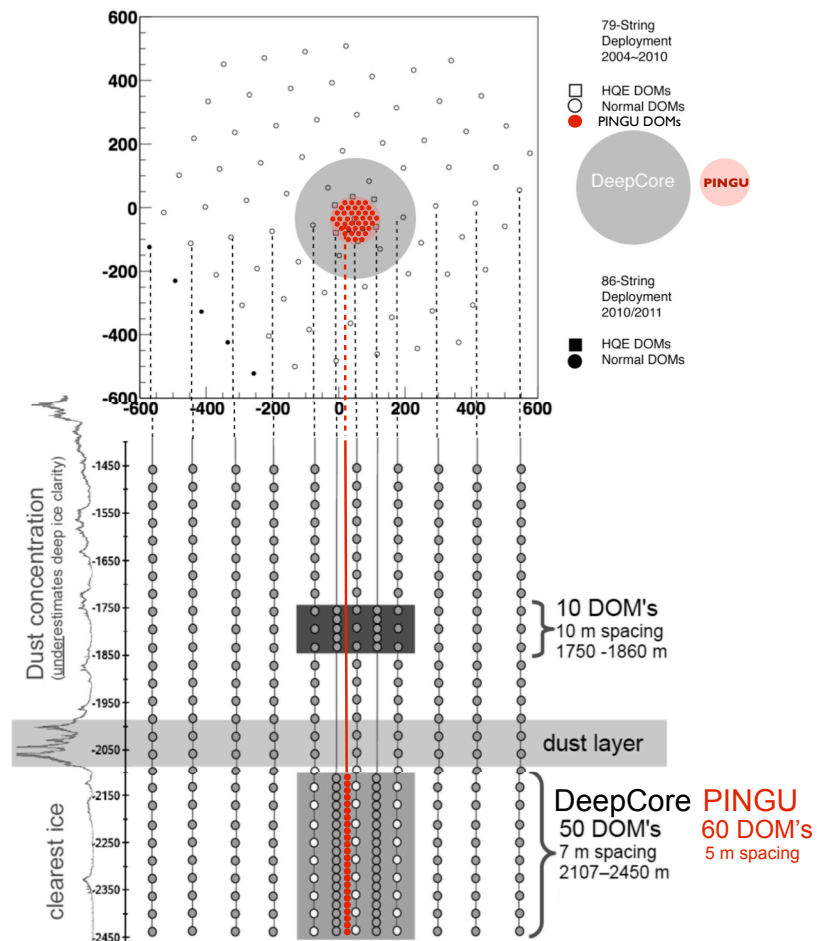


Figure 11.4: The proposed 40 string PINGU geometry Ref. [61].

12 Fast neutrino reconstruction with PINGU

Neutrino measurements with the IceCube detector relies on accurate estimation of the direction, energy, interaction point and flavor of the incoming neutrinos. To estimate these parameters, that customarily are defined as

$$\vec{\Phi} = \{E_\nu, azimuth_\nu, zenith_\nu, x_{\nu LX}, y_{\nu LX}, z_{\nu LX}, t_{\nu LX}, type\} \quad (12.1)$$

a likelihood maximisation method is employed. The likelihood function compares the detector response from a series of track segments with the actual data. That method requires significant look-up time and is in general time consuming.

While the method described in this paper is similar, the photonic tables have been replaced by a simple parametrization of the hit time signal for a given CC neutrino interaction.

12.1 Modelling light propagation in ice

The propagation speed of a photon with wavelength λ in ice is the phase speed of light due to traveling in a dielectric medium $c_{ice}(\lambda)$. A muon moving at a speed $\beta c_{vac} > c_{ice}$ emits Cherenkov radiation (see Sec. 4.1.6).

In Figure 12.1 a neutrino-nucleus interaction \vec{v} has taken place at $\vec{x} = \{t_0, x_0, y_0, z_0\}$ and a muon with energy E is emitted in a direction $\hat{\mu}$. A DOM is situated at $\vec{d} = \{d_x, d_y, d_z\}$ receives a signal at time t from photons emitted by the initial interaction at \vec{v} or somewhere along the muon trajectory. Depending on whether the signal was caused by a muon or the initial interaction the time would vary as the propagation length and time is different for the two scenarios

$$t_{direct} = t_0 + \frac{\|\vec{v} - \vec{d}\|}{c_{ice}}, \quad t_{muon} = t_0 + \frac{\|\vec{v} - \vec{e}\|}{\beta_{mu} c_{vac}} + \frac{\|\vec{e} - \vec{d}\|}{c_{ice}}. \quad (12.2)$$

In (4.31) we noted that $\cos \theta_c = (1/n(\lambda)\beta)$ which imply that for a medium with a refractive index $n(\lambda)$ a charged particle with a speed β will emit Cherenkov light at a specific angle relative to its trajectory. The Cherenkov angle θ_c allow us to calculate the position \vec{e} along the muon trajectory where, if the muon caused the signal, it should have been emitted. First we note that the point \vec{p} where the DOM position is perpendicular to the muon trajectory is

$$\vec{p} = \vec{v} + \hat{\mu} \left[(\vec{d} - \vec{v}) \cdot \hat{\mu} \right]. \quad (12.3)$$

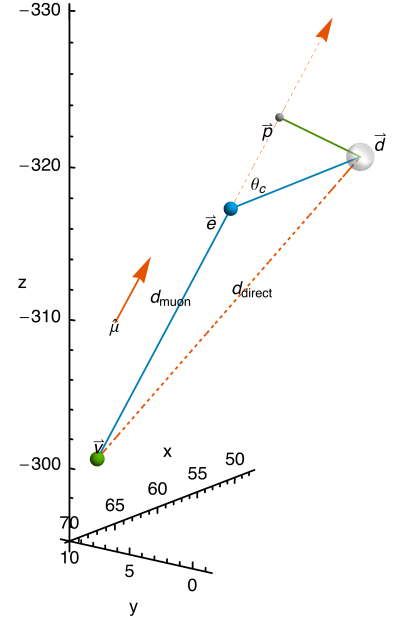


Figure 12.1: A signal from a neutrino-nucleus interaction can travel two ways before hitting a specific DOM in the model. The blue path d_{muon} is the distance of a signal emitted by a secondary muon that emits a Cherenkov photon at \vec{e} , while the dashed orange line d_{direct} assumes the photon to be emitted directly from the interaction

From Figure 12.1 we see that \vec{p} together with \vec{d} and the emission point \vec{e} forms a right-angled triangle. Based on plane geometry we calculate the position of \vec{e} with the knowledge of θ_c

$$\vec{e} = \vec{p} - \hat{\mu} \frac{\|\vec{p} - \vec{d}\|}{\tan \theta_c}. \quad (12.4)$$

Determining \vec{e} enables us to further require the point to lie within a distance spanned by the point of the vertex and a maximum distance the muon can travel before its energy falls below the Cherenkov emission threshold (4.32). Defining these to points as $\vec{i}p$ and $\vec{e}p$ for interaction point and end point respectively, \vec{e} must conform to

$$\|\vec{e} - \vec{e}p\| < \|\vec{i}p - \vec{e}p\| \text{ and } \|\vec{e} - \vec{i}p\| < \|\vec{i}p - \vec{e}p\| \quad (12.5)$$

for it to lie ‘on-track’. Having calculated these properties we can produce a log-likelihood estimate on a set of event parameters Φ by the following algorithm

Figure 12.2: Calculation of the log-likelihood llh for a set of parameters $E_\mu, \hat{\mu}, \vec{v}, v_t$ given a set of detector hits.

```

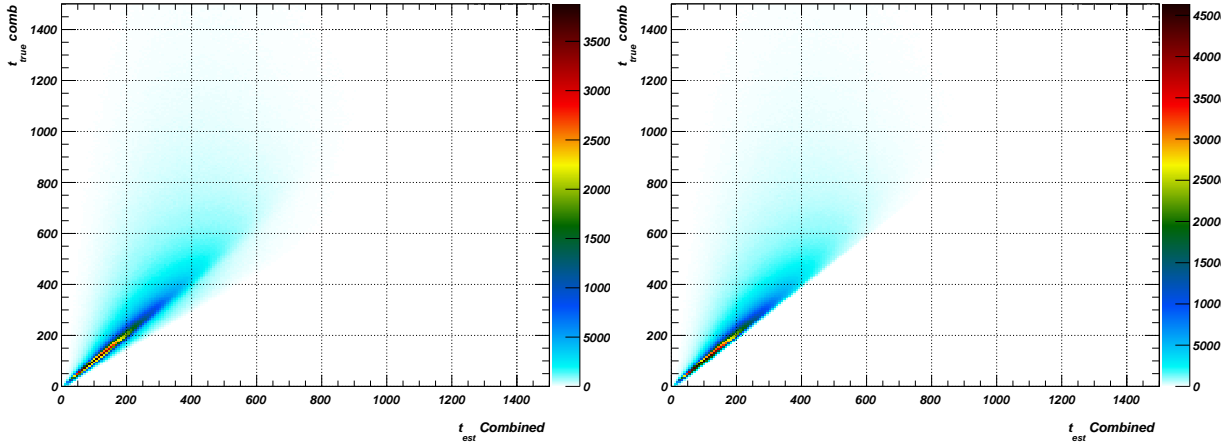
1: function COMPUTELOGLIKELIHOOD( $E_\mu, \hat{\mu}, \vec{v}, v_t$ )
2:    $llh \leftarrow 0$ 
3:   for each  $i$  dom hit,  $\vec{d}[i]$   $d_t[i]$  do
4:      $\vec{p} \leftarrow \vec{v} + \hat{\mu} \left[ (\vec{d}[i] - \vec{v}) \cdot \hat{\mu} \right]$ 
5:      $\vec{e} \leftarrow \vec{p} - \hat{\mu} \frac{\|\vec{p} - \vec{d}[i]\|}{\tan \theta_c}$ 
6:      $\vec{i}p \leftarrow \vec{v}$ 
7:      $\vec{e}p \leftarrow \text{MaxRange}(E_\mu)$ 
8:     if  $\|\vec{e} - \vec{e}p\| < \|\vec{i}p - \vec{e}p\|$  and  $\|\vec{e} - \vec{i}p\| < \|\vec{i}p - \vec{e}p\|$  then
9:        $t \leftarrow t_0 + \frac{\|\vec{v} - \vec{e}\|}{\beta_{mu} c_{vac}} + \frac{\|\vec{e} - \vec{d}[i]\|}{c_{ice}}$ 
10:     else
11:        $t \leftarrow t_0 + \frac{\|\vec{v} - \vec{d}[i]\|}{c_{ice}}$ 
12:     end if
13:      $llh \leftarrow llh + \log \text{Gauss}(t - d_t[i], \sigma[i])$ 
14:   end for
15:   return  $llh$ 
16: end function

```

The log-likelihood depends on the measurement uncertainty $\sigma[i]$ which in this ideal form is the only tolerance parameter.

The validity of this model can be inspected by plotting the estimate time of arrival at DOMs with the actual measured arrival time. In Figure 12.3 this comparison is made for two cases, one where the model assumes all signals originally emanated from the interaction vertex and another where the additional assumption that light that could have been emitted by a traversing muon is treated as such. The plots show that in general either of the models give a consistent response but also an upward and a downward dispersion from the expected 1:1 correlation. Any hits along the x -axis suggest that the model estimate is slower than the actual arrival time, while hits along the y -axis suggests that the model assumes to early an arrival time. The main difference between the two histograms is indeed that the model with the muon emission assumption correct the estimates that where too slow compared to the actual times, which can be taken a validation of the model.

The large dispersive region above the diagonal is a product of scattering in ice. This effect is stochastic and cumulative meaning that any deterministic model such as this one will be unable to correct it. Looking at the resolution



(a) Time of arrival correlation assuming a signals came directly from the interaction point $t_0 + \frac{\|\vec{v}-\vec{d}\|}{c_{ice}}$. (b) Time of arrival estimate assuming that $t_{muon} = t_0 + \frac{\|\vec{v}-\vec{e}\|}{\beta_{mu}c_{vac}} + \frac{\|\vec{e}-\vec{d}\|}{c_{ice}}$ is the model.

plot in Figure 12.4 it can be seen that the scattering indeed contributes significantly to the overall difference between the model and the actual time.

Figure 12.3: The estimated time of arrival at each DOM compared to the actual arrival time.

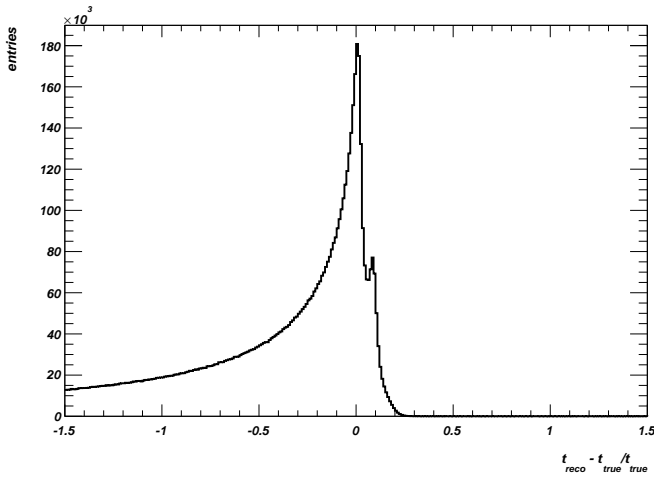


Figure 12.4: Time resolution based on the muon-track model.

The scattering length in the ice where PINGU is situated is roughly 30 meters (Depth less than $-200m$ in Figure 12.5). At each scatter the photon is deflected 20 degrees on average [119]. To reduce contributions from scattering all hits assumed to come from the primary interaction that has traveled more than 30 meters are discarded. The photons emitted from the muon track are kept. The small peak on the right side of central value in Figure 12.4 is caused by after pulses in the PMTs¹ and is removed by rejecting hits with an associated charge less than 0.65 PE. In Figure 12.6 the result of these cuts are shown.

The reduction in correctly estimated hits is quite dramatic. The peak moves from 180×10^3 to 150×10^3 further study may show if it is necessary to apply such hard cuts or if robustness can be won in the later likelihood estimation.

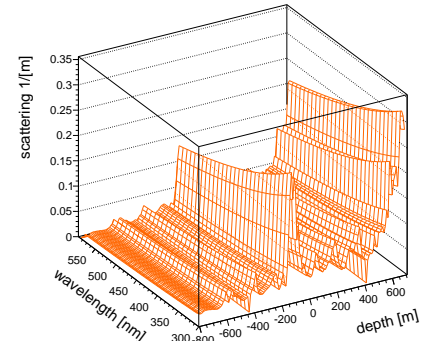


Figure 12.5: Inverse scattering length in Ice-Cube. <http://icecube.wisc.edu/~dima/work/WISC/ppc/spice/paper/a.pdf>

¹ This is based on simulation which explains the fairly well defined shape.

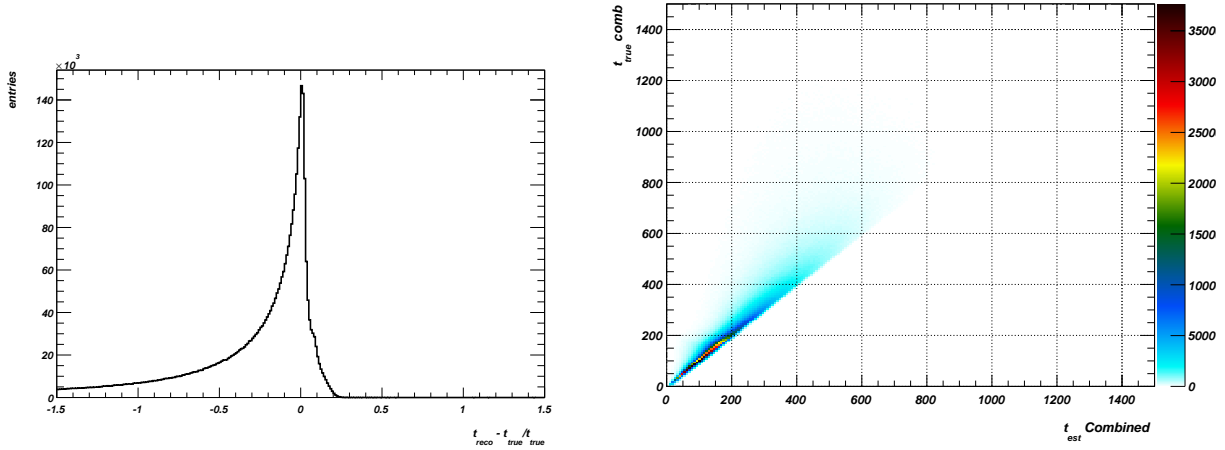


Figure 12.6: Time of arrival resolution after applying a charge and scattering cut.

(b)

12.1.1 Maximum Likelihood Estimation

In Maximum Likelihood Estimation (MLE) the goal is to produce the best estimate for a set of model parameters given data. This is done by calculating the likelihood that a parameter estimate leads to the observed data given the model. Multiple observations are multiplied to form a combined likelihood. As the individual probabilities typically are rather small numbers such multiplications can become numerically unstable when calculated at finite precision. It is therefore more practical to calculate the log-likelihood where the product of the contributions are added together

$$\mathcal{L}(\Phi) = \sum_{i=1}^n \log(f(t_i|\Phi)) \quad (12.6)$$

If we assume that an estimated arrival time t is normal distributed around the observed arrival time d_{t_i} with an uncertainty σ then the likelihood function is

$$f(d_{t_1}, d_{t_2}, \dots, d_{t_n} | t_1, t_2, \dots, t_n, \sigma) = \prod_i \frac{1}{\sigma\sqrt{2\pi}} \exp\left(-\frac{(t_i - d_{t_i})^2}{2\sigma^2}\right) \quad (12.7)$$

The logarithm of (12.7) is

$$\mathcal{L} = -n \log \sigma - \frac{n}{2} \log 2\pi - \frac{1}{2\sigma^2} \sum_{i=1}^n (t_i - d_{t_i})^2. \quad (12.8)$$

The best estimate of the parameters Φ is then

$$\arg \max_{\theta \in \Theta} \mathcal{L}(\Phi | t_1, \dots, t_n) \quad (12.9)$$

Where Θ is the full physical parameter space in which Φ can be found. The problem of maximising (12.9) requires a numerical sampling method that efficiently scans the eight-dimensional parameter space. Traditional methods such as iteration is impractical due to the curse of dimensionality [22] as the number of points in the parameter space grows geometrically with each added dimension. Markov Chain Monte Carlo methods such as the Metropolis–Hastings algorithm that performs a random walk in the parameter space

have been shown to perform acceptable with this number of dimensions. Recent developments in Bayesian inference techniques has led to what is known as Nested Sampling [94] which efficiently handles complicated likelihood spaces with multiple modalities. For this study an implementation called MULTINEST [48] is used. Figure 12.7 show how a projection in the parameter space might look like.

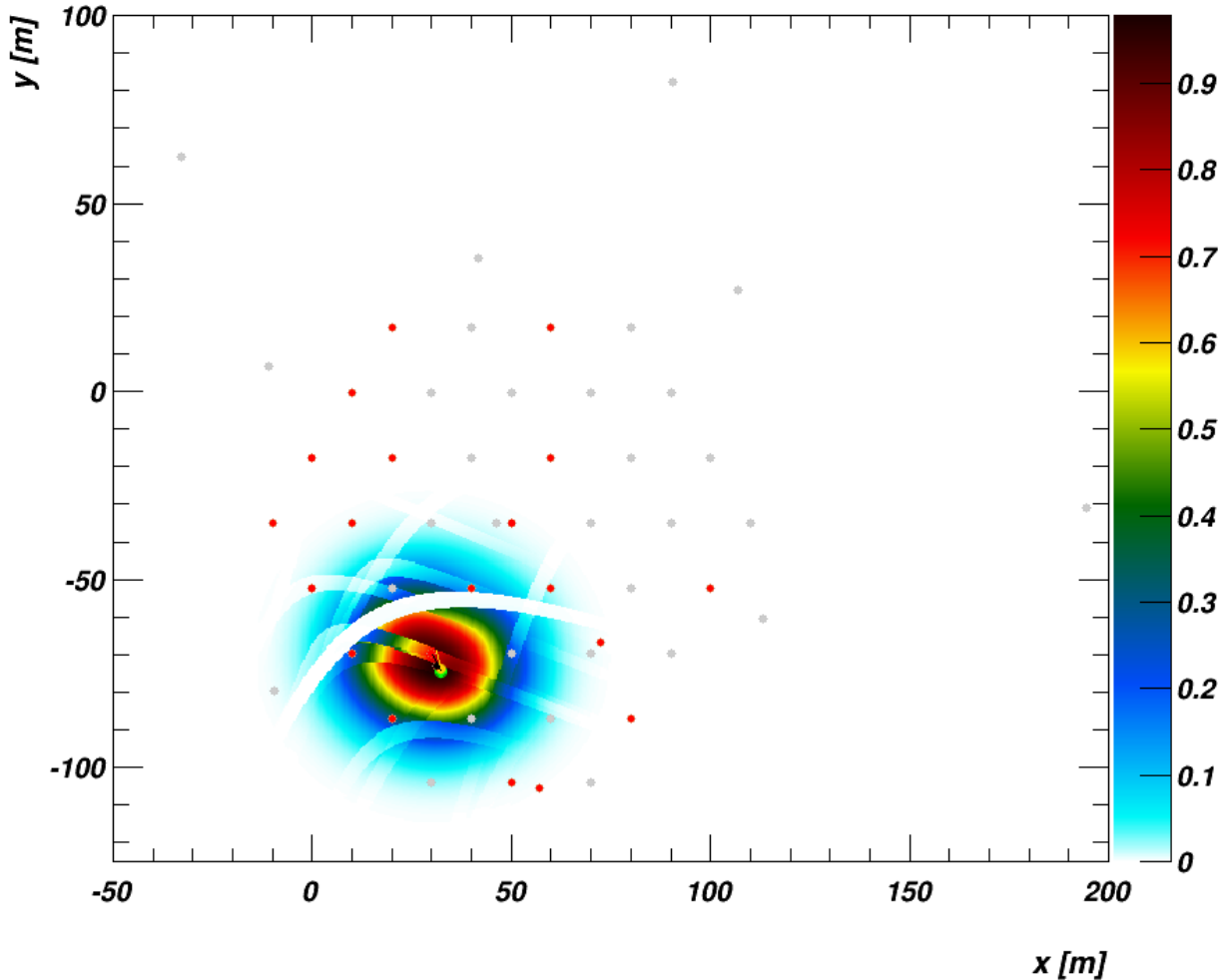


Figure 12.7: A likelihood space for a charge current ν_μ event with $E_\nu = 1.8$ GeV arriving in PINGU with a zenith angle of 1.6. The parameters not plotted are kept at their true values which means that the effective likelihood space will look different to the 8D fitter.

The green dot is the true parameter value and the yellow dot is the maximum likelihood in the plane. The grey dots are DOMs and the red dots are DOMs with associated hits that contributes to the likelihood estimates. The overall (gaussian) contour is contributions from isotropic photons assumed to come from the primary interaction. The parabolic lines are regions of likelihood space where the muon hypothesis exclude the probability of a vertex position. The lines coming out of the dots are the direction of the muon. For the estimated direction a similar plot is produced with the angle in Azimuth-Zenith co-ordinates. For this particular event with a neutrino energy of $E = 1.8$ GeV the projections show good agreement with the true value. It is not possible to plot the full likelihood space in any detail but

the result provides some indication that low-energy neutrino reconstruction is possible with the proposed PINGU geometry.

12.2 Preliminary results

The method outlined in this chapter is still quite immature and the results shown here should be taken with a pinch of salt.

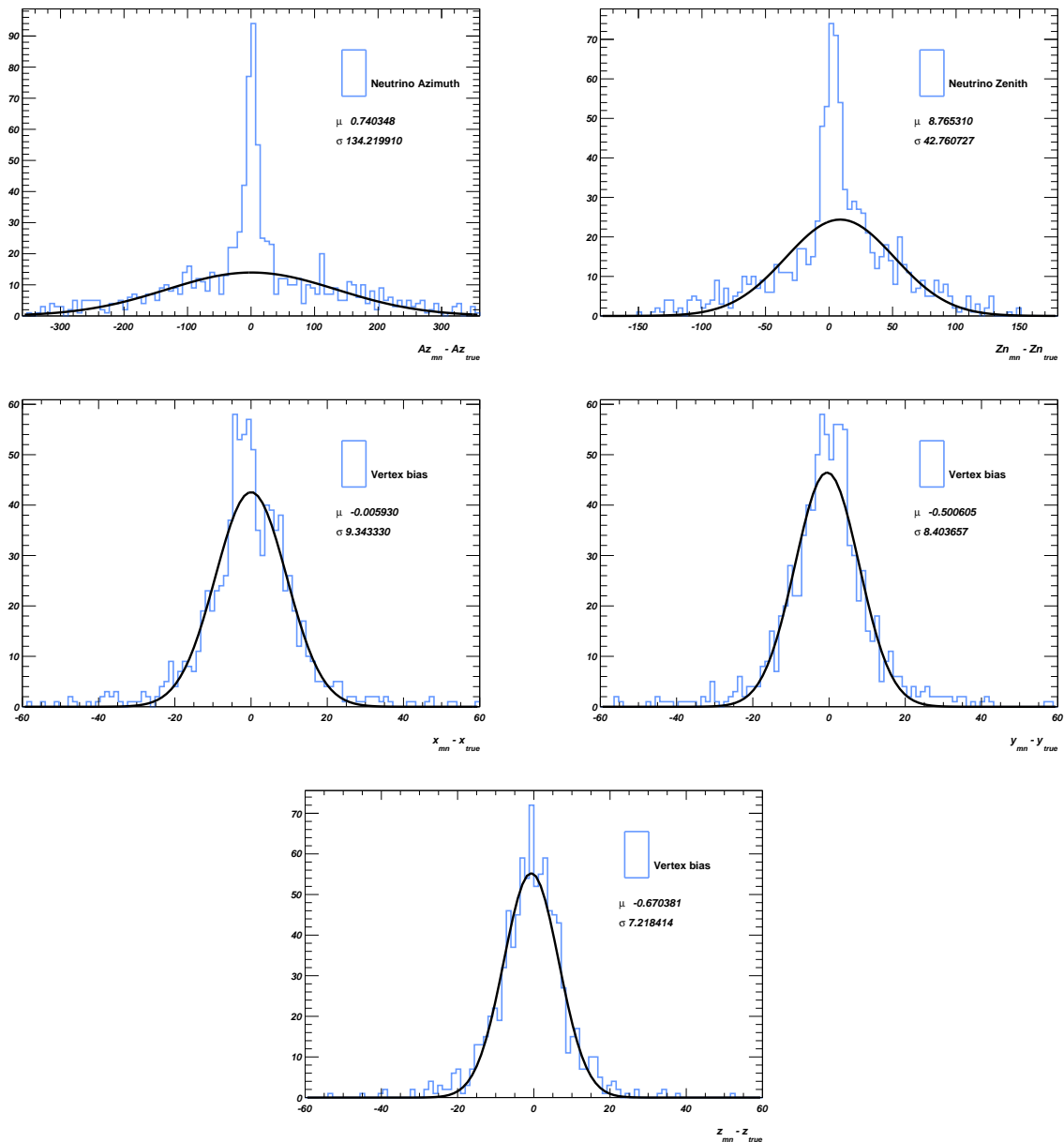


Figure 12.8: Position and direction reconstruction based on the method outlined in this chapter. Time and Energy distributions were not available at the time of writing.

In Figures 12.8 the variation from the true values are shown for reconstructions of $x, y, z, Azimuth, Zenith$. All plots show convergence around the true value, but it is too early to conclude anything regarding resolution.

12.3 Outlook and conclusion

The likelihood based reconstruction method presented here in a semi-conceptual form is still in its infancy. The average reconstruction time is around 25 seconds but is highly dependent on the required precision and factors affecting the modality of the likelihood space. It has not been possible to finalise the project within the timeframe of my contract (as it was undertaken a few months before the end) but the implementation is freely available for anyone who would like to continue the work ².

²<http://git.mdj.dk/mdj/icedam>

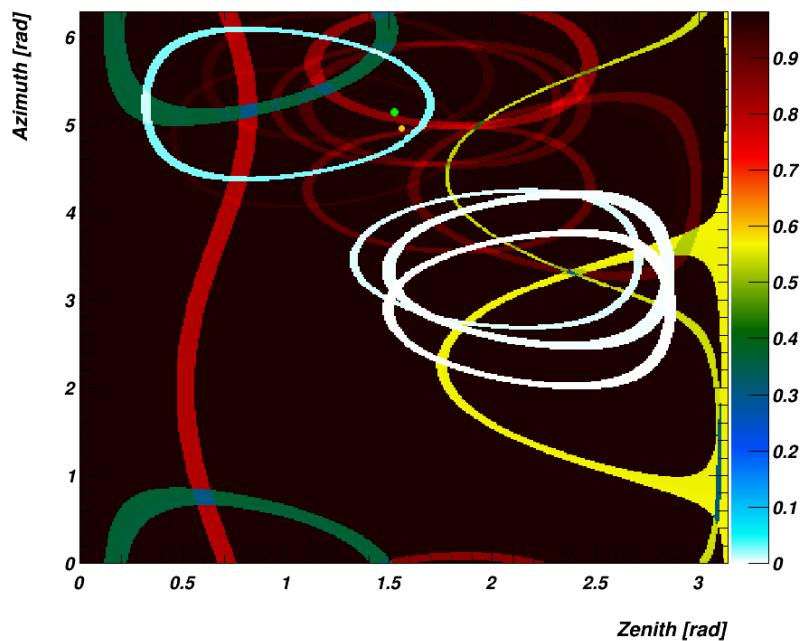


Figure 12.9: Likelihoods for the Azimuth-Zenith space for the same event as shown in Figure 12.7.

13 Particle identification of low energy neutrinos with PINGU

The event reconstruction outlined in the previous chapter assumes a track component to the event. If that is not the case the energy of the neutrino is miss calculated. Since only charge current muon neutrinos produces an extended track at low energies ($E < 50$ GeV) a way is needed to separate these neutrinos from other flavours and interactions. IceCube and PINGU are in principle huge calorimeters when the entire energy of a neutrino is absorbed within the volume. If an event is caused by a charge current electron neutrino, the resulting electron will quickly lose its energy due to bremsstrahlung (Sec. 4.1.3) creating an electromagnetic cascade within a few meters [118] of the primary interaction. Tracking the direction of incoming neutrinos requires the event signature to be elongated to such a degree that a dipole can be seen. This is most easily done when a muon produces hits over a range comparable with the detector spacing. If the muon escapes the volume or the primary interaction falls outside the detector volume the energy measurement is biased. Signatures involving neutral current interactions are harder to identify due to a new escaping neutrino. For all practical purposes we therefore separate all events into two categories: Cascade-like and Track-like. In the search for WIMP dark matter this is of little importance, but resolving the neutrino mass hierarchy (Sec. 2.5.4) requires knowledge of how many of the observed neutrinos are muon neutrinos. In Figure 12.3a we can find a first hint as to how it would be possible to separate Cascade-like from Track-like events. If any hits requires the assumption of a track to satisfy the arrival time it is a sign of a CC ν_μ event. The first technique explored in this chapter is based on this idea.

13.1 Superluminal hits

Assuming it is possible to find a well defined primary interaction point \vec{v} with a precise time estimate \vec{v}_t then any DOM hits \vec{d}_i with time measurements d_{t_i} that satisfy

$$N_{super} = \sum_{i=N_{ch}} (\sigma_i > (d_{t_i} - \vec{v}_t)) - \frac{\vec{d} - \vec{v}}{c_{ice}} \quad (13.1)$$

within uncertainties σ_i due to the intrinsic time resolution of the PMTs and scattering must have been emitted from a muon at a point closer to the DOM position than the vertex position. This method becomes gradually better at higher energies as the increased range of the muon allows for a larger devi-

ation of the signal relative to the time if the photon was emanating from the vertex.

Figure 13.1: The ratio between the number of hits that satisfies (13.1) and those that don't within PINGU assuming knowledge of the true position and time of the vertex.

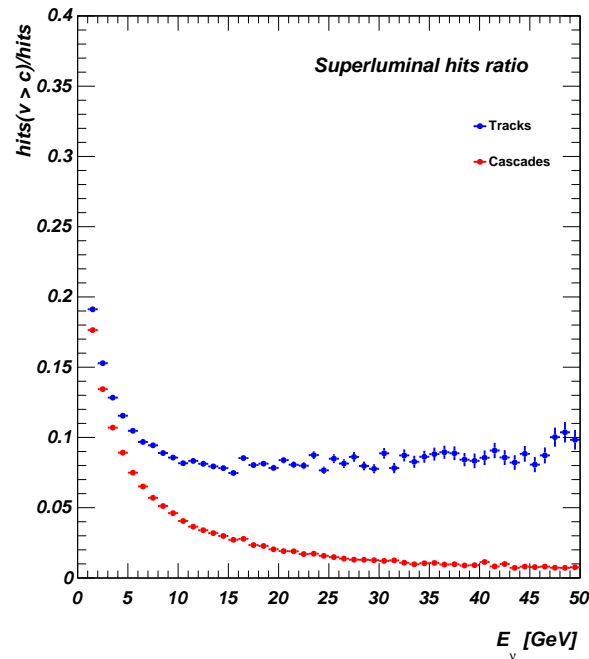


Figure 13.1 show how the increased range of the muon in higher- E_ν events leads to a larger separation between the cascade and track samples. An advantage with this method is that it can be calculated as part of the algorithm in Figure 12.2 at no additional cost.

13.2 Global Event Shapes

In (lepton) collider physics the overall event-shape contains meaningful information about the underlying event. A variable called ‘Thrust’ was invented in 1978 and used at PETRA to recognise n-jet events. The idea behind thrust is to find a direction \hat{n} that maximises the longitudinal momentum components

$$T = \max_{\hat{n}} \left(\frac{\sum_i |\vec{p}_i \cdot \hat{n}|}{\sum_i |\vec{p}_i|} \right). \quad (13.2)$$

If $T = 1$ all particles are produced along the direction \hat{n} . If $T = 0.5$ the particle momenta forms a perfectly isotropic sphere with equal contributions in all directions. For particle identification the idea is that the measure of an event-shape that can be either elongated or spherical fits perfectly with the two PID categories defined above. Since IceCube and PINGU don't have a concept of momentum it must be replaced by another metric. In the course of this study it has been tried to replace the momentum with the following metrics

- Summed charge: $m = \sum_i q_i$
- Spatial distance: $m = \|\vec{d}_i - \vec{v}\|$

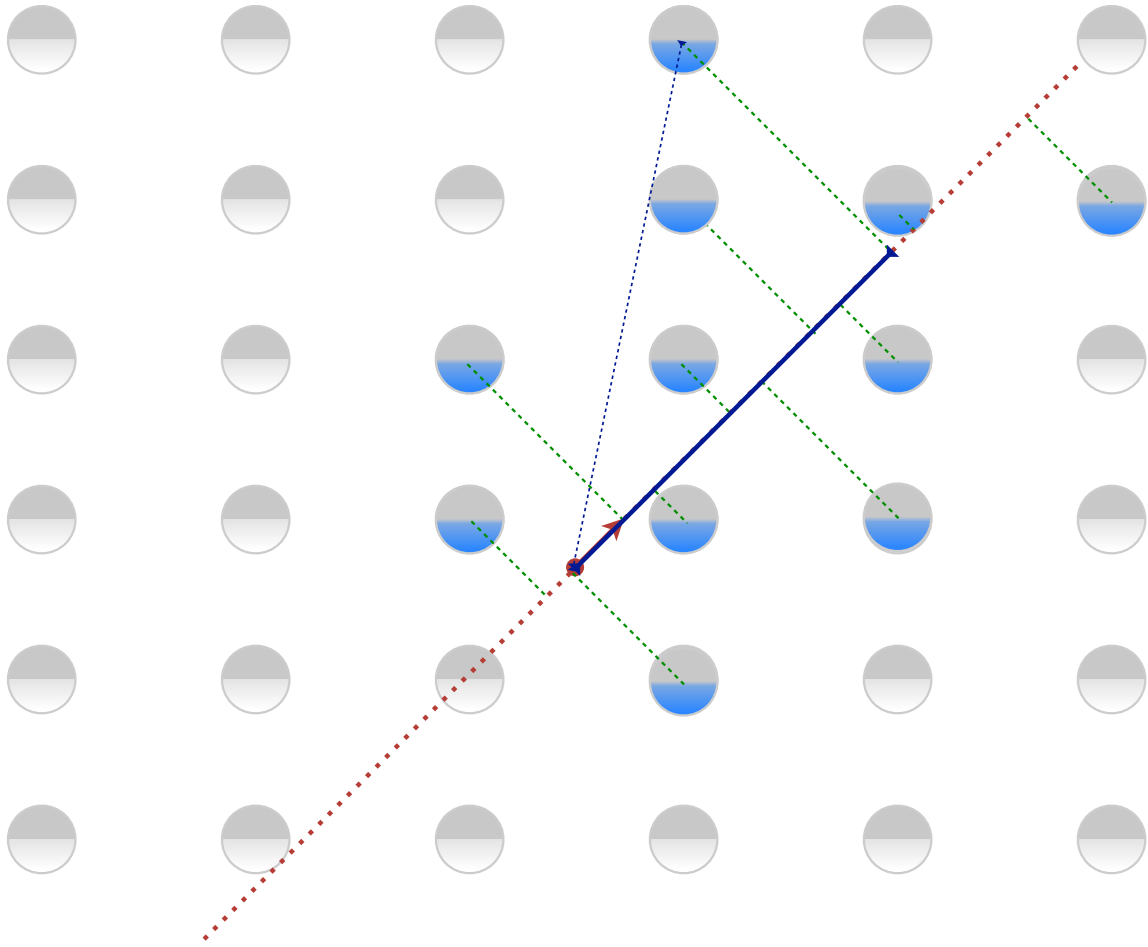


Figure 13.2: Illustration of the thrust calculation. Thrust is the sum of all the lengths from the vertex position to the point where each of the green dashed lines intersects the dotted red trajectory of the muon. Varying the trajectory will change the Thrust. For an event with a track contribution the largest sum would be found along the direction of the track.

- Unit sphere: $m = \sum_i (q_i) \exp\left(\frac{|\vec{d}_i - \vec{v}}{\lambda_{ice}}\right)$
- Time distance: $m = d_t - v_t$
- Space-time Interval: $m = \Delta r^2 - c^2 \Delta t^2$
- Absolute time $m = |d_t - v_t|$

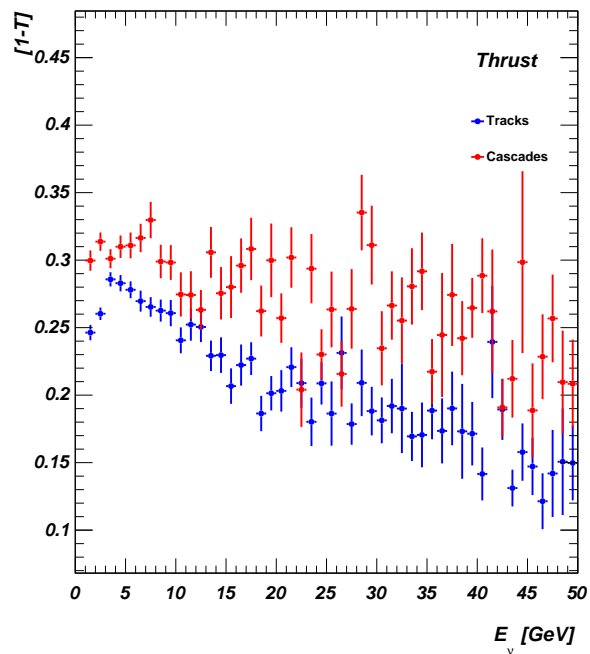
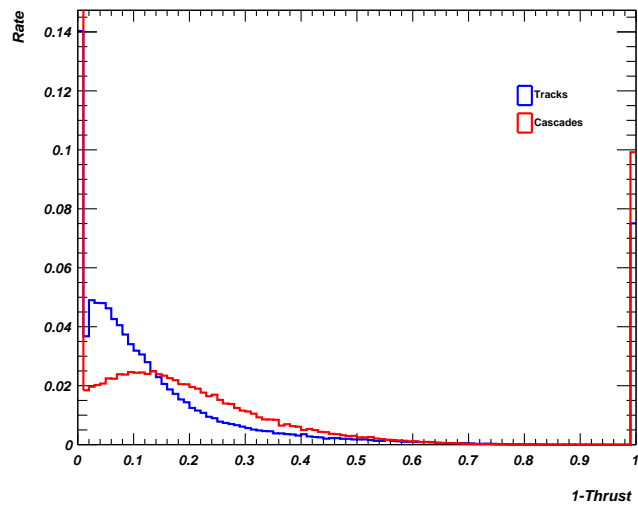
The metrics m modifies (13.2) by replacing \vec{p}_i

$$\vec{p}_i \leftarrow m \frac{\vec{d} - \vec{v}}{\|\vec{d} - \vec{v}\|}. \quad (13.3)$$

The direction \hat{n} is then found by maximising T with the MINUIT minimiser built into CERN's ROOT framework.

The principle is illustrated in Figure 13.2. The 11 blue DOMs in the figure are hit by photons. A muon is generated at the root of the red arrow and propagates in the direction of the arrow. For each DOM the dot product between the direction \hat{n} and the scaled distance \vec{p}_i is calculated. For the topmost DOM the thick blue line represent the magnitude of the dot product. The sum of these products are the thrust T . If \hat{n} is pointing in any other direction than along the trajectory the sum will become smaller. In figure 13.3 some preliminary results from the study are shown.

Figure 13.3: Results from the thrust algorithm. (a) $1 - T$ with the Space-time Interval metric. (b) Energy dependence assuming the metric is the summed charge on the DOM.



13.3 Conclusion

These early studies are still closer to the conceptual development stage than to full implementation. The first method is currently being pursued at Pennsylvania State University and the second at the Niels Bohr Institute. Early prototype code is found here: <http://git.mdj.dk/mdj/icedam/blob/master/IceConeReco/private/FrozenLEPVariables.cxx>.

14 *Thesis conclusion*

A search for hadronising long-lived massive particles at the Large Hadron Collider was conducted with the ATLAS detector. No excess events were found. Based on statistical analysis, upper limits on the production cross section were observed to be between 0.01 pb and 0.006 pb for colour octet particles with masses ranging from 300 GeV/ c^2 to 1400 GeV/ c^2 , and 0.01 pb to 0.004 pb for colour triplet particles. In the context of Supersymmetry with decoupled sfermion and sboson sectors (Split-SUSY) this gives a lower limit on the gluino mass of 989 GeV/ c^2 , and 683 GeV/ c^2 for the stop mass.

A new method was presented in Chapter 8 that improves the speed (β) estimation for long-lived particles in the ATLAS Tile calorimeter with a factor of 7 improvement in resolution at low- β and a factor of 2 at high- β . An additional advantage of the new method is that the β -response is flat within the range of acceptance ($0.2 < \beta \leq 0.9$) with an average β -resolution of 2.2%.

In Chapter 7, the resolution of the speed estimate using the ATLAS pixel tracker has been improved by a factor of 3 at low β to a factor of 2 at higher β . The new method also introduces a flat response compared with previous methods.

In Chapter 10.3, a simulation of magnetically charged monopoles was presented. Based on the simulation, magnetic monopoles with Dirac charges $g_D > 10$ will predominantly be trapped in the LHC beam-pipe if produced within ATLAS, two regions were identified as optimal for the extraction of the beam-pipe in a magnetometer-based search, one at the interaction point in the middle of the detector and the other at the end of the magnetic field where monopoles that are accelerated in the magnetic field while close to the beam-pipe will be brought to rest due to electromagnetic energy loss.

The proposed low-energy extension to the IceCube neutrino detector called PINGU will improve the neutrino sensitivity to $E_\nu \sim 1$ GeV. Motivated by indirect search for Dark Matter annihilation in the sun, a likelihood based reconstruction method was developed in Chapter 12 that allows neutrino interaction vertex, energy, and direction estimation at this lower energy. The method provides a fast estimate based on a newly developed parametric model and multi-dimensional nested sampling. In addition, two neutrino flavour detection algorithms were developed in Chapter 13 which allow separation of charge-current muon events from other neutrino events.

This thesis as a PDF file, illustrations, source code and personal datasets are available at:

<http://llp.gluino.com>

VI *Appendices*

A *Schematics*

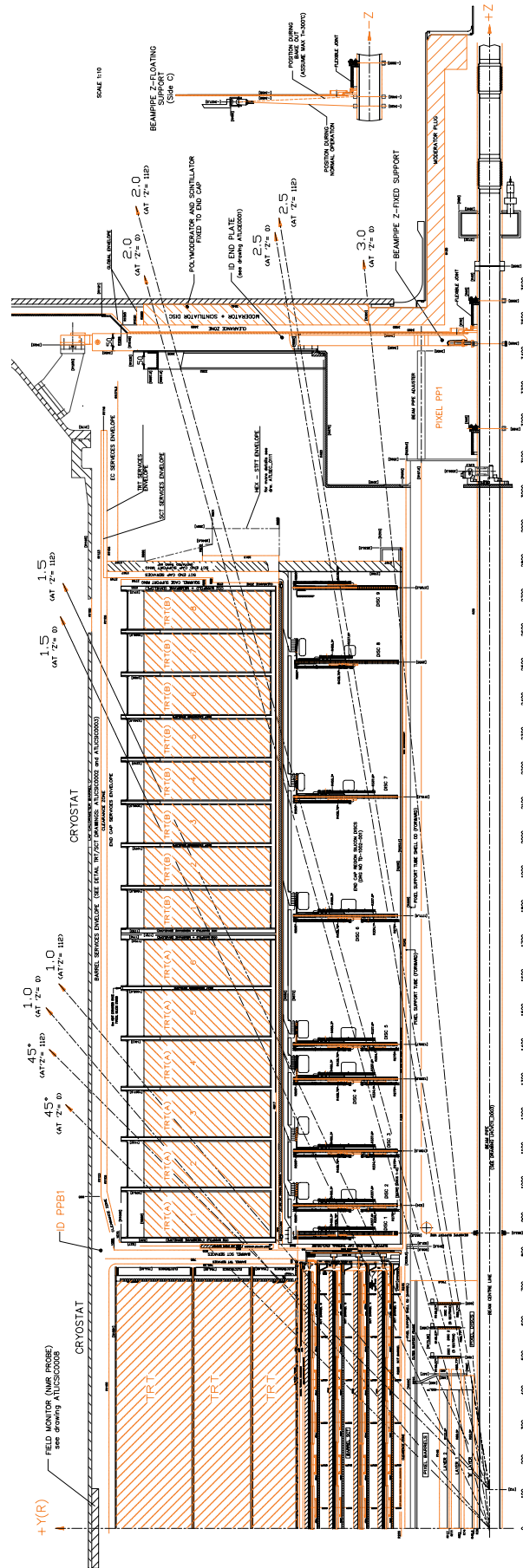


Figure A.1: ATLAS Inner detector $r-\phi$ view

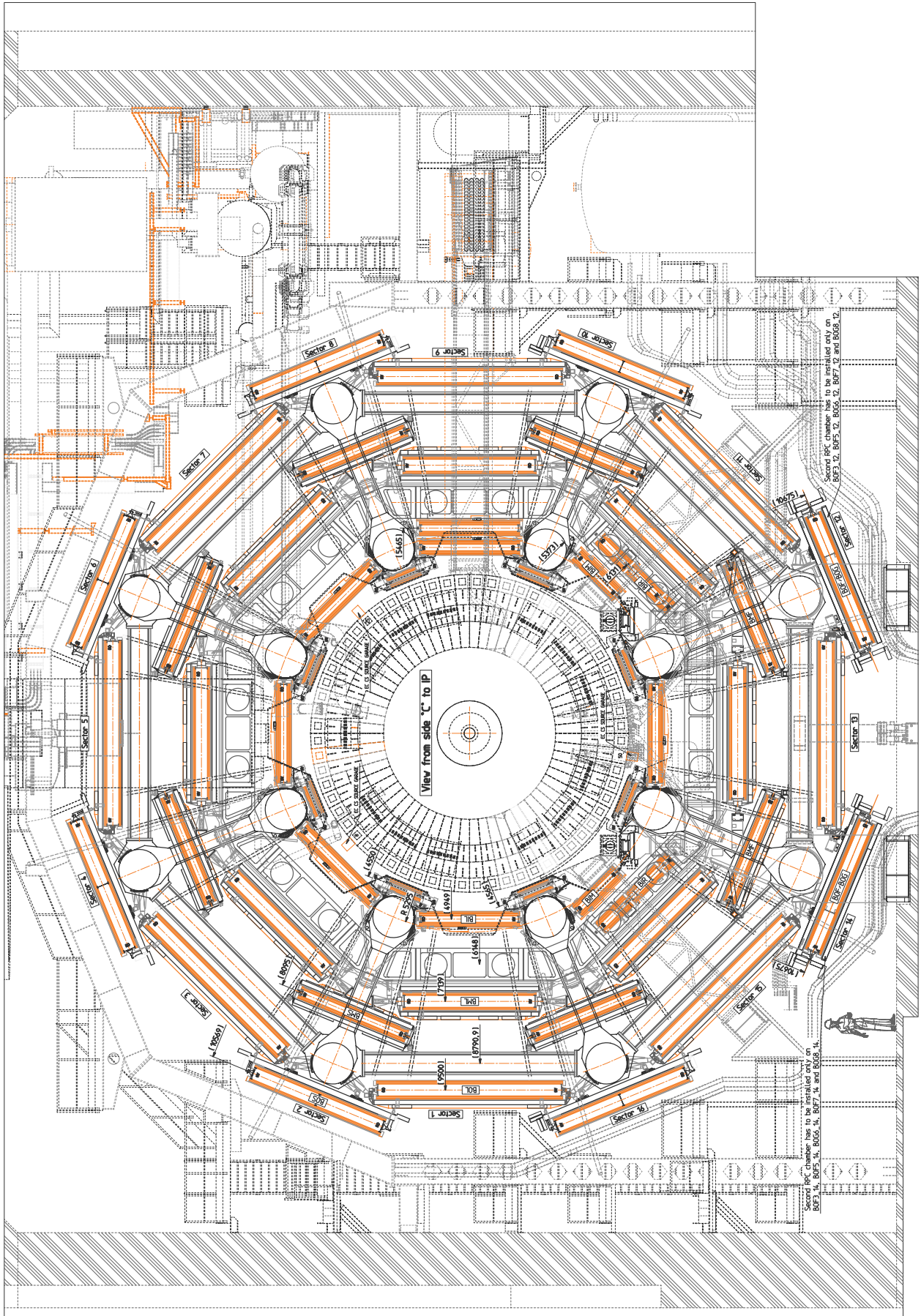


Figure A.2: ATLAS Muon spectrometer cross sectional view

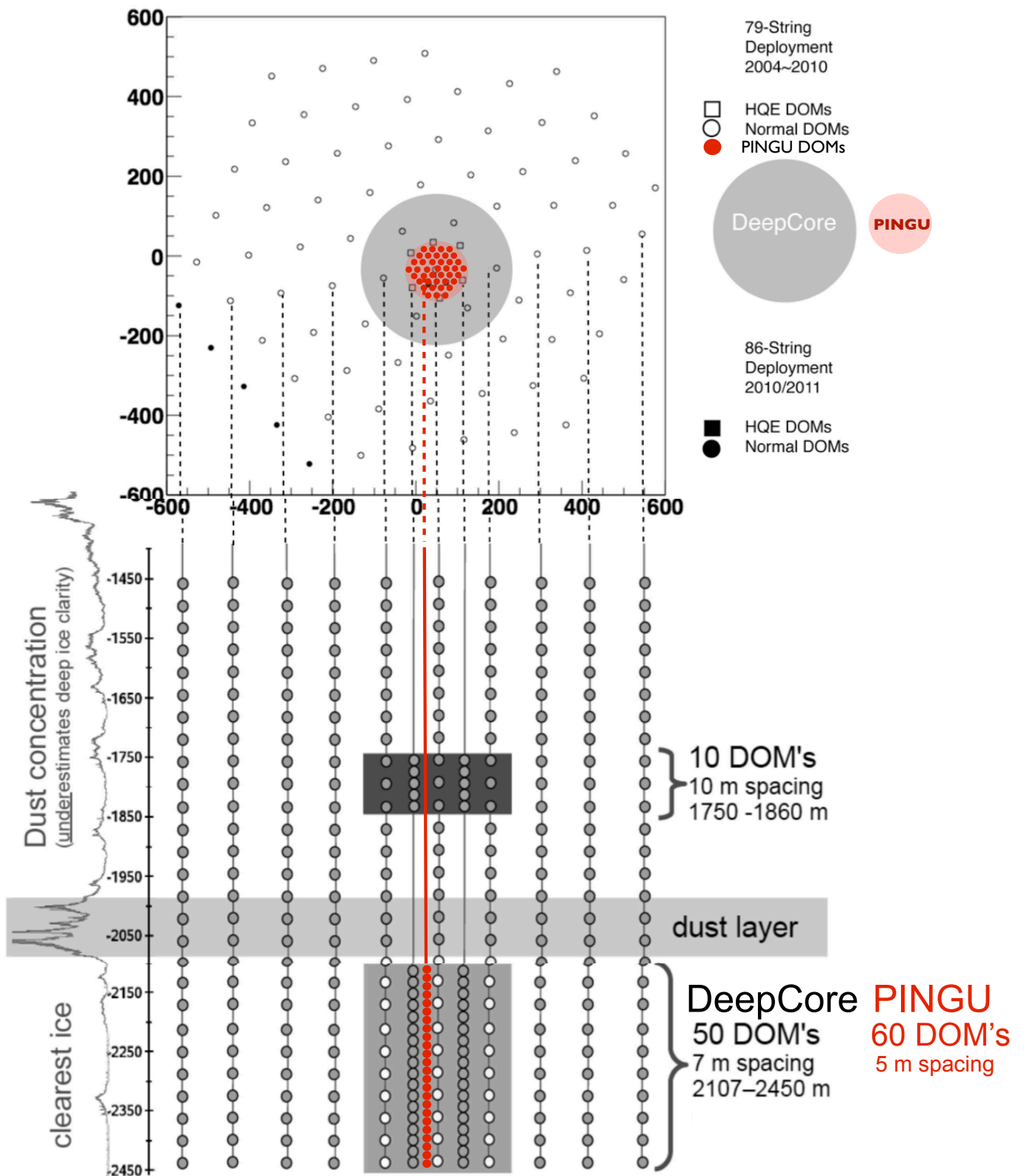


Figure A.3: The proposed 40 string PINGU geometry Ref. [61].

References

- [1] C E Aalseth, P S Barbeau, J Colaresi, J I Collar, J Diaz Leon, and others. Search for an Annual Modulation in a P-type Point Contact Germanium Dark Matter Detector. *Physical Review Letters*, 107:141301, 2011.
- [2] C E Aalseth and others. Results from a Search for Light-Mass Dark Matter with a P-type Point Contact Germanium Detector. *Physical Review Letters*, 106:131301, 2011.
- [3] M G Aartsen and others. Search for dark matter annihilations in the Sun with the 79-string IceCube detector. *Physical Review Letters*, 110:131302, 2013.
- [4] R Agnese and others. Silicon Detector Dark Matter Results from the Final Exposure of CDMS II. *Physical Review Letters*, 111:251301, 2013.
- [5] M G Albrow, D P Barber, P Benz, B Bošnjaković, J R Brooks, C Y Chang, A B Clegg, F C Ern e, P Kooijman, F K Loebinger, N A McCubbin, P G Murphy, A Rudge, J C Sens, A L Sessoms, J Singh, and J Timmer. Search for stable particles of charge ± 1 and mass \leq deuteron mass. *Nuclear Physics B*, 97(2):189–200, October 1975.
- [6] ALEPH, DELPHI, L3, OPAL, SLD, LEP Electro Weak Working Group, the SLD electroweak, and heavy flavour groups. Precision electroweak measurements on the Z resonance. *Physics reports*, 427:257–454, March 2006.
- [7] T Alv ager and R A Naumann. Search for stable heavy massive particles of positive integral charge. *Physics Letters B*, 24(13-14):647–648, June 1967.
- [8] L W Alvarez, P H Eberhard, R R Ross, and R D Watt. Search for Magnetic Monopoles in the Lunar Sample. *Science*, 167(3918):701–703, January 1970.
- [9] N Arkani-Hamed, S Dimopoulos, G F Giudice, and A Romanino. Aspects of Split Supersymmetry. *Nuclear Physics B*, 709(1-2):3–46, March 2005.
- [10] Nima Arkani-Hamed and Savas Dimopoulos. Supersymmetric unification without low energy supersymmetry and signatures for fine-tuning at the LHC. *Journal of High Energy Physics*, 2005(06):073–073, June 2005.
- [11] Nima Arkani-Hamed, Savas Dimopoulos, and Gia Dvali. The hierarchy problem and new dimensions at a millimeter. *Physics Letters B*, 429(3-4):263–272, June 1998.
- [12] ATLAS Collaboration. dE/dx measurement in the ATLAS Pixel Detector and its use for particle identification. Technical report, CERN, Geneva, 2011.
- [13] ATLAS Collaboration. Search for long-lived, multi-charged particles in pp collisions at using the ATLAS detector. *arXiv.org*, January 2013.

- [14] John N Bahcall, Aldo M Serenelli, and Sarbani Basu. New Solar Opacities, Abundances, Helioseismology, and Neutrino Fluxes. *The Astrophysical Journal*, 621(1):L85–L88, January 2005.
- [15] H Barber, T Bowen, D Delise, E Jenkins, J Jones, R Kalbach, and A Pifer. Predictions and measurements of mass spectra of the charged nucleonic component of cosmic rays at mountain altitude. *Physical Review D*, 22(11):2667–2687, December 1980.
- [16] W Beenakker. Squark and gluino production at hadron colliders. *Nuclear Physics B*, 492(1-2):51–103, May 1997.
- [17] W Beenakker, R Höpker, M Spira, and P M Zerwas. Squark and gluino production at hadron colliders. *Nuclear Physics B*, 492(1–2):51–103.
- [18] R Bernabei, P Belli, F Cappella, R Cerulli, C J Dai, A d’ Angelo, H L He, A Incicchitti, H H Kuang, X H Ma, F Montecchia, F Nozzoli, D Prospero, X D Sheng, R G Wang, and Z P Ye. New results from DAMA/LIBRA. *arXiv.org*, pages 39–49, February 2010.
- [19] Gianfranco Bertone, Dan Hooper, and Joseph Silk. Particle Dark Matter: Evidence, Candidates and Constraints. *arXiv.org*, April 2004.
- [20] H Bethe. Energy Production in Stars. *Physical Review*, 55(5):434–456, March 1939.
- [21] Andreas Birkedal, Andrew Noble, Maxim Perelstein, and Andrew Spray. Little Higgs dark matter. *Physical Review D*, 74(3):035002, August 2006.
- [22] Christopher M Bishop. *Pattern Recognition and Machine Learning*. Springer Verlag, August 2006.
- [23] N Bohr. II. On the theory of the decrease of velocity of moving electrified particles on passing through matter. *Philosophical Magazine Series 6*, 25(145):10–31, January 1913.
- [24] N Bohr. LX. On the decrease of velocity of swiftly moving electrified particles in passing through matter. *Philosophical Magazine Series 6*, 30(178):581–612, October 1915.
- [25] Frédérick Bordry. The High Luminosity LHC . In *ECFA High Luminosity LHC Experiments Workshop*, October 2013.
- [26] Michiel Botje, Jon Butterworth, Amanda Cooper-Sarkar, Albert De Roeck, Joel Feltesse, Stefano Forte, Alexander Glazov, Joey Huston, Ronan McNulty, Torbjörn Sjöstrand, and Robert Thorne. The PDF4LHC Working Group Interim Recommendations. January 2011.
- [27] Shikma Bressler and Shlomit Tarem. *Search for Heavy Long-Lived Charged Particles with the ATLAS detector in pp collisions at = 7 TeV*. PhD thesis, Technion, 2010.
- [28] Johannes Christof de Fine Licht. *GPU Simulation of Radiation in Matter*. PhD thesis, University of Copenhagen, July 2013.
- [29] Douglas Clowe, Maruša Bradač, Anthony H Gonzalez, Maxim Markevitch, Scott W Randall, Christine Jones, and Dennis Zaritsky. A Direct Empirical Proof of the Existence of Dark Matter. *The Astrophysical Journal*, 648(2):L109–L113, August 2006.
- [30] Sidney Coleman and Jeffrey Mandula. All Possible Symmetries of the S Matrix. *Physical Review*, 159(5):1251–1256, July 1967.
- [31] John A Conley, James S Gainer, JoAnne L Hewett, My Phuong Le, and Thomas G Rizzo. Supersymmetry without prejudice at the LHC. *Il Nuovo Cimento*, 71(7):1697–35, July 2011.

- [32] Gennaro Corcella, Ian G Knowles, Giuseppe Marchesini, Stefano Moretti, Kosuke Odagiri, Peter Richardson, Michael H Seymour, and Bryan R Webber. HERWIG 6: an event generator for hadron emission reactions with interfering gluons (including supersymmetric processes). *Journal of High Energy Physics*, 2001(01):010–010, January 2001.
- [33] Laura Covi, Hang Bae Kim, Jihn E Kim, and Leszek Roszkowski. Axinos as dark matter. *Journal of High Energy Physics*, 2001(05):033–033, May 2001.
- [34] C L Cowan, F Reines, F B Harrison, H W Kruse, and A D McGuire. Detection of the Free Neutrino: a Confirmation. *Science*, 124(3212):103–104, July 1956.
- [35] G Cowan and E Gross. Discovery significance with statistical uncertainty in the background estimate, May 2008.
- [36] Raymond Davis, Don S Harmer, and Kenneth C Hoffman. Search for Neutrinos from the Sun. *Physical Review Letters*, 20(21):1205–1209, May 1968.
- [37] Savas Dimopoulos, David Eichler, Rahim Esmailzadeh, and Glenn Starkman. Getting a charge out of dark matter. *Physical Review D*, 41(8):2388–2397, April 1990.
- [38] Scott Dodelson and Lawrence Widrow. Sterile neutrinos as dark matter. *Physical Review Letters*, 72(1):17–20, January 1994.
- [39] Boris Dolgoshein. Transition radiation detectors. *Nuclear Instruments and Methods in Physics Research Section A: Accelerators, Spectrometers, Detectors and Associated Equipment*, 326(3):434–469, March 1993.
- [40] A S Eddington. The Internal Constitution of the Stars. *The Internal Constitution of the Stars*, Cambridge: Cambridge University Press, 1926. ISBN 9780521337083., -1, 1926.
- [41] John Ellis, V Mayes, and D Nanopoulos. Ultrahigh-energy cosmic rays particle spectra from crypton decays. *Physical Review D*, 74(11):115003, December 2006.
- [42] Sebastian Euler. *Observation of oscillationsof atmospheric neutrinos with the IceCube Neutrino Observatory*. PhD thesis, physik.rwth-aachen.de.
- [43] Lyndon Evans. The Large Hadron Collider. *New Journal of Physics*, 9(9):335–335, September 2007.
- [44] Lyndon Evans and Philip Bryant. LHC Machine. *Journal of Instrumentation*, 3(08):S08001–S08001, August 2008.
- [45] M Fairbairn, A C Kraan, D A Milstead, and T Sjöstrand. ScienceDirect.com - Physics Reports - Stable massive particles at colliders. *Physics reports*, 2007.
- [46] E Fehlberg. Classical fourth- and lower order Runge-Kutta formulas with stepsize control and their application to heat transfer problems. *Computing*, 6(1-2):61–71, March 1970.
- [47] Jonathan Feng, Arvind Rajaraman, and Fumihiko Takayama. Superweakly Interacting Massive Particles. *Physical Review Letters*, 91(1):011302, July 2003.
- [48] F Feroz, M P Hobson, and M Bridges. MultiNest: an efficient and robust Bayesian inference tool for cosmology and particle physics. *Monthly Notices of the Royal Astronomical Society*, 398(4):1601–1614, October 2009.
- [49] Roshan Foadi, Mads Frandsen, Thomas Rytov, and Francesco Sannino. Minimal walking technicolor: Setup for collider physics. *Physical Review D*, 76(5):055005, September 2007.

- [50] Joshua Frieman, Graciela Gelmini, Marcelo Gleiser, and Edward Kolb. Primordial Origin of Non-topological Solitons. *Physical Review Letters*, 60(21):2101–2104, May 1988.
- [51] Stefano Frixione and Bryan R Webber. Matching NLO QCD computations and parton shower simulations. *Journal of High Energy Physics*, 2002(06):029–029, June 2002.
- [52] G F Giudice and R Rattazzi. Theories with gauge-mediated supersymmetry breaking. *Physics reports*, 322(6):419–499, December 1999.
- [53] Gian F Giudice and Alessandro Strumia. Probing High-Scale and Split Supersymmetry with Higgs Mass Measurements. August 2011.
- [54] Kim Griest, Agnieszka M Cieplak, and Matthew J Lehner. New Limits on Primordial Black Hole Dark Matter from an Analysis of Kepler Source Microlensing Data. *Physical Review Letters*, 111(18):181302, October 2013.
- [55] D Griffiths. *Introduction to Elementary Particles - David Griffiths - Google Books*. 2008.
- [56] Claus Grupen and Boris Shwartz. *Particle Detectors*. Cambridge University Press, March 2008.
- [57] Rudolf Haag, Jan T Łopuszański, and Martin Sohnius. All possible generators of supersymmetries of the S-matrix. *Nuclear Physics B*, 88(2):257–274, 1975.
- [58] S Hellman, M Johansen, R Mackeprang, P Mermod, D Milstead, C Ohm, and A Solodkov. Measuring time-of-flight and identifying exotic stable massive particles with the ATLAS Tile calorimeter. Technical Report ATL-COM-TILECAL-2009-028, The ATLAS Collaboration, 2009.
- [59] T Hemmick, D Elmore, T Gentile, P Kubik, S Olsen, D Ciampa, D Nitz, H Kagan, P Haas, P Smith, B McInTeer, and J Bigeleisen. Search for low-Z nuclei containing massive stable particles. *Physical Review D*, 41(7):2074–2080, April 1990.
- [60] Hardy Hodges. Mirror baryons as the dark matter. *Physical Review D*, 47(2):456–459, January 1993.
- [61] IceCube-PINGU Collaboration. Letter of Intent: The Precision IceCube Next Generation Upgrade (PINGU). January 2014.
- [62] Frederick E James. *Statistical Methods in Experimental Physics; 2nd ed*. World Scientific, Singapore, 2006.
- [63] M D Joergensen. *Search for long lived massive particles with the ATLAS detector at the LHC*. PhD thesis, cds.cern.ch, February 2011.
- [64] Kjell Johnsen. The ISR in the time of Jentschke. *CERN Courier*, May 2003.
- [65] Boris Kayser. Neutrino Mass, Mixing, and Flavor Change. November 2002.
- [66] A C Kraan, J B Hansen, and P Nevski. Discovery potential of R-hadrons with the ATLAS detector. *Il Nuovo Cimento*, 49(2):623–640, December 2006.
- [67] Aafke Christine Kraan. *Interactions of heavy stable hadronising particles*. PhD thesis, University of Copenhagen, November 2004.
- [68] Alexander Kusenko and Mikhail Shaposhnikov. Supersymmetric Q-balls as dark matter. *Physics Letters B*, 418(1–2):46–54, January 1998.

- [69] R Leitner, P Tas, and V V Shmakova. Time resolution of the ATLAS Tile calorimeter and its performance for a measurement of heavy stable particles. (ATL-TILECAL-PUB-2007-002. ATL-COM-TILECAL-2007-008. CERN-ATL-COM-TILECAL-2007-008), 2007.
- [70] LHC Higgs Cross Section Working Group. Handbook of LHC Higgs Cross Sections: 2. Differential Distributions. *cds.cern.ch*, January 2012.
- [71] R Mackeprang. *Stable Heavy Hadrons in ATLAS*. PhD thesis, Niels Bohr Institute, University of Copenhagen, August 2007.
- [72] A D Martin, W J Stirling, R S Thorne, and G Watt. Parton distributions for the LHC. *Il Nuovo Cimento*, 63(2):189–285, July 2009.
- [73] Stephen P Martin. A Supersymmetry Primer. September 1997.
- [74] F Moulin. Magnetic monopoles and Lorentz force. March 2002.
- [75] E Noether. Invariante Variationsprobleme. *Nachrichten von der Gesellschaft der Wissenschaften zu Göttingen, Mathematisch-Physikalische Klasse*, 1918:235–257, 1918.
- [76] S Nussinov. Technocosmology — could a technibaryon excess provide a “natural” missing mass candidate? *Physics Letters B*, 165(1–3):55–58.
- [77] J H Oort. The force exerted by the stellar system in the direction perpendicular to the galactic plane and some related problems. *Bull. Astron. Inst. Netherlands*, 6:249–287, 1932.
- [78] W Pauli. Liebe Radioaktive Damen und Herren. December 1930.
- [79] Michael E Peskin and Daniel V Schroeder. *An Introduction To Quantum Field Theory*. Westview Press, October 1995.
- [80] B Pontecorvo. Neutrino Experiments and the Problem of Conservation of Leptonic Charge. *Soviet Journal of Experimental and Theoretical Physics*, 26:984, May 1968.
- [81] P B Price and K Woschnagg. Role of group and phase velocity in high-energy neutrino observatories. *Astroparticle Physics*, 15(1):97–100, March 2001.
- [82] F Ragusa. An Introduction to Charged Particles Tracking. In *Italo-Hellenic School of Physics 2006 The Physics of LHC: Theoretical Tools and Experimental Challenges*. Università di Milano, Italy, April 2006.
- [83] A Roeck, H P Hächler, A M Hirt, M D Joergensen, A Katre, P Mermod, D Milstead, and T Sloan. Development of a magnetometer-based search strategy for stopped monopoles at the Large Hadron Collider. *Il Nuovo Cimento*, 72(12):2212, December 2012.
- [84] A Roeck, A Katre, P Mermod, D Milstead, and T Sloan. Sensitivity of LHC experiments to exotic highly ionising particles. *Il Nuovo Cimento*, 72(4):1985–18, April 2012.
- [85] C Savage, G Gelmini, P Gondolo, and K Freese. Compatibility of DAMA/LIBRA dark matter detection with other searches. *JCAP*, 0904:010, 2009.
- [86] M Schmidt and H Lipson. Distilling Free-Form Natural Laws from Experimental Data. *Science*, 324(5923):81–85, April 2009.
- [87] H C Schultz-Coulon. Lectures on Interactions of Particles with Matter . In *kip.uni-heidelberg.de*, December 2011.

- [88] Géraldine Servant and Tim M P Tait. Is the lightest Kaluza–Klein particle a viable dark matter candidate? *Nuclear Physics B*, 650(1-2):391–419, February 2003.
- [89] Gary Shiu and Lian-Tao Wang. D matter. *Physical Review D*, 69(12):126007, June 2004.
- [90] Yakov M Shnir. *Magnetic Monopoles*. Springer Berlin Heidelberg, Berlin, Heidelberg, 2005.
- [91] Peter Sigmund. *Particle Penetration and Radiation Effects*. General Aspects and Stopping of Swift Point Charges. Springer, March 2006.
- [92] Torbjörn Sjöstrand. Conversation regarding gluon-gluino fraction in R-Hadrons.
- [93] Torbjörn Sjöstrand, Stephen Mrenna, and Peter Skands. PYTHIA 6.4 physics and manual. *Journal of High Energy Physics*, (5), May 2006.
- [94] John Skilling. Nested Sampling. In *BAYESIAN INFERENCE AND MAXIMUM ENTROPY METHODS IN SCIENCE AND ENGINEERING: 24th International Workshop on Bayesian Inference and Maximum Entropy Methods in Science and Engineering*, pages 395–405. AIP.
- [95] P F Smith. Terrestrial searches for new stable particles. *Contemporary Physics*, 29(2):159–186, March 1988.
- [96] P F Smith, J R J Bennett, G J Homer, J D Lewin, H E Walford, and W A Smith. A search for anomalous hydrogen in enriched D₂O, using a time-of-flight spectrometer. *Nuclear Physics B*, 206(3):333–348, October 1982.
- [97] Martin Spangenberg. Calorimeter calibration and search for R-hadrons at $\sqrt{s} = 7\text{TeV}$ with the ATLAS experiment. Master’s thesis, Niels Bohr Institute.
- [98] David Spergel and Paul Steinhardt. Observational Evidence for Self-Interacting Cold Dark Matter. *Physical Review Letters*, 84(17):3760–3763, April 2000.
- [99] W J Stirling. Parton luminosity and cross section plots.
- [100] Super-Kamiokande Collaboration. Evidence for Oscillation of Atmospheric Neutrinos. *Physical Review Letters*, 81(8):1562–1567, August 1998.
- [101] The ATLAS Collaboration. ATLAS pixel detector electronics and sensors. *Journal of Instrumentation*, 3(07):P07007–P07007, July 2008.
- [102] The ATLAS Collaboration. The ATLAS Experiment at the CERN Large Hadron Collider. *Journal of Instrumentation*, 3, August 2008.
- [103] The ATLAS Collaboration. Luminosity determination in pp collisions at $\sqrt{s} = 7\text{ TeV}$ using the ATLAS detector at the LHC. *Il Nuovo Cimento*, 71(4):1630, April 2011.
- [104] The ATLAS Collaboration. Particle Identification Performance of the ATLAS Transition Radiation Tracker. August 2011.
- [105] The ATLAS Collaboration. Search for stable hadronising squarks and gluinos with the ATLAS experiment at the LHC. *Physics Letters B*, B701(1):1–19, June 2011.
- [106] The ATLAS Collaboration. Observation of a new particle in the search for the Standard Model Higgs boson with the ATLAS detector at the LHC. *Physics Letters B*, 716(1):1–29, September 2012.
- [107] The ATLAS Collaboration. Search for Magnetic Monopoles in $\sqrt{s}=7\text{TeV}$ pp Collisions with the ATLAS Detector. *Physical Review Letters*, 109(26):261803, December 2012.

- [108] The ATLAS Collaboration. dE/dx measurement in the ATLAS SCT detector and its potential for particle identification and performance tracking. July 2013.
- [109] The ATLAS Collaboration. Improved luminosity determination in pp collisions at $\sqrt{s} = 7$ TeV using the ATLAS detector at the LHC. *European Physical Journal C*, 73(8):1–39, 2013.
- [110] The ATLAS Collaboration. Search for long-lived stopped R-hadrons decaying out of time with pp collisions using the ATLAS detector. *Physical Review D*, 88(11):112003, December 2013.
- [111] The ATLAS Collaboration. Searches for heavy long-lived sleptons and R-hadrons with the ATLAS detector in pp collisions at. *Physics Letters B*, February 2013.
- [112] The CDF Collaboration. Search for Long-Lived Massive Charged Particles in 1.96 TeV pp^- Collisions. *Physical Review Letters*, 103(2):021802, July 2009.
- [113] The CMS Collaboration. Observation of a new boson at a mass of 125 GeV with the CMS experiment at the LHC. *Physics Letters B*, 716(1):30–61, September 2012.
- [114] The CMS Collaboration. Searches for long-lived charged particles in pp collisions at $\sqrt{s} = 7$ and 8 TeV. *arXiv.org*, page 122. 45 p, May 2013.
- [115] The D0 Collaboration. Search for charged massive long-lived particles at $s = 1.96$ TeV. *Physical Review D*, 87(5):052011, March 2013.
- [116] The Daya Bay Collaboration. Observation of Electron-Antineutrino Disappearance at Daya Bay. *Physical Review Letters*, 108(17):171803, April 2012.
- [117] The H1 Collaboration. Measurement of anti-deuteron photoproduction and a search for heavy stable charged particles at HERA. *European Physical Journal C*, 36(4):413–423, August 2004.
- [118] The IceCube Collaboration. Energy Reconstruction Methods and Performance in the IceCube Neutrino Detector .
- [119] The IceCube Collaboration. Optical properties in deep glacial ice at the South Pole.
- [120] The IceCube Collaboration. The Design and Performance of IceCube DeepCore.
- [121] The IceCube Collaboration. Calibration and characterization of the IceCube photomultiplier tube. *Nuclear Instruments and Methods in Physics Research Section A: Accelerators, Spectrometers, Detectors and Associated Equipment*, 618(1-3):139–152, June 2010.
- [122] The IceCube-PINGU Collaboration. Letter of Intent: The Precision IceCube Next Generation Upgrade (PINGU). January 2014.
- [123] The KamLAND Collaboration. Precision Measurement of Neutrino Oscillation Parameters with KamLAND. *Physical Review Letters*, 100(22):221803, June 2008.
- [124] The MINOS Collaboration. Measurement of Neutrino and Antineutrino Oscillations Using Beam and Atmospheric Data in MINOS. *Physical Review Letters*, 110(25):251801, June 2013.
- [125] The Particle Data Group. Review of Particle Physics. *Physical Review D*, 86(1):010001, July 2012.
- [126] The Planck Collaboration. Planck 2013 results. I. Overview of products and scientific results. March 2013.

- [127] The SNO Collaboration. Measurement of the Rate of $\nu_e + d \rightarrow p + p + e^-$ Interactions Produced by B8 Solar Neutrinos at the Sudbury Neutrino Observatory. *Physical Review Letters*, 87(7):071301, July 2001.
- [128] The SNO Collaboration. Direct Evidence for Neutrino Flavor Transformation from Neutral-Current Interactions in the Sudbury Neutrino Observatory. *Physical Review Letters*, 89(1):011301, June 2002.
- [129] The SNO Collaboration. Combined analysis of all three phases of solar neutrino data from the Sudbury Neutrino Observatory. *Physical Review C*, 88(2):025501, August 2013.
- [130] P Verkerk, G Grynberg, B Pichard, M Spiro, S Zylberajch, M Goldberg, and P Fayet. Search for superheavy hydrogen in sea water. *Physical Review Letters*, 68(8):1116–1119, February 1992.
- [131] J Wess and B Zumino. Supergauge transformations in four dimensions. *Nuclear Physics B*, 70(1):39–50, February 1974.
- [132] G C Wick. Range of Nuclear Forces in Yukawa’s Theory. *Nature*, 142(3605):993–994, December 1938.
- [133] L Wolfenstein. Neutrino oscillations in matter. *Physical Review D*, 17(9):2369–2374, May 1978.
- [134] Stephen Wolfram. Abundances of new stable particles produced in the early universe. *Physics Letters B*, 82(1):65–68, March 1979.
- [135] T Yamagata, Y Takamori, and H Utsunomiya. Search for anomalously heavy hydrogen in deep sea water at 4000 m. *Physical Review D*, 47(3):1231–1234, February 1993.
- [136] Wei-Min Yang. Model of four generation fermions and cold dark matter and matter-antimatter asymmetry. *Physical Review D*, 87(9):095003, May 2013.
- [137] S Zimmermann. A search for stable massive particles carrying electric charges in the range of $2e$ to $6e$ in proton-proton collisions at $s = 7$ TeV recorded with the ATLAS detector at the LHC .
- [138] F Zwicky. Die Rotverschiebung von extragalaktischen Nebeln. *Helv.Phys.Acta*, 6:110–127, 1933.